Neck Injury Risk in Non-Neutral Position Rear Impact Scenarios Using a Reference Geometry-Based Repositioning

by

Matheus Seif Reis

A thesis

presented to the University of Waterloo

in fulfillment of the

thesis requirement for the degree of

Master of Applied Science

in

Mechanical and Mechatronics Engineering

Waterloo, Ontario, Canada, 2024

© Matheus Seif Reis 2024

Author's Declaration

This thesis consists of material all of which I authored or co-authored: see Statement of Contributions included in the thesis. This is a true copy of the thesis, including any required final revisions, as accepted by my examiners.

I understand that my thesis may be made electronically available to the public.

Statement of Contributions

Some of the thesis content has been previously published in a conference proceeding:

Reis, M. S., & Cronin, D. (2024). Neck Injury Risk in Out-of-Position Rear Impact Scenarios Using a Reference Geometry-Based Head Repositioning. *SAE International Journal of Transportation Safety*, *12*(2), 187–192. https://doi.org/10.4271/09-12-02-0020

MSR developed the methodology, performed the model simulations and data post-processing, and drafted the manuscript. DC conceptualized the project idea and planning, provided technical guidance, and reviewed the manuscript.

The co-author agrees with the evaluation of roles and contributions:

(Duane Cronin)

Abstract

Rear-end vehicle collisions may lead to whiplash-associated disorders (WADs), comprising a variety of neck and head pain responses. The source of WADs is an active area of research, but the facet joints, cervical spine ligaments, neck muscles, nerve roots, vertebral arteries, and intervertebral discs have been postulated to be potential injury sources. While most investigations focus on whiplash injuries in neutral position impacts, front-seat vehicle occupants tend to spend a significant amount of time outside the neutral axial head position. Multiple cervical tissues can experience increased mechanical loads and, consequently, higher injury risks during head-rotated impacts. Given the limited experimental data for non-neutral position rear impacts, computational human body models (HBMs) can inform the potential for tissue-level injury. Previous studies have considered external boundary conditions to reposition the head axially but were limited in reproducing a biofidelic movement for a detailed finite element (FE) head and neck model. The objectives of this study were to implement a novel head repositioning method using soft tissue stress initialization to achieve targeted axial head rotations, validate the model intervertebral motion against experimental data, and simulate neutral and non-neutral rear impacts to assess the model tissue-level response and quantify the injury risk.

The head and neck model was extracted from the detailed commercial Global Human Body Models Consortium (GHBMC) M50-O FE model, representing a 50th percentile male occupant. The repositioning used a novel method to achieve equilibrium in the target axial rotations of 24.5°, 33.5°, 42.5°, 51.5°, and 60.5°, by pre-stretching the neck soft tissues. The head-rotated models underwent verification tests to ensure the target positions and equilibrium were achieved, and the method was validated by comparing spinal rotations to experimental results. A neutral position and five head-rotated models were evaluated at three rear impact severities (4g, 7g, and 10g) with and without muscle activation. Head motion, ligament distractions, muscle strains, nerve root compressions, and annulus fibrosus (AF) strains were assessed and compared with physiological limits to estimate the injury risks.

The repositioning method was able to rotate the head to the five target positions, showing general agreement with reported intervertebral rotations. Under the rear impact scenarios, higher axial head rotations increased the combined three-plane rotations experienced by the head. Increasing head rotations led to higher ligament distractions and muscle strains during rear impacts, increasing their potential for injury. The trends for AF strains varied depending on the muscle activation, with peak strains being observed for initial rotations of 0° and 60.5° without muscle contraction and only for 0°

with muscle contraction. Overall, muscle activation decreased ligament displacements, muscle strains, and AF strains, while higher impact severity increased the injury risk for these same tissues. Nerve root compression was minimally affected by head rotation, muscle activation, and impact severity. The models predicted injury potential for the ligaments and muscles starting at a 4g rear impact acceleration and for the AF starting at 7g, particularly under high head rotations. Therefore, the proposed repositioning method introduced in this study enabled the model to achieve steady head rotations with realistic cervical spine movements, increasing the biofidelity of non-neutral rear impact simulations. The tissue-level assessment revealed the effect of varying head rotations, muscle activation, and impact severities on cervical tissues, allowing for a comprehensive estimation of injury thresholds across ligaments, muscles, nerve roots, and AFs. The results of this study can be applied to future assessments and design of head restraints and protection systems.

Acknowledgements

I am deeply grateful for the support and encouragement I received from many people throughout my Master's journey.

First, I would like to thank my supervisor, Prof. Duane Cronin, for his exceptional support and guidance throughout my research. I am grateful to him for introducing me to the inspiring field of impact biomechanics, where I was able to explore fascinating topics in a prestigious research group.

I would like to express my gratitude to my parents, José and Estrela, and my brother, Thiago, for their enduring love and emotional support. Despite the distance, their presence and assurance always felt close and were a constant source of strength throughout my journey. I am also thankful to my aunts, cousins, and relatives for their unconditional support and belief in me.

I would like to thank my girlfriend, Elly, for her unwavering love, support, and patience. Her presence made this adventure much more enjoyable, and I am grateful to have her by my side.

I would like to thank my friends João Paulo and Gustavo for their generous hospitality from even before my move to Canada and for the unforgettable memories together. I also extend my thanks to my friend Lucas, who was a supportive companion during my studies.

I would like to thank the Impact Mechanics and Material Characterization (IMMC) group for being such wonderful colleagues and for all the moments together. Special thanks to my mentors, Jeffrey Barker, Miguel Corrales, and Aleksander Rycman, for guiding me from the introductions to the complex debugging of the models.

I would like to acknowledge the Global Human Body Models Consortium (GHBMC) for the detailed head and neck model and the Digital Research Alliance of Canada for computing resources.

I would like to acknowledge the Natural Sciences and Engineering Research Council of Canada and the Canada Research Chairs Program for the financial support.

Dedication

To my parents and brother.

Table of Contents

Author's Declaration ii

Statement of Contributions iii

Abstract iv

Acknowledgements vi

Dedication vii

List of Figures xii

List of Tables xix

List of Abbreviations xx

Chapter 1 Introduction 1

1.1 Research Motivation 1

1.2 Research Objectives 2

1.3 Thesis Organization 3

Chapter 2 Background 5

2.1 Human Neck Anatomy 5

2.1.1 Anatomical and Motion Terminologies 5

2.1.2 Vertebrae 6

2.1.3 Intervertebral Discs 11

2.1.4 Facet Joints 12

2.1.5 Ligaments 13

2.1.6 Spinal Cord and Nerves 20

2.1.7 Muscles 22

2.2 Whiplash-Associated Disorders 31

2.2.1 Symptoms and Classification 31

2.2.2 Impact Direction and Severity Thresholds 33
2.2.3 Pain Sources 34
2.3 Non-Neutral Position Impact Scenarios 41
2.3.1 Head Positions of Front-Seat Occupants 41
2.3.2 Whiplash Injuries in Non-Neutral Position Impacts 41
2.4 Human Body Models 43
2.4.1 Anthropomorphic Test Devices 43
2.4.2 Finite Element Human Models 44
2.5 Numerical Modelling of Non-Neutral Position Impacts 45
2.5.1 Experimental Rear Impact Studies for Boundary Conditions 45
2.5.2 Computational Repositioning Methods 47
2.5.3 Non-Neutral Position Rear Impact Studies 48
2.6 GHBMC Human Body Models 50
2.6.1 Description of GHBMC M50-O Neck Model 51
2.6.2 Validation of GHBMC M50-O Neck Model 58
2.6.3 Muscle Activation in the GHBMC M50-O Neck Model 59
2.7 Stress Initialization in Finite Element Models 62
Chapter 3 Methods 65
3.1 Implementation and Verification of a Novel Head Repositioning Method 66
3.1.1 Development of a Reference Geometry-Based Repositioning 66
3.1.2 Verification of Head Stabilization and Validation of Intervertebral Rotations 69
3.2 Assessment of Neutral and Non-Neutral Head Position Models in Rear Impact Scenarios 70
3.2.1 Rear Impact Boundary Conditions 71
3.2.2 Muscle Activation Schemes 73

3.2.3 Kinematics Comparison 74
3.2.4 Soft Tissue Injury Evaluation 74
Chapter 4 Results 81
4.1 Reference Geometry-Based Head Repositioning 81
4.1.1 Head Repositioning to Target Rotations 81
4.1.2 Verification of Head Stabilization 82
4.1.3 Validation of Intervertebral Rotations 84
4.2 Neutral and Non-Neutral Head Position Models in Rear Impact Scenarios 85
4.2.1 Kinematics Comparison 86
4.2.2 Ligament Distraction Evaluation 89
4.2.3 Muscle Strain Evaluation 94
4.2.4 Nerve Root Compression Evaluation 96
4.2.5 Annulus Fibrosus Strain Evaluation 97
Chapter 5 Discussion 99
5.1 Head Equilibrium and Intervertebral Kinematics in Reference Geometry-Based Head Repositioning 99
5.1.1 Development of a Novel Repositioning Method 99
5.1.2 Validation against Experimental Intervertebral Motion 100
5.2 Head Motion Analysis in Neutral and Non-Neutral Position Rear Impact Scenarios 101
5.3 Tissue-Level Response in Neutral and Non-Neutral Position Rear Impact Scenarios 104
5.3.1 Influence of Initial Head Position on Soft Tissue Responses 104
5.3.2 Influence of Muscle Activation on Soft Tissue Responses 106
5.3.3 Influence of Impact Severity on Soft Tissue Responses 107
5.3.4 Evaluation of Soft Tissue Injury Risks 108

5.4 Study Limitations 111
Chapter 6 Conclusions 113
Chapter 7 Recommendations 115
Letters of Copyright Permission 116
References 123
Appendix A Rear Impact Kinematics 143
Appendix B Ligament Distraction Results 146
Appendix C Muscle Strain Results 152
Appendix D Intervertebral Foramen Height and Width Reduction Results 156
Appendix E Annulus Fibrosus Strain Results 158

List of Figures

Figure 2-1: Anatomical planes and directions. 5
Figure 2-2: Primary neck motion terminology. 6
Figure 2-3: Lateral view of the human vertebral column and its regions. 7
Figure 2-4: Typical structure of a cervical vertebra (superior and lateral views) 8
Figure 2-5: Structure of the first cervical vertebra (superior view). 9
Figure 2-6: Structure of the second cervical vertebra (superior and lateral views). 10
Figure 2-7: Vertebra bone composition (section view). 11
Figure 2-8: Location and structure of the intervertebral disc. 12
Figure 2-9: Typical structure of a synovial joint. 13
Figure 2-10: Lateral section view of the spinal ligaments 14
Figure 2-11: Lateral view of the spinal ligaments. 15
Figure 2-12: Anterior view of the occipital-atlanto-axial ligaments. 16
Figure 2-13: Posterior view of the occipital-atlanto-axial ligaments. 17
Figure 2-14: Posterior section view of the occipital-atlanto-axial ligaments. 18
Figure 2-15: Lateral section view of the occipital-atlanto-axial ligaments. 19
Figure 2-16: Typical mechanical response of ligaments with their different response regions. 20
Figure 2-17: Lateral scheme (a) and superior section view (b) of the spinal cord and nerves. 21
Figure 2-18: Lateral view of the neck muscles 23
Figure 2-19: Anterior view of the neck muscles. 24
Figure 2-20: Anterior view of the anterior and lateral vertebral muscles 25
Figure 2-21: Posterior view of superficial neck muscles. 26
Figure 2-22: Posterior view of deep neck muscles. 27
Figure 2-23: Hierarchical structure of skeletal muscles. 28
Figure 2-24: Arrangement of actin and myosin filaments in the sarcomere. 29
Figure 2-25: Sliding actin and myosin filaments during muscle contraction. 30
Figure 2-26: Relations between HBM inputs (blue) and outputs (orange) to estimate injury potential. 43
Figure 2-27: Forward-dynamic (a) and inverse-dynamic (b) repositioning approaches. 47
Figure 2-28: GHBMC M50-O full-body model. 50
Figure 2-29: GHBMC M50-O head and neck model. 51

Figure 2-30: GHBMC M50-O vertebral model. 52
Figure 2-31: GHBMC M50-O intervertebral disc model. 53
Figure 2-32: GHBMC M50-O annular fiber orientations for the five concentric layers. 54
Figure 2-33: GHBMC M50-O ligament models. 55
Figure 2-34: GHBMC M50-O passive and active muscle models. 56
Figure 2-35: GHBMC M50-O adipose tissue and skin models. 57
Figure 2-36: Quadrant division for the GHBMC M50-O active muscle elements. 59
Figure 2-37: Muscle activation curve for the extensor (20%) and flexor (100%) muscles. 61
Figure 2-38: Scaling factor of the muscle activation based on the stretch (a) and strain rate (b). 62
Figure 2-39: Comparison between models without (a) and with (b) stress initialization using reference geometry. 64
Figure 3-1: Implementation of the reference geometry-based head repositioning: prescribed skull rotation to define reference geometry (Stage 1) and model repositioning to a head-turned equilibrium position resulting from soft tissue pre-stretching (Stage 2). 67
Figure 3-2: Prescribed axial rotation for the skull (Stage 1 of repositioning). 68
Figure 3-3: Additional boundary conditions: axial rotation of the skull rigid part (a) and global damping (b). 68
Figure 3-4: Calculation of Euler angles representing the relative rotation between the skull and T1 vertebra. 70
Figure 3-5: Experimental T1 kinematics (a) and integrated T1 inputs (b) for a 4g rear impact scenario (Ono et al., 1997; Sato et al., 2014). 71
Figure 3-6: Experimental T1 kinematics (a) and integrated T1 inputs (b) for a 7g rear impact scenario (Deng, 1999). 72
Figure 3-7: Experimental T1 kinematics (a) and integrated T1 inputs (b) for a 10g rear impact scenario (Deng, 1999). 73
Figure 3-8: Adapted muscle activation curves for the non-neutral position impact simulations. 74
Figure 3-9: Neck ligament implementation, including 1D tension-only and 2D shell elements. 75
Figure 3-10: Displacement evaluation of capsular (a) and cruciform (b) ligaments. 76
Figure 3-11: Schematic of the method to obtain the strain in the direction of the fibers for each muscle solid element. 77

Figure 3-12: Definition of the section and nodes to obtain the foramen height (h) and width (w) between two vertebrae of the model. 78
Figure 3-13: Calculation of the average fiber-direction strains for each quadrant of the annular collagen fibers. 80
Figure 4-1: Correlation to estimate the initial head rotation (Stage 1) that would rotate the model to a target position using soft tissue pre-stretching (Stage 2). 81
Figure 4-2: Head and neck models repositioned to the five target head rotations using the reference geometry approach. 82
Figure 4-3: Axial head-T1 rotation for the five repositioned models during the stabilization phase... 83
Figure 4-4: Lateral bending (a) and flexion/extension (b) between head and T1 for the five repositioned models during the stabilization phase. 83
Figure 4-5: Intervertebral axial rotation comparison between the model with a 51.5° head rotation and the experiment with a 53.3° head rotation (Ivancic, 2013). 85
Figure 4-6: Motion sequence of the head-rotated models during a 7g rear impact scenario without muscle activation. 86
Figure 4-7: Head-T1 axial rotation under a 7g rear impact, without and with muscle activation for five head axial rotation positions. 87
Figure 4-8: Head-T1 lateral bending under a 7g rear impact condition, without and with muscle activation for five head axial rotation positions. 87
Figure 4-9: Head-T1 flexion/extension under a 7g rear impact condition, without and with muscle activation for five head axial rotation positions. 88
Figure 4-10: Maximum quadrant displacement of capsular ligaments during a 7g rear impact scenario without and with muscle activation compared with the response regions (Mattucci et al., 2012, 2013) for each intervertebral level. 89
Figure 4-11: Average displacement of interspinous ligaments during a 7g rear impact scenario without and with muscle activation compared with the response regions (Mattucci et al., 2012) for each intervertebral level. 90
Figure 4-12: Average displacement of anterior longitudinal ligaments during a 7g rear impact scenario without and with muscle activation compared with the response regions (Mattucci et al., 2012) for each intervertebral level. 91

Figure 4-13: Average displacement of posterior longitudinal ligaments during a 7g rear impact scenario without and with muscle activation compared with the response regions (Mattucci et al., 2012) for each intervertebral level. 92
Figure 4-14: Average displacement of ligamenta flava during a 7g rear impact scenario without and with muscle activation compared with the response regions (Mattucci et al., 2012) for each intervertebral level. 92
Figure 4-15: Average displacement of upper cervical spine ligaments during a 7g rear impact scenario without and with muscle activation compared with the response regions (Mattucci et al., 2013) for each ligament. 93
Figure 4-16: 95th percentile muscle fiber-direction strains during a 7g rear impact scenario without muscle activation compared with the failure region for non-activated muscles (Best et al., 1995; Morrow et al., 2010). 94
Figure 4-17: 95th percentile muscle fiber-direction strains during a 7g rear impact scenario with muscle activation compared with the failure region for activated muscles (Hasselman et al., 1995). 95
Figure 4-18: Maximum intervertebral foramen height reductions during a 7g rear impact scenario without and with muscle activation compared with the threshold values. 96
Figure 4-19: Maximum intervertebral foramen width reductions during a 7g rear impact scenario without and with muscle activation compared with the threshold values. 97
Figure 4-20: Maximum quadrant fiber-direction strain of annulus fibrosus during a 7g rear impact scenario without and with muscle activation compared with the failure corridor (Iatridis et al., 2005) for each intervertebral level. 98
Figure 5-1: Peak head-T1 extension for the three impact severities, without and with muscle activation. 101
Figure 5-2: Maximum variation in head-T1 lateral bending for the three impact severities, without and with muscle activation. 103
Figure 5-3: Maximum variation in head-T1 axial rotation for the three impact severities, without and with muscle activation. 104
Figure 5-4: Stretching of Hill-type muscle elements reducing the effect of muscle activation on models with high head rotation. 107
Figure A-1: Head-T1 axial rotation under a 4g rear impact condition without and with muscle activation for each head position. 143

Figure A-2: Head-T1 axial rotation under a 10g rear impact condition without and with muscle activation for each head position. 143
Figure A-3: Head-T1 lateral bending under a 4g rear impact condition without and with muscle activation for each head position. 144
Figure A-4: Head-T1 lateral bending under a 10g rear impact condition without and with muscle activation for each head position. 144
Figure A-5: Head-T1 flexion/extension under a 4g rear impact condition without and with muscle activation for each head position. 145
Figure A-6: Head-T1 flexion/extension under a 10g rear impact condition without and with muscle activation for each head position. 145
Figure B-1: Maximum quadrant displacement of capsular ligaments during a 4g rear impact scenario without and with muscle activation compared with the response regions (Mattucci et al., 2012, 2013) for each intervertebral level. 146
Figure B-2: Maximum quadrant displacement of capsular ligaments during a 10g rear impact scenario without and with muscle activation compared with the response regions (Mattucci et al., 2012, 2013) for each intervertebral level. 146
Figure B-3: Average displacement of interspinous ligaments during a 4g rear impact scenario without and with muscle activation compared with the response regions (Mattucci et al., 2012) for each intervertebral level. 147
Figure B-4: Average displacement of interspinous ligaments during a 10g rear impact scenario without and with muscle activation compared with the response regions (Mattucci et al., 2012) for each intervertebral level. 147
Figure B-5: Average displacement of anterior longitudinal ligaments during a 4g rear impact scenario without and with muscle activation compared with the response regions (Mattucci et al., 2012) for each intervertebral level. 148
Figure B-6: Average displacement of anterior longitudinal ligaments during a 10g rear impact scenario without and with muscle activation compared with the response regions (Mattucci et al., 2012) for each intervertebral level. 148
Figure B-7: Average displacement of posterior longitudinal ligaments during a 4g rear impact scenario without and with muscle activation compared with the response regions (Mattucci et al., 2012) for each intervertebral level. 149

Figure B-8: Average displacement of posterior longitudinal ligaments during a 10g rear impact scenario without and with muscle activation compared with the response regions (Mattucci et al., 2012) for each intervertebral level. 149
Figure B-9: Average displacement of ligamenta flava during a 4g rear impact scenario without and with muscle activation compared with the response regions (Mattucci et al., 2012) for each intervertebral level. 150
Figure B-10: Average displacement of ligamenta flava during a 10g rear impact scenario without and with muscle activation compared with the response regions (Mattucci et al., 2012) for each intervertebral level. 150
Figure B-11: Average displacement of upper cervical spine ligaments during a 4g rear impact scenario without and with muscle activation compared with the response regions (Mattucci et al., 2013) for each ligament. 151
Figure B-12: Average displacement of upper cervical spine ligaments during a 10g rear impact scenario without and with muscle activation compared with the response regions (Mattucci et al., 2013) for each ligament. 151
Figure C-1: 95th percentile muscle fiber-direction strains during a 4g rear impact scenario without muscle activation compared with the failure region for non-activated muscles (Best et al., 1995; Morrow et al., 2010). 152
Figure C-2: 95th percentile muscle fiber-direction strains during a 4g rear impact scenario with muscle activation compared with the failure region for activated muscles (Hasselman et al., 1995). 153
Figure C-3: 95th percentile muscle fiber-direction strains during a 10g rear impact scenario without muscle activation compared with the failure region for non-activated muscles (Best et al., 1995; Morrow et al., 2010). 154
Figure C-4: 95th percentile muscle fiber-direction strains during a 10g rear impact scenario with muscle activation compared with the failure region for activated muscles (Hasselman et al., 1995). 155
Figure D-1: Maximum intervertebral foramen height reductions during a 4g rear impact scenario without and with muscle activation compared with the threshold values. 156
Figure D-2: Maximum intervertebral foramen width reductions during a 4g rear impact scenario without and with muscle activation compared with the threshold values. 156
Figure D-3: Maximum intervertebral foramen height reductions during a 10g rear impact scenario without and with muscle activation compared with the threshold values. 157

Figure D-4: Maximum intervertebral foramen width reductions during a 10g rear impact scenario without and with muscle activation compared with the threshold values. 157
Figure E-1: Maximum quadrant fiber-direction strain of annulus fibrosus during a 4g rear impact scenario without and with muscle activation compared with the failure corridor (Iatridis et al., 2005) for each intervertebral level. 158
Figure E-2: Maximum quadrant fiber-direction strain of annulus fibrosus during a 10g rear impact scenario without and with muscle activation compared with the failure corridor (Iatridis et al., 2005) for each intervertebral level. 158

List of Tables

Table 2-1: AIS injury scale and examples for the cervical spine. 32
Table 2-2: Clinical classification of WADs. 33
Table 2-3: Average change in velocity, mean acceleration and peak acceleration for different injury classifications. 34
Table 2-4: Mechanical properties of the vertebral components in the GHBMC M50-O model. 52
Table 2-5: Material constants for the annular ground substance model. 54
Table 2-6: Material constants for the skin Ogden model. 58
Table 3-1: Summary of rear impact simulations. 65
Table 3-2: Average range of motion (standard deviation) for each spinal level for the ligamentous spine models undergoing right and left axial rotation (Ivancic, 2013). 69
Table 3-3: IVF height and width reduction thresholds based on the experimental dimensions of the nerve root (Alleyne et al., 1998). 79
Table 4-1: Axial head rotations used in soft tissue nodal selection (Stage 1) to achieve the target rotations using reference geometries (Stage 2) and the differences from the nominal target angles. 82
Table 4-2: Head-T1 rotation values (150 ms), their maximum variation (between 150 and 250 ms), and the stabilization threshold for the head-rotated models. 84
Table 5-1: Summary of neck injury evaluation. 109

List of Abbreviations

AA-AM	Anterior atlanto-axial membrane
AA-OM	Anterior occipital-axial membrane
AF	Annulus fibrosus
AIS	Abbreviated injury scale
ALL	Anterior longitudinal ligament
ATD	Anthropomorphic test devices
CL	Capsular ligament
CMA	Co-contraction muscle activation
COE	Center of Expertise
EMG	Electromyography
FE	Finite element
GHBMC	Global Human Body Model Consortium
HBM	Human body model
ISL	Interspinous ligament
ISS	Injury Severity Score
IVF	Intervertebral foramen
LF	Ligamenta flava
LN	Ligamentum nuchae
MMA	Maximum muscle activation
MRI	Magnetic resonance imaging
NMA	No muscle activation
NP	Nucleus pulposus
OMA	Optimized muscle activation
PA-AM	Posterior atlanto-axial membrane
PA-OM	Posterior occipital-axial membrane
PCSA	Physiologic cross-section area
PLL	Posterior longitudinal ligament
PMHS	Post-mortem human subject
THUMS	Total Human Model for Safety
TL	Transverse ligament
TM	Tectorial membrane
ViVA	Virtual Vehicle-Safety Assessment
WAD	Whiplash-associated disorder

Chapter 1
Introduction

1.1 Research Motivation

Whiplash injuries are the most frequent injury resulting from a motor vehicle crash (Berglund et al., 2003). The annual societal cost of whiplash-associated disorders (WADs) was estimated to reach $28 billion in the United States (Freeman, 1998), £3.1 billion in the United Kingdom (Galasko et al., 2002), and €10 billion in Europe (Richter et al., 2000). An evidence synthesis performed between 1980 and 2007 showed that the occurrence of WADs has considerably increased over these three decades in Western countries (Holm et al., 2009). The annual incident in North America and Western Europe was estimated to be more than 300 per 100,000 inhabitants (Holm et al., 2009). In Canada, the incidence of WADs can vary considerably depending on the province. A study in Quebec showed an occurrence rate of 70 whiplash compensations per 100,000 inhabitants in 1987 (Spitzer et al., 1995). In Saskatchewan, the annual incidence of insurance claims for whiplash injuries was 677 per 100,000 inhabitants between 1994 and 1995 (J. D. Cassidy et al., 2000). Whiplash injuries accounted for 68% and 83% of insurance claims for traffic injuries in British Columbia and Saskatchewan, respectively (J. D. Cassidy et al., 2000; Giroux, 1991). The recovery rates of whiplash patients have been estimated to be around 50%, meaning that approximately half of the individuals continue to experience symptoms in the long term (Carroll et al., 2008; Gargan & Bannister, 1994). Patients with a decrease in symptoms during the first 3 months are more susceptible to fully recovering (Kamper et al., 2008). High initial pain and disability, older age, and worse psychological health have been consistent factors for a poor prognosis of WADs (Carroll et al., 2008; Kamper et al., 2008).

The majority of whiplash studies were performed evaluating the occurrence of soft tissue injuries when the occupant had a neutral position with their head facing forward. In real life, drivers are required to scan the surroundings through eye and head movements in many driving situations. For example, driving safely through an intersection requires a large amplitude of gaze in the axial plane (Kito et al., 1989). In-car pilot studies observed that drivers spent 13.0% of the time outside the neutral axial head position with average peak angles of 35.7° (± 14.2°) and 42.5° (± 18.0°) for left and right cervical axial rotation (Shugg et al., 2011). Non-neutral positions for front-seat passengers happen even more frequently than for drivers, with axial head rotation occurring for 33% of the travel time (Reed et al., 2020). The axial rotation of the head modifies the alignment of the cervical spine, which redistributes the forces across active and passive neck structures. Non-neutral head and neck positions increase the

postural load, causing local muscle fatigue and discomfort (Lutz et al., 2001). During vehicle collisions, the combination of non-neutral occupant positions with impact forces can amplify the strains in the cervical soft tissues and potentialize the whiplash injury risk (Ivancic et al., 2006; Siegmund et al., 2008; Tominaga et al., 2006).

Current experimental testing of non-neutral rear impacts is limited to simplified cadaveric models, which may not accurately represent the in vivo biomechanical responses. In addition, human volunteer testing is restricted to non-injurious impact scenarios due to ethical concerns about human safety and well-being. In this context, numerical human body models (HBMs) can inform the potential for tissue-level response and injury risk. Although human neck rotations are achieved using muscle activation, reproducing axial rotation in a finite element (FE) model is a complex task. Due to insufficient data for defining realistic activation levels for the muscles, several authors have considered alternative head repositioning methods, such as external rotation boundary conditions. Previous numerical studies on head-rotated impacts have prescribed relative rotations between bony structures to achieve non-neutral head positions in FE head and neck models (Palepu, 2013; Shateri, 2012; Shateri & Cronin, 2015; Storvik & Stemper, 2011). These models have predicted increased ligament strains during head-rotated impacts, aligning with experimental findings. However, the head repositioning using external rotations has generated unrealistic intervertebral motion in some models. The absence of three-dimensional musculature and other soft tissues has also limited the biofidelity during impact scenarios. Therefore, the numerical repositioning studies have been limited in achieving a static head and neck non-neutral position with realistic intervertebral motion for a detailed HBM.

1.2 Research Objectives

The proposed research aimed to evaluate the potential for soft tissue injury during non-neutral position rear impacts using a detailed FE head and neck model. To achieve this goal, three objectives were defined: (1) implementing a novel computational head repositioning method using soft tissue stress initialization, (2) achieving targeted axial head rotations, verifying the model equilibrium, and validating the model intervertebral motion against experimental data, and (3) simulating neutral and non-neutral rear impacts to assess the tissue-level responses and quantify the injury risks.

The first objective was to develop a novel repositioning method using a stress initialization approach. A comprehensive literature review was performed on available computational repositioning methods and non-neutral position FE human models tested in whiplash-type impact simulations, identifying the

limitations of the available techniques. The requirements for a biofidelic head repositioning were listed and used to define the verification and validation metrics. Soft tissue pre-stretching was implemented in a detailed FE head and neck model, which generated initial stresses in the passive muscle, adipose tissue, and skin to rotate the head to stable non-neutral positions.

The second objective was to verify and validate the proposed repositioning method. In-car driving studies were used to define the typical non-neutral axial rotations of front-seat occupants, and five target head positions were selected based on these measurements. The detailed FE head and neck model used the proposed repositioning method to achieve the five target axial head rotations. The head-T1 rotations were tracked to verify the convergence to the target axial positions and the equilibrium of the repositioned head and neck model. With the models in steady non-neutral positions, the intervertebral motion of one of the models was monitored for each spinal level and compared to experimental data.

The third objective was to simulate rear impact scenarios with neutral and non-neutral position occupants to calculate the soft tissue responses and estimate the injury potentials during these conditions. After the verification and validation tests, the neutral and non-neutral position models were subjected to three different rear impact conditions to simulate their dynamic responses during rear-end vehicle collisions. The effect of muscle contraction was tested using two muscle activation schemes, which were adjusted to start with the impact conditions. An initial analysis of the head rotational motion was performed to identify the stages of whiplash and contribute to the successive tissue-level evaluation. The main sources of whiplash pain during non-neutral rear impacts were used to define the injury mechanisms to be studied in the FE model. The soft tissue responses during the rear impacts were monitored and compared with physiological limits to quantify the risk of injury in different impact conditions. The effects of head rotation, muscle activation, and impact severity on soft tissue responses were analyzed by comparing results from different cases.

1.3 Thesis Organization

This thesis is organized into seven chapters. Chapter 1 outlines the research problem and objectives. Chapter 2 provides background information necessary for understanding the subsequent sections of the thesis. Chapter 3 describes the methodology for developing the repositioning method, verifying and validating the head-rotated models, simulating rear impact conditions, and assessing the tissue-level responses and injury potentials for each simulation. Chapter 4 reports the repositioning and impact results, including verification of head stabilization, validation of intervertebral rotations, head

kinematics evaluation, neck soft tissue responses, and injury risks. Chapter 5 discusses the repositioning results, the influence of head position, impact severity, and muscle activation on the impact simulations, and the study limitations. Chapter 6 summarizes the research findings and presents the conclusions. Chapter 7 provides recommendations for future studies based on the research findings.

Chapter 2
Background

2.1 Human Neck Anatomy

2.1.1 Anatomical and Motion Terminologies

The definition of reference position, planes and directions is essential to standardize the description of human anatomy. The anatomic position of a human describes a reference posture where the individual is standing upright with arms and legs extended, and the head, palms of the hands, and toes are facing forward (Standring, 2016) (Figure 2-1).

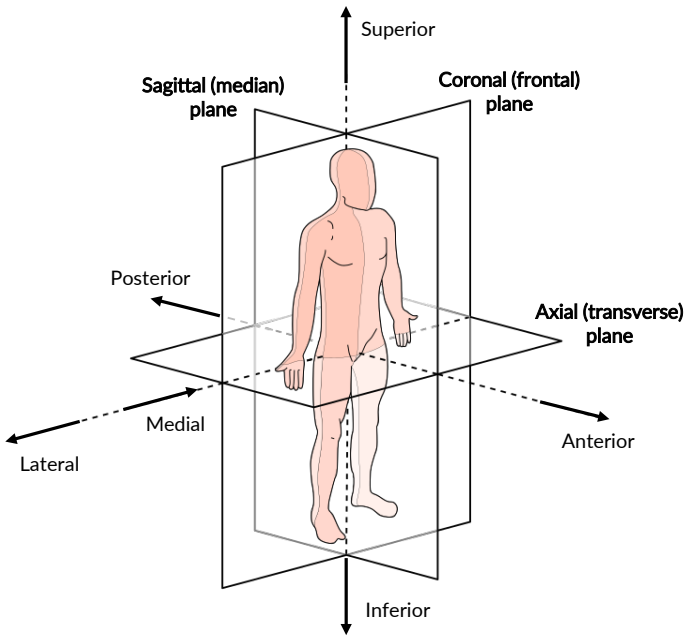


Figure 2-1: Anatomical planes and directions.

Note. Adapted from CFCF. (2014, June 9). *Anatomical Planes*. Wikimedia Commons. https://commons.wikimedia.org/wiki/File:Anatomical_Planes.svg.

Three orthogonal planes and their respective directions are defined in the anatomic position (Standring, 2016). The coronal (frontal) plane divides the body vertically into front and back sections. The anterior (ventral) and posterior (dorsal) directions are orthogonal to the coronal plane and point towards the

front and back of the body, respectively. The sagittal (median) plane divides the body vertically into left and right sections. Orthogonal to the sagittal plane, the lateral (distal) and medial directions point away from and towards the same plane, respectively. The axial (transverse) plane divides the body horizontally into top and bottom parts sections. The superior (cranial) and inferior (caudal) directions are orthogonal to the axial plane and point upwards to the head and downwards to the feet, respectively.

The primary motion of the head and neck can be divided into four basic movements, including flexion, extension, axial rotation, and lateral bending (Standring, 2016) (Figure 2-2). Flexion and extension refer to head and neck rotations around the lateral direction in the sagittal plane. Flexion is used for the anterior bending of the head, and extension is used for the posterior bending of the head. Axial rotation refers to the head and neck rotation around the superior-inferior direction in the axial plane. Lateral bending refers to the head and neck rotation around the anterior-posterior direction in the coronal plane.

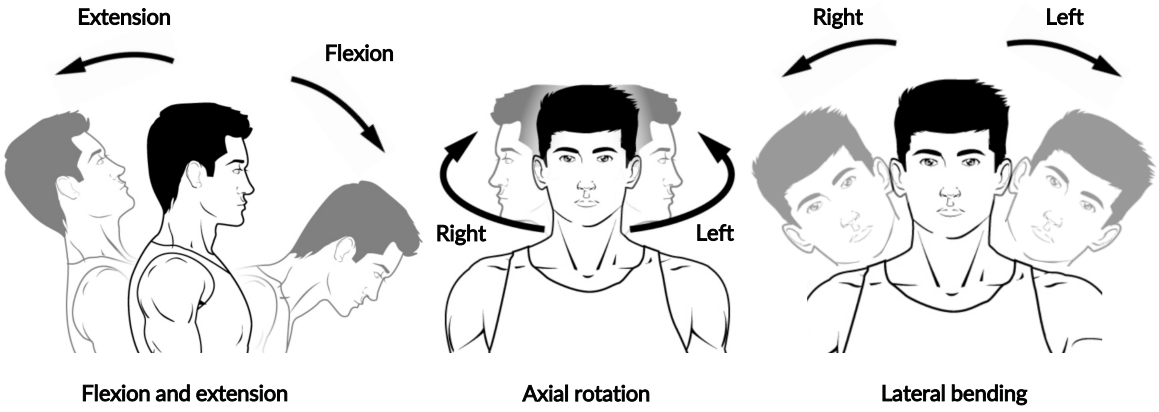


Figure 2-2: Primary neck motion terminology.

Note. Adapted from Betts, J. G., Desaix, P., Johnson, E., Johnson, J. E., Korol, O., Kruse, D., Poe, B., Wise, J. A., Womble, M., & Younge, K. A. (2022). *Anatomy and Physiology* (2nd ed.). OpenStax, Rice University. Access for free at openstax.org.

2.1.2 Vertebrae

The vertebral column is a curved structure composed of bones called vertebrae, extending from the neck to the lower back (Standring, 2016). Its main functions are to protect the spinal cord and nerve roots, to mechanically support the head and upper body, and to enable smooth movement through its various components. There are usually thirty-three vertebrae in the human body, being divided into five regions (cervical, thoracic, lumbar, sacral, and coccygeal) according to their curvatures and positions

in the vertebral column (Figure 2-3). In general, an adult human body has seven cervical (C1-C7), twelve thoracic (T1-T12), five lumbar (L1-L5), five sacral (S1-S5), and four coccygeal (Co1-Co4) vertebrae. Each vertebra is named as a concatenation of letters denoting its region, C, T, L, S, or Co, and a number indicating its position, starting from one and ascending in the inferior direction (Standring, 2016). The occipital bone in the skull is also referred to as C0 due to its connection with the first cervical vertebra (C1).

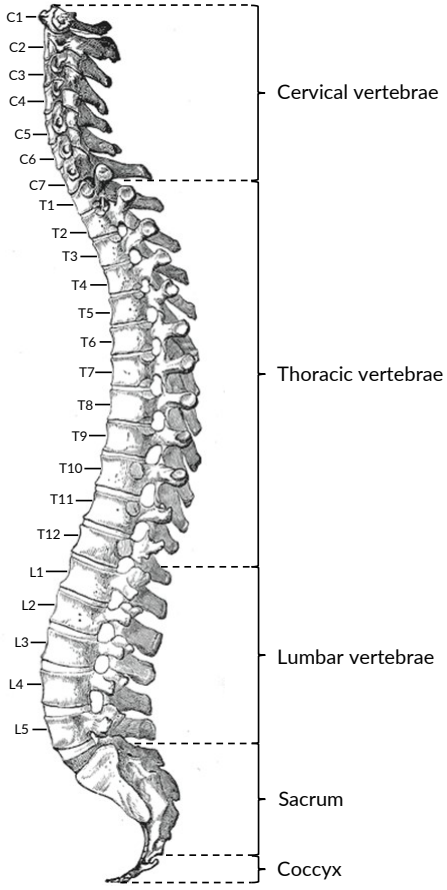


Figure 2-3: Lateral view of the human vertebral column and its regions.

Note. Adapted from Gray, H. (1918). *Anatomy of the Human Body* (20th ed.). Lea & Febiger.

The shape and size of the vertebrae vary depending on the function and position (Standring, 2016). The cervical spine has small and flexible bones to allow for an extensive range of motion for the head and neck. In contrast, thoracic and lumbar vertebrae are larger and more stable as they support more weight than the cervical portion. The sacral and coccygeal bones have the most distinct shapes as they are

merged into single structures, the sacrum and coccyx, to provide stability to the pelvic region (Standring, 2016). The presacral vertebrae (C1-L5) have similar features to facilitate their connections and the circulation of the central nervous system. The vertebral foramina are central openings in these vertebrae that align to form the vertebral canal, where the spinal cord is located. Similarly, the intervertebral foramina (IVFs) are lateral openings between adjacent vertebrae to allow the passage of the spinal nerves. The intervertebral discs can also be found between two subsequent presacral vertebrae, with the exception of the two first cervical segments (Standring, 2016).

The cervical segments can be divided into two groups. The upper cervical spine encompasses the first two vertebrae, C1 and C2, while the lower cervical spine considers the other five vertebrae, from C3 to C7 (Standring, 2016). In addition to their location, this division is based on the similarities in the general structure of the vertebrae. The lower cervical vertebrae are small and broad, being composed of a body, an arch, and seven processes (Standring, 2016) (Figure 2-4). The vertebral body is a large load-bearing structure located in the anterior portion of the vertebra. The anterior and posterior surfaces of the body provide attachment points to longitudinal ligaments, while the superior discal surface is saddle-shaped to prevent gliding movements between adjacent vertebrae. The vertebral arch connects the body and the processes through the pedicles and laminae. Pedicles are short and thick structures that attach to the sides of the vertebral body, while laminae are long and thin plates that connect to the pedicles and merge in the midsection, forming the posterior arch. The body and arch form the triangular-shaped vertebral foramen to accommodate the spinal cord (Standring, 2016).

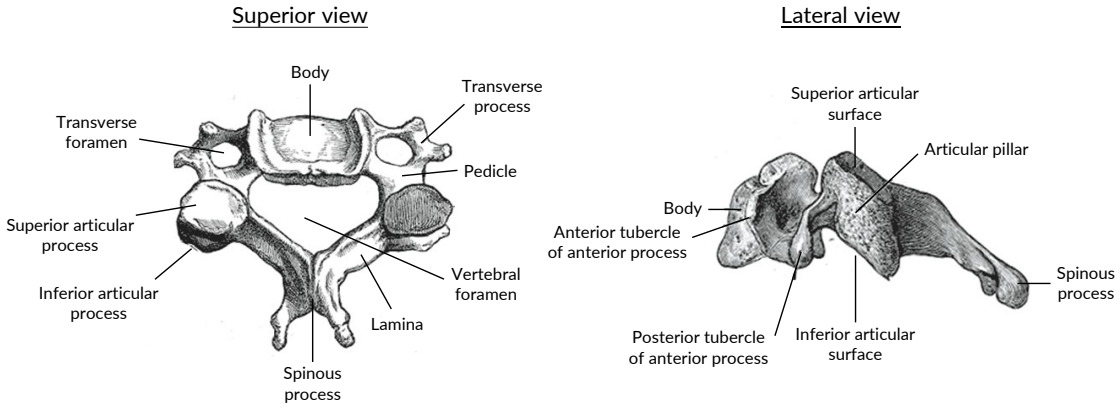


Figure 2-4: Typical structure of a cervical vertebra (superior and lateral views).

Note. Adapted from Gray, H. (1918). *Anatomy of the Human Body* (20th ed.). Lea & Febiger.

A lower cervical vertebra has one spinous, two transverse, and four articular processes (Standring, 2016). The spinous process emerges posteriorly from the laminae junction and acts as a lever arm for attached muscles that can control the vertebral movement. The transverse processes also connect to muscles and ligaments, being located anteriorly to the articular processes and laterally to the pedicles. The superior and inferior articular processes emerge from the connection of pedicles and laminae with the function of aligning and articulating adjacent vertebrae. Their superior and inferior surfaces, where adjacent vertebrae connect, are denoted articular facets. The transverse process and pedicle form the transverse foramen on each side to accommodate the vertebral artery (Standring, 2016).

In contrast to the lower cervical spine, the upper cervical segments have unique features. The first cervical vertebra, commonly referred to as the atlas, supports and facilitates the rotation of the skull (Standring, 2016) (Figure 2-5). The atlas does not have a vertebral body, which results in the absence of intervertebral discs connected to this bone. The ring-shaped vertebra comprises two lateral structures connected by the anterior and posterior arches. Each lateral structure is formed of a transverse foramen surrounded by the medial articular processes and the distal transverse process. The superior articular facets are shaped to accommodate the occipital condyles on the skull. The vertebral foramen is larger in the atlas, divided by the transverse ligament (TL) into an anterior compartment for the protuberance from the second vertebra and a posterior compartment for the spinal cord (Standring, 2016).

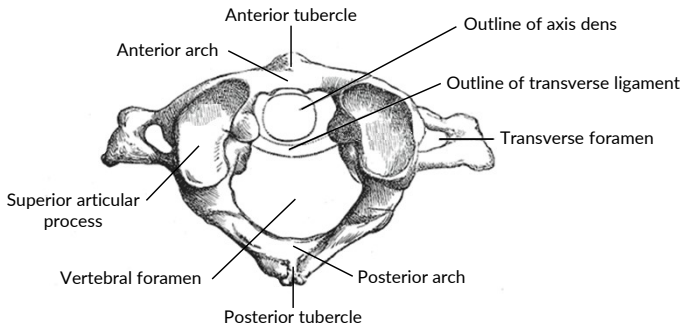


Figure 2-5: Structure of the first cervical vertebra (superior view).

Note. Adapted from Gray, H. (1918). *Anatomy of the Human Body* (20th ed.). Lea & Febiger.

The second cervical vertebrae, also referred to as the axis, is coupled with the atlas to assist the rotational motion of the head (Standring, 2016). The main feature of this vertebra is the strong odontoid process (dens), located superiorly to the vertebral body (Figure 2-6). Apical and alar ligaments are

connected to the dens, whose movement is restricted by the TL and anterior arch of the atlas. Compared to the lower cervical segments, the axis has thicker pedicles, laminae, and spinous process, but smaller transverse processes (Standring, 2016).

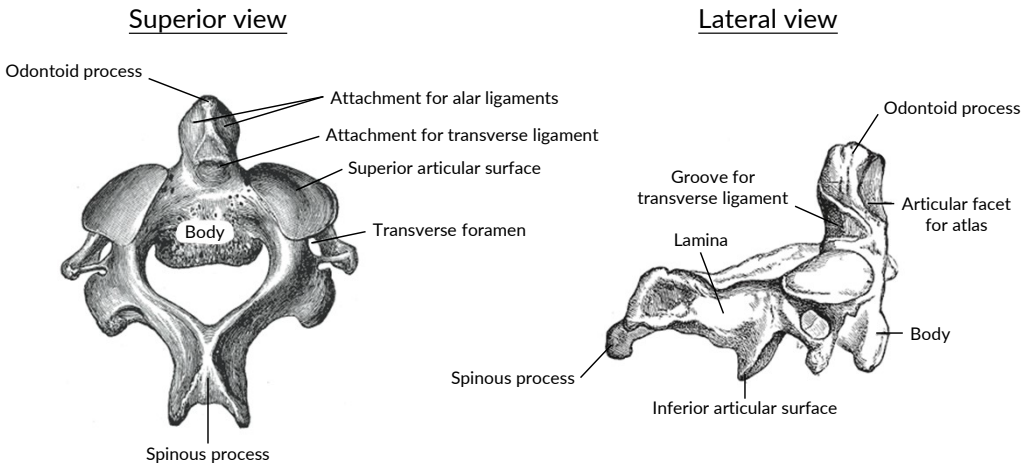


Figure 2-6: Structure of the second cervical vertebra (superior and lateral views).
Note. Adapted from Gray, H. (1918). *Anatomy of the Human Body* (20th ed.). Lea & Febiger.

Vertebrae are composed of a core of trabecular (cancellous) bone encompassed by a layer of cortical (compact) bone (Standring, 2016) (Figure 2-7). The vertebral body contains the most trabecular bone in the vertebra, while the arch and processes have thicker shells of cortical bone. Cortical bones have dense structures with elevated strength and stiffness, showing linear behavior under compression and bilinear under tension along the longitudinal direction (Morgan et al., 2018). In contrast, trabecular bones have a highly porous structure with a lower density, presenting a non-linear viscoelastic response (Morgan et al., 2018). The trabecular bone has lower mechanical strength than the cortical bone but can resist higher strains before failing. Both materials are anisotropic with the highest strength in compression (Morgan et al., 2018).

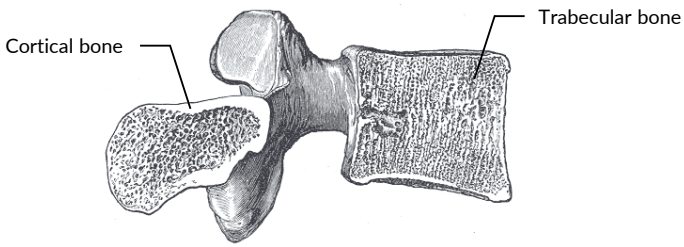


Figure 2-7: Vertebra bone composition (section view).

Note. Adapted from Gray, H. (1918). *Anatomy of the Human Body* (20th ed.). Lea & Febiger.

2.1.3 Intervertebral Discs

The intervertebral discs are the main joint between adjacent vertebral bodies from the second cervical segment to the first sacral segment (Standring, 2016). They are attached to the vertebrae through the vertebral endplates, which are thin layers of cartilage located longitudinally to the vertebral body. The intervertebral discs are also supported by longitudinal ligaments in their anterior and posterior surfaces. The anterior heights of the cervical discs are higher than the posterior dimensions, contributing to the lordotic curvature of the cervical spine (Standring, 2016). The intervertebral discs have the complementary roles of mechanical support by resisting compressive load and absorbing shock while assisting the mobility of the vertebral column.

Each intervertebral disc is composed of two main structures: the nucleus pulposus (NP) and the annulus fibrosus (AF) (Figure 2-8). The NP is a hydrated gel located internally within the disc, composed mainly of water, type-II collagen fibers, and proteoglycans (Standring, 2016). Due to its soft structure, the NP is highly deformable and mainly contributes to load distribution across the surfaces of the vertebra bodies. The AF is a fibrous ring that surrounds the NP in the intervertebral disc (Standring, 2016). Its structure consists of fifteen to twenty-five concentric sheets of collagen, known as lamellae. Adjacent laminae have alternating orientations to their collagenous fibers, usually aligned at ± 65° to the vertical. The outermost layers are harder and primarily composed of type-I collagen, while the innermost layers are softer and composed of type-II collagen (Standring, 2016). The orientation and composition of the fibrous layers allow for a combination of multidirectional load resistance, stiffness, and flexibility.

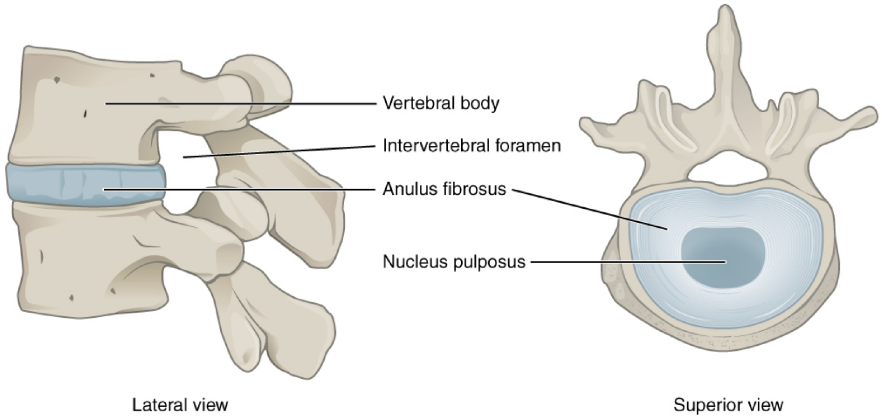


Figure 2-8: Location and structure of the intervertebral disc.

Note. Reproduced from Betts, J. G., Desaix, P., Johnson, E., Johnson, J. E., Korol, O., Kruse, D., Poe, B., Wise, J. A., Womble, M., & Younge, K. A. (2022). *Anatomy and Physiology* (2nd ed.). OpenStax, Rice University. Access for free at openstax.org.

2.1.4 Facet Joints

The facet (zygapophysial) joints are bilateral synovial joints connecting articular processes of adjacent vertebrae (Standring, 2016) (Figure 2-9). The articulating surfaces, which are the superior and inferior articular surfaces, are covered in slippery and smooth hyaline cartilages to reduce friction between the bones. The facet joint is surrounded by the fibrous capsule, a thin fibrous membrane that seals and provides stability to the joint (Standring, 2016). The synovial membrane is attached to the inner surfaces of the fibrous capsule and the articulating cartilages, being responsible for synthesizing the synovial fluid. This fluid is viscous due to the presence of hyaluronic acid and has the primary function of lubricating the joint to reduce friction between the articular surfaces (Standring, 2016).

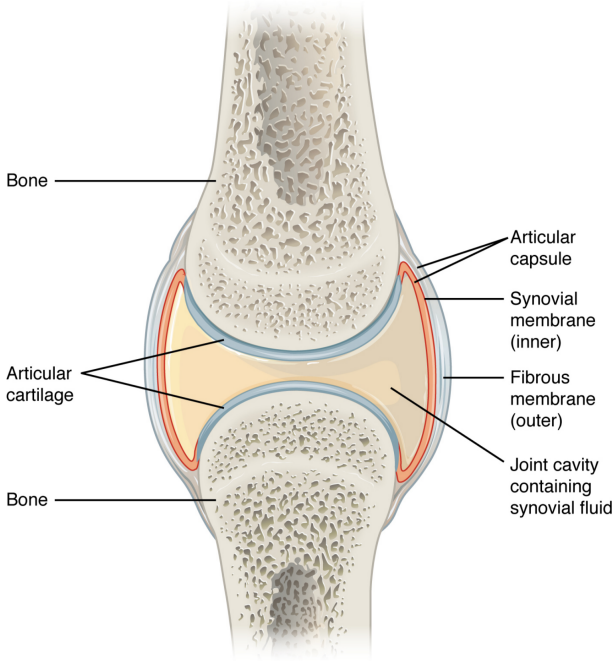


Figure 2-9: Typical structure of a synovial joint.

Note. Reproduced from Betts, J. G., Desaix, P., Johnson, E., Johnson, J. E., Korol, O., Kruse, D., Poe, B., Wise, J. A., Womble, M., & Younge, K. A. (2022). *Anatomy and Physiology* (2nd ed.). OpenStax, Rice University. Access for free at openstax.org.

The main functions of the facet joint are distributing the compressive load in the articular processes and limiting the relative movement between vertebrae, especially flexion and axial rotation (Yoganandan et al., 2001). The shape and orientation of the facet joints are highly affected by the vertebrae geometry and, consequently, by the spinal level (Nowitzke et al., 1994). The elliptical surfaces of the cervical facet joints form mean angles between 30° and 60° with the axial plane and 5° to 30° with the sagittal plane (Panjabi et al., 1993). These orientations create a coupled movement between axial rotation and lateral bending in the cervical spine (Bogduk & Mercer, 2000).

2.1.5 Ligaments

Ligaments are dense connective tissues that attach two bones together to provide joint stability and support (Standring, 2016). They are generally ribbon-shaped, but their structures are adapted to their function and position in the body. In the vertebral column, ligaments connect adjacent vertebrae and contribute to the spinal alignment and ranges of motion. Due to the unique vertebra features and absence

of intervertebral discs, the upper cervical spine ligaments differ considerably from the lower cervical spine and the rest of the vertebral column (Standring, 2016).

The longitudinal ligaments are strong bands connecting longitudinally the vertebral column. These multi-layered ligaments are attached to the surfaces of vertebral bodies and intervertebral discs (Standring, 2016). The anterior longitudinal ligament (ALL) connects the anterior surfaces of vertebral bodies and extends from the occipital bone to the upper sacrum (Figure 2-10). Between the skull and the axis, the ALL is attached to the anterior tubercle of the atlas. Conversely, the posterior longitudinal ligament (PLL) connects the posterior surfaces of the vertebral bodies from the axis to the sacrum (Figure 2-10). While both longitudinal ligaments assist in spine stabilization, the ALL and PLL have the specific roles of restricting neck extension and flexion, respectively.

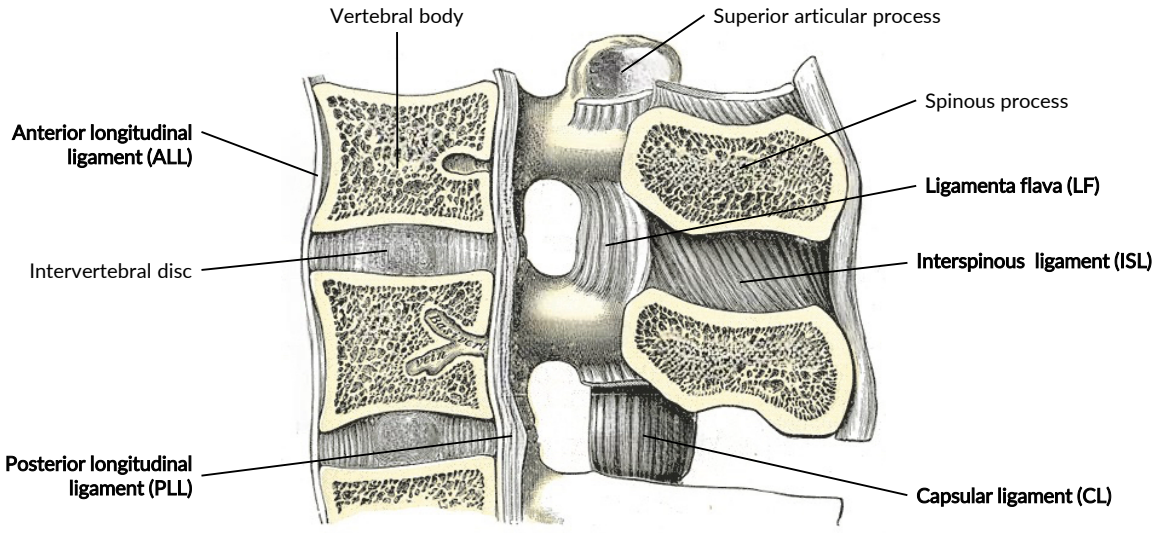


Figure 2-10: Lateral section view of the spinal ligaments.

Note. Adapted from Gray, H. (1918). *Anatomy of the Human Body* (20th ed.). Lea & Febiger.

The capsular ligament (CL) is attached peripherally to each articular process of adjacent vertebrae, enclosing the facet joint (Figure 2-10). The CL is the thickening of the fibrous capsule, being present in all intervertebral levels between the skull and the first sacral vertebra (Standring, 2016). While their primary functions are to seal and protect the articulation, the CL also resist excessive axial rotation and flexion of the spine. The ligamenta flava (LF) are located posteriorly to the vertebral canal, connecting the laminae of adjacent vertebrae from the axis to the sacrum (Figure 2-10). They are divided into two symmetric portions for each intervertebral level, extending from the articular to the spinous processes

of each lamina (Standring, 2016). Due to their posterior location in the vertebra, the LF can restrict the movement between subsequent laminae and resist neck flexion.

The interspinous ligament (ISL) is composed of thin sheets connecting the spinous processes of adjacent vertebrae from the atlas to the first sacral segment (Figure 2-10). The ISL extends from the root to the apex of each spinous process, connecting anteriorly with the LF and posteriorly with the nuchal ligament in the cervical region and with the supraspinous ligament in the thoracic and lumbar regions (Standring, 2016) (Figure 2-11). The ISL restrict the movement between subsequent spinous processes and limits neck flexion. The ligamentum nuchae (LN), also known as the nuchal ligament, has a unique membranous structure that connects the external occipital protuberance with the C7 spinous process (Figure 2-11). The LN is attached to the ISL and supraspinous ligaments, creating a midline partition for the left and right neck muscles (Standring, 2016). Apart from resisting neck flexion, the LN also provide a midline attachment for the muscles.

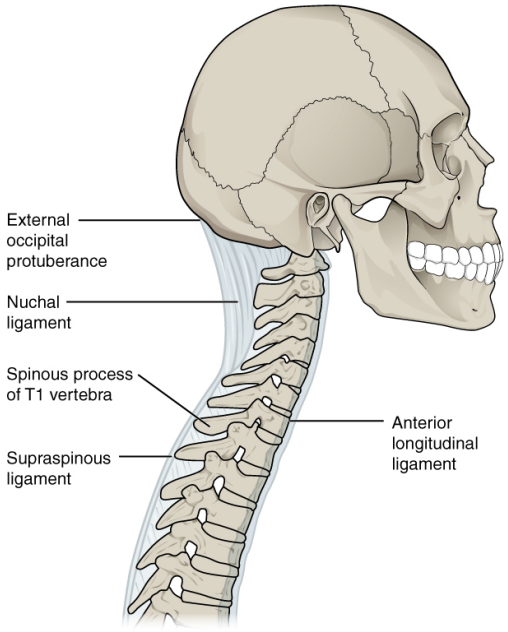


Figure 2-11: Lateral view of the spinal ligaments.

Note. Reproduced from Betts, J. G., Desaix, P., Johnson, E., Johnson, J. E., Korol, O., Kruse, D., Poe, B., Wise, J. A., Womble, M., & Younge, K. A. (2022). *Anatomy and Physiology* (2nd ed.). OpenStax, Rice University. Access for free at openstax.org.

The upper cervical spine ligaments can be divided according to their attachments with the skull, atlas, and axis. The atlanto-occipital ligaments connect the atlas to the skull (Standring, 2016). The anterior atlanto-occipital membrane (AA-OM) attaches the anterior arch of the atlas to the foramen magnum in the skull (Figure 2-12). Conversely, the posterior atlanto-occipital membrane (PA-OM) connects the posterior arch of the atlas to the foramen magnum (Figure 2-13). Due to the absence of an atlantal vertebral body, the AA-OM and PA-OM perform analogous functions to the ALL and PLL in resisting extension and flexion, respectively. The ALL, CLs, and LN also connect the atlas to the skull.

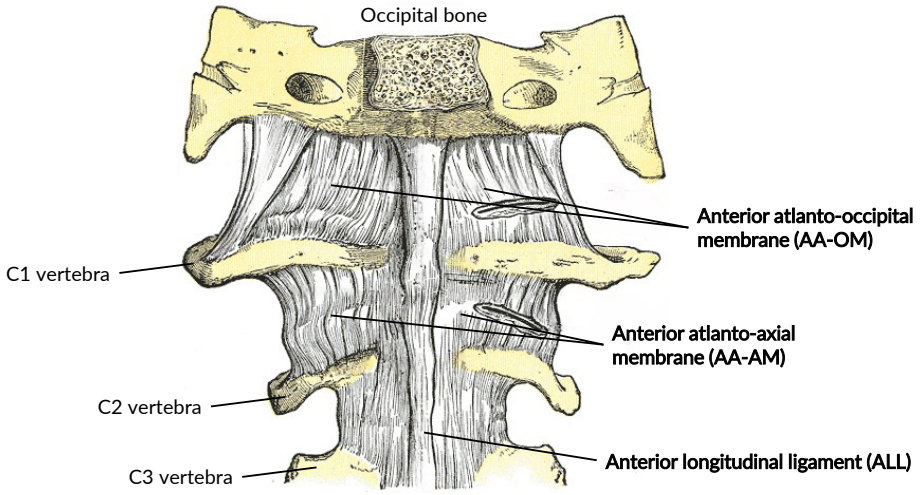


Figure 2-12: Anterior view of the occipital-atlanto-axial ligaments.

Note. Adapted from Gray, H. (1918). *Anatomy of the Human Body* (20th ed.). Lea & Febiger.

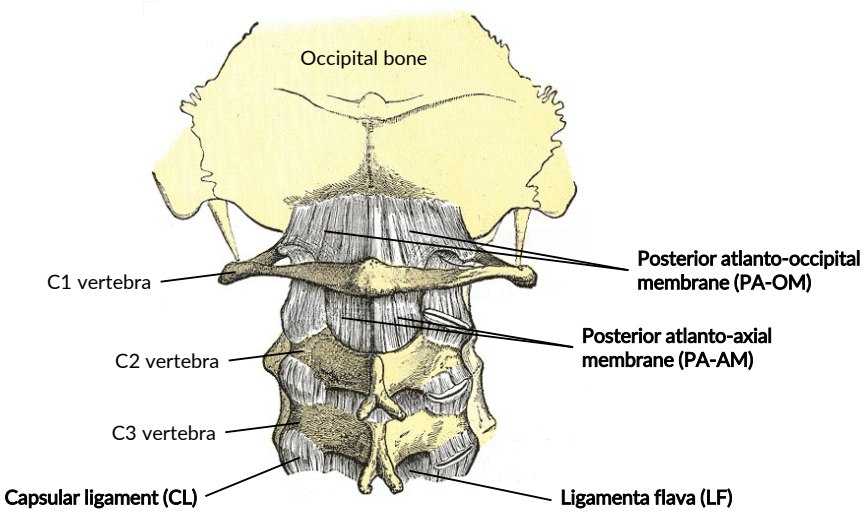


Figure 2-13: Posterior view of the occipital-atlanto-axial ligaments.

Note. Adapted from Gray, H. (1918). *Anatomy of the Human Body* (20th ed.). Lea & Febiger.

The atlanto-axial ligaments connect the atlas to the axis (Standring, 2016). The anterior atlanto-axial membrane (AA-AM) attaches the anterior arch of the atlas to the anterior surface of the axial vertebral body (Figure 2-12). The posterior atlanto-axial membrane (PA-AM) connects the posterior arch of the atlas to the axial laminae, acting as a continuation of the LF (Figure 2-13). The two atlanto-axial membranes have the main function of limiting neck motion, while the PA-AM also contributes to protecting the spinal cord. The transverse ligament (TL) connects the two lateral surfaces of the atlantal lateral masses, dividing the vertebral foramen into two compartments (Figure 2-14). The TL stabilizes the axial dens in the posterior compartment, especially during rotational movements. Two longitudinal bands arise from the middle of the TL, connecting to the occipital bone and to the posterior axial surface (Standring, 2016). The union of the TL with the superior and inferior longitudinal fibers constitutes the cruciform ligament (Figure 2-14). While the main portion of the alar ligaments connects the skull and the axis, individuals may have fibers connecting the anterior surface of the atlas with the anterior atlantal arch (Standring, 2016). The ALL, CLs and LN also connect the atlas to the axis.

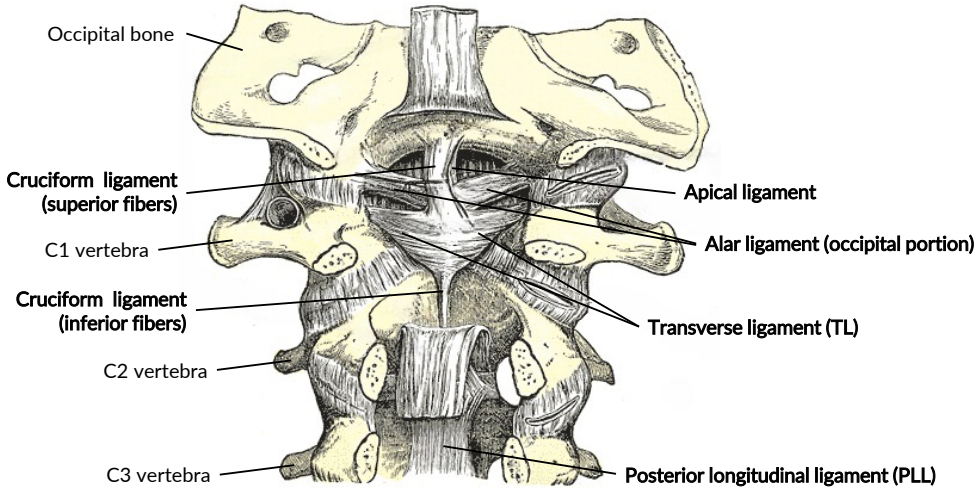


Figure 2-14: Posterior section view of the occipital-atlanto-axial ligaments.

Note. Adapted from Gray, H. (1918). *Anatomy of the Human Body* (20th ed.). Lea & Febiger.

The last group of upper cervical spine ligaments connect the axis and the skull (Standring, 2016). Located inside the vertebral canal, the tectorial membrane (TM) connects the posterior surface of the axial body to the occipital bone (Figure 2-15). The TM acts as a continuation of the PLL and forms a protective layer between the cruciform ligament and the spinal cord. The occipital pair of the alar ligaments attach the lateral surfaces of the dens to the medial side of the occipital condyles, limiting the flexion, axial rotation and lateral bending of the neck (Figure 2-14). Located between the alar ligaments, the apical ligament connects the apex of the axial dens to the foramen magnum and provides stability to the odontoid process (Figure 2-15). The ALL and LN also connect the axis to the skull.

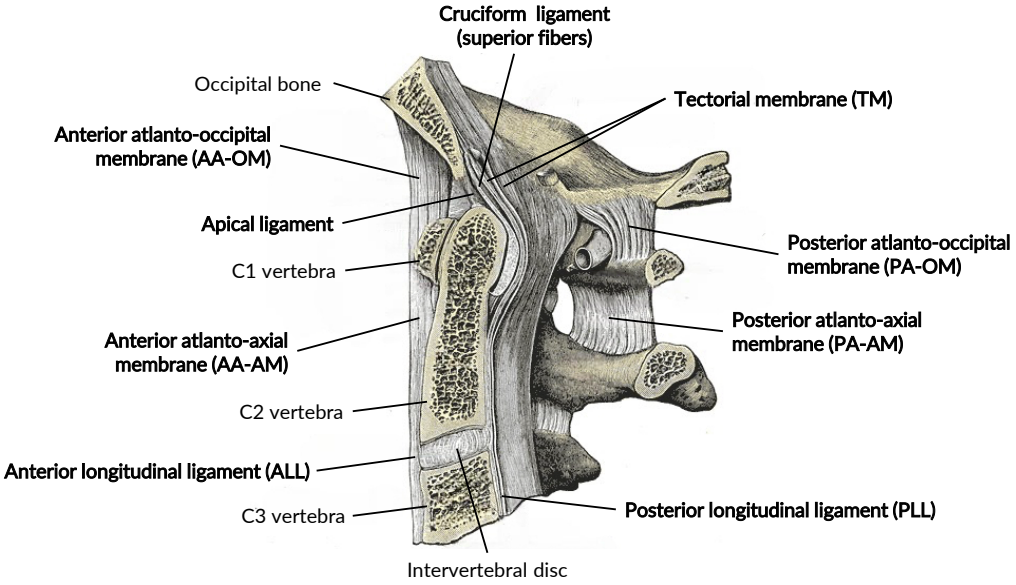


Figure 2-15: Lateral section view of the occipital-atlanto-axial ligaments.

Note. Adapted from Gray, H. (1918). *Anatomy of the Human Body* (20th ed.). Lea & Febiger.

Ligaments are formed of parallel bundles of type-I collagen and elastin proteins that have complementary roles in their mechanical response (Standring, 2016). Collagen fibers are viscoelastic and provide increased tensile strength, while elastin is hyperelastic and can withstand elevated deformations before failure. Therefore, ligaments exhibit a hyper-viscoelastic behavior, which varies according to the percentual of collagen and elastin in their composition (Yoganandan et al., 2001). Depending on their function and position, ligaments can have bundles oriented in a range of directions to allow for a multidirectional motion of the attached bones (Yoganandan et al., 2001). The force-displacement curve of a ligament is usually divided into four regions: toe, linear, traumatic, and post-traumatic (Standring, 2016; Yoganandan et al., 2001) (Figure 2-16). The toe region is an initial non-linear region with low stiffness, where the crimped collagen fibers are straightened. The linear region is the subsequent region with a linear stiffer behavior, where the straight fibers are stretched. The traumatic region refers to the stretch beyond the linear limit, where plastic deformation starts due to the rupture of some ligament fibers. Lastly, the post-traumatic (failure) region happens after the ultimate tensile force is reached and multiple fiber fail, leading to the ligament tear (Standring, 2016; Yoganandan et al., 2001).

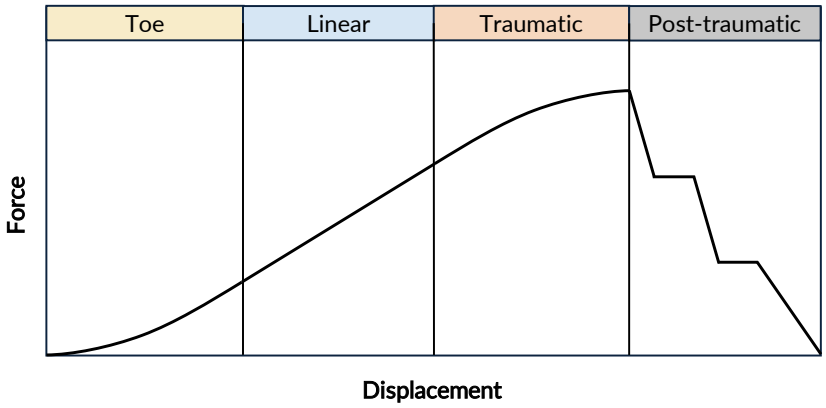


Figure 2-16: Typical mechanical response of ligaments with their different response regions.

2.1.6 Spinal Cord and Nerves

The spinal cord is part of the central nervous system, while its nerves are part of the peripheral nervous system (Standring, 2016). The spinal cord is elongated and resides in the vertebral canal, extending from the brain to a conical extremity at the beginning of the lumbar region (Figure 2-17a). Its structure is formed of a butterfly-shaped core of grey matter containing neuronal cell bodies and an outer layer of white matter encompassing bundles of axons (Standring, 2016) (Figure 2-17b). Three protective layers (meninges) encapsulate the spinal cord: the dura mater, the arachnoid, and the pia mater. The dura mater is the outermost layer, consisting of a thick and robust membrane. The arachnoid is a thin sheath that lies inside the dura mater and separates from the pia mater by a cavity filled with cerebrospinal fluid. The pia mater is a thin and fibrous structure that adheres to the surface of the spinal cord and connects to the dura mater by the denticulate ligaments (Standring, 2016). The primary function of meninges is to protect and support the vascularization of the spinal cord.

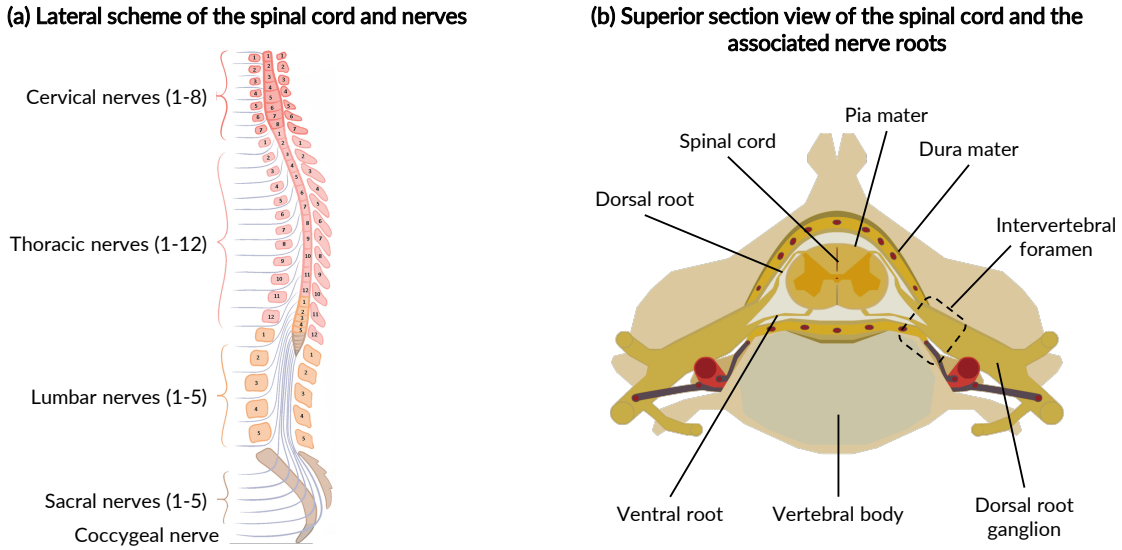


Figure 2-17: Lateral scheme (a) and superior section view (b) of the spinal cord and nerves.

Note. Figure 2-17a adapted from Sheryl, T., Faull, L., & Curtis, A. (2022, September 13). Spinal cord details. Wikimedia Commons. https://commons.wikimedia.org/wiki/File:Spinal_cord_details.jpg. Figure 2-17b adapted from Time3000. (2006, December 20). Spinal cord direv. Wikimedia Commons. https://commons.wikimedia.org/wiki/File:Spinal_cord_direv.svg CFCF. (2014, June 9). *Anatomical Planes*. Wikimedia Commons. https://commons.wikimedia.org/wiki/File:Anatomical_Planes.svg.

The spinal nerves emerge from the spinal cord, carrying signals between the central nervous system and the body (Standring, 2016). The pair of nerves are categorized according to their spinal level (cervical, thoracic, lumbar, sacral, and coccygeal), extending from the first cervical to the first coccygeal vertebra (Figure 2-17a). The cervical nerves are generally referenced according to the vertebra located inferiorly to the root (e.g., the C4 nerve is located between C3 and C4), while the nerves from other spinal regions are designated by their superior vertebrae (e.g., the T5 is located between T5 and T6). Each nerve has a dorsal and a ventral root, which consists of bundles of nerve fibres. The dorsal root is characterized by the presence of a distinguished oval swelling, the ganglion. The dorsal root ganglion is a cluster of neurons that enlarge the diameter of the root and usually lies in the IVF (Standring, 2016). The dorsal root merges with the ventral root inside the subarachnoid cavity to form a spinal nerve and exit the dura mater (Figure 2-17b).

2.1.7 Muscles

The muscle tissues can be categorized into skeletal, cardiac, and smooth, according to their function, structure, location, and contraction type (Standring, 2016). The skeletal muscles are striated with voluntary contraction, attached to bones through tendons, and responsible for body support and movement. The cardiac muscles are striated with involuntary contraction, located in the walls of the heart, and are essential for pumping blood around the body. The smooth muscles are non-striated with involuntary contraction, located in the walls of other visceral organs and throughout blood vessels, and function to regulate and control the multiple body systems (Standring, 2016).

The neck musculature is formed of thirty-one layered skeletal muscles that generate forces to support and protect the cervical spine and to stabilize and move the head and neck (Standring, 2016). They are connected to the bones through the tendons, which are dense fibrous structures similar to the ligaments. The attachment points at the end of muscles are referred to as origin and insertion, depending on which part moves during contraction. The origin stays stationary while the insertion moves during muscle activation. The neck muscles are symmetrical around the sagittal plane and can be divided into anterior and posterior regions. The anterior portion encompasses the sternocleidomastoid, hyoid, anterior vertebral, and lateral vertebral muscles, while the posterior portion comprises the scapular, splenius, erector spinae, transversospinal, and suboccipital muscles (Standring, 2016).

The sternocleidomastoid is the superficial neck muscle that arises from the sternum and the clavicle (two heads) and inserts into the mastoid process (Standring, 2016) (Figure 2-18). Due to the connection between the anterior and posterior portions of the neck, the sternocleidomastoid performs the axial rotation (unilateral activation), lateral bending (unilateral activation), and flexion (bilateral activation) of the head (Standring, 2016).

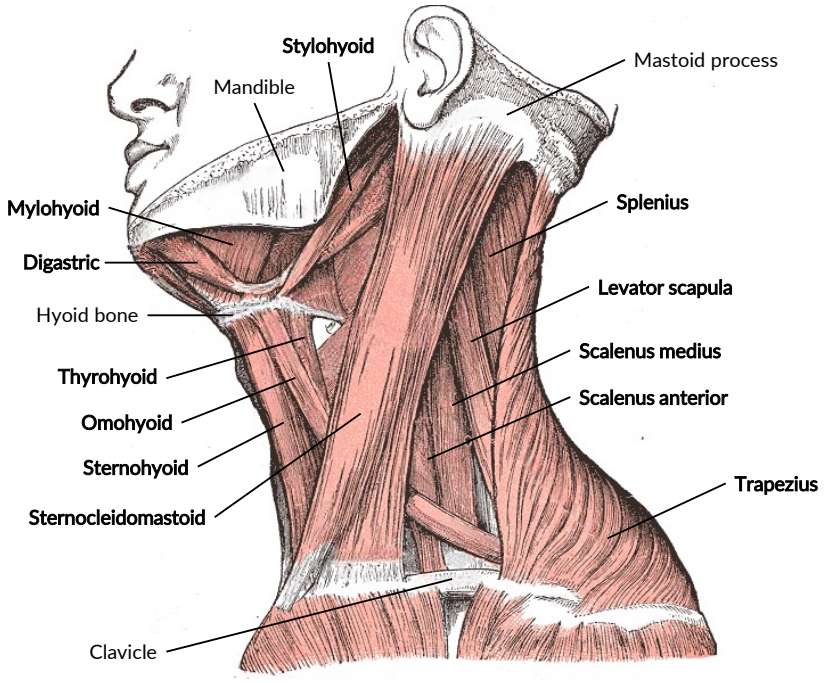


Figure 2-18: Lateral view of the neck muscles.

Note. Adapted from Gray, H. (1918). *Anatomy of the Human Body* (20th ed.). Lea & Febiger.

The hyoid muscles in the human neck are attached to the hyoid bone, being subdivided into suprahyoid and infrahyoid (Standring, 2016). The suprahyoid group is located superiorly to the hyoid bone, comprising the digastric, geniohyoid, mylohyoid, and stylohyoid (Figure 2-19). They originate either from the mandible or the skull, contributing to the deglutition process by elevating the hyoid bone and the floor of the mouth (Standring, 2016). The infrahyoid group is located inferiorly to the hyoid bone, including the sternohyoid, omohyoid, sternothyroid, and thyrohyoid (Figure 2-19). The sternohyoid originates from the medial end of the clavicle and inserts into the hyoid bone. The omohyoid is divided into an inferior belly, connecting the medial end of the clavicle to the intermediate tendon, and a superior belly, continuing from the intermediate tendon to the hyoid bone. The sternothyroid arises from the sternum and the cartilage of the first rib, being inserted into the thyroid cartilage. The thyrohyoid acts as a continuation of the sternothyroid, connecting the thyroid cartilage (origin) with the hyoid bone (insertion). The infrahyoid muscles are responsible for lowering the hyoid bone after elevation and moving the larynx during swallowing or speaking (Standring, 2016).

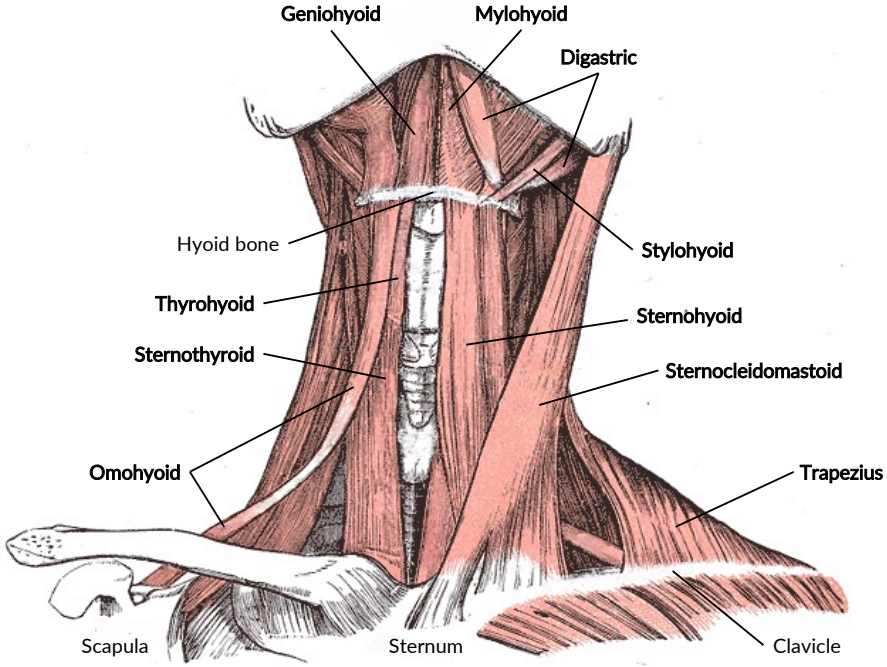


Figure 2-19: Anterior view of the neck muscles.

Note. Adapted from Gray, H. (1918). *Anatomy of the Human Body* (20th ed.). Lea & Febiger.

The anterior vertebral muscles consist of two rectus capitis (anterior and lateral) and two longus (capitis and colli) on each side (Figure 2-20). The rectus capitis muscles originate from the transverse process of the atlas and are inserted into the occipital bone. The rectus capitis anterior portion contributes to atlanto-occipital flexion, while the rectus capitis lateral performs the lateral bending in the same joint (Standring, 2016). The longus capitis arises from the anterior tubercles of the transverse processes of the vertebrae between the C3 and C6, being inserted into the occipital bone. The longus colli originates from the vertebral bodies of the segments between C3 and T3, being connected to the transverse processes of C2 and C6 and the anterior arch of the atlas. Both longus muscles contribute to head flexion, while the longus colli also axially rotate the head (Standring, 2016).

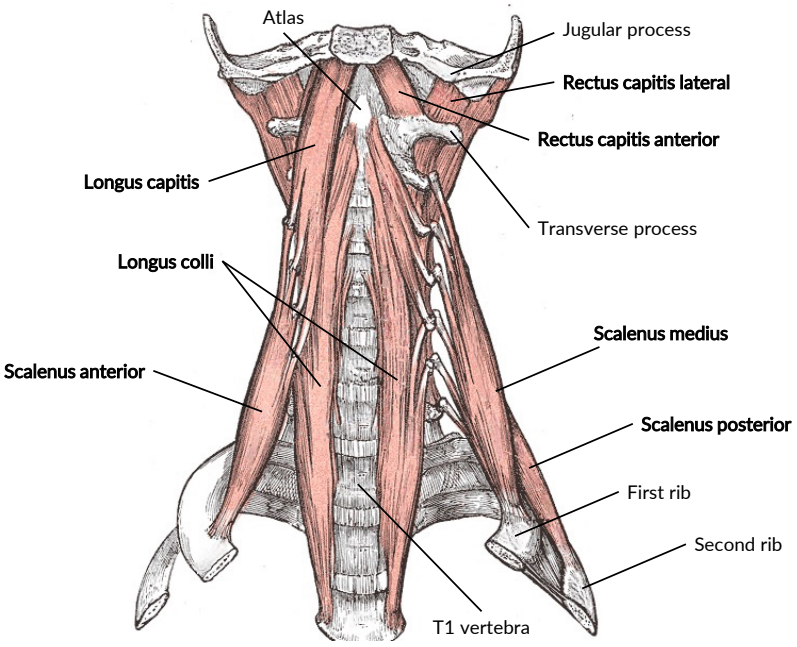


Figure 2-20: Anterior view of the anterior and lateral vertebral muscles.

Note. Adapted from Gray, H. (1918). *Anatomy of the Human Body* (20th ed.). Lea & Febiger.

The lateral vertebral muscles include the scalenus anterior, medius and posterior (Figure 2-20). The scalenus anterior arises from the transverse processes of vertebrae between C3 and C6 and is inserted into the first rib. The scalenus medius originates from the transverse processes of vertebrae between C2 and C6, being attached to the first rib. The scalenus posterior attaches C4, C5, and C6 transverse processes to the second rib. The three scaleni produce the flexion and lateral bending of the cervical vertebral column (Standring, 2016). The combination of the anterior and lateral vertebral muscles forms the prevertebral group of the neck musculature.

The scapular muscles are the neck posterior musculature inserted into the scapula and comprise the trapezius, levator scapula, and rhomboid minor (Figure 2-21). The trapezius is a superficial muscle that arises from multiple attachments, including the external occipital protuberance, the LN, and the spinous processes between 7 and T12. The trapezius moves and stabilizes the scapula but can also assist in head extension (Standring, 2016). The levator scapulae originate from the transverse processes of the first two cervical vertebrae, contributing to scapula elevation and lateral bending (Standring, 2016). The rhomboid minor arises from the lower LN and the spinous processes of C7 and T1, performing scapular and shoulder retraction (Standring, 2016).

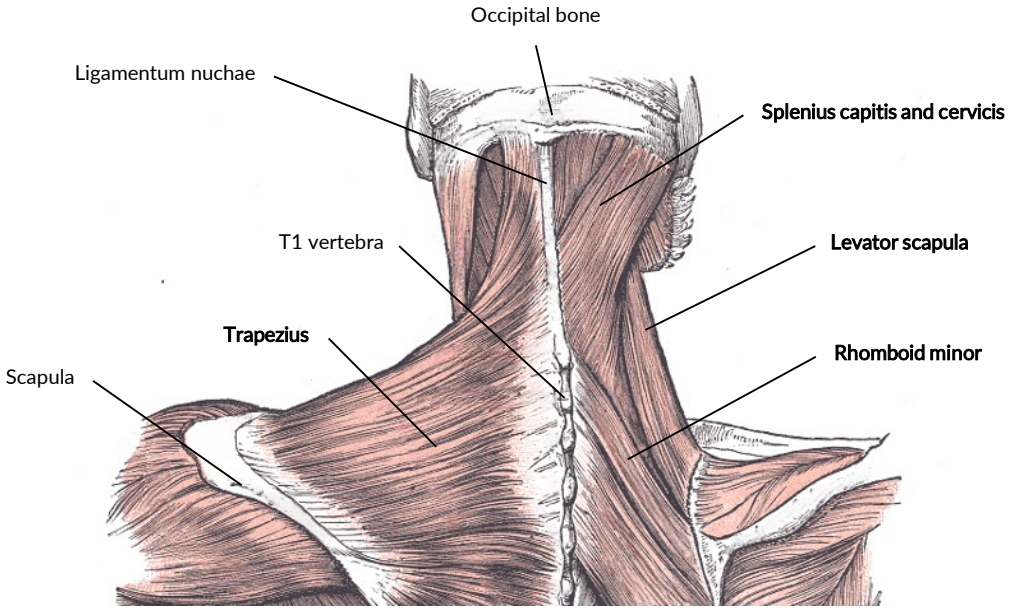


Figure 2-21: Posterior view of superficial neck muscles.

Note. Adapted from Gray, H. (1918). *Anatomy of the Human Body* (20th ed.). Lea & Febiger.

The splenius capitis arises from the mastoid process and inserts into the spinous processes and interspinous ligaments located between C7 and T3 (Figure 2-21). The splenius capitis contributes to the axial head rotation when activated unilaterally and to head extension when activated bilaterally (Standring, 2016). The splenius cervicis arises similarly from the transverse processes of C1 and C2 and the posterior tubercle of C3, attaching to spinous processes between T3 and T6 (Figure 2-21). The splenius cervicis contributes to axial rotation (unilateral activation) and extension (bilateral activation) of the head (Standring, 2016).

The erector spinae in the neck consists of the longissimus capitis, longissimus cervicis, and iliocostalis cervicis (Figure 2-22). The longissimus capitis originates from the mastoid process and connects to the transverse processes of vertebrae from C5 to T4. The longissimus cervicis arises from the transverse processes of C2 to C6 vertebrae and inserts into the transverse of the first four thoracic segments. The iliocostalis cervicis originates from the C4, C5, and C6 transverse processes and is inserted in the third to sixth ribs. While the force capacity of the cervical and capital erector spinae is limited, these muscles can contribute to the extension and axial rotation of the head (Standring, 2016).

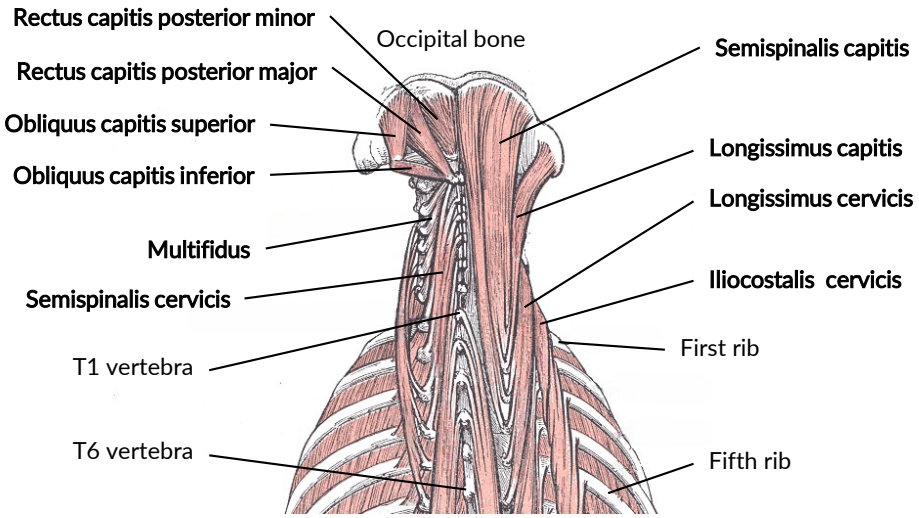


Figure 2-22: Posterior view of deep neck muscles.

Note. Adapted from Gray, H. (1918). *Anatomy of the Human Body* (20th ed.). Lea & Febiger.

The transversospinal group in the neck includes the muscles that connect the transverse and spinous processes of vertebrae, encompassing the multifidus, semispinalis cervicis, and semispinalis capitis (Figure 2-22). The multifidus arises from the lateral surfaces of the spinous process and is inserted into the articular processes of vertebrae from lower levels. The semispinalis cervicis originates from the spinous processes of C2 to C5, being attached to the transverse processes of T1 to T6 vertebrae. The semispinalis capitis arises from the occipital bone and inserts into the articular processes of C4 to C7 and the transverse processes of T1 to T6 vertebrae. Due to their longitudinal fiber orientation, the transversospinal muscles primarily contribute to the extension of the origin bone (Standring, 2016).

The suboccipital muscles originate from the first two cervical vertebrae and insert into the occipital bone, including the rectus capitis posterior (major and minor) and the obliquus capitis (inferior and superior) (Figure 2-22). The rectus posterior capitis major arises from the spinous process of the axis, contributing to the head extension and axial head rotation (Standring, 2016). The rectus capitis posterior minor originates from the posterior process of the atlas and is responsible for head extension. The oblique capitis inferior arises from the lateral process and lamina of the axis, performing extension and axial rotation of the head (Standring, 2016). The oblique capitis superior originates from the transverse process of the atlas, contributing to the extension and lateral bending of the head.

The skeletal muscle features a well-organized hierarchical structure, being divided from the whole muscle down to the individual contraction units (Standring, 2016) (Figure 2-23). The whole muscle comprises fascicles and their associated blood vessels, surrounded by a dense connective tissue sheath called epimysium. Each fascicle is composed of multiple muscle fibers enclosed by a similar sheath called perimysium. The muscle fiber is a long, cylindrical structure containing myofibrils, nuclei, mitochondria, and nerves, covered by a thin connective tissue called endomysium. An individual myofibril is composed of myofilaments and is surrounded by the sarcoplasmic reticulum, which is a complex network responsible for the regulation of the concentration of calcium ions (Standring, 2016).

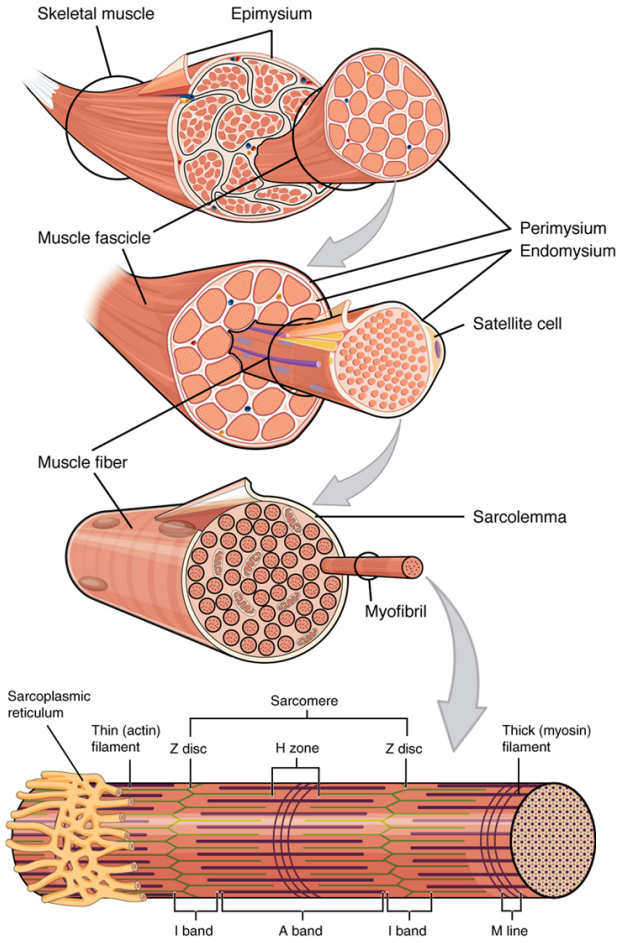


Figure 2-23: Hierarchical structure of skeletal muscles.

Note. Adapted from Betts, J. G., Desaix, P., Johnson, E., Johnson, J. E., Korol, O., Kruse, D., Poe, B., Wise, J. A., Womble, M., & Younge, K. A. (2022). *Anatomy and Physiology* (2nd ed.). OpenStax, Rice University. Access for free at openstax.org.

Myofilaments are the essential protein for muscle contraction, being organized in periodic contractile units called sarcomeres (Standring, 2016). Each sarcomere is composed of thin (actin) and thick (myosin) filaments that are aligned longitudinally (Figure 2-24). The longitudinal boundaries of the sarcomere are delimitated by thin transverse dark segments (Z-lines), while its center is delimited by a transverse visible material that connects the thick ligaments (M-line). The A-band encompasses the whole length of the myosin filaments, while the I-band consists of actin filaments of adjacent sarcomeres that are not overlapped by myosin. The H-zone is the central portion of the A-band that is not penetrated by actin filaments (Standring, 2016).

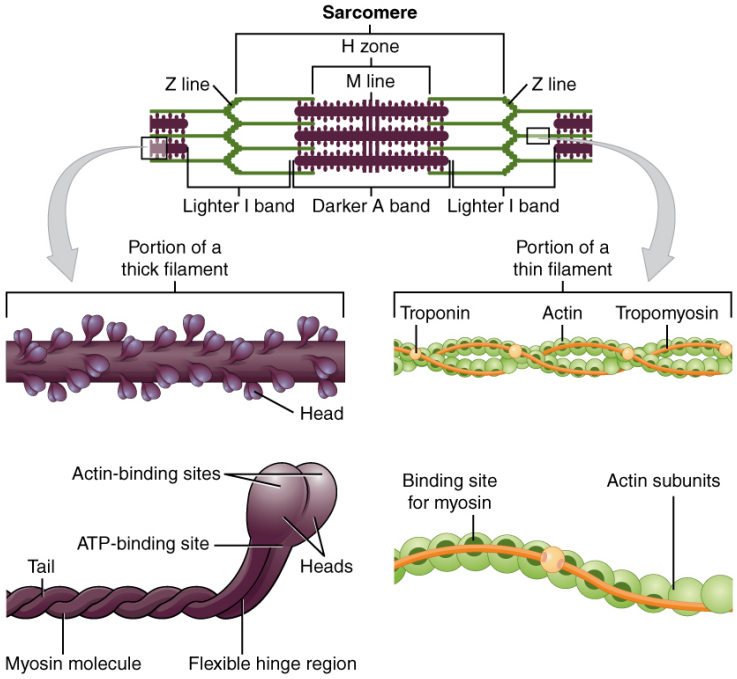


Figure 2-24: Arrangement of actin and myosin filaments in the sarcomere.

Note. Reproduced from Betts, J. G., Desaix, P., Johnson, E., Johnson, J. E., Korol, O., Kruse, D., Poe, B., Wise, J. A., Womble, M., & Younge, K. A. (2022). *Anatomy and Physiology* (2nd ed.). OpenStax, Rice University. Access for free at openstax.org.

The process of muscle contraction begins with the arrival of neural stimulation at the neuromuscular junction, causing acetylcholine to be released (Standring, 2016). Signal receptors bind this neurotransmitter and cause a local depolarization of the sarcolemma, a specialized membrane beneath the endomysium. The action potential is promptly transmitted to the whole fiber through the

sarcolemma extensions (T-tubules), triggering the release of calcium from the sarcoplasmic reticulum. The calcium ions bind to troponin C, which are calcium-sensitive switches in actin filaments, inducing changes in the actin proteins (Gash et al., 2018). The modified actin shapes allow for connections with myosin heads, forming the cross-bridges and causing the filaments to slide past each other to initiate the contraction (Figure 2-25). The I- and H-bands drastically shorten during this process, while the A-band remains approximately the same. When the excitation ceases, the sarcolemma repolarizes, and the calcium ions return to the sarcoplasmic reticulum. The actin bindings are covered, causing the myosin filaments to slide back into the relaxed position (Standring, 2016).

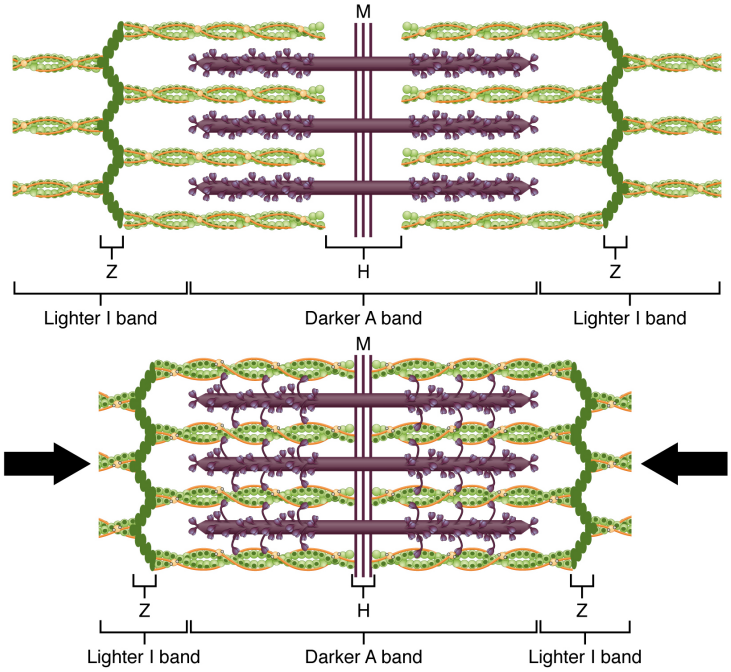


Figure 2-25: Sliding actin and myosin filaments during muscle contraction.

Note. Reproduced from Betts, J. G., Desaix, P., Johnson, E., Johnson, J. E., Korol, O., Kruse, D., Poe, B., Wise, J. A., Womble, M., & Younge, K. A. (2022). *Anatomy and Physiology* (2nd ed.). OpenStax, Rice University. Access for free at openstax.org.

The mechanical response of the muscles is slightly different from the other soft tissues due to the influence of contraction, being a combination of passive and active components. The passive behavior of the muscle tissues can be described as non-linear and viscoelastic, with extended elongations before failure (Best et al., 1995; Morrow et al., 2010). This portion represents the properties of a relaxed

muscle that does not experience any level of contraction. In contrast, the active behaviour is a function of the activation level and current mechanical state (length and velocity) of the muscle (Winters & Woo, 1990). The generation of active force increases the stiffness and reduces the elongation before the failure of the muscles (Hasselman et al., 1995).

2.2 Whiplash-Associated Disorders

The concept of whiplash was initially introduced to describe a neck injury occurring from a sudden acceleration or deceleration due to external loads (Crowe, 1928, 1964). After appearing in the first medical publication (A. G. Davis, 1945), the term was rapidly adopted for decades to refer to the injury, its mechanism and even its symptoms. The Quebec Task Force identified this ambiguity and redefined the meaning of whiplash as "an acceleration-deceleration mechanism of energy transfer to the neck" (Spitzer et al., 1995, p. 22S). Whiplash injuries were defined as the bony or soft-tissue injuries consequence of whiplash, while whiplash-associated disorders (WADs) were adopted to describe the variety of clinical entities associated with those injuries (Spitzer et al., 1995).

2.2.1 Symptoms and Classification

The symptoms of a whiplash injury include neck and shoulder pain, headache, visual and auditory obstructions, dizziness, dysphagia, paresthesia, and cognitive and psychological alterations (Barnsley et al., 1994; Norris & Watt, 1983; Spitzer et al., 1995). While their source may be unclear, the initial symptoms are hypothesized to have an organic basis (Siegmund et al., 2009). These symptoms can be divided into acute and chronic, depending on the residual effects after a defined period of time. Acute pain is short-term (lasting less than 3 months), while chronic pain is long-term (persisting for more than 3 to 6 months) and more difficult to resolve (Niv & Devor, 2007). In addition to headaches, neck and shoulder pains are the most frequent acute and chronic symptoms when multiple whiplash studies are considered (Bogduk, 2006).

Due to the extensive list of symptoms and their durations, the definition of consistent scales to standardize the injury severity was necessary for precise assessments and appropriate treatments. Developed by the Association for the Advancement of Automotive Medicine, the abbreviated injury scale (AIS) is an international grading system for anatomic injuries under each specific body system (Committee on Medical Aspects of Automotive Safety, 1971). The ranking defines six severity rates, varying from AIS 1 (minor) to AIS 6 (fatal). The AIS injury scale of the cervical spine can be used to

assess the severity of whiplash injuries (Association for the Advancement of Automotive Medicine, 2008), which are usually classified as AIS 1 and 2 (Table 2-1). To complement the AIS, the Injury Severity Score (ISS) was introduced to provide a combined severity score for patients with multiple injuries around the body (Baker et al., 1974).

Table 2-1: AIS injury scale and examples for the cervical spine.

AIS Code	Injury Examples
1 (minor)	Spinous ligament injury, strain (acute) with no fracture or dislocation
2 (moderate)	Disc injury, dislocation (no cord involvement, no fracture), fracture of the spinous process, transverse process, facet, lamina, pedicle (no cord involvement), nerve root contusion or laceration
3 (serious)	Cord contusion, odontoid fracture, bilateral facet dislocation, vertebral body burst fracture (>20% loss of anterior height)
4 (severe)	Incomplete cord syndrome
5 (critical)	Complete cord syndrome (C4 or below), cord laceration (C4 or below)
6 (fatal)	Complete cord syndrome (C3 or above), cord laceration (C3 or above)

Note. Reproduced from Association for the Advancement of Automotive Medicine. (2008). *The Abbreviated Injury Scale 2005 Update 2008*. AAAM, Des Plaines, Illinois.

The classification of whiplash injuries with the AIS scale can be broad as it may not consider different symptoms related to soft tissue injuries in the neck and their durations. The Quebec Classification of Whiplash-Associated Disorders, proposed by the Quebec Task Force, categorizes WADs according to clinical-anatomic and time references. The clinical classification divides the clinical entities into five grades of severity (Table 2-2). The time classification was defined to guide the clinical management, and patients were graded based on the duration of their symptoms: less than 4 days, from 4 to 21 days, from 22 to 45 days, from 46 to 180 days, and more than 6 months (Spitzer et al., 1995).

Table 2-2: Clinical classification of WADs.

Grade	Clinical presentation
0	No complaint about the neck No physical sign(s)
I	Neck complaint of pain, stiffness, or tenderness only No physical sign(s)
II	Neck complaint and musculoskeletal sign(s)*
III	Neck complaint and neurological sign(s)†
IV	Neck complaint and fracture or dislocation

* Musculoskeletal signs include decreased range of motion and point tenderness.
† Neurologic signs include decreased or absent deep tendon reflexes, weakness, and sensory deficits.
Symptoms and disorders that can be manifested in all grades include deafness, dizziness, tinnitus, headache, memory loss, dysphagia, and temporomandibular joint pain.
Dotted lines indicate limits of terms of reference of Task Force

Note. Reproduced from Spitzer, W. O., Skovron, M. L., Salmi, L. R., Cassidy, J. D., Duranceau, J., Suissa, S., Zeiss, E., Weinstein, J. N., & Nogbuk, N. (1995). Section 3: Consensus Findings. In *Scientific monograph of the Quebec Task Force on whiplash-associated disorders: Redefining "Whiplash" and its management*. Spine, 20(8).

2.2.2 Impact Direction and Severity Thresholds

When considering the initial symptoms, several factors have been investigated and associated with an increased occurrence of WADs, including the impact direction and crash severity. Among the types of vehicle collisions, epidemiological data suggest that whiplash injuries are predominant in rear impacts, followed by frontal (Berglund et al., 2003; Kullgren et al., 2013; Martin et al., 2008). Evaluating crash severities in rear impacts helps correlate impact kinematics, such as velocity and acceleration, with the risk of WADs. A study with the crash pulses from 66 rear impacts verified that for mean acceleration between 6 g and 7 g, all cases experienced WADs within the first month, with over 80% having symptoms for more than one month (Krafft et al., 2002). In contrast, no individual sustained WADs for more than one month when the mean impact acceleration was lower than 3 g (Krafft et al., 2002). The average change in velocity and mean acceleration to cause whiplash symptoms for more than one month were found to be 20.0 km/h and 5.3 g (Table 2-3). According to the Quebec Classification of Whiplash-Associated Disorders, occupants sustained WAD grades 0, 1, and 2+ with average peak accelerations

of 6.7 g, 8.6 g, and 10.1 g, respectively (Krafft et al., 2002). Another study with 207 occupants in 150 rear-end vehicle collisions correlated different whiplash injury risks with changes in velocity and mean accelerations (Krafft et al., 2005). The risk of whiplash symptoms for more than one month was 50% at a change in velocity of 23 km/h and a mean acceleration of 6.1 g (Krafft et al., 2005). The study also confirmed that for accelerations under 3 g, no symptoms were expected one month after the accident.

Table 2-3: Average change in velocity, mean acceleration and peak acceleration for different injury classifications.

Injury classification	Category	No. of cases	Change in velocity (km/h)	Mean acceleration (g)	Peak acceleration (g)
All		94	10.4 (± 2.0)	3.6 (± 0.3)	7.9 (± 0.7)
Reporting	No reported neck injury	53	7.7 (± 1.2)	3.0 (± 0.3)	6.7 (± 0.7)
	Reported neck injury	41	13.9 (± 2.6)	4.4 (± 0.4)	9.5 (± 1.0)
Duration of WADs	Less than 1 month	26	10.3 (± 2.1)	3.9 (± 0.5)	8.7 (± 1.3)
	More than 1 month	15	20.0 (± 4.8)	5.3 (± 0.6)	10.8 (± 1.4)
	More than 6 months	11	20.7 (± 6.2)	5.5 (± 0.7)	11.1 (± 1.6)
WAD category	WAD 0	53	7.7 (± 1.2)	3.0 (± 0.3)	6.7 (± 0.8)
	WAD 1	20	10.1 (± 2.3)	3.9 (± 0.6)	8.6 (± 1.5)
	WAD 2 and 3	18	16.2 (± 3.8)	4.8 (± 0.6)	10.1 (± 1.5)

Note. Reproduced from Krafft, M., Kullgren, A., Ydenius, A., & Tingvall, C. (2002). Influence of crash pulse characteristics on whiplash associated disorders in rear impacts-crash recording in real life crashes. Traffic Injury Prevention, 3(2). https://doi.org/10.1080/15389580212001

2.2.3 Pain Sources

The pain originating from whiplash injuries can be classified into two different pathophysiology forms, somatic and radicular, according to its source. Somatic pain is generated from musculoskeletal structures when their tissues are damaged. This pain is caused by electrical signals generated in the nociceptors of the affected tissue and transmitted along their nerves to the central nervous system (Bogduk, 2003). Referred somatic pain is a subcategory of somatic pain that is sensed in a region of the body different from its primary source. Pain occurring from neck soft tissues may also be perceived in the head, shoulder, upper limbs, and chest walls (Bogduk, 2003). Radicular pain originates from compression and subsequent inflammation of the spinal nerves or nerve roots. This pain is caused by

abnormal electrical impulses in the nociceptors of the dorsal root ganglion or the affected nerve roots (Bogduk, 2003). Alternative symptoms, such as paresthesia, may appear with radicular pain and are the consequence of neurological signs produced by the blocking axon conduction, restriction of blood supply, or compression of nociceptors. Similar to the referred somatic pain, radicular symptoms may also be perceived in other regions of the body (Bogduk, 2003).

The source of initial WADs can be uncertain (Binder, 2007), but multiple cervical sites have been postulated to be potential injury sources. The list is composed of innervated structures, including the facet joints, cervical spine ligaments, neck muscles, nerve roots, vertebral arteries, and intervertebral discs (Bogduk, 2003; Siegmund et al., 2009).

Facet Joints

The cervical facet joints have been identified as the most common source of neck pain, accounting for 54% to 60% of chronic whiplash injuries (Aprill & Bogduk, 1992; Barnsley et al., 1994, 1995; Lord et al., 1996). Barnsley et al. (1995) and Lord et al. (1996) studied double-bind diagnostic anesthetic blocks in groups of 68 and 50 whiplash patients with chronic neck pain, respectively. Both studies demonstrated that most patients experience pain relief with the facet blocks, while the latter also verified that C2-C3 and C5-C6 were the spinal levels with the highest frequency of facet joint symptoms. Facet joints are highly innervated, and several studies demonstrated the presence of nociceptors in their cervical portion (Giles & Harvey, 1987; Inami et al., 2001; Kallakuri et al., 2004).

Many authors investigated the motion of the articular processes and facet capsules during whiplash (Cusick et al., 2001; Pearson et al., 2004; K. H. Yang & King, 2003). Considering the results of those studies, two injury mechanisms have been proposed for the facet joints: the compression of the synovial fold and excessive strain of the CLs (Siegmund et al., 2009). The compression of the synovial fold was initially hypothesized by investigating the response of the cervical spine segments during whiplash, which demonstrated vertebral rotations beyond their ranges of motion (Kaneoka et al., 1999; Ono et al., 1997). This abnormal movement generated elevated compression in the facet joints of lower cervical segments, causing their center of rotation to move upwards. This could cause the inferior articular facet to collide with the superior articular facet, which was suggested to pinch the synovial fold and cause the pain process (Kaneoka et al., 1999; Ono et al., 1997). While nociceptors were found in the synovial folds (Inami et al., 2001), no further investigation has confirmed the mechanism that activates those pain receptors (Siegmund et al., 2009).

Conversely, the excessive strain of the facet capsules has been widely investigated and proposed as a primary injury mechanism of the facet joints during whiplash impacts (Panjabi et al., 1998; Pearson et al., 2004; K. H. Yang & King, 2003). The combined effect of axial compression and shear force was first suggested to contribute to large strains in the facet joint capsule (K. H. Yang et al., 1997). This initial hypothesis was further investigated in a series of experiments with cadaveric specimens that confirmed elevated stretching of the CLs during whiplash (Panjabi et al., 1998; Pearson et al., 2004). Panjabi et al. (1998) measured in situ CL elongations in fresh cadavers during whiplash impacts and verified peak strains up to 29.5% (6.5 g) and 35.4% (10.5 g) at the C6-C7 level. Pearson et al. (2004) performed a similar study with a cervical spine model and measured a maximum C6-C7 capsule strain of 39.9% for an acceleration of 8 g. These studies showed that the peak strains were higher in the lower cervical spine and exceeded the physiological values for multiple spinal levels (Panjabi et al., 1998; Pearson et al., 2004). The measured cervical facet capsular strain for partial rupture ranged between 35% and 65%, indicating that CLs may experience sub-catastrophic failure during whiplash (Siegmund et al., 2001; Winkelstein et al., 2000). Another cadaveric experiment used pretorque on cervical spine motion segments to simulate head-rotated impacts and assess the effect of head position on facet capsule strains (Siegmund et al., 2008). Results showed that peak capsule strains with pretorque, 34%, were double the values for models without pretorque, 17%, and close to partial failure thresholds (Siegmund et al., 2008). These findings suggest that head rotation can potentialize the effect of whiplash-type impacts on the capsular ligaments and increase their risk of injury.

Facet capsules contain nerve fibers that transmit nociceptive signals, reinforcing the theory that extensive CL elongation can cause pain (Cavanaugh, 2000). Lu et al. (2005a, 2005b) studied the effect of mechanical load on afferent signalling experienced in caprine facet capsules. The model identified low threshold receptors, starting at 10% strain and saturating at 34% to 44% strain, and high threshold receptors, saturating at 47% strain. The low threshold receptors were hypothesized to activate mechanoreceptors and warn for potential injury, while the high threshold receptors would activate nociceptors and initiate the pain process (Lu et al., 2005a, 2005b). These results indicate that the pain (44% strain) may occur before the sub-catastrophic failure (35% to 65% strain) of the facet capsules. The intensity and duration of pain are affected by the mechanical load in the facet capsule, and sub-catastrophic failure strain was associated with persistent sensitivity in rodent models (Lee et al., 2004; Quinn et al., 2007). A similar level of strain can also disorganize the orientation of collagen fibers in the CLs (Quinn et al., 2007).

Ligaments

Ligamentous injuries in whiplash patients have been mainly identified through magnetic resonance and autopsy examinations (Jónsson et al., 1991; Kaale et al., 2005a, 2005b; Krakenes & Kaale, 2006). These studies verified that whiplash impacts caused structural damage in upper cervical spine ligaments, especially the alar ligaments. Similar to the CLs, the other cervical ligaments are highly innervated with mechanoreceptive and nociceptive endings (Kojima et al., 1990; Siegmund et al., 2009). Injury in the cervical ligaments and their innervations may cause whiplash symptoms and instabilities in the cervical spine (Siegmund et al., 2009).

To further understand the injury locations and thresholds, the ligament motions during whiplash were investigated in whole cadaveric cervical spine models (Ito et al., 2004; Ivancic et al., 2004, 2005; Panjabi, Pearson, et al., 2004). The spinal models were tested in rear impact scenarios and predicted increased ALL strains for higher impact severity, reaching a peak value of 29.3% at 8 g (Ivancic et al., 2004). The ALL strains were the highest in the lower cervical spine but mainly below the failure threshold (Ivancic et al., 2004). The intervertebral levels with injured ligaments also experienced an increase in the neutral zone and ranges of motion, indicating that ligamentous injury generates instabilities in the spine (Ito et al., 2004; Ivancic et al., 2004). The extension neutral zone started to have a significant increase (39.8%) for rear impact severities of 5 g, indicating a possible injury threshold acceleration (Ito et al., 2004). For frontal impacts, the cervical spine models experienced elevated LF and ISL strains with peak values at C3-C4 (Panjabi, Pearson, et al., 2004). These ligaments exceeded the physiologic limit at a 4g impact, while the PLLs did not experience strains outside of the physiological motion for any severity (Panjabi, Pearson, et al., 2004).

The effect of head positioning on the cervical ligaments was studied initially in a comparison of magnetic resonance imaging (MRI) of several whiplash patients (Kaale et al., 2005a). Individuals with the head rotated prior to impact experienced more severe injuries in the alar and TL ligaments than the ones with the head in the neutral position. The TM had a modest increase in the occurrence of severe lesions with head rotation, while the PA-OM did not show a statistically significant difference (Kaale et al., 2005a). Whole cervical spine models were used to simulate head-rotated rear impacts and to reproduce similar injuries in the upper cervical ligaments (Maak et al., 2006). The experiments did not detect injuries in the alar, TL, and apical ligaments for any impact condition up to 8 g. In addition, the peak strains of these ligaments did not show significant increases with impact severity (Maak et al.,

2006). These findings suggest that the reported ligamentous injuries may have occurred in head-rotated impacts with accelerations higher than 8 g.

Muscles

Muscle pain in the neck is frequent in whiplash patients (Evans, 1992). The increased number of the enzyme creatine kinase in the muscle was suggested to be a sensitive indicator of muscle damage (Sarichter et al., 1995). Some patients with whiplash injuries experienced a rise in serum creatine kinase in the first 24 hours after the accident, but the enzyme concentration returned to normal after 48 hours (S. Scott & Sanderson, 2002). The direct injury mechanism of neck muscles happens from eccentric contractions, which involve excessive stretching during muscle contraction (Siegmund et al., 2009). Kinematic and electromyography (EMG) studies verified the active lengthening of the neck muscles during whiplash (Brault et al., 2000; Vasavada et al., 2007). The sternocleidomastoid actively stretched during the retraction phase of whiplash (Brault et al., 2000), while the splenius capitis, semispinalis capitis, and trapezius actively stretched during the rebound phase (Vasavada et al., 2007). The splenius and semispinalis capitis had, respectively, peak strains up to 21% and 17.9% while activated, which exceeded the injury threshold for eccentric contraction (Hasselman et al., 1995; Vasavada et al., 2007). These findings suggest that acute injury in the neck muscles may occur following whiplash events, but no clinical evidence indicates that muscle injury may lead to chronic neck symptoms. The effect of head position on the occurrence of muscle injury has not been assessed, but the elevated strains added from rotation may increase the effect of whiplash and the risk of tissue damage.

Nerve Roots

The nerve roots and ganglia may be injured following a vehicle collision, which could explain some whiplash symptoms, such as headache, vertigo, and vision disturbance (Siegmund et al., 2009). Increasing sensitivity to pain and widespread referred pain are often documented in whiplash patients, suggesting possible damage to local sensory processing (Greening et al., 2005; Koelbaek Johansen et al., 1999; D. Scott et al., 2005). Two mechanisms have been proposed as potential sources of pain response in the nerve roots: pressure change in the spinal canal and transverse compression (Siegmund et al., 2009). The rotation of the cervical spine can change the volume of the spinal canal, which can induce a pressure change between the inside and outside regions during rapid whiplash-type movements (Aldman, 1986; Siegmund et al., 2009). Whiplash studies monitoring the pressure of the spinal canal pressure of anesthetized porcine subjects confirmed the pressure gradients and injuries to the spinal

ganglia (Svensson et al., 2000). Cadaveric rear impact studies also reported the pressure pulses of the cerebrospinal fluid (Eichberger et al., 2000), but the correlation between these pressure effects and injuries in the nerve roots and ganglia could not be proved.

Alternatively, many authors have suggested that IVFs could change their shapes and compress the nerve roots during whiplash (Carter et al., 2000; Yoo et al., 1992). Whole cervical spine models were used to track the narrowing of the IVFs in head-forward and head-rotated rear impacts (Panjabi, Maak, et al., 2006; Tominaga et al., 2006). During head-forward impacts, the foraminal width and area narrowing started to be statistically significant for an acceleration of 3.5 g (Panjabi, Maak, et al., 2006). The study indicated a great potential for ganglion compression at C5-C6 and C6-C7, and nerve root impingement at C5-C6 (Panjabi, Maak, et al., 2006). When the head was rotated, the models predicted a significant foraminal height and width reduction for accelerations of 5 g and 8 g, respectively (Tominaga et al., 2006). The investigation confirmed a high potential for ganglion compression at C5-C6 and C6-C7, while C3-C4 and C4-C5 levels represented particularly increased potentials for injury when compared to head-forward impacts (Tominaga et al., 2006). Further studies in rodent specimens applied transient compressive loads and verified increased pain symptoms (Hubbard et al., 2008; Hubbard & Winkelstein, 2005; Rothman et al., 2005). These findings support that nerve root impingement is directly associated with pain response.

Vertebral Arteries

The vertebral arteries enter the spine bilaterally at C6 and travel superiorly through the transverse foramina to C1 (Standring, 2016). After exiting the spine, they travel around the lateral mass of C1 and enter the skull through the foramen magnum. The vertebral artery has a viscoelastic structure, with the main function of providing blood supply to the brain (Standring, 2016). The positioning of the vertebral arteries contributes to the hypothesis that injury can be caused by the coupled extension and axial rotation of the cervical spine (Barton & Margolis, 1975; Chung & Han, 2002; Dobrin, 1978). Stretching the vertebral artery reduces the vasculature diameter through Poisson's effect, which could alter the vessel pressure and compromise the blood flow pattern (Dobrin, 1978). Alternatively, head rotation can induce partial or total obstruction of the vertebral artery at C1-C2 (Barton & Margolis, 1975). These alterations in the vertebral artery may cause headache, dizziness, vertigo, tinnitus, and other whiplash symptoms (Barton & Margolis, 1975; Siegmund et al., 2009).

Whole cervical models were used to investigate the elongation of the vertebral artery in frontal, side, and rear impacts (Carlson et al., 2007; Ivancic et al., 2006). The highest elongation between C6 and occiput during the frontal impact, 2.5 mm, did not exceed the physiological limit of 7.1 mm (Carlson et al., 2007). In contrast, the peak vertebral artery elongations measured in the side impact started exceeding considerably the physiological limit at 5 g and had a maximum value of 17.4 mm (Carlson et al., 2007). For the rear impact study, the effect of head position was tested by comparing head-forward and head-rotated experiments (Ivancic et al., 2006). The head-forward models experienced peak vertebral artery elongations up to 5.8 mm and did not exceed the physiological limit of 8.1 mm. In contrast, the maximum elongations during head-rotated rear impacts were significantly unphysiological from a 5 g acceleration and had a peak value of 30.5 mm (Ivancic et al., 2006). These findings suggested that vertebral artery injuries are more likely to occur in side impacts compared to frontal and rear impacts and in non-neutral head positions compared to head-forward cases.

Intervertebral Discs

Clinical and radiographic examinations have suggested that intervertebral disc injury is a source of chronic neck pain in whiplash-type impacts (Jonsson et al., 1994). MRI studies performed on thirty-nine whiplash patients identified that thirteen of them (33%) experienced moderate to severe disc herniation (Pettersson et al., 1997). Five of six patients with severe herniation (grade 3) had persistent symptoms two years after the accident. Autopsy studies have identified additional disc lesions following vehicle collisions, including AF ruptures and vertebral endplate separations (Drottning et al., 2002; Jónsson et al., 1991; Taylor & Twomey, 1993).

Cervical spinal models were tested in rear and frontal impact scenarios to quantify the intervertebral disc strains (Ito et al., 2005; Panjabi, Ito, et al., 2004). During rear impacts, AF strains exceeded the physiologic limits during an acceleration of 3.5 g, with the highest values being located at C5-C6 (Panjabi, Ito, et al., 2004). These strains happened in the posterior portion of the disc and increased for higher impact severities, reaching a maximum of 51.4%. The AF shear strains had unphysiological values at C5-C6 during a 3.5 g impact and at most levels during a 5 g impact (Panjabi, Ito, et al., 2004). For frontal impacts, peak AF strains first exceed their physiological ranges at C4-C5 during a 4 g acceleration and at most spinal levels during a 10 g acceleration (Ito et al., 2005). The disc shear strains experienced abnormal values at C5-C6 during a 3.5 g impact, and both the fiber strain and disc shear strain were located posteriorly to the disc (Ito et al., 2005). These findings suggested that sub-

catastrophic failure of the discs was caused by the combination of flexion/extension movements and shearing of the intervertebral discs caused sub-catastrophic failure.

2.3 Non-Neutral Position Impact Scenarios

2.3.1 Head Positions of Front-Seat Occupants

A pilot study was performed on eleven subjects driving along a specific route around Guelph in Ontario, Canada (Shugg et al., 2011). The investigation aimed to evaluate the range of axial head rotation and duration of non-neutral neck positions during various in-car driving conditions. Drivers spent around 13.0% of the travel time outside of the neutral axial position, which the author defined as any position where axial angles were lower than 15° (Shugg et al., 2011). The percentage of time spent with non-neutral head positions was the highest in residential areas (19.1%), followed by thruways (10.5%) and highways (9.3%). The average peak angles were 35.7° (± 14.2°) and 42.5° (± 18.0°) for left and right cervical axial rotation, respectively (Shugg et al., 2011). Another naturalistic driving study was performed with inertial sensors on twenty drivers along a defined route between Richmond and Vancouver in British Columbia, Canada (Fice et al., 2018). The study intended to quantify head positions during specific driving tasks, such as shoulder and mirror checks. The peak axial head rotations were 81.5° and 84.3° for left and right shoulder checks, 34.3° and 42.1° for left and right mirror checks, 16.2° for rearview mirror checks, and 58.2° for passenger looks (Fice et al., 2018). Drivers spent 10.2% of the travel time performing one of these movements, with longer durations when the vehicle was stationary (17.5%) than when moving (8.2%). The average values for peak axial rotation angles were 40.8° (left) and 43.9° (right), consistent with the pilot measurements from Shugg et al. (2011). The occurrence of non-neutral positions also extends to front-seat passengers, happening mainly from interactions with the driver or hand-held devices (Reed et al., 2020). During the study, the passengers had their heads axially rotated for 33% of the travel time and flexed for 29% of the travel time. The torso was axially rotated and flexed for approximately 10% of the time (Reed et al., 2020).

2.3.2 Whiplash Injuries in Non-Neutral Position Impacts

Head rotation can affect the risk and persistency of AIS 1 neck injury during vehicle collisions (Jakobsson, 2004; Sturzenegger et al., 1994, 1995). A cohort study with 137 whiplash patients from multiple impact directions identified that 27.7% of individuals had their heads axially rotated at the moment of the accident (Sturzenegger et al., 1994). Non-neutral head positions were reported to

increase the frequency of multiple symptoms, including headache and neck pain. Rear-end collisions were also associated with a higher incidence of initial symptoms, especially neural irritations (Sturzenegger et al., 1994). A consecutive study performed with 117 whiplash patients extended the analysis to long-term symptoms (Sturzenegger et al., 1995). A total of 61.9% of head-rotated impacts resulted in symptoms over a year, while only 12.5% of head-forward impacts resulted in persistent symptoms. Another field analysis was performed with 1,608 front-seat occupants involved in rear-end vehicle collisions between 1999 and 2002 (Jakobsson, 2004). From a subset of 980 individuals without prior neck injuries, 25.1% had the head axially rotated at the impact. The occurrence and persistency of WAD were higher for non-neutral head position impacts when compared to head-forward cases. Initial symptoms happened for 40.2% of head-turned impacts and 26.3% of head-forward impacts, while chronic symptoms occurred for 13.8% of head-turned impacts and 5.4% of head-forward impacts (Jakobsson, 2004). Therefore, the axial head rotation from the neutral position has been consistently associated with increasing incidence and persistency of neck symptoms.

Considering this trend, the anatomical sites and injury mechanisms affected by head position during impacts have been investigated. An early study reported that axial head rotations of 45° decrease the physiological range of extension by 50%, which can facilitate injury in the posterior joints during rear impacts (Macnab, 1971). The TL and alar ligaments were hypothesized to be overstretched or even ruptured during combined head rotation and impact load during whiplash events (Saldinger et al., 1990). MRI examinations confirmed that whiplash patients had more frequent and severe injuries in the TL and alar ligament when the head was rotated at the collision (Kaale et al., 2005a). Following the trend of upper cervical spine ligaments, a cadaveric study with cervical motion segments verified that CLs doubled their strains in simulated head-rotated impacts compared to the neutral position impacts (Siegmund et al., 2008). The effect of head rotation on other pain sources has been investigated using whole cervical spine models in simulated rear impact conditions (Ivancic et al., 2006; Tominaga et al., 2006). IVF narrowing was higher from C3-C4 and C4-C5 in head-rotated impacts than in head-forward impacts, indicating an increased potential for nerve root impingement (Tominaga et al., 2006). The peak elongations of vertebral arteries were significantly higher during head-rotated impacts, exceeding physiological limits from 5 g impact accelerations (Ivancic et al., 2006). Thus, MRI and cadaveric studies have suggested that neck ligaments, nerve roots, and vertebral arteries can experience increased mechanical loads during head-rotated impacts, potentially resulting in tissue damage and neck pain.

2.4 Human Body Models

Human body models (HBMs) are physical or numerical representations of the human body. The main objective of HBMs is to mimic the biomechanical and physiological behavior of the body to estimate its response to various loading events (K. H. Yang, 2018). In the automotive industry, these responses of HBMs can be used to enhance safety systems and vehicle design to reduce the risk of injury in typical impact situations. Three main inputs are necessary for any type of HBM: anatomical geometry, material properties, and loading conditions (Cronin, 2011; K. H. Yang, 2018) (Figure 2-26). The proper definition of anatomical or anthropometric shapes and dimensions (geometry), constitutive laws and material data (material properties), and external forces and constraints (loading) are crucial for a biofidelic response of the model. The kinetic and kinematic responses of the HBMs are the primary outputs and can be used to calculate injury potentials (K. H. Yang, 2018).

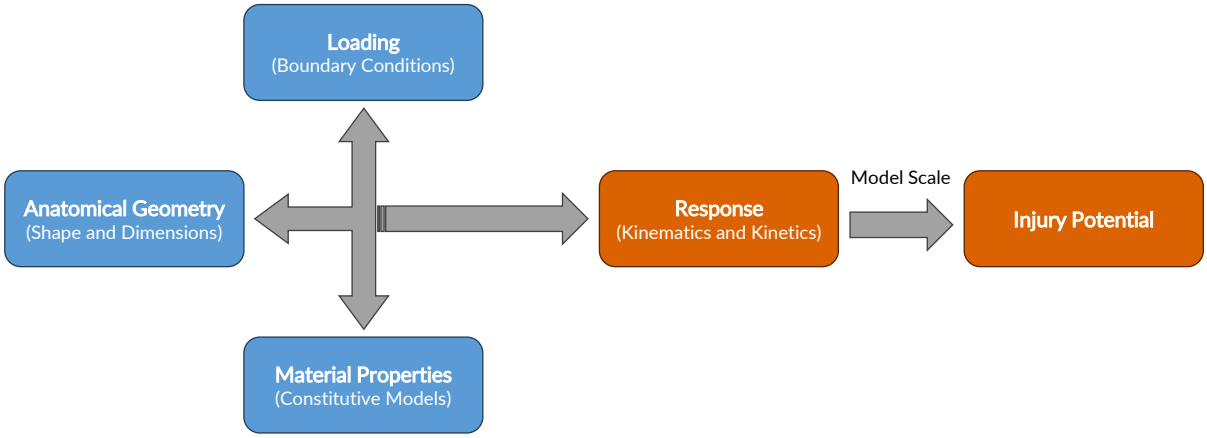


Figure 2-26: Relations between HBM inputs (blue) and outputs (orange) to estimate injury potential.

Note. Adapted from Cronin, D. S. (2011). Explicit finite element method applied to impact biomechanics problems. *2011 IRCOBI Conference Proceedings - International Research Council on the Biomechanics of Injury.*

2.4.1 Anthropomorphic Test Devices

HBMs can be divided into physical and numerical surrogates. Physical surrogates include dummy and post-mortem human subject (PMHS) models, while numerical surrogates include finite element (FE) and multi-body dynamic models (Cronin, 2011). Anthropomorphic test devices (ATDs), also referred to as crash-test dummies, are human surrogates engineered to replicate the physical response of the

human body during vehicle collisions (Mertz, 1993; K. H. Yang, 2018). To reproduce the behavior of a human body, ATDs have their geometry and material properties based on a specific portion of the population (e.g., 50th percentile or average stature male). The first crash-test dummies were created in the 1950s, with the development of the Hybrid III by General Motors in the 1970s being the basis for safety vehicle testing (Cronin, 2011). In general, these devices are designed to be seated in or standing outside a vehicle to simulate accident scenarios. Transducers are positioned in their exterior and interior to measure relevant loadings and kinematics, such as acceleration in the head center of gravity (Mertz, 1993). The measured forces, accelerations, and deformations are compared with standardized injury criteria to estimate the risk of injury in different body parts. Due to the lack of individual organs, the crash-test dummies are restricted in investigating the response of global body regions and cannot directly estimate tissue-level injury (K. H. Yang, 2018). In addition, these devices cannot simulate multidirectional impact scenarios as they are optimized for unidirectional testing.

2.4.2 Finite Element Human Models

Due to the rapid improvement in computational processing, numerical surrogates have become more popular (Cronin, 2011). Numerical surrogates intend to solve multiple partial differential equations that represent the physics of a biomechanical problem. These series of equations are often nonlinear and multidimensional, requiring considerable computational resources for their numerical solutions (Cronin, 2011). The first computational HBMs used elastic elements, such as springs, to connect rigid elements and create multi-body models to simulate the general response of a body part. While being computationally efficient, the multi-body models lack the ability to assess the mechanical response at the tissue level (Cronin, 2011). To address this issue, FE models with improved tissue representations have been developed. Early FE human models focused on the development of individual ribs and lumped viscoelastic organs, validating the predictions with PMHS tests (Huang et al., 1994; Plank & Eppinger, 1989). Later, researchers implemented elastic bodies in an FE thorax model (Happee et al., 1998). This model was validated in both frontal and rear impact scenarios, demonstrating the potential for numerical HBMs to predict occupant responses in multiple directions.

Modern FE human models have increased levels of detail and biofidelity due to accurate anatomical geometries defined from MRI scans, robust material models obtained from tissue testing, and the implementation of muscle activation. These improvements allow the current computational HBMs to provide consistent tissue-level injury assessments of the most complex loading scenarios. At present,

three FE human models have been adopted worldwide: the Global Human Body Model Consortium (GHBMC) (Gayzik et al., 2011; Schwartz et al., 2015), the Total Human Model for Safety (THUMS) (Iwamoto et al., 2015; Kato et al., 2018), and the Virtual Vehicle-Safety Assessment (ViVA) (Östh et al., 2016, 2017). The GHBMC is an international consortium focused on the development of FE HBMs to predict and prevent crash-induced injury) (Gayzik et al., 2011; Schwartz et al., 2015). The GHBMC family of models include two male adults, two female adults, and a six-year-old child in occupant and pedestrian postures (Combest, 2018). The THUMS consists of FE HBMs created by Toyota Motor Corporation and Toyota Central R&D Labs., Inc. (Iwamoto et al., 2015; Kato et al., 2018). The THUMS has a wide range of occupant and pedestrian models, varying in age, physique, and posture (Kato et al., 2018). The ViVA model is an open-source FE HBM of a 50^{th} percentile female created to evaluate whiplash injuries and safety systems (Östh et al., 2016, 2017). The average-stature female occupant is the base model, being used to obtain male and standing derivative models (John et al., 2022).

2.5 Numerical Modelling of Non-Neutral Position Impacts

The experimental testing of non-neutral position rear impacts and their implications in neck soft tissue injuries is currently limited to simplified cadaveric models, such as ligamentous cervical spines and motion segments. These models can provide an isolated study of some injury mechanisms under specific load conditions, but the lack of interactions with other anatomical sites can directly affect the representation of the biomechanical response and, consequently, injury prediction. In addition, in vivo testing of injurious impact scenarios is restricted due to ethical considerations regarding the safety and well-being of human subjects. In this context, the numerical modelling of whiplash scenarios is crucial to understanding the human body response during impact conditions. These simulations must be precisely designed to incorporate biofidelic HBMs and appropriate loading conditions. For a non-neutral position scenario, the repositioning method raises an additional challenge as it should accurately simulate the dynamics of a realistic head and neck rotation.

2.5.1 Experimental Rear Impact Studies for Boundary Conditions

To simulate a rear impact scenario, the kinematics of volunteer or cadaveric subjects exposed to similar rear impact conditions can be used as the boundary conditions of the numerical HBM. The vehicle acceleration profile during a crash can be prescribed to a seat model, which accommodates a full-body model, to reproduce the impact scenario. Alternatively, the measured kinematics of the T1 vertebra is

often prescribed to the same segment of a head and neck model to simulate its dynamic response with a reduced computational cost (Barker & Cronin, 2021, 2022).

Volunteer Test Data

Subjecting human volunteers to sled impacts can provide an accurate representation of the in vivo kinematics during a vehicle collision. Twelve male volunteers were subjected to low-speed rear impacts to simulate the effect of rear-end vehicle collisions (Ono et al., 1997). Three changes in speed (4 km/h, 6 km/h, and 8 km/h) were performed using the test setup, consisting of the human subjects seated on an inclined sled without a headrest. The impacts generated a maximum sled acceleration of 3.77 g, and the head and spinal kinematics were tracked with biaxial accelerometers and high-speed video cameras. Eleven human volunteers were subjected to twenty-three rear-end impact simulations in another sled study (Davidsson et al., 2001). The subjects were seated in a bullet sled with a head restraint, hitting a stationary target sled to generate changes in velocity (acceleration) of 5 km/h (3.1 g) and 7 km/h (3.9 g). Head and thoracic acceleration were measured using uniaxial accelerometers and high-speed cameras. Six human volunteers (four males and two females) were seated in a rigid sled without a headrest and subjected to low-impact horizontal rear impacts (Ono et al., 2006). The change in velocity of 6 km/h generated a maximum sled acceleration of 4.3 g, and head and thoracic kinematics were monitored to evaluate neck injury risk. A more recent study reanalyzed some of the earlier rear-impact sled tests (Ono et al., 1997, 2006) with the addition of eight female subjects that were not previously published (Sato et al., 2014). The combined test series registered maximum sled accelerations of 2.75 g and 3.77 g for impact velocities of 6.2 km/h and 7.9 km/h, respectively. Although these volunteer experiments report the motion of the T1 vertebra to be used in numerical head and neck models, they are limited to low velocities (up to 10 km/h) due to safety and ethical reasons.

PHMS Test Data

To simulate impacts in which injuries are more likely to occur, head and neck motion data from PHMS impact tests can be used. Six whole-body PHMS specimens were subjected to twenty-six rear impact tests using an HYGE-type mini-sled (Deng, 1999). The maximum sled accelerations ranged from 4.99 g to 9.76 g, and peak impact velocities varied from 4.91 km/h to 15.48 km/h. A head restraint was used in twelve impact tests, and a seatback angle of 20° was used in fifteen tests. The head and thoracic kinematics were processed from accelerometers and lateral target rotations captured by a high-speed

camera. This series of experiments can be used in FE head and neck models to reproduce the T1 boundary condition of injurious rear impact scenarios with velocities up to 15.48 km/h.

2.5.2 Computational Repositioning Methods

Numerical HBMs are designed with initially neutral postures, so computational methods are required to reposition these models to non-neutral positions. Reproducing the accurate kinematics of in vivo repositioning can be challenging due to the complexity of biomechanical interactions and individual variabilities. In this context, multiple repositioning methods have been proposed, being divided into forward-dynamic and inverse-dynamic approaches (Hadagali, 2024) (Figure 2-27).

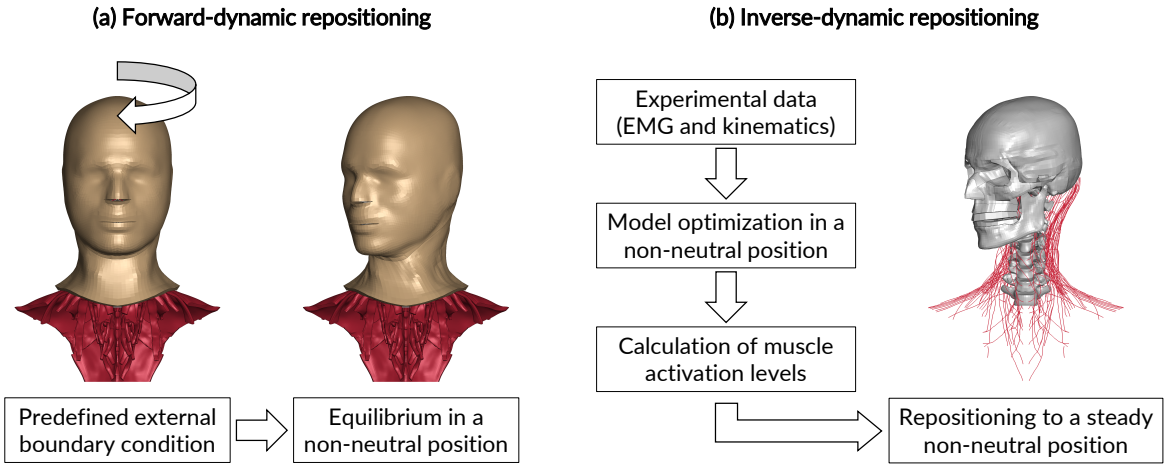


Figure 2-27: Forward-dynamic (a) and inverse-dynamic (b) repositioning approaches.

The forward-dynamic approaches use a predefined boundary condition, typically pre-determined loads or prescribed kinematics, to simulate the motion of the model to the target non-neutral position (Alizadeh, Knapik, et al., 2020; Hadagali, 2024). In head and neck FE models, the setting often consists of constraining the T1 vertebra and applying a moment or rotation in the skull to generate a relative movement between these parts (Barker & Cronin, 2021; Hadagali & Cronin, 2023; Palepu, 2013; Shateri, 2012; Shateri & Cronin, 2015; Storvik & Stemper, 2011). This method represents a practical solution to reposition a numerical HBM while retaining the stresses and strains in the tissues but may not reproduce a biofidelic motion and loading. The inverse-dynamic methods utilize experimental data from tissue kinematics and EMG activity to calculate some model parameters, such as muscle activation levels, to reproduce a specific movement (Alizadeh, Knapik, et al., 2020; Faber et al., 2018; Hadagali,

2024). This calculation involves the use of static optimization tools to estimate the forces to balance the model and achieve a stable non-neutral position (Alizadeh, Aurand, et al., 2020; Cazzola et al., 2017; Hadagali, 2024; Mortensen et al., 2018). The inverse-dynamic approach generally provides a more biofidelic representation of the human body motion due to its ability to reproduce real-life loading conditions. However, the inverse-dynamic method can be complex to implement in FE models and may be restricted to specific body movements due to the limited in vivo repositioning experiments.

2.5.3 Non-Neutral Position Rear Impact Studies

A limited number of studies assessed the non-neutral HBM positions during rear impact simulations. Storvik & Stemper (2011) verified the effect of axial head rotation on the CL strains during low-speed rear impacts in a simplified occupant model. The head and neck model used Hill-type muscle elements and was repositioned with the prescription of C1-C2 joint rotation. The model predicted increasing CL strains between C3-C4 and C6-C7 for higher head rotations, with magnitudes increasing by 47 to 196% for a 60° head rotation (Storvik & Stemper, 2011). However, imposing an axial rotation in the C1-C2 joint generated a concentration of the cervical spine rotation at the same spinal level (between 86% and 94% of the total rotation). These values were considerably higher than reported cadaveric studies (Panjabi, Ivancic, et al., 2006).

Palepu (2013) developed an osseoligamentous FE human model to evaluate the effect of different occupant positions during rear impact scenarios. In the case of an axial head rotation, the author constrained the T2 vertebra and prescribed the desired rotation in the skull. Non-neutral positions increased the ranges of motion and mechanical load in the cervical spine, with a particular increase in CL and alar ligament strain during axial head rotation (Palepu, 2013). The distribution of axial rotation through the cervical spinal levels improved compared to the previous study, having an adequate correlation with experimental data. The main limitation of the model was the lack of muscle representation in both active and passive configurations, which affected the response of other neck soft tissues during whiplash simulations.

Another non-neutral position rear impact study was performed in a detailed FE head and neck model with the neck musculature being represented as Hill-type axial elements (Shateri, 2012; Shateri & Cronin, 2015). Upper cervical spine ligament laxities were implemented in the original model to improve the representation of joint kinematics and load distribution. To simulate non-neutral head position scenarios, the T1 vertebra was constrained, and an axial skull rotation around the occipital

condyle was prescribed. The non-neutral position impact simulations verified an increase in ligament strains compared to neutral position cases, especially in the CL and alar ligaments. Muscle activation reduced the neck motion and the upper cervical spine ligament strains, while impact severity increased the potential for ligament injury. The addition of laxity to the HBM showed an improved agreement with experimental cadaveric data for axial rotation (Panjabi, Ivancic, et al., 2006). While showing realistic intervertebral rotations and considering muscle activation, this model used an axial implementation of muscles that oversimplifies the stress distribution and force generation.

In summary, the numerical non-neutral position whiplash studies have focused on applying an external boundary condition to enforce a relative rotation between two bony structures of an FE human model. The representation of the neck musculature has been limited to unidimensional Hill-type elements, and the interaction with other soft tissues (adipose tissue and skin) has not been considered. The repositioned models have been validated against axial rotation data from cadaveric experiments, showing better agreements when the imposed rotation happens between the skull and a thoracic vertebra. Finally, the whiplash injury studies to date have focused mainly on evaluating cervical ligament strain, indicating increasing values for head-rotated models.

Current Limitations

In vivo physiologic head repositioning initiates with the contraction of the neck muscles to rotate the head from the neutral position. The active tensile forces generated by the muscles are then balanced with reactive compressive forces and moments from other tissues of the cervical spinal, which stabilizes the head in a desired position (Barrett et al., 2020; Straker et al., 2009). Therefore, numerical repositioning should focus on reproducing similar configurations regarding load distribution and vertebral kinematics. Retaining stresses and strains is essential for the kinetics, kinematics, and tissue-level responses of repositioned models in a subsequent analysis (Boakye-Yiadom & Cronin, 2018).

The in vivo head rotation can be better represented with inverse-dynamic repositioning methods, using optimization to calculate the tissue forces in the model. However, the insufficient experimental data for defining muscle activation levels during axial head rotation is an obstacle to implementing realistic muscle-based repositioning. External boundary conditions have been extensively used to reposition the head in numerical HBMs, but this approach may not precisely represent the in vivo motion in the FE model. Imposing a rotational displacement for a specific model part constrains its movement, affecting the head kinematics and tissue-level response during the impact scenario. In addition, the previous non-

neutral position rear impact studies have used simplified models and have not considered the contribution of the 3D musculature and other neck soft tissues. Therefore, numerical studies have been limited in achieving a static head and neck non-neutral position with biofidelic intervertebral movements for a detailed FE head and neck model.

2.6 GHBMC Human Body Models

The GHBMC 50th percentile male occupant model (M50-O) was developed based on a 26-year-old male volunteer with a height of 174.9 cm and a weight of 78.6 kg (Figure 2-28). The M50-O geometry was created using the segmentation of medical images generated from MRI and computed tomography (Gayzik et al., 2011; Schwartz et al., 2015). The M50-O full-body model consists of 1,851,181 solid elements, 740,789 shell elements, and 16,593 beam elements. The HBM development was divided into five body regions: head, neck, thorax, abdomen, and plex (pelvis and lower extremity). Each body region model was engineered and validated by a different institution around the world, referred to as the Center of Expertise (COE). These body regions were then integrated into the full-body model and further validated with experimental data from frontal, rear, side, and oblique impact tests.

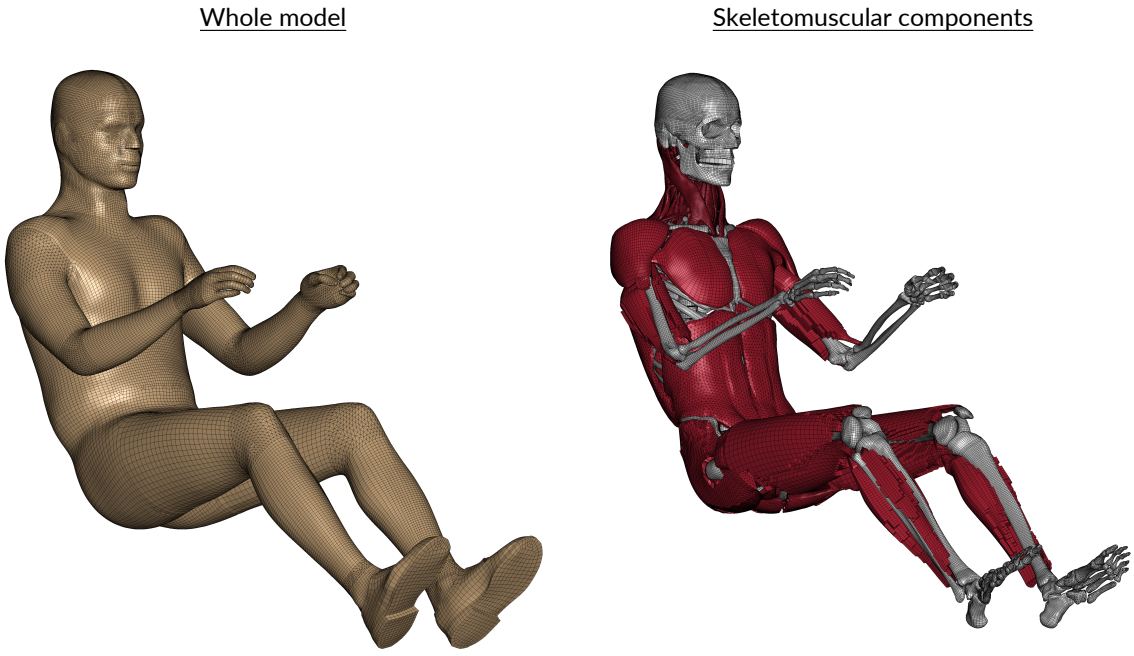


Figure 2-28: GHBMC M50-O full-body model.

2.6.1 Description of GHBMC M50-O Neck Model

The neck region of the GHBMC M50-O was developed by the COE of the neck model at the University of Waterloo, Ontario, Canada (DeWit & Cronin, 2012; Fice et al., 2011). The M50-O neck model comprises vertebrae, ligaments, intervertebral discs, cartilages, spinal cord, muscles (active and passive), tendons, adipose tissue, and skin (Figure 2-29). The M50-O neck model, not including the head, has a total of 241,433 solid elements, 62,969 shell elements, and 13,355 beam elements.

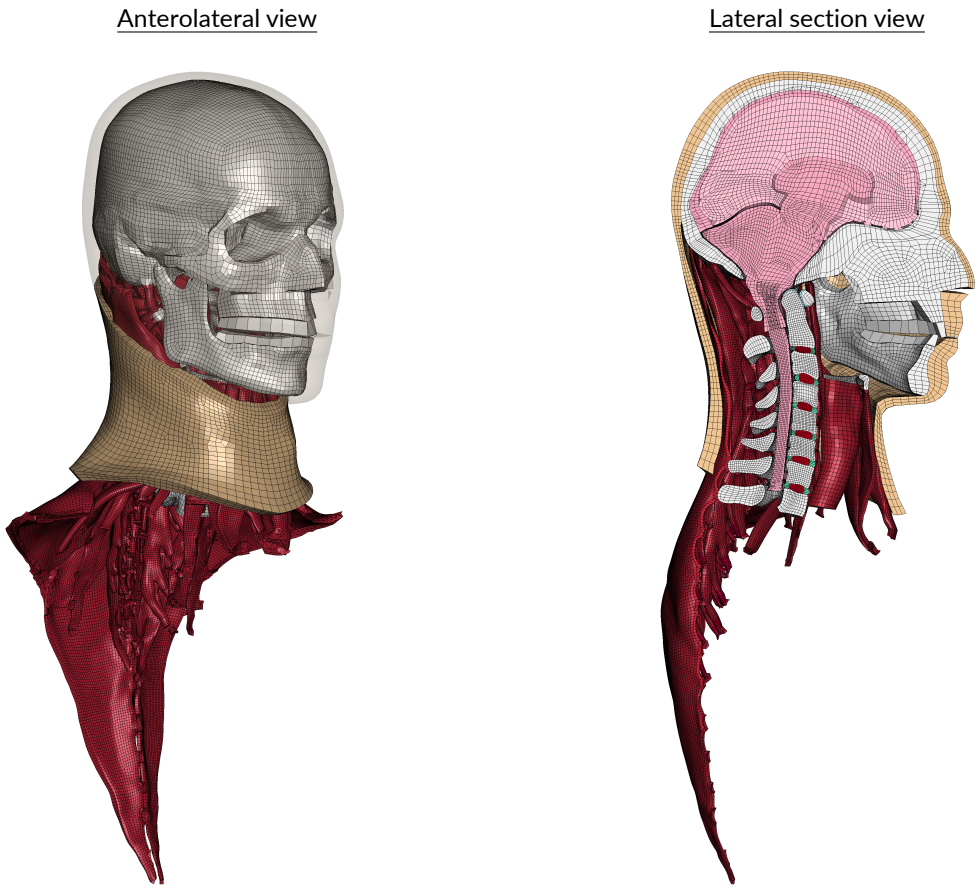


Figure 2-29: GHBMC M50-O head and neck model.

Vertebrae

Each vertebra is modelled as three distinct parts: trabecular bone, cortical bone, and vertebral body endplates (Figure 2-30). The inner core of trabecular bone was modelled with hexahedral solid

elements, while the outer layers of cortical bone and body endplates were modelled with quadrilateral shell elements (DeWit & Cronin, 2012).

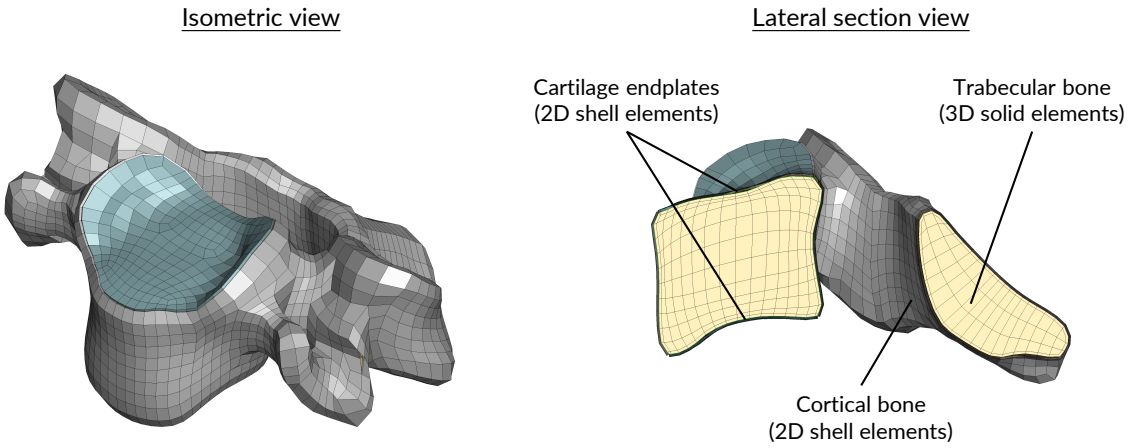


Figure 2-30: GHBMC M50-O vertebral model.

The vertebra was represented with linear-plastic constitutive models, including plastic strain-based failure mechanisms (Barker et al., 2017). The trabecular bone used an isotropic elastic-plastic material model (*MAT_ISOTROPIC_ELASTIC_PLASTIC), while the cortical bone and endplates used an isotropic elastic-plastic material model with kinematic hardening (*MAT_PLASTIC_KINEMATIC). The failure strains of trabecular and cortical bone were specified as 9.5% and 1.78%, respectively. The failure and mechanical properties of the three vertebral components were defined from experimental studies of the bone (Barker et al., 2017; Best et al., 1995; Keaveny et al., 2001; Lindahl, 1976; Reilly et al., 1974) (Table 2-4).

Table 2-4: Mechanical properties of the vertebral components in the GHBMC M50-O model.

Vertebral Part	Trabecular bone	Cortical bone	Endplates
Elastic modulus (GPa)	0.442	18.4	5.6
Poisson's ratio	0.30	0.28	0.30
Yield stress (GPa)	0.00283	0.190	0.0367
Plastic modulus (GPa)	0.030	1.25	0.298
Failure strain	0.095	0.0178	-

Intervertebral Discs

The intervertebral discs were divided into the NP, AF ground substance, and AF fibers (Figure 2-31). The NP and AF ground substance were modelled using hexahedral solid elements to represent the inner and outer portions of the disc, respectively. Embedded in the AF ground substance, the AF fibers were modelled as five concentric layers of quadrilateral shell elements. Each layer comprises a pair of superimposing shells with a thickness of 0.27 mm, representing the lamellae with different fiber orientations. The ten layers of lamellae and the ground substance are connected through shared nodes (DeWit & Cronin, 2012).

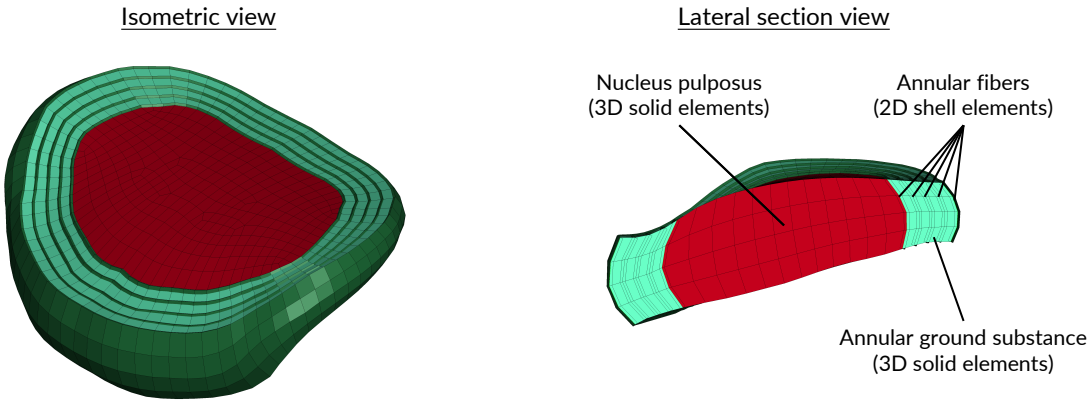


Figure 2-31: GHBMC M50-O intervertebral disc model.

Due to their distinct compositions, each part of the intervertebral disc used a different constitutive model. The NP used an elastic fluid material model (*MAT_ELASTIC_FLUID) with a bulk modulus of 1.72 GPa (Barker et al., 2017; K. H. Yang & Kish, 1988). The AF ground substance used a highly compressible foam material model based on the Hill strain energy density function (*MAT_HILL_FOAM) (Barker et al., 2017; Hill, 1979). The Hill strain energy density function (W) is given by Equation 2-1 in terms of principal stretches (λ_1, λ_2, and λ_3) and material constants (C_j, b_j, and n). Radial and compressive experimental test data were used to fit the strain energy density function and obtain the material constants (Fujita et al., 1997; Iatridis et al., 1998) (Table 2-5).

$$W = \sum_{j=1}^{m} \frac{C_j}{b_j}\left[\lambda_1^{b_j} + \lambda_2^{b_j} + \lambda_3^{b_j} - 3 + \frac{1}{n}\left(J^{-nb_j} - 1\right)\right];\ n = 2\ ;\ m = 3\ ;\ J = \lambda_1\lambda_2\lambda_3 \qquad (2\text{-}1)$$

Table 2-5: Material constants for the annular ground substance model.

Index	C_j	λ_i
1	- 0.895 MPa	- 2
2	2.101 MPa	- 1
3	0.115 MPa	4

The AF fibers used a non-linear anisotropic elastic material model (*MAT_FABRIC) with mechanical properties obtained from tensile test data (Barker et al., 2017; Ebara et al., 1996; Holzapfel et al., 2005; Skaggs et al., 1994). The fiber orientation of each lamina was modelled using the material angles with respect to the axial plane, varying from ± 25° (outermost layer) to ± 45° (innermost layer) with increments of 5° (J. J. Cassidy et al., 1989; Wagner & Lotz, 2004) (Figure 2-32). For each concentric layer, the two laminae had opposite angles to simulate the alternating pattern of the AF.

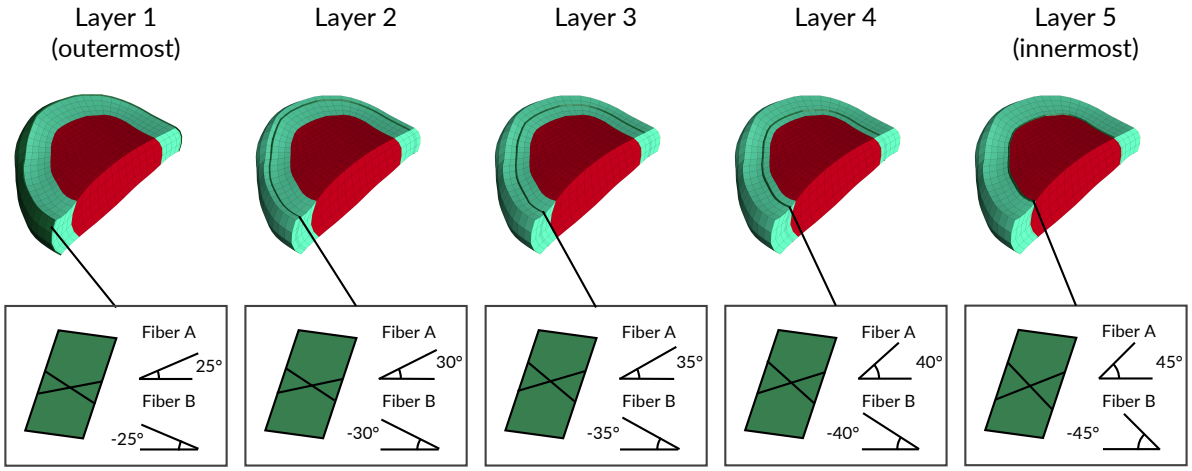


Figure 2-32: GHBMC M50-O annular fiber orientations for the five concentric layers.

The superior and inferior surfaces of the discs were connected to the vertebral endplates using a tiebreak interface (*CONTACT_AUTOMATIC_ONE_WAY_SURFACE_TO_SURFACE_TIEBREAK). The contact constraints two surfaces until a failure criterion is reached and the bonds are released. To simulate the intervertebral disc avulsion from the vertebral endplates, a failure stress of 0.03 GPa was calculated with the average contact area and the experimental failure force (Kasra et al., 2004).

Ligaments

The cervical ligaments were modelled using a series of unidimensional beam elements to represent their fibers (Figure 2-33). The beam representation allowed for the distribution of total force sustained by a ligament through the axial elements and their attachment points (DeWit & Cronin, 2012). The attachment points were defined according to the anatomic insertion with a minimum distance between nodes of 1 mm. The exception for the beam implementation was the cruciform ligament, modelled with two-dimensional quadrilateral shell elements due to its complex shape.

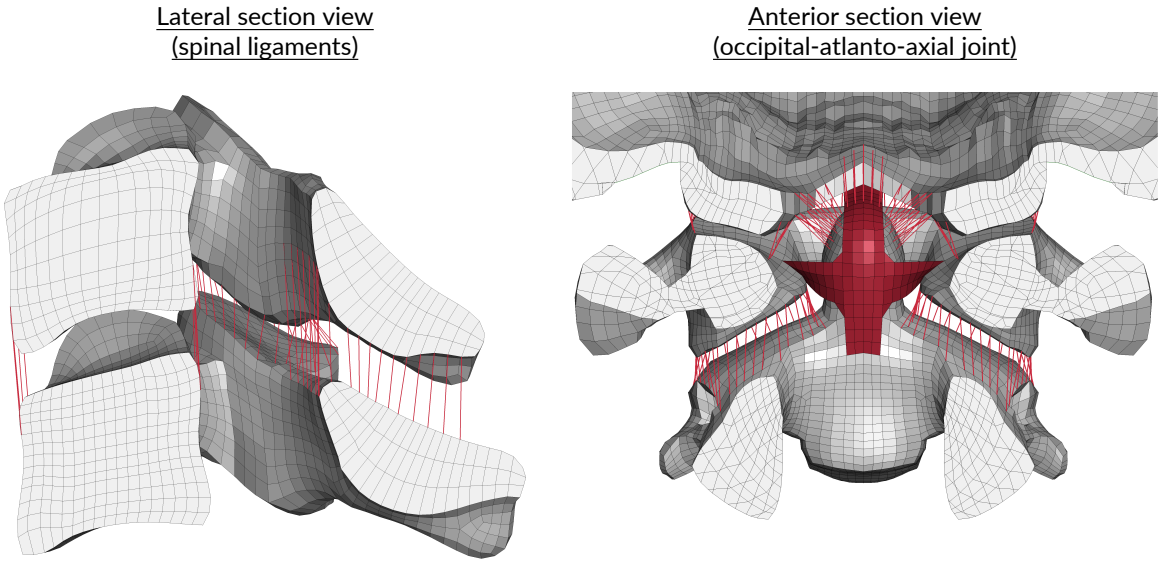


Figure 2-33: GHBMC M50-O ligament models.

The unidimensional ligament parts used a non-linear elastic spring material model with damping (*MAT_ELASTIC_SPRING_DISCRETE_BEAM). Their mechanical responses were defined by force-displacement curves with strain rate effects based on tensile tests on young human cervical spine ligaments (Mattucci et al., 2012, 2013). A failure displacement value that would cause element erosion was defined for each ligament model. The cruciform ligament shell used a non-linear anisotropic elastic material model (*MAT_FABRIC). The mechanical responses were based on stress-strain curves calculated from tensile experiments in the transverse and longitudinal fibers of the cruciform ligament, respectively (Mattucci et al., 2013).

Musculature

The implementation of the neck musculature in the GHBMC M50-O was divided into passive and active muscle elements (Figure 2-34). The passive portion was modelled with hexahedral solid elements, while the active portion was modelled with two-node beam elements (Barker & Cronin, 2021). The physiologic cross-section area (PCSA) was assigned to each muscle beam according to reported values (Panzer, 2006; Van Ee & Nightingale, 2000). The active beam elements were embedded in the passive solid elements to create this hybrid approach.

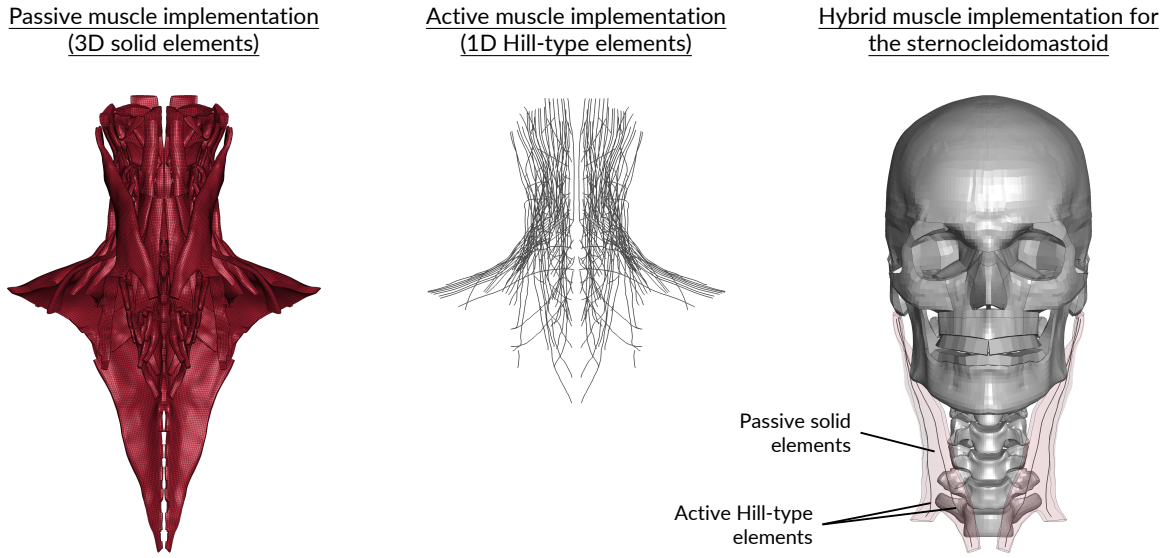


Figure 2-34: GHBMC M50-O passive and active muscle models.

The passive elements of the muscle used a hyperelastic rubber and foam material model with strain effects (*MAT_SIMPLIFIED_RUBBER/FOAM). Stress-strain curves were defined for six strain rates, from 0.01 s^{-1} to 1000 s^{-1}, to reproduce their mechanical behavior (Gierczycka et al., 2021). These curves were calculated from interpolations of tensile test data at 0.001, 1, and 25 s^{-1} rates (J. Davis et al., 2003; Myers et al., 1998) and compression test data at 0.01 and 1000 s^{-1} rates (Van Sligtenhorst et al., 2006). The active elements of the muscle used a Hill-type muscle material model (*MAT_MUSCLE). In this formulation, the stress generated in the beam is the sum of the stresses generated by the muscle activation, the passive component and the damping component. The passive and damping components were neglected in the current modelling due to the presence of solid elements that represent the passive behavior of the musculature. The activation stress (σ_{act}) is given by Equation 2-2 in terms of the

maximum isometric stress (σ_{max}), activation level (a), the force-stretch scaling factor (f), and the force-strain rate scaling factor (g). The maximum isometric stress of the muscle was defined as 0.5 MPa based on values from literature (Panzer, 2006; Winters & Stark, 1988). The muscle activation level and scaling factors are further explained in Section 2.6.3.

$$\sigma_{act} = \sigma_{max} a(t) f(\lambda) g\left(\dot{\bar{\varepsilon}}\right) \tag{2-2}$$

Adipose Tissue and Skin

The adipose tissue was modelled with hexahedral solid elements, while the skin was modelled with quadrilateral shell elements (Gierczycka et al., 2021) (Figure 2-35). The outer surface of the adipose tissue shared nodes with the skin to generate the connection between these two soft tissues.

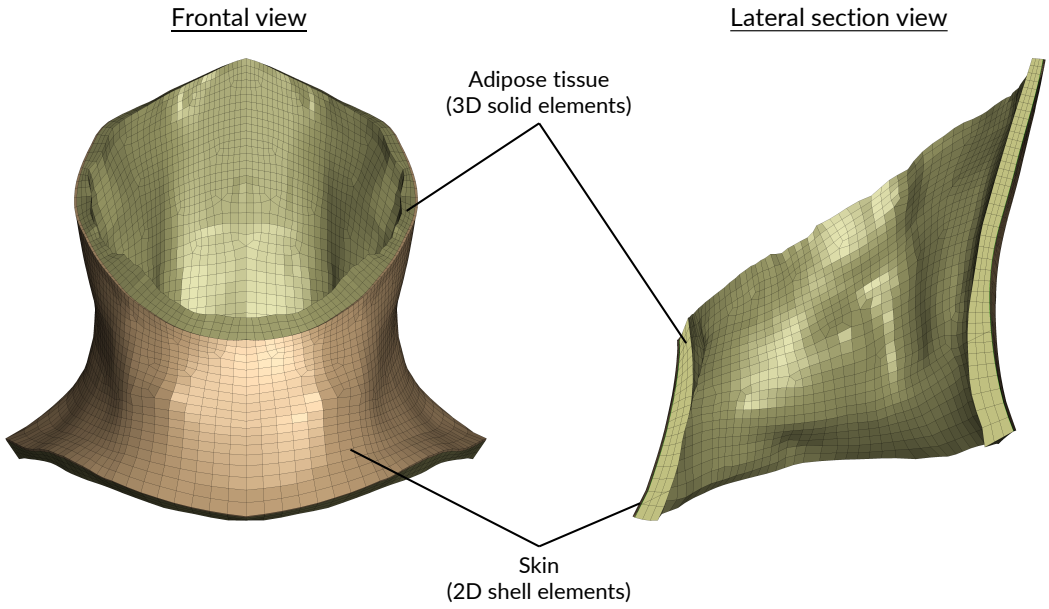


Figure 2-35: GHBMC M50-O adipose tissue and skin models.

The adipose tissue used a hyperelastic rubber and foam material model with strain effects (*MAT_SIMPLIFIED_RUBBER/FOAM). Stress-strain curves were defined for six strain rates, from 0.002 s^{-1} to 250 s^{-1}, based on experimental compressive tests (Comley & Fleck, 2012; Gierczycka et al., 2021). The skin used a hyperelastic rubber model with strain rate effects based on the Ogden strain energy function (*MAT_OGDEN_RUBBER) (Gierczycka et al., 2021). The Ogden strain energy

density function (W) is given by Equation 2-3 in terms of principal stretches (λ_j) and material constants (μ_j, α_j, and K). The shear moduli (G_i) and decay constants (β_j) were also required to account for strain rate effects. Tensile and compressive skin test data were used to fit the strain energy function and obtain the coefficients (Gierczycka et al., 2021; Lim et al., 2011; Shergold et al., 2006) (Table 2-6).

$$W = \sum_{i=1}^{3}\sum_{j=1}^{n}\frac{\mu_j}{\alpha_j}\left(\lambda_i^{\alpha_j} - 1\right) + K(J - 1 - \ln J)\ ;\ J = \lambda_1\lambda_2\lambda_3 \tag{2-3}$$

Table 2-6: Material constants for the skin Ogden model.

Index	λ_i	α_i	G_i	β_j
1	- 0.601 MPa	- 0.971	1.347 MPa	0.307 s^{-1}
2	0.473 MPa	- 2.393	24.08 MPa	16.7 s^{-1}
3	- 0.143 MPa	- 3.845	97.73 MPa	79.67 s^{-1}
4	-	-	839.1 MPa	1246 s^{-1}

2.6.2 Validation of GHBMC M50-O Neck Model

The biofidelity of the GHBMC M50-O neck model was assessed through multi-level validations against experimental human volunteer and PMHS test data, varying from single-element material testing to the full neck kinematic evaluation. The implementation of each material model was followed by single-element test cases to reproduce the experimental setup and validate its mechanical response. The spinal motion segments, also known as functional spinal units, were then assembled with two adjacent vertebrae and associated soft tissues for C0-C1 to C7-T1. The upper cervical spine motion segments (C0-C1 and C1-C2) were validated against experimental tests for flexion, extension, lateral bending, and axial rotation (Lasswell et al., 2017). The lower cervical spine motion segments (C2-C3 to C7-T1) were tested for flexion, extension, lateral bending, and axial rotation in quasi-static and dynamic loading and validated against experimental data (Barker et al., 2017). The following step included validating the ligamentous cervical spine model, assembled with the motion segments, for axial rotation, axial tension, 8 g frontal impact, and 8 g rear impact against cadaveric spine specimens (Barker & Cronin, 2021). The final step to validate the GHBMC M50-O neck model was integrating all components into the full neck model and testing its dynamic response for multiple impact conditions. The model kinematics were validated against human volunteer and PHMS tests for frontal impacts at

2 g to 15 g, lateral impacts at 4 g to 7 g, oblique impacts at 4 g to 11 g, and a rear impact at 7 g (Barker & Cronin, 2021, 2022).

2.6.3 Muscle Activation in the GHBMC M50-O Neck Model

During impact scenarios, the motion and tissue-level response of the model can be influenced by the activation levels of the musculature. The detailed neck model of the GHBMC M50-O included a total of twenty-seven pairs of muscles, represented by three-dimensional solids and one-dimensional Hill-type beams. The solid elements of the musculature, comprising most of the neck volume, represented its passive behavior with a hyper-viscoelastic mechanical response that does not depend on the muscle activation levels. In contrast, the Hill-type beam elements represented the active muscle response, considering the activation dynamics (peak isometric stress and response curves) and the PCSA of each muscle. Due to the complexity of defining the activation level for each muscle, the muscles were grouped into the following four quadrants: right extensors, left extensors, right flexors, and left flexors (Correia et al., 2021) (Figure 2-36). The quadrant division assumed that the muscles of each group would follow the same activation profile, which simplifies the real-life scenario where individual motor units from each muscle activate independently (Correia et al., 2021).

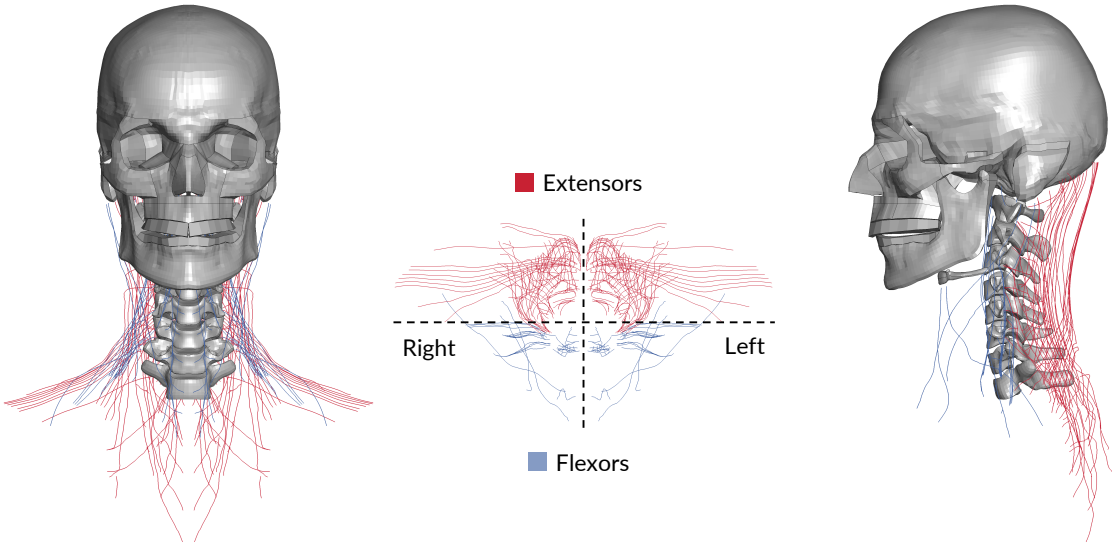


Figure 2-36: Quadrant division for the GHBMC M50-O active muscle elements.

Activation Strategies for Neutral Position

Due to the lateral symmetry of frontal and rear impact situations, the activation strategy can usually be reduced to two muscle groups: extensors and flexors (Panzer et al., 2011). Considering this division, various muscle activation schemes have been investigated in neutral position HBMs. Panzer et al. (2011) and Fice et al. (2011) implemented muscle activation in a detailed FE head and neck model to investigate the influence of muscle activation in rear impact scenarios. The proposed activation levels of 100% for extensors and 70% for flexors were based on normalized EMG data from unaware volunteers undergoing whiplash impacts (Siegmund et al., 2003). These studies were pioneers in investigating the effects of muscle activation on reducing ligament strains during simulated impacts, but the activation strategy generated head overextension compared to volunteer data.

The original activation scheme for the GHBMC models was based on an activation pulse of 100% for both extensor and flexor muscles (Shen & Cronin, 2017). This strategy, also known as Maximum Muscle Activation (MMA), generated a maximum activation of 0.871 (Happee, 1994) and used an onset time of 74 ms (Siegmund et al., 2003). A more recent study optimized the muscle activation of the GHBMC M50-O in frontal impact scenarios (Correia et al., 2020). In addition to MMA, three activation schemes were defined: No Muscle Activation (NMA) with extensors and flexors at 0%, Co-contraction Muscle Activation (CMA) with extensors at 20% and flexors at 100%, and Optimized Muscle Activation (OMA) with a variation of onset time and the group activation level. The last scheme was optimized to the head motion compared to reported volunteer data, and the responses of the model under nine different frontal impact severities were assessed.

The models with OMA had increasing activations for higher severities and improved agreements with measured kinematics compared to the MMA scheme. The NMA cases also performed better than MMA, but not considering muscle activation does not mimic what happens in real life. Compared to CMA, the OMA scheme had, on average, an increase of only 6% in the correlation rating. This indicates that a single scheme considering activations of 20% for extensors and 100% for flexors can represent an adequate approximation of the muscle response during neutral position impact scenarios. In addition, this division of muscle activations could maintain the head in a steady neutral position when no external loading was applied.

Activation Curves and Parameters

The activation scaling for each muscle group is one of the variables considered for implementing muscle contraction in an HBM (Equation 2-2). The curve profile, including the onset time and maximum activation state, needed to be defined. The muscle activation onset time comprises the delay that the occupant experiences between the beginning of the impact and the initiation of muscle contraction. The baseline value used for the GHBMC models, 74 ms, was based on the average reported values for human volunteer experiments (Ono et al., 1997; Siegmund et al., 2003; Szabo & Welcher, 1996). The general shape of the muscle activation curve over time was based on two first-order differential equations used to describe neural excitation and active state dynamics (Happee, 1994). The maximum value of the activation function, 0.871, and the time to achieve the peak value, 100 ms, were also obtained from this study. These curves were scaled according to the muscle group to obtain the activation level over time for the beam elements of each muscle (Figure 2-37).

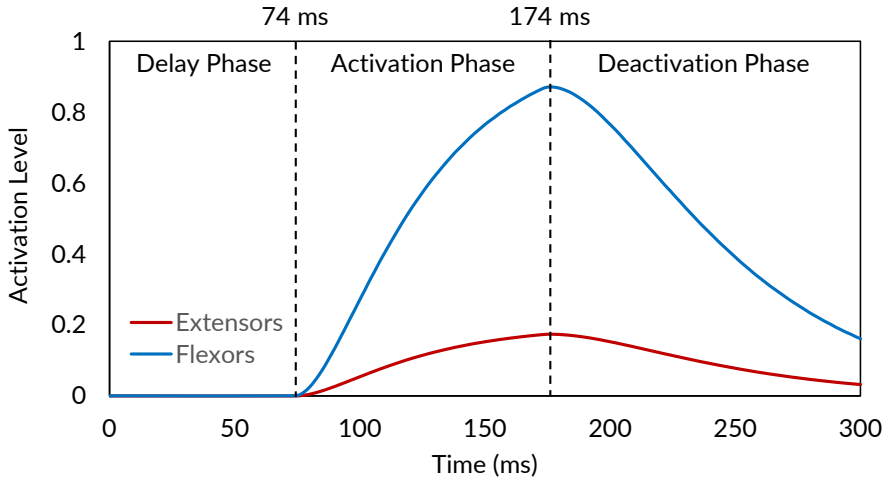


Figure 2-37: Muscle activation curve for the extensor (20%) and flexor (100%) muscles.

The mechanical responses, including the current stretch and strain rate, of the Hill-type elements also affect the active muscle force. Muscles achieve their peak force for a stretch of approximately 1.05 and have reduced capabilities for shorter or longer lengths (Winters & Woo, 1990). The relationship between muscle force and stretch was described as a Gaussian function (Figure 2-38a). Regarding the strain rate effects, the active force is considerably reduced when muscle fibers are shortening (Winters & Woo, 1990). In contrast, muscle lengthening can increase the active force up to 130% depending on

the deformation rate (Winters & Woo, 1990). The relationship between muscle force and strain rate was described as a continuous curve with two distinct hyperbolic regions for tensile and compressive strain rates (Figure 2-38b).

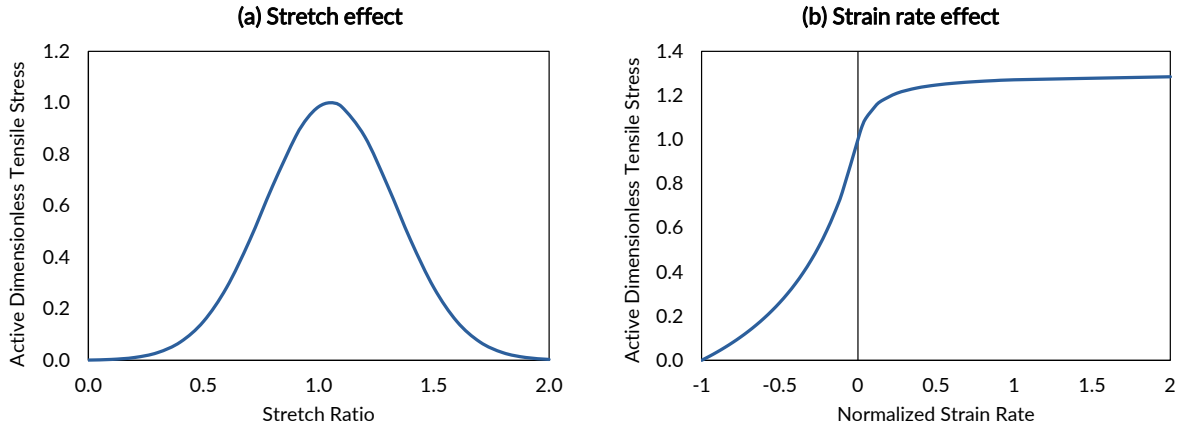


Figure 2-38: Scaling factor of the muscle activation based on the stretch (a) and strain rate (b).

2.7 Stress Initialization in Finite Element Models

The accurate definition of the FE model geometries is essential to realistically represent the physics of the problem (Cronin, 2011; K. H. Yang, 2018). The initial geometries are typically defined as stress-free positions, meaning that the model begins the simulations with all elements in a completely relaxed state. If no external load is applied, the model maintains this relaxed state without deformation. However, in real-life scenarios, the materials often experience initial stresses due to various loading conditions or interactions preceding their current loading. In crash dummies, elastic deformations that occur during positioning and pre-loaded components introduced during assembly are the primary sources of initial stresses (Franz et al., 2004). In the human neck, cadaveric dissections verified that muscles in situ also present a level of deformation (Borst et al., 2011), which influence their mechanical properties during various movements. Therefore, numerical models need to account for the initial stresses of components to accurately simulate their behavior under subsequent loading conditions.

The implementation of initial stresses in an FE model can be performed using different techniques, being divided into implicit and explicit approaches (Franz et al., 2004; J. Yang et al., 2020). Usually, the stress initialization methods consider two simulations: the initial analysis to define the pre-stretch of the material and the subsequent dynamic analysis of interest. The dynamic relaxation method

approximates a dynamic problem to static by applying artificial damping to reach a steady pre-stressed state (J. Yang et al., 2020). The explicit dynamic relaxation, applicable to elastic materials with small initial deformation, uses an initial analysis until convergence to pre-deform the material and proceed to the dynamic analysis. The initial dynamic relaxation can also be solved implicitly, addressing larger initial deformations and highly non-linear problems. Another implicit method involves the generation of stress and strain files from the initial implicit simulation to be used in a subsequent dynamic analysis to pre-stretch the model (Franz et al., 2004; J. Yang et al., 2020). In contrast, the reference geometry method uses an undeformed geometry to initialize the stresses in an FE model, being particularly useful for hyperelastic materials (Franz et al., 2004).

Pre-Stretching Using Reference Geometry

Reference geometry is a predefined deformed configuration (set of nodal positions) used to update the undeformed state in specific parts of an FE model. This definition is valuable for cases when the initial geometry of the model does not represent the undeformed configuration. Consequently, the initial geometry becomes a deformed configuration, having its stresses initialized at the start of the simulation. In the case of hyperelastic materials, the stresses only depend on the deformation gradient matrix (Livermore Software Technology Corporation, 2016). Equation 2-4 shows the deformation gradient matrix, F_{ij}, in terms of the deformed configuration, x_i, and the undeformed configuration, X_j.

$$F_{ij} = \frac{\partial x_i}{\partial X_j} \tag{2-4}$$

The reference geometry method offers one of the most straightforward implementations for numerical stress initialization, as the deformed geometries are typically obtained without multiple iterations. The low-complexity approach is particularly advantageous in large-scale FE models where computational efficiency must also be considered. Figure 2-39 compares a model without stress initialization to one using the reference geometry pre-stretching. In the model without stress initialization, no deformation occurs in the absence of an external load. In contrast, the pre-stretched model shows initial stresses that deform the material even before any external load is applied, reflecting its natural response to return to the relaxed position.

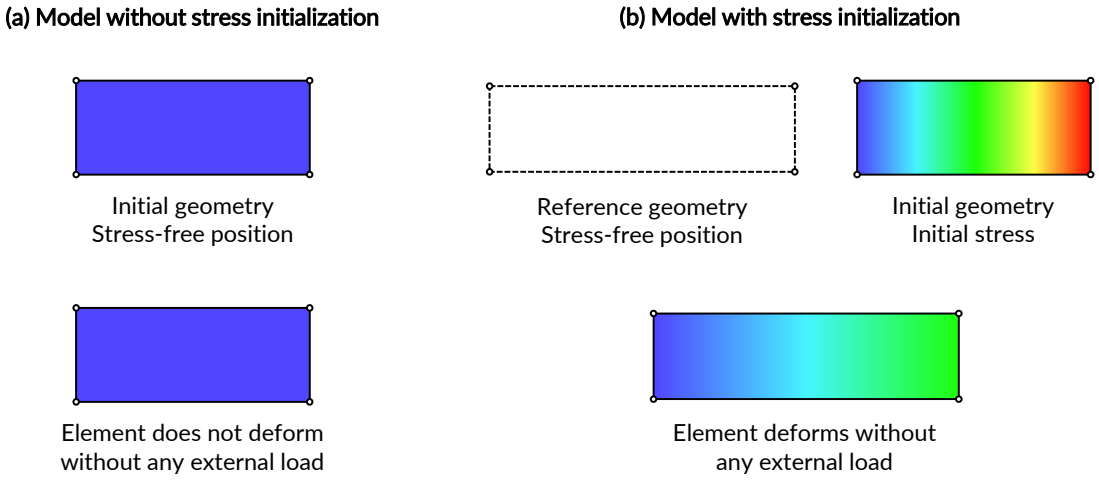


Figure 2-39: Comparison between models without (a) and with (b) stress initialization using reference geometry.

Chapter 3
Methods

The main goal of the current study was to assess the soft tissue injury risk during non-neutral position rear impacts using a detailed FE HBM. The head and neck model was extracted from the detailed commercial FE model GHBMC M50-O v6.0f, representing a male occupant of average stature (50th percentile). A repositioning study was then conducted in the extracted model, including the implementation of a novel stress initialization methodology, definition of target positions, verification of head equilibrium, and validation of intervertebral kinematics. A reference geometry approach was used to pre-stretch the muscle, adipose and skin tissues so the head could achieve an equilibrium condition in the target axial rotations of 24.5°, 33.5°, 42.5°, 51.5°, and 60.5°. The models underwent rotational and stability verifications to confirm that the target non-neutral positions were achieved and that the head and neck were approximately in equilibrium after repositioning. Finally, the repositioning method was validated by comparing intervertebral rotations with experimental results.

The next step was simulating rear impact scenarios on occupant models with neutral and head-rotated positions. A total of six head positions were evaluated in three impact conditions considering two muscle activation schemes. The neutral position model was based on the initial position of the extracted model, and the non-neutral position models had axial head rotations of 24.5°, 33.5°, 42.5°, 51.5°, and 60.5° using the proposed reference geometry approach. Rear impact boundary conditions, including translational and rotational motions, were applied to the T1 vertebra of the models at 4g, 7g, and 10g severities. The influence of muscle activation on injury outcomes was evaluated by assessing each model with and without muscle contraction during the impact. Table 3-1 lists the thirty-six simulations, combining six head positions, three impact severities, and two muscle activation schemes.

Table 3-1: Summary of rear impact simulations.

Group	Rear impact severity	Muscle activation scheme	Initial axial head rotations					
			0°	24.5°	33.5°	42.5°	51.5°	60.5°
1	4g	Non-activated	✓	✓	✓	✓	✓	✓
2		Activated	✓	✓	✓	✓	✓	✓
3	7g	Non-activated	✓	✓	✓	✓	✓	✓
4		Activated	✓	✓	✓	✓	✓	✓
5	10g	Non-activated	✓	✓	✓	✓	✓	✓
6		Activated	✓	✓	✓	✓	✓	✓

The models were solved using commercial explicit FE software (LS-DYNA MPI version 9.2 single-precision) on an MPP heterogeneous cluster (Graham cluster from the Digital Research Alliance of Canada at the University of Waterloo) using 16 cores. An initial analysis of the head kinematics was performed, followed by a tissue-level assessment of the neck. Ligament distractions, muscle strains, nerve root compressions, and AF distractions were monitored through the impact and compared with physiological limits from the literature. The dynamic response of the models and the soft tissue evaluations were visualized and performed using commercial post-processing software (LS-PrePost version 4.9.5). Finally, these results were used to evaluate which tissues potentially experience pain or failure and how head position, impact severity, and muscle activity affected these predictions.

3.1 Implementation and Verification of a Novel Head Repositioning Method

3.1.1 Development of a Reference Geometry-Based Repositioning

A new iterative method for repositioning the head in axial rotation was developed to simulate head-turned rear impacts, so the model was required to stabilize and achieve equilibrium in target head-rotated positions. In addition, it was desirable to retain stresses and strains occurring due to the head rotation as it was hypothesized that pre-stretch of tissues could contribute to injury. Based on these requirements, a repositioning method using reference geometries was proposed to pre-stretch the neck soft tissues (passive muscle, adipose tissue, and skin) and achieve an equilibrium position that would generate a target head rotation.

The repositioning method aimed to define reference geometries for the neck soft tissues, being divided into two stages: prescribing an axial head rotation to define reference nodal positions and pre-stretching the soft tissues to reposition the head (Figure 3-1). In Stage 1, an axial rotation was prescribed to the skull to achieve a head rotation greater than the target and obtain the nodal positions of the soft tissues. In Stage 2, the model was initialized from a neutral position with the calculated reference nodal positions, causing the head and neck model to axially rotate and achieve equilibrium while generating deformations in the soft tissues. These tissues interacted with other neck parts, such as vertebrae, which did not have their stresses initialized so the model would reach equilibrium between the neutral position and the prescribed rotation. The method was iterative, as several axial head rotations needed to be prescribed in Stage 1 to obtain the desired axial rotation in Stage 2.

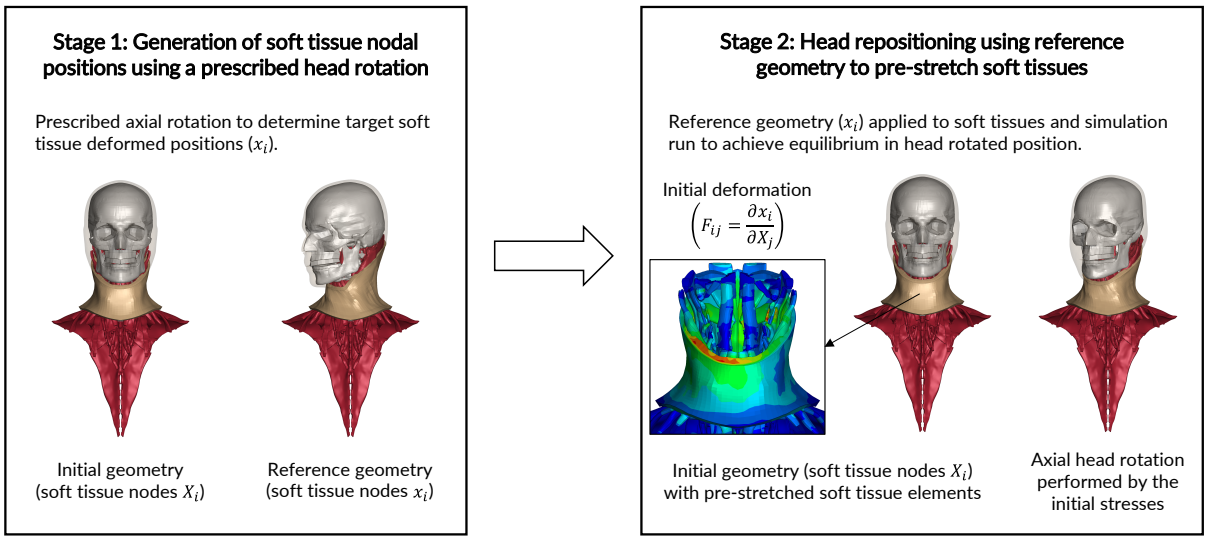


Figure 3-1: Implementation of the reference geometry-based head repositioning: prescribed skull rotation to define reference geometry (Stage 1) and model repositioning to a head-turned equilibrium position resulting from soft tissue pre-stretching (Stage 2).

The current study focused on assessing the influence of axial head rotation in vehicle collisions, so in-car driving measurements were considered to define target positions. The previously discussed pilot investigation (Shugg et al., 2011) showed peak angles of 35.7° (± 14.2°) and 42.5° (± 18.0°) for left and right cervical axial rotation during driving in various routes. The following five right axial rotations were defined as the target head positions based on the right cervical measurements and half a standard deviation from the previous findings: 24.5°, 33.5°, 42.5°, 51.5°, and 60.5°. This division allowed for a sensitivity study between several rotations based on mean peak angles measured in real life.

After defining the target axial rotations, the first stage of the repositioning was implemented. A sigmoidal curve with a peak of 150° was prescribed as the right axial rotation of a skull rigid part (Figure 3-2). The prolonged and elevated rotation allowed sets of nodes to be obtained at various intermediate rotations from the same simulation, reducing the computational effort of Stage 1. Since the equilibrium was based on complex interactions between the head and neck parts, the target rotations were obtained by an iterative process. Sets of nodes from different positions in Stage 1 were iteratively tested until reaching the desired rotation in Stage 2.

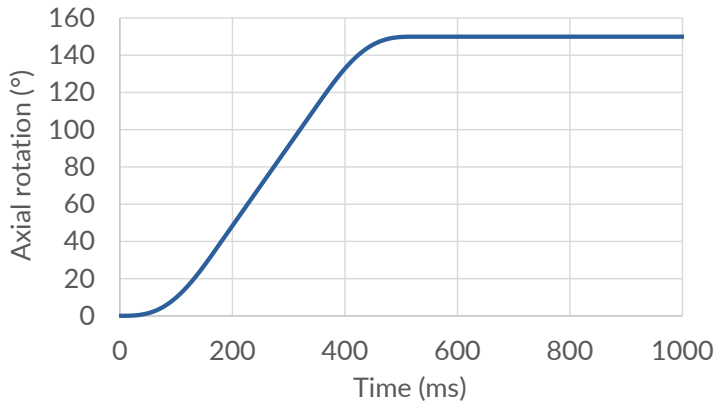


Figure 3-2: Prescribed axial rotation for the skull (Stage 1 of repositioning).

The next stage of repositioning was performed by implementing the soft tissue nodal coordinates as the reference geometries. This configuration defined the coordinates as the new stress-free state for the soft tissues, which initialized the stresses in the model. In LS-DYNA, an initial foam reference geometry configuration (*INITIAL_FOAM_REFERENCE_GEOMETRY) was specified. To ensure a smooth movement in this stage, two additional boundary conditions were defined for the initial 100 ms (Figure 3-3). A skull rotation was prescribed to enable the head to converge to the target position, and damping was applied to the model to reduce oscillations during repositioning.

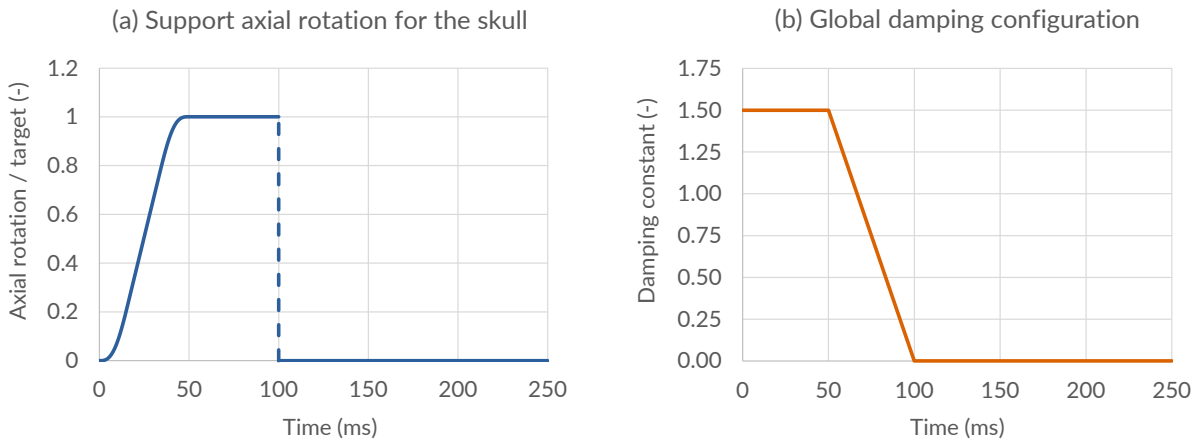


Figure 3-3: Additional boundary conditions: axial rotation of the skull rigid part (a) and global damping (b).

3.1.2 Verification of Head Stabilization and Validation of Intervertebral Rotations

To guarantee that the equilibrium position was reached, the axial rotation, lateral bending, and flexion of the skull needed to be monitored. A stability criterion was used to define when the model achieved equilibrium within a prescribed tolerance. For the repositioning simulations, each C0-T1 rotation of the model was required to remain within a maximum variation of 5% of the target value to be considered in equilibrium. In addition, the final C0-T1 axial rotation was compared with the nominal target angle to verify if the model achieved the target non-neutral position within the same 5% tolerance.

To validate the axial repositioning method, the spinal kinematics of the head-rotated model were compared with reported intervertebral ranges of motion from human ligamentous cervical spine models subjected to pure axial moments (Ivancic, 2013) (Table 3-2). The average experimental range of motion between the head and T1 was 53.3° (± 14.2°) for the right axial rotation, so the 51.5° head-rotated model had the closest C0-T1 rotation and was selected for the physiological evaluation.

Table 3-2: Average range of motion (standard deviation) for each spinal level for the ligamentous spine models undergoing right and left axial rotation (Ivancic, 2013).

Level	C0-C1	C1-C2	C2-C3	C3-C4	C4-C5	C5-C6	C6-C7	C7-T1	C0-T1
Right Rotation	5.1° (2.0°)	27.7° (7.4°)	2.9° (2.0°)	3.7° (2.9°)	3.8° (1.3°)	3.6° (1.3°)	3.0° (1.5°)	3.3° (1.8°)	53.3° (14.2°)
Left Rotation	5.1° (2.0°)	35.1° (8.5°)	2.9° (2.0°)	3.7° (2.9°)	3.8° (1.3°)	3.6° (1.2°)	3.0° (1.5°)	3.3° (1.8°)	63.2° (18.1°)

To obtain the relative rotation between the vertebrae, the measurement method reported in the experiments was implemented in the model. The motion measurements were relative to the directly inferior segment, meaning that the superior vertebra kinematics were expressed in terms of the local coordinate system of the inferior one. The coordinate system of each vertebra was defined by two local directions that expressed the z-axis (horizontal and positive forward) and x-axis (horizontal and positive to the left). The local y-axis was obtained by the cross-product of these two vectors, being vertical and positive upward. After obtaining the relative movement of each intervertebral level, the Euler angles were calculated in the sequence x-y-z (roll-pitch-yaw) based on the transformation in Equation 3-1.

$$R = R_X R_Y R_Z = \begin{bmatrix} 1 & 0 & 0 \\ 0 & \cos\alpha & -\sin\alpha \\ 0 & \sin\alpha & \cos\alpha \end{bmatrix} \begin{bmatrix} \cos\beta & 0 & \sin\beta \\ 0 & 1 & 0 \\ -\sin\beta & 0 & \cos\beta \end{bmatrix} \begin{bmatrix} \cos\gamma & -\sin\gamma & 0 \\ \sin\gamma & \cos\gamma & 0 \\ 0 & 0 & 1 \end{bmatrix} \quad (3\text{-}1)$$

Where α, β, and γ are the roll, pitch, and yaw angles, R_X, R_Y, and R_Z are the Euler rotation matrices, and R is the relative rotation matrix. In the current model, the R matrix was obtained by solving a linear system between the global rotation matrices of subsequent vertebrae. The Euler angles were calculated from the R matrix from each time step, and the final axial rotation (pitch angle) of each intervertebral level was compared with the experimental values (Table 3-2). The temporal variations of the roll, pitch, and yaw angles between C0 and T1 were used to verify the repositioning equilibrium according to the stabilization criterion previously defined. Figure 3-4 illustrates the process of calculating the Euler angles between the skull and T1, which was used for rotational and equilibrium verifications. The same procedure was applied between subsequent vertebrae to validate the intervertebral motion.

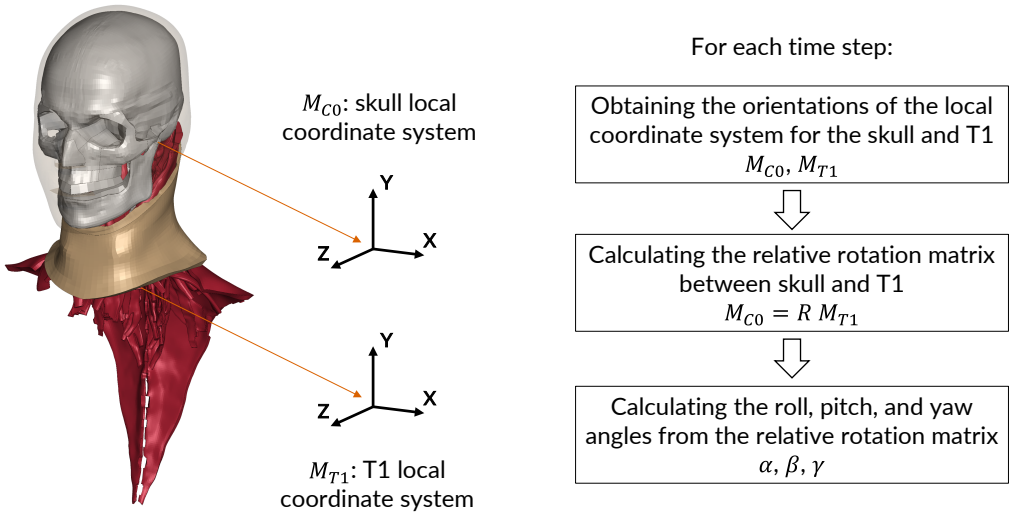


Figure 3-4: Calculation of Euler angles representing the relative rotation between the skull and T1 vertebra.

3.2 Assessment of Neutral and Non-Neutral Head Position Models in Rear Impact Scenarios

After completing previous tests and verifications, the steady head-rotated models could be simulated in rear impact scenarios. One neutral position and five non-neutral position models (head rotations of 0°,

24.5°, 33.5°, 42.5°, 51.5°, and 60.5°) were evaluated in three rear impact scenarios and two muscle activation schemes. The resulting head kinematics and tissue-level responses of the thirty-six simulations were calculated to evaluate the injury risk for neck soft tissues.

3.2.1 Rear Impact Boundary Conditions

While full-body models utilize sled pulses to reproduce vehicle impact conditions, T1 boundary conditions reported from voluntary and cadaveric studies can be used to simulate the impact scenarios using a head and neck model (Barker & Cronin, 2021, 2022). The T1 motion during rear impacts, consisting of two translational accelerations (anterior and superior) and one rotational displacement (lateral), was obtained for impact severities of 4g, 7g, and 10g. To facilitate T1 constraining during the repositioning phase, the acceleration profiles were double-integrated into displacement inputs. The T1 vertebra was fully constrained during the repositioning phase and partially constrained in the lateral (translation), anterior (rotation), and superior (rotation) directions during the impact phase.

4g Rear Impact Boundary Conditions

The T1 boundary conditions for the 4g rear impact were obtained from the rear impact study performed on human volunteers using a sled with a maximum impact speed of 7.9 km/h and a peak acceleration of 3.77 g (Ono et al., 1997; Sato et al., 2014). The head and T1 kinematics were calculated by tracing the motion recorded using a high-speed video camera. The average T1 motion was described immediately after the sled pulse for a total of 250 ms (Figure 3-5).

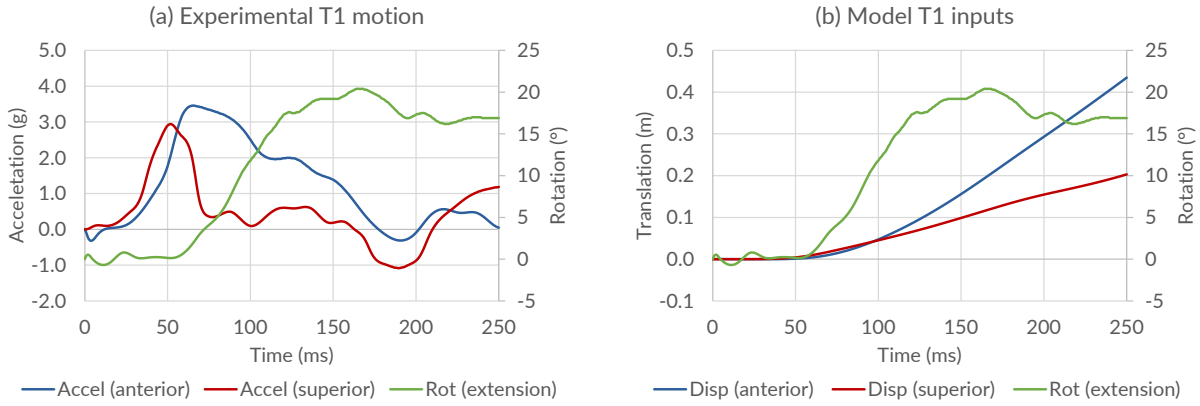


Figure 3-5: Experimental T1 kinematics (a) and integrated T1 inputs (b) for a 4g rear impact scenario (Ono et al., 1997; Sato et al., 2014).

7g Rear Impact Boundary Conditions

The T1 boundary conditions for the 7g rear impact were obtained from the group of rear-end impact experiments using PMHS specimens (Deng, 1999). The T1 motion from a subject with a peak sled acceleration of 8.20 g was selected to describe the 7g rear impact condition (Figure 3-6). This profile had a total duration of 300 ms, with the sled pulse starting at 62 ms.

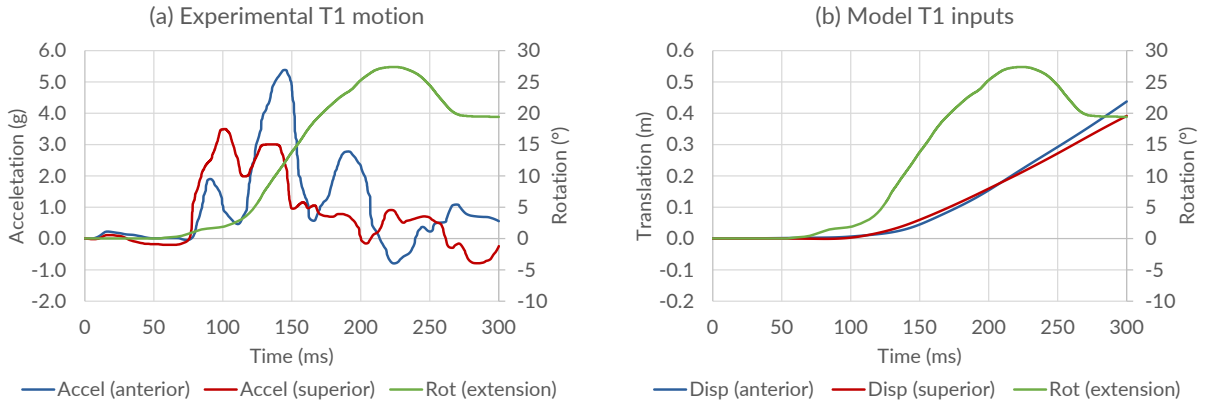


Figure 3-6: Experimental T1 kinematics (a) and integrated T1 inputs (b) for a 7g rear impact scenario (Deng, 1999).

10g Rear Impact Boundary Conditions

The T1 boundary conditions for the 10g rear impact were obtained from the same set of PMHS experiments (Deng, 1999). To simulate this impact, the acceleration and rotational profiles were used from specimens undergoing peak sled accelerations of 9.76 g and 9.36 g, respectively. Two different experiments were used due to the unrealistic rotations reported for the first case (sled pulse of 9.76 g), showing a need for an alternative T1 rotational profile. The subject used to obtain the linear accelerations experienced a T1 peak extension of nearly 70°, which was substantially higher than the 20° to 40° range reported in other experiments. The combined T1 motion had a total duration of 300 ms, with the sled pulse starting at 52 ms (Figure 3-7).

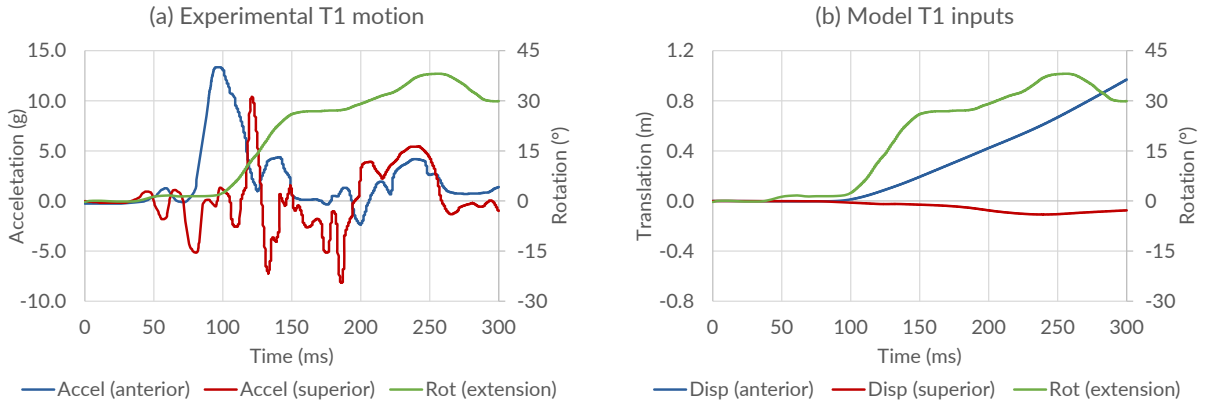


Figure 3-7: Experimental T1 kinematics (a) and integrated T1 inputs (b) for a 10g rear impact scenario (Deng, 1999).

3.2.2 Muscle Activation Schemes

For each rear impact scenario, the effect of muscle activation was evaluated by implementing and comparing the NMA and CMA schemes in the neutral and non-neutral position models. The NMA scheme (extensors and flexors at 0%) was used to simulate cases without muscle activation, while the CMA scheme (extensors at 20% and flexors at 100%) was used to reproduce the muscle contraction in the models. The activation curves and parameters were maintained as the baseline for the GHBMC head and neck models. To synchronize the muscle contraction with the impact conditions, the sled pulse delays were used to offset the muscle activation curve start (Figure 3-8). For the head-rotated models, the offset time also included the time required to reposition the model to a stable non-neutral position.

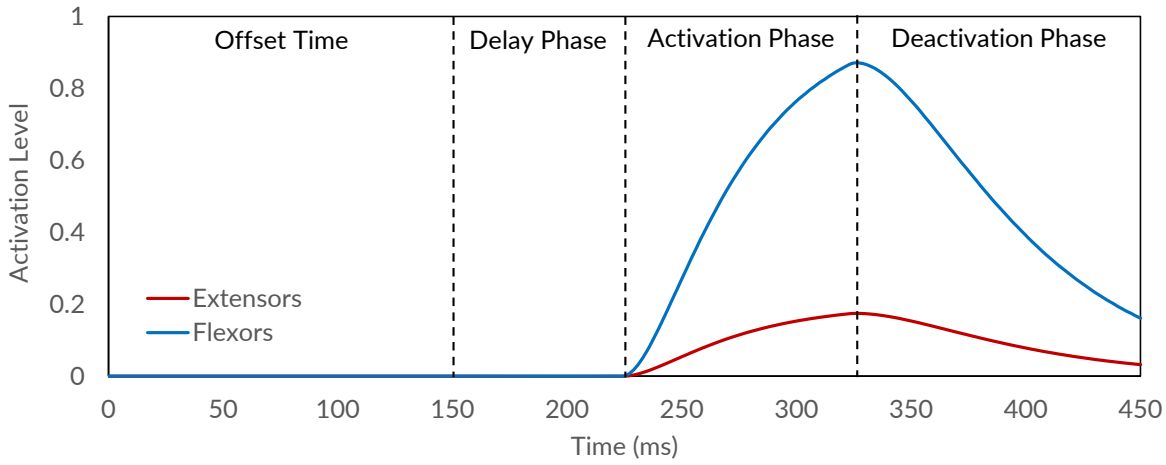


Figure 3-8: Adapted muscle activation curves for the non-neutral position impact simulations.

3.2.3 Kinematics Comparison

While the primary goal of the rear impact models was to evaluate the potential for injury in the neck soft tissues, the head motion was used to identify trends across the different phases of whiplash and enhance the understanding of the subsequent tissue-level assessment. The head movement remained in the sagittal plane during neutral position impacts but became more complex due to the asymmetry added in the repositioned cases. Therefore, the head-T1 roll (flexion/extension), pitch (axial rotation), and yaw (lateral bending) angles were calculated using Euler angles in the sequence x-y-z (roll-pitch-yaw) (Figure 3-4). This definition enabled consistent rotation measurements, aligning with prior verifications and validations using Euler angles.

3.2.4 Soft Tissue Injury Evaluation

The tissue-level response and injury potential were evaluated in the neck soft tissues clinically associated with pain response during whiplash. The ligament distraction, muscle strain, nerve root compression, and AF strain were investigated and compared with physiological limits.

Ligament Distraction

Most ligaments were implemented as 1D tension-only elements in the neck model (Figure 3-9), so their displacements were tracked as the change in distance between their two nodes. The displacement profile of each 1D element was averaged within each ligament group to represent its general response and

minimize the effect of any elements with abnormally high displacements. The maximum values experienced during the impact phase were reported for each case.

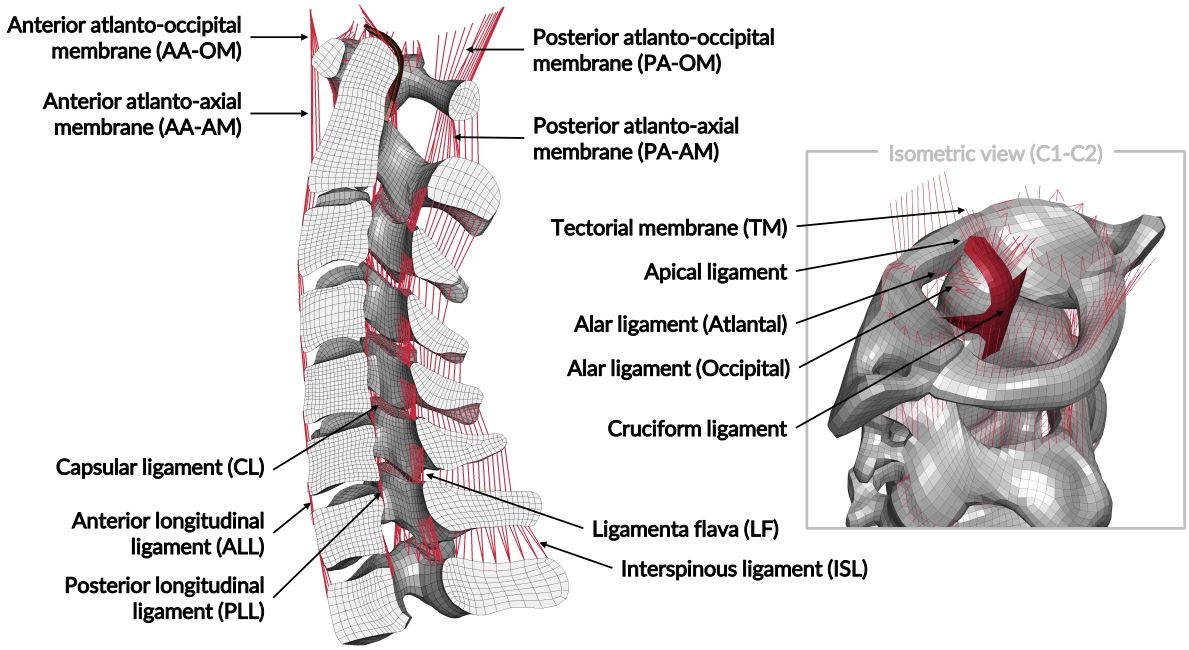


Figure 3-9: Neck ligament implementation, including 1D tension-only and 2D shell elements.

Unlike the other ligament groups, the CL displacement profiles can have significant variations depending on the beam positions, so averaging their curves may compromise the ligament assessment. Instead, a quadrant evaluation was proposed based on the division of the CL elements into eight regions (Figure 3-10a). The displacement profiles were averaged for beam elements inside the same region, and the curve with the highest displacements was selected for the subsequent injury assessment.

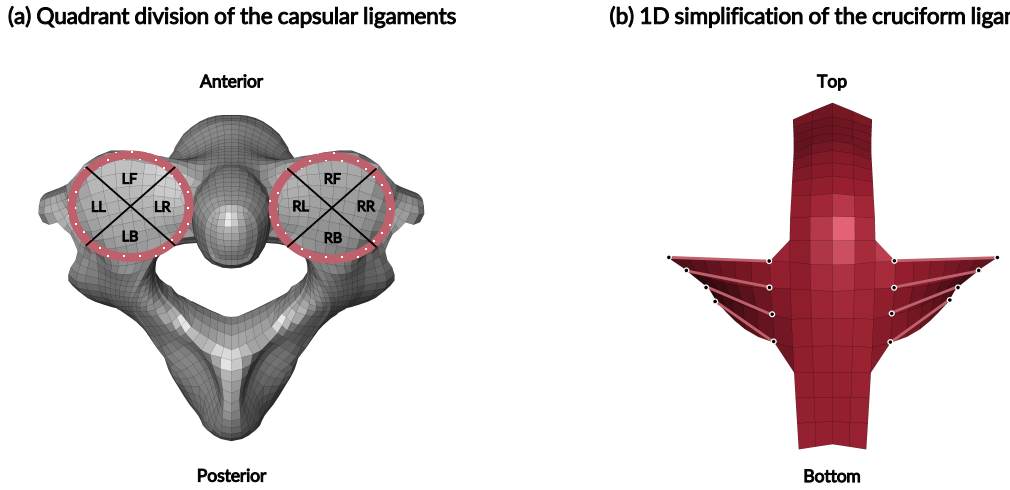


Figure 3-10: Displacement evaluation of capsular (a) and cruciform (b) ligaments.

The exception for the 1D tension-only implementation was the cruciform ligament, formed of 2D shell elements due to its complex shape. While being a combination of the TL with the superior and inferior longitudinal fibers, the load-bearing function of the crux is concentrated in its lateral portion (TL). By concentrating the study on this portion, the ligament considerably reduced its shape complexity and could be simplified to a 1D evaluation. Therefore, the TL displacements were calculated as the change in distance between the innermost and outermost nodes (Figure 3-10b). Note that this assumption was only valid for low displacements.

The ligament injury risk was evaluated by comparing the maximum averaged displacement with their measured response regions. Converting displacement to strain was not necessary since the response regions were obtained from force-displacement curves (Mattucci et al., 2012, 2013). The displacement threshold for the toe, linear, traumatic, and post-traumatic regions was obtained from ligament data and used to evaluate the potential for pain response and tissue failure (Figure 2-16).

Muscle Strain

The muscle failure strain is significantly higher in the transverse direction (Morrow et al., 2010), so the fiber-direction strain is critical for the injury analysis considering the isotropic implementation in the current model version. Considering that the complex muscle structure is simplified as solid hexahedral elements, obtaining the strain in the direction of the fibers can be challenging. The main problem is the definition of the fiber direction of each element, which varies depending on its local coordinate system.

To obtain the fiber-direction strain for all hexahedral muscle elements, a Python script was developed to identify the element edges that align best with the closest 1D beam element of the muscle (Figure 3-11). First, for each solid element of a specific muscle, the code went through all beam elements for that same muscle and identified the closest beam element to the solid element. The closest beam had its direction calculated to represent the fiber direction of the element and was used to find the edges that were best aligned with the fibers. The edges whose directions had the highest dot product (best alignment) with the fiber direction were selected. The length variation of these edges was obtained and used to calculate the stretches. Finally, the stretches were averaged and converted to true strain, representing the fiber-direction strain component of the element. The Python script was tested and assessed for several muscle elements during a rear impact condition, showing an adequate correspondence with the fiber-direction strains calculated from LS-PrePost.

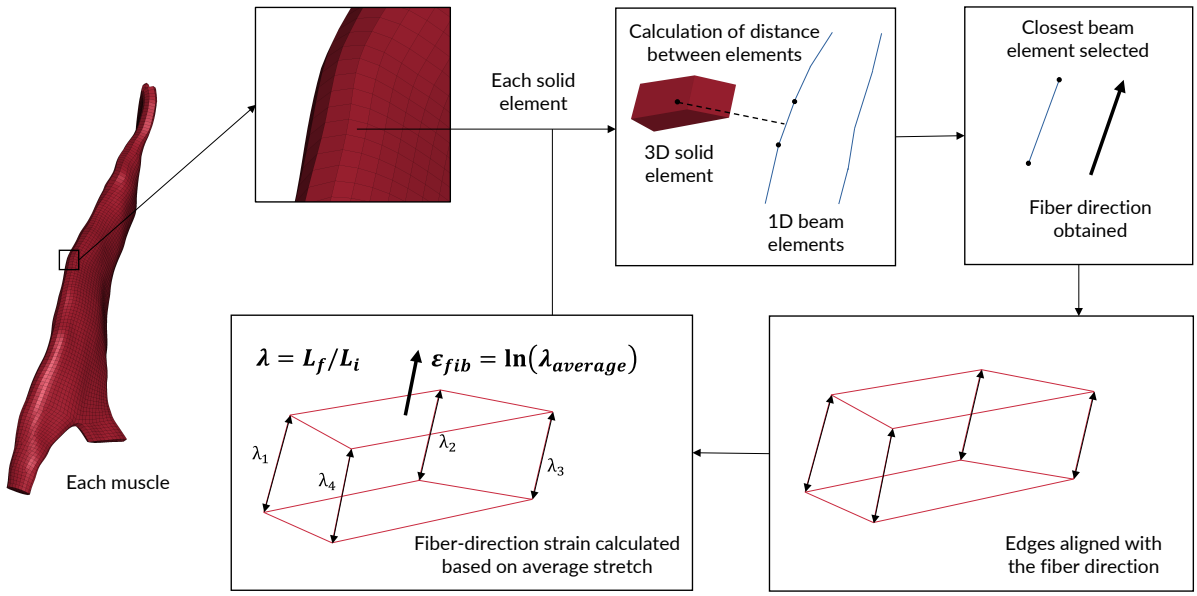


Figure 3-11: Schematic of the method to obtain the strain in the direction of the fibers for each muscle solid element.

The 95th percentile strain was then calculated for each muscle by sorting the peak strains and identifying the value that was exceeded by 5% of the elements. The 95th percentile was selected to remove the effect of any spurious high-strain elements. The calculated fiber-direction strains were compared with measured muscle failure values, which varied depending on the specimen and the muscle contraction.

Studies have reported failure strains between 0.35 and 0.40 for non-active muscles (Best et al., 1995; Morrow et al., 2010) and between 0.21 and 0.30 for active muscles (Hasselman et al., 1995).

Nerve Root Compression

The current model lacks an explicit implementation of nerve roots, so their transverse compression could be estimated by tracking the narrowing of the IVF space. Studies have investigated the potential for nerve root impingement by measuring the change in the height and width of the IVF and comparing the peak narrowing with a baseline (Panjabi, Maak, et al., 2006; Tominaga et al., 2006). Following these experimental procedures, a cross-section was defined at 45° to the midsagittal plane to determine the nodes used to track the change in IVF height and width for each intervertebral level (Figure 3-12). Considering the variation during the impact phase, the maximum reduction values for IVF heights and widths were obtained and compared with reduction thresholds. These reference values were calculated by subtracting the initial value of the IVF dimensions and the reported dimensions of the nerve root (Alleyne et al., 1998).

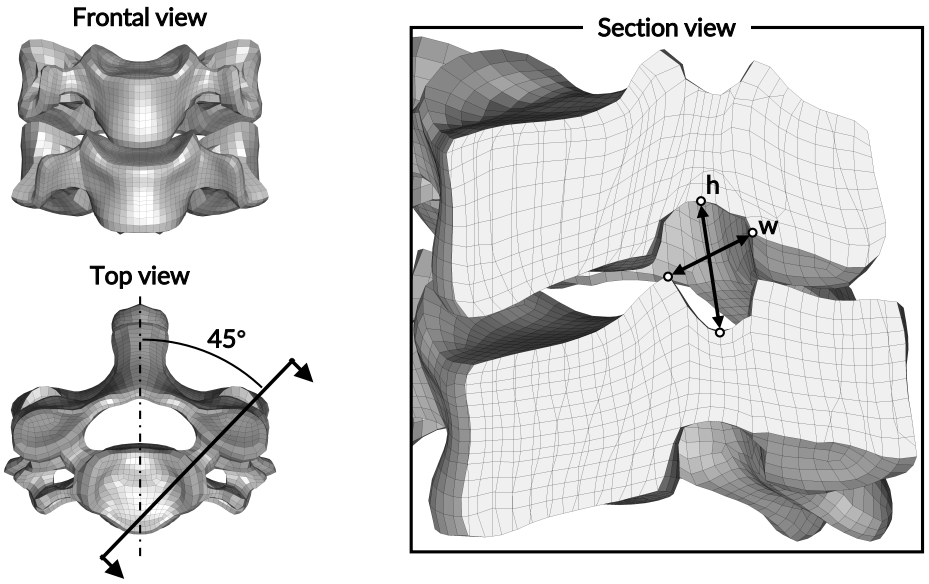


Figure 3-12: Definition of the section and nodes to obtain the foramen height (h) and width (w) between two vertebrae of the model.

Table 3-3: IVF height and width reduction thresholds based on the experimental dimensions of the nerve root (Alleyne et al., 1998).

Level	IVF height	IVF width	Nerve root height	Nerve root width	IVF height reduction threshold	IVF width reduction threshold
C2-C3	12.82 mm	9.32 mm	5.3 mm	3.8 mm	**7.52 mm**	**5.52 mm**
C3-C4	10.35 mm	9.2 mm	5.1 mm	3.4 mm	**5.25 mm**	**5.8 mm**
C4-C5	11.63 mm	8.43 mm	5.8 mm	3.8 mm	**5.83 mm**	**4.63 mm**
C5-C6	11.48 mm	8.05 mm	6.6 mm	4.4 mm	**4.88 mm**	**3.65 mm**
C6-C7	9.55 mm	10.67 mm	7.3 mm	5.7 mm	**2.25 mm**	**4.97 mm**
C7-T1	9.06 mm	11.26 mm	6.7 mm	4.6 mm	**2.36 mm**	**6.66 mm**

Annulus Fibrosus Strain

The layers of annular collagen fibers, represented using 2D shell elements in the model, had their fiber-direction strains calculated throughout the impact for each intervertebral level. The implementation of the annular material (*MAT_FABRIC) allowed for a quick definition of the orientation of the collagen fibers and, consequently, the measurement of the strains in these directions (Figure 3-13). Fiber-direction strains were expected to vary across the annular collagen fibers based on their position. Therefore, the AF elements were divided into four quadrants and had their strains averaged for each section. The maximum strain among all quadrants was obtained for each intervertebral level and compared with measured failure values from experiments that tested annular specimens along the fiber orientation (Iatridis et al., 2005).

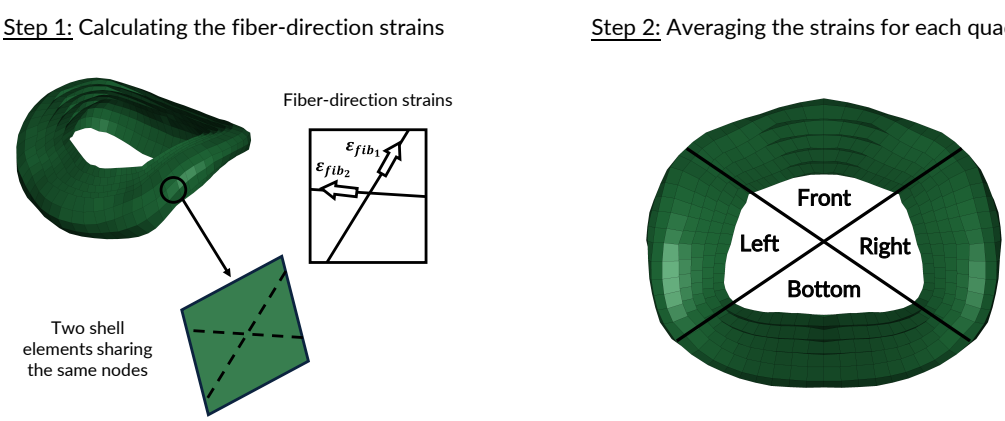


Figure 3-13: Calculation of the average fiber-direction strains for each quadrant of the annular collagen fibers.

Chapter 4

Results

4.1 Reference Geometry-Based Head Repositioning

4.1.1 Head Repositioning to Target Rotations

After obtaining the results of the initial nine tests, it was possible to correlate the head rotations in Stage 1 that would generate target rotations in Stage 2 using a logarithmic fit (Figure 4-1). The curve shows that the model needs exponentially more rotation in Stage 1 to obtain higher axial rotations in Stage 2. This fit was a reasonable estimation for obtaining a specific head rotation using the reference geometry-based head repositioning, avoiding additional iterations in future simulations.

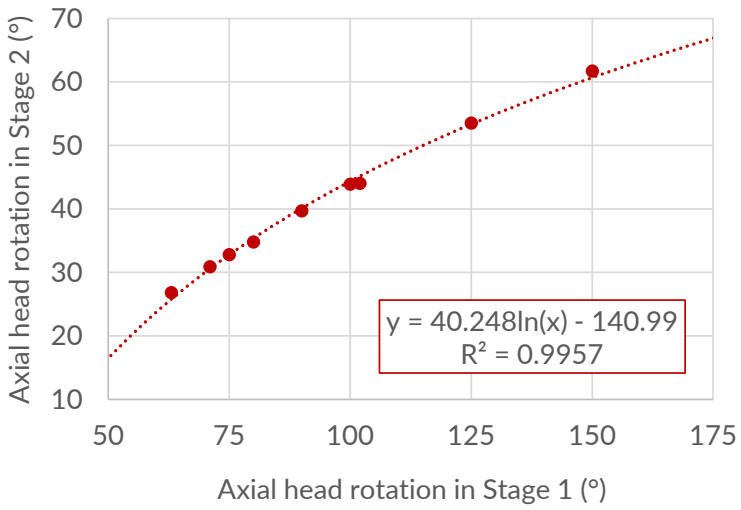


Figure 4-1: Correlation to estimate the initial head rotation (Stage 1) that would rotate the model to a target position using soft tissue pre-stretching (Stage 2).

Using the logarithmic fit, it was possible to obtain the axial head rotations needed to define the soft tissue nodes in Stage 1 and the target positions achieved through soft tissue pre-stretching in Stage 2 (Table 4-1). The five head and neck models achieved the target head-T1 axial rotations of 25.6°, 33.8°, 43.0°, 51.6°, and 60.5°, each within a 5% tolerance of the nominal target angles (Figure 4-2).

Table 4-1: Axial head rotations used in soft tissue nodal selection (Stage 1) to achieve the target rotations using reference geometries (Stage 2) and the differences from the nominal target angles.

Nominal target rotation	Axial head rotation during the selection of soft tissue nodal positions (Stage 1)	Axial head rotation after the reference geometry-based repositioning (Stage 2)	Relative difference between calculated and nominal target angle
24.5°	59.0°	25.6°	4.5%
33.5°	75.6°	33.8°	1.0%
42.5°	96.8°	43.0°	1.1%
51.5°	120.3°	51.6°	0.3%
60.5°	146.1°	60.5°	0.0%

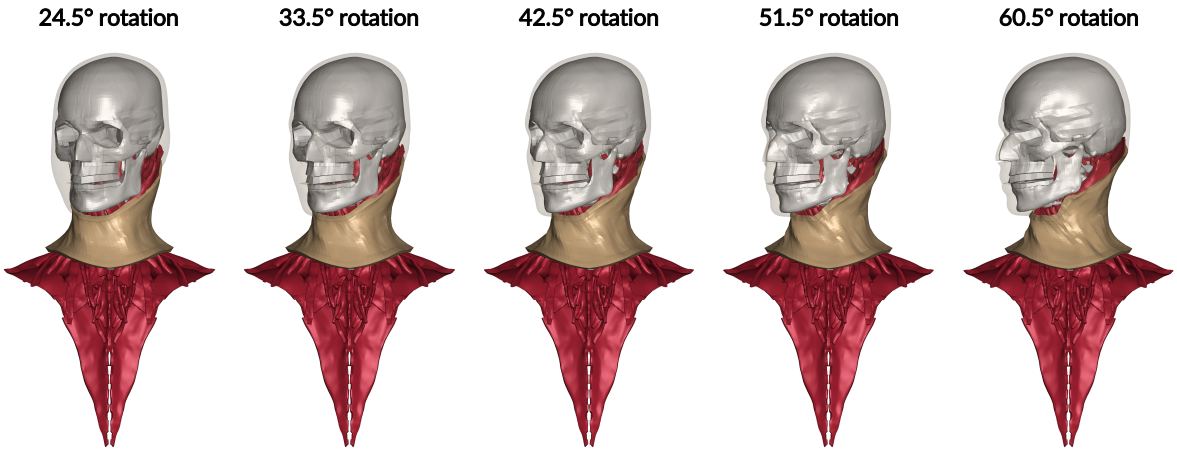


Figure 4-2: Head and neck models repositioned to the five target head rotations using the reference geometry approach.

4.1.2 Verification of Head Stabilization

The axial head-T1 rotations of the five models were monitored throughout the repositioning simulations (Figure 4-3). The head and neck models had maximum variations of 0.50° (24.5°), 0.50° (33.5°), 0.52° (42.5°), 0.53° (51.5°), and 0.64° (60.5°) in their axial rotations. These values represented variations of 2.0%, 1.5%, 1.2%, 1.0%, and 1.1%, respectively, indicating that the models reached equilibrium according to the predefined stabilization criterion of 5% of the target rotation. While being secondary

in the analysis, the variation of the lateral bending and flexion was tracked and indicated equilibrium according to the same criteria (Figure 4-4). In the figures, the positive Y-axes correspond to right axial rotation, right lateral bending, and flexion. The simulation time required for all three rotations to achieve equilibrium within the specified criterion was 150 ms, which was used to offset the T1 impact boundary conditions for the non-neutral position models.

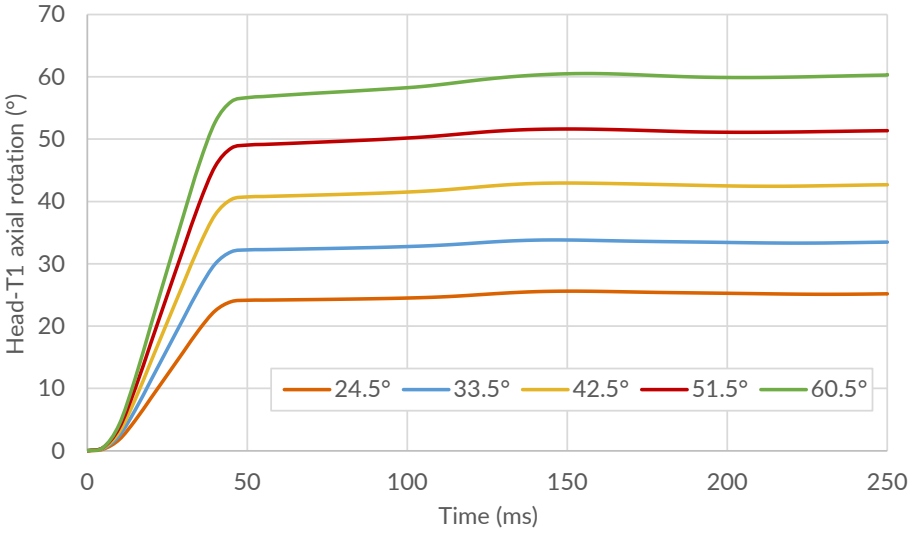


Figure 4-3: Axial head-T1 rotation for the five repositioned models during the stabilization phase.

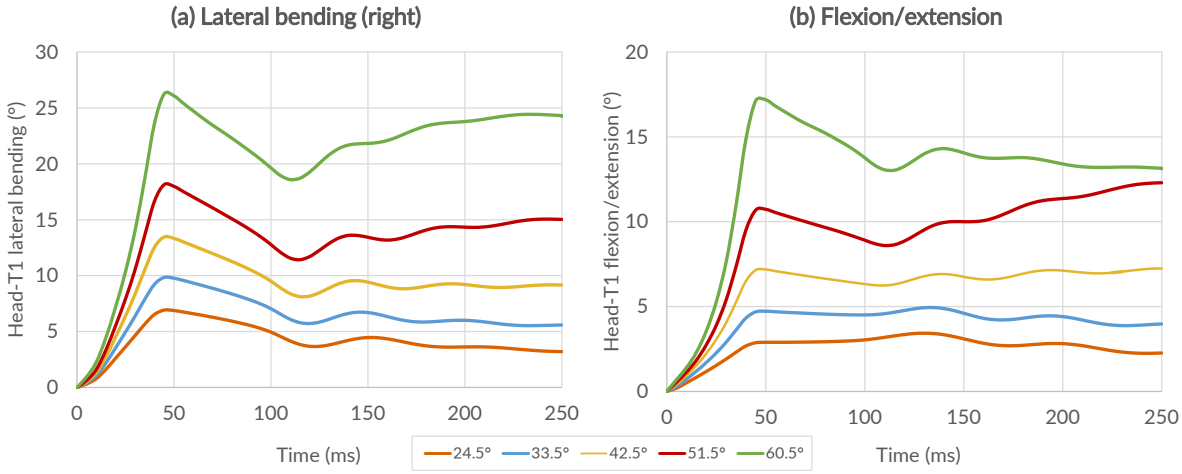


Figure 4-4: Lateral bending (a) and flexion/extension (b) between head and T1 for the five repositioned models during the stabilization phase.

Observing the path of the head until it achieves a steady position, it was possible to verify that the additional boundary conditions helped reduce the oscillations for the initial 100 ms, and the final steady state was achieved at a simulation time of 150 ms. The axial rotation value at a time of 150 ms was used to verify that the nominal target values were achieved. The other two rotational profiles also showed some interesting responses during the repositioning. Both lateral bending and flexion increased for higher axial rotation values, achieving angles of 21.8° and 14.1° for an axial rotation of 60.5° (Table 4-2). While these values were lower than the axial rotations for all cases, they still contributed to a combined rotation of the model.

Table 4-2: Head-T1 rotation values (150 ms), their maximum variation (between 150 and 250 ms), and the stabilization threshold for the head-rotated models.

Nominal target rotation	Axial rotation (max variation)	Lateral bending (max variation)	Flexion (max variation)	Stabilization threshold
24.5°	25.6° (0.5°)	4.5° (1.2°)	3.1° (0.3°)	1.3°
33.5°	33.8° (0.5°)	6.7° (1.2°)	4.6° (0.7°)	1.7°
42.5°	43.0° (0.5°)	9.5° (0.6°)	6.7° (0.6°)	2.1°
51.5°	51.6° (0.5°)	13.4° (1.9°)	10.0° (2.3°)	2.6°
60.5°	60.5° (0.6°)	21.8° (2.6°)	14.1° (0.9°)	3.0°

4.1.3 Validation of Intervertebral Rotations

The model with an axial head rotation of 51.5° was selected for the validation of the intervertebral kinematics. The calculated rotation of the model, 51.6°, was 3.2% lower than the average axial right rotation in the experiment, 53.3°. This indicates that the differences in head-T1 rotations between the models were statistically negligible (less than 5%) and had a minimal effect on the cervical spine motion comparison. The intervertebral measurements in the model generally agreed with the reported experimental axial rotation (Figure 4-5). C1-C2 and all intervertebral levels between C3 and C7 had axial rotations similar to the experimental values for a right axial head rotation. In contrast, C7-T1 showed the highest difference compared to the experimental range, being overpredicted by 3.4°. C0-C1 and C2-C3 rotations were also outside the measured ranges of motion with values of 0.9° and 0.4° below the lower measured boundary.

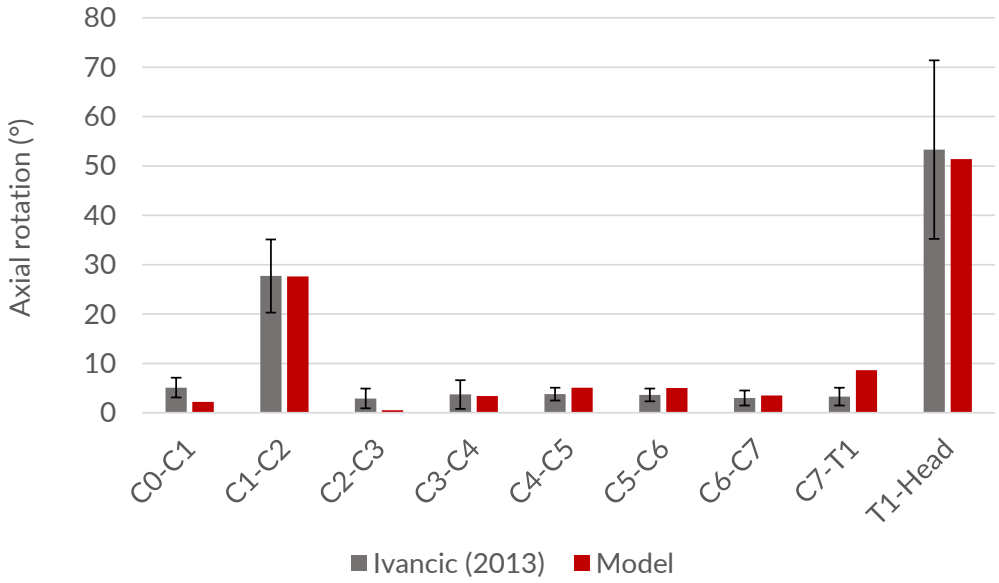


Figure 4-5: Intervertebral axial rotation comparison between the model with a 51.5° head rotation and the experiment with a 53.3° head rotation (Ivancic, 2013).

4.2 Neutral and Non-Neutral Head Position Models in Rear Impact Scenarios

After obtaining the five steady head-rotated models, the non-neutral position rear impact simulations could be performed and compared with the neutral position model. To facilitate the comparison between the head-rotated and neutral position cases, the results were synchronized with the beginning of the sled pulse at 0 ms. Therefore, the non-neutral position simulations were divided into the repositioning phase (initial 150 ms) and the impact phase (final 250-300 ms), while the neutral position simulations only had the impact phase (final 250-300 ms). Figure 4-6 shows the response of the head and neck models without muscle contraction during the 7g rear impact conditions.

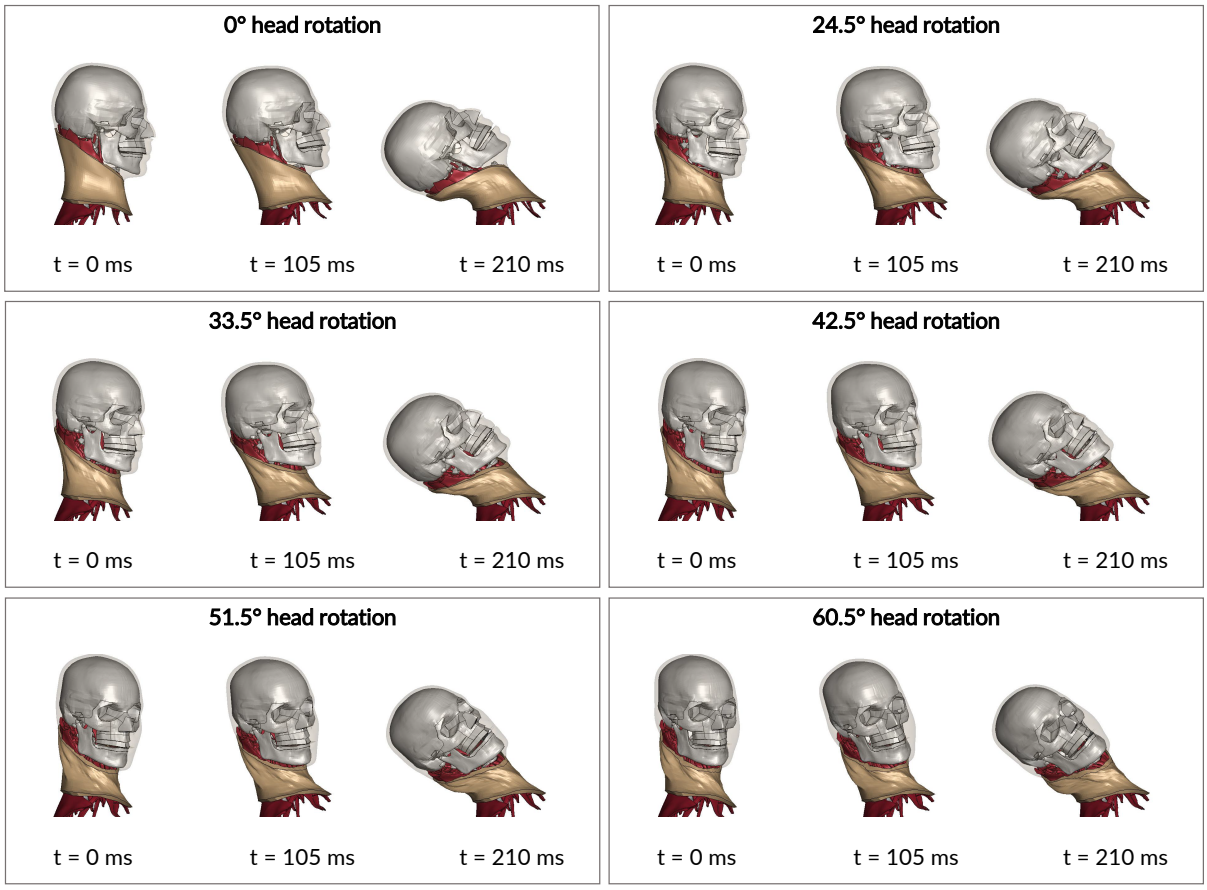


Figure 4-6: Motion sequence of the head-rotated models during a 7g rear impact scenario without muscle activation.

4.2.1 Kinematics Comparison

The head-T1 axial rotation, lateral bending and flexion were obtained to complement the initial graphic evaluation of the different head positions undergoing rear impact conditions (Figure 4-7, Figure 4-8, Figure 4-9, Appendix A). In the figures, the positive Y-axes correspond to right axial rotation, right lateral bending, and flexion. The neutral position cases had their head movements restricted to the sagittal plane, meaning that only the flexion angle varied over time. This response was expected due to the geometric symmetry and T1 motion restriction around the same plane. In contrast, the head-rotated models did not experience pure extension during the rear impact scenarios, as the axial rotation and lateral bending variations became relevant. The geometric asymmetry added by the initial head rotations generated complex rotations throughout the impact simulations.

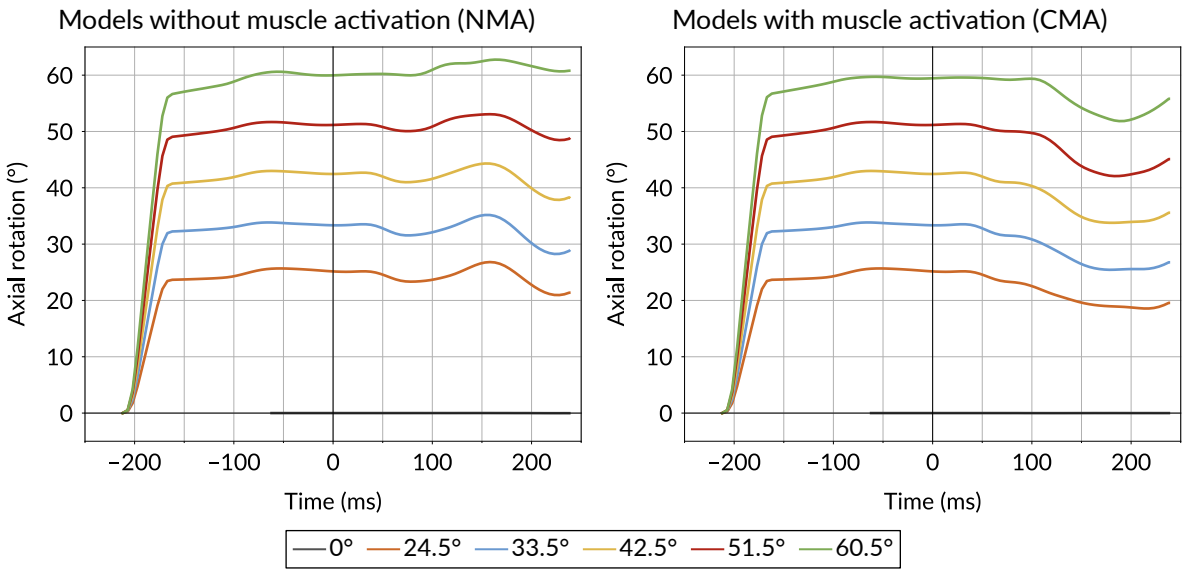


Figure 4-7: Head-T1 axial rotation under a 7g rear impact, without and with muscle activation for five head axial rotation positions.

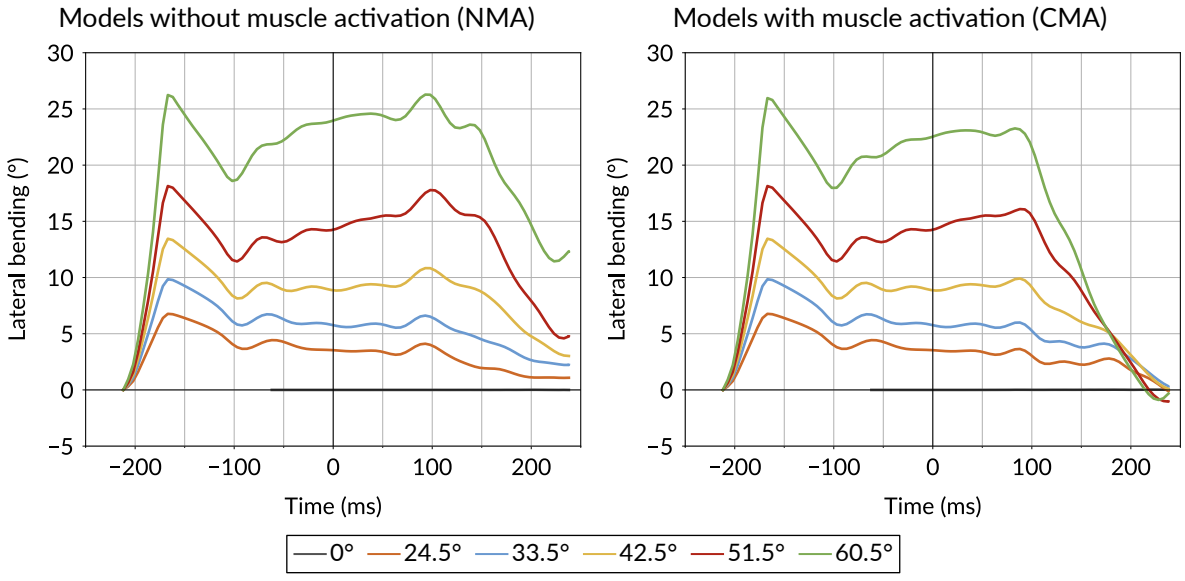


Figure 4-8: Head-T1 lateral bending under a 7g rear impact condition, without and with muscle activation for five head axial rotation positions.

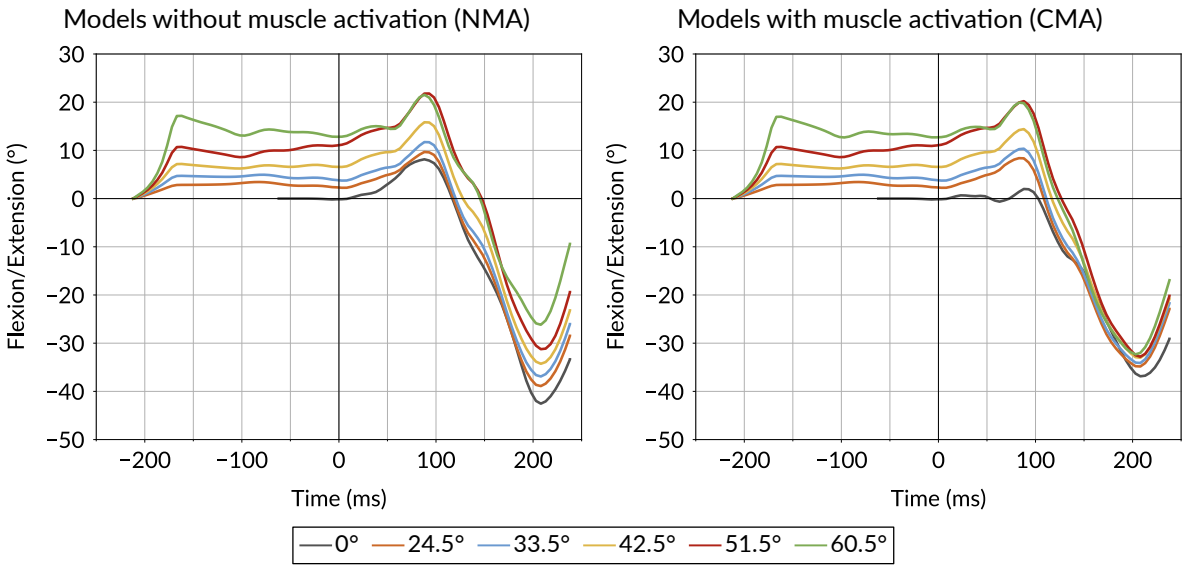


Figure 4-9: Head-T1 flexion/extension under a 7g rear impact condition, without and with muscle activation for five head axial rotation positions.

The head-T1 axial rotations were similar for all impact severities and muscle activation schemes, having the lowest variations among the three angles. The models without muscle activation had slight oscillations around the initial head rotations, while those with muscle activation had consistent decreases in the axial angle. The lateral bending angles experienced significant reductions throughout the impact and were affected by the different conditions, especially muscle activation. When muscle activation was not used, the models had smaller decreases in the lateral bending and ended with positive values (right lateral bending) for all three impact severities. The models using the CMA scheme experienced high reductions in lateral head bending, converging to values close to 0°.

The flexion angles had the most complex behavior, as their variations were highly affected by the initial axial head rotation, impact severity, and muscle activation. As a general trend, the head and neck models experienced a reduced level of flexion followed by a high extension. For the 10g rear impact, the hyperextension was followed by a rebound phase, characterized by a decrease in extension followed by another extension peak. The 10g impact severity also showed sooner hyperextension peaks than the 4g and 7g cases, which had similar profiles. Muscle activation caused the head responses to converge to a similar path during hyperextension regardless of the initial head position. In contrast, the groups without muscle activation had much sparser responses for different head positions. The influence of the

initial head position could be verified by the initial flexion added to the impact phase. The cases with higher head rotations initially had higher flexion levels followed by lower extension levels. Therefore, models with lower head rotations had higher hyperextension peaks.

4.2.2 Ligament Distraction Evaluation

The cervical spine ligaments had different displacement patterns depending on their locations in the neck, with some head-rotated models exhibiting values close to the linear limit. The CLs had maximum quadrant displacements located between the middle and the end of the linear region for the most severe cases. The highest displacements happened for lower cervical levels (below C3), with C3-C4 and C5-C6 having the most severe outcomes. As a general trend, the CL ligament distractions were substantially affected by the head position and showed increasing values for higher rotations (Figure 4-10, Appendix B). The 60.5° head-rotated impact experienced the highest quadrant distractions, being close to the linear limit for up to six levels (from C1-C2 to C6-C7). A head rotation of 51.5° also generated elevated displacements during the impact conditions, being located between the middle and the end of the linear region for up to two levels (C3-C4 and C5-C6). The models with rotations between 24.5° and 42.5° had moderate distractions, without any quadrant value close to the linear limit. The neutral position case had the lowest CL displacements with maximum values entering the linear region.

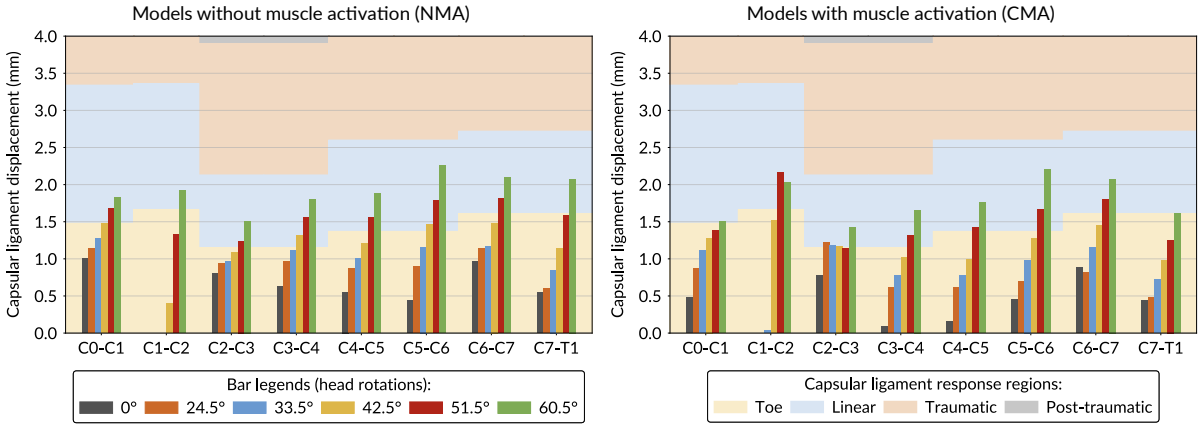


Figure 4-10: Maximum quadrant displacement of capsular ligaments during a 7g rear impact scenario without and with muscle activation compared with the response regions (Mattucci et al., 2012, 2013) for each intervertebral level.

The head repositioning also changed the location where the maximum displacements occurred due to the asymmetry added. While the neutral position model experienced CLs with peak displacements mainly on the frontal and lateral parts, the repositioned cases had a concentration of critical ligaments in the lateral portion of the facet joints. Muscle activation induced a slight reduction in the quadrant displacements for all levels except C1-C2, which had the opposite trend with increased distractions. Impact severity also increased ligament distractions, especially in cases without muscle activation. Higher impact severities generally increased the CL distractions, with the 10g impact condition generating the highest displacement values.

The ISLs had distinct injury potentials depending on the spinal level (Figure 4-11, Appendix B). Models with high head rotation experienced elevated C1-C2 distractions, representing a high risk of tissue pain. In contrast, the distractions for all the other levels were low and located inside the toe region, representing a considerably reduced injury risk. Similar to the CLs, the distractions were higher for increasing head rotations. The exceptions were some low cervical spine cases that had abrupt displacement growths with muscle activation. In general, muscle contraction contributed to slight displacement reductions and had a higher influence on the upper levels. Increasing the impact severity also had limited effects on these ligaments, with more relevant increases between 7g and 10g.

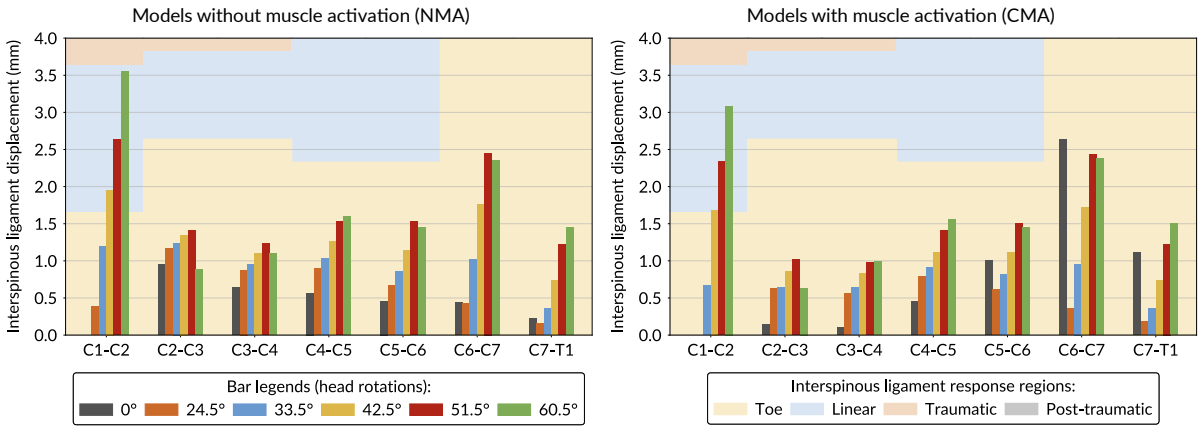


Figure 4-11: Average displacement of interspinous ligaments during a 7g rear impact scenario without and with muscle activation compared with the response regions (Mattucci et al., 2012) for each intervertebral level.

The ALLs had moderate to high displacements during the rear impact scenarios, primarily located in the linear response region (Figure 4-12, Appendix B). C4-C5 and C5-C6 were the critical levels, with

values close to the linear limit for some head-rotated models without muscle activation. The other cervical levels had moderate displacements, at most in the middle of the linear region, and did not represent an elevated risk of pain response. In general, increasing head rotations slightly increased ligament displacements, with the highest values happening for the 60.5° case. However, muscle activation reduced those differences and even changed the trend for some impact scenarios, with the peak values happening for the neutral position. Muscle activation also reduced ligament distractions during rear impacts, especially for the most severe levels (below C4).

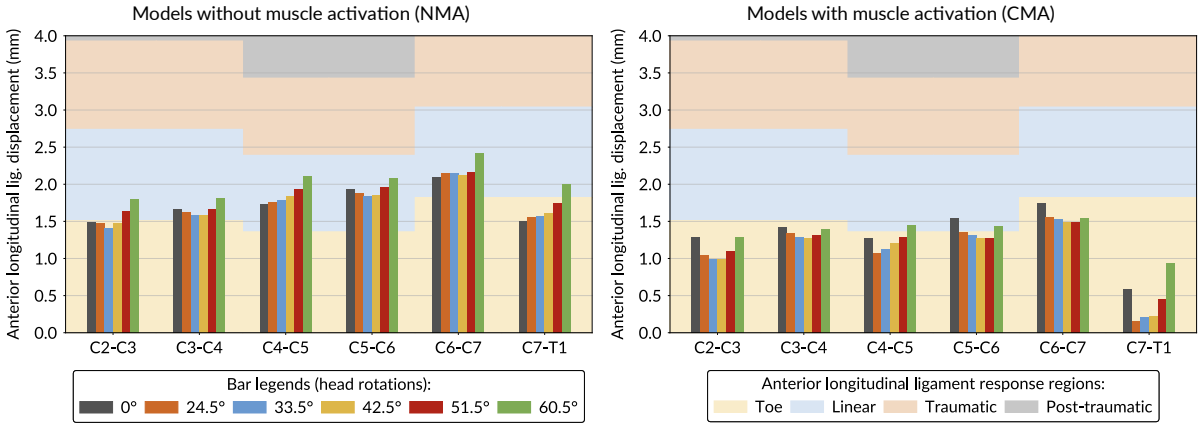


Figure 4-12: Average displacement of anterior longitudinal ligaments during a 7g rear impact scenario without and with muscle activation compared with the response regions (Mattucci et al., 2012) for each intervertebral level.

The PLLs had lower distractions compared to the ALLs, with values below 1.5 mm (Figure 4-13, Appendix B). All ligaments were inside the toe region for 4g and 7g severities, representing a low injury risk. Some models undergoing a 10g rear impact condition had their ligaments entering the linear region, slightly increasing the risks of pain. Muscle activation contributed to a general reduction in distractions while increasing impact severity generated higher ligament outcomes. Located in the posterior portion of the cervical spine, these ligaments were substantially affected by the rebound phase and, consequently, by the 10g rear impact condition.

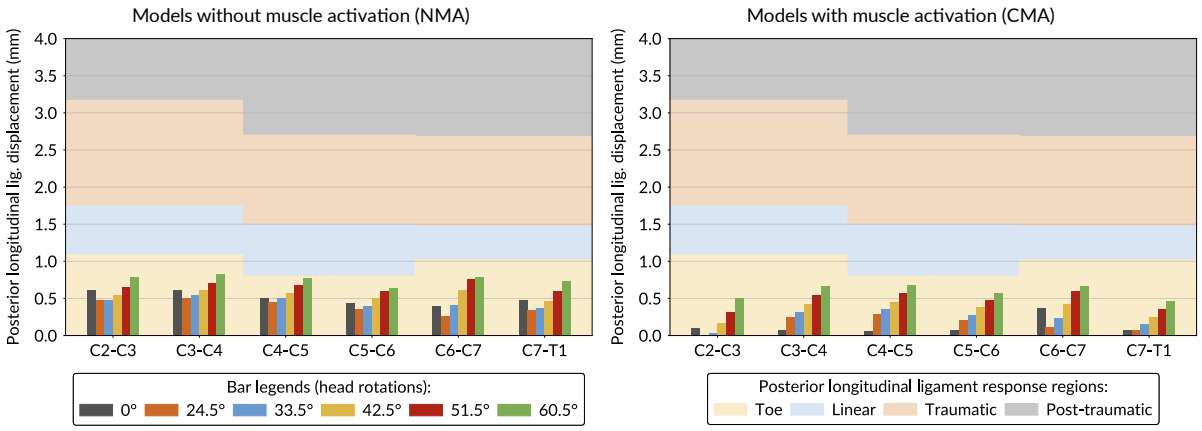


Figure 4-13: Average displacement of posterior longitudinal ligaments during a 7g rear impact scenario without and with muscle activation compared with the response regions (Mattucci et al., 2012) for each intervertebral level.

The LF had low displacements, situated generally at the beginning of the toe region (Figure 4-14, Appendix B). The head positioning and the impact conditions had limited influence on these ligaments, with minimal risk of damage. The overall trend followed the other ligaments and showed increased displacements for higher head rotations. Apart from some neutral position cases, muscle activation reduced the ligament distractions during the impact scenarios. The increase in impact severity had a limited effect between 4g and 7g but generated higher displacement values for the 10g rear impact.

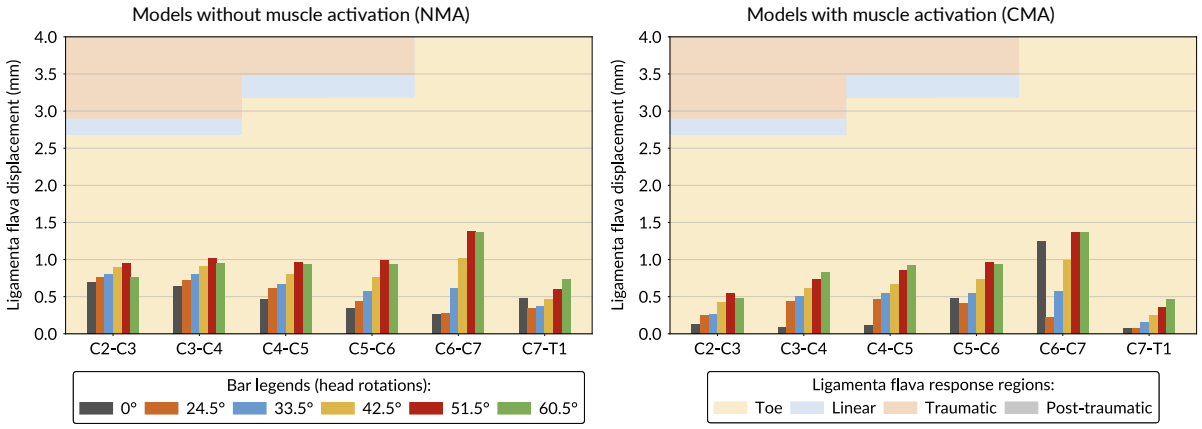


Figure 4-14: Average displacement of ligamenta flava during a 7g rear impact scenario without and with muscle activation compared with the response regions (Mattucci et al., 2012) for each intervertebral level.

The remaining ligaments in the upper cervical spine had different behaviors depending on the impact condition (Figure 4-15, Appendix B). For the 4g and 7g impact severities, all these ligaments had low distraction and were located inside the toe region. The 10g rear impact cases had several ligaments entering the linear region, including alar, apical, and TM.

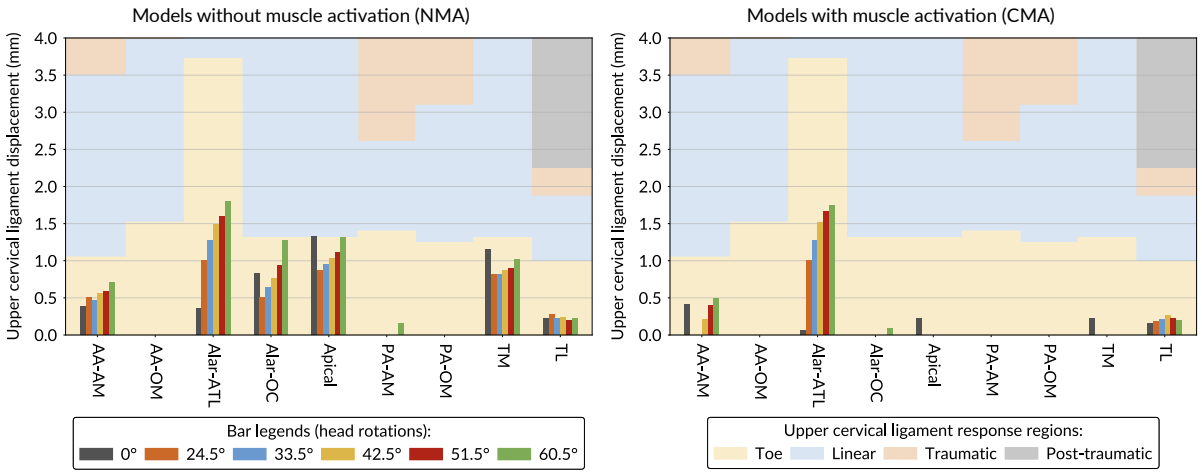


Figure 4-15: Average displacement of upper cervical spine ligaments during a 7g rear impact scenario without and with muscle activation compared with the response regions (Mattucci et al., 2013) for each ligament.

The effect of the head position was diverse among the upper cervical spine ligaments. The AA-AM, PA-AM, and alar ligament experienced increasing displacement values for higher head rotations. Conversely, the TM and apical ligament experienced their highest displacements with the limit cases (rotations of 0° and 60.5°) during 4g and 7g rear impacts. The 10g severity had a different influence on those ligaments, with lower displacements being experienced for increasing head rotations. The AA-OM, PA-OM, and TL had reduced values and showed no clear trend when varying head positions. The use of muscle activation had a high effect in reducing ligament distractions. Regarding the effect of impact severity, few differences were verified between the 4g and 7g cases. However, the increase in impact severity to 10g highly affected some ligaments, such as alar and apical, due to the rebound phase being considered in this condition.

4.2.3 Muscle Strain Evaluation

The fiber-direction strain evaluation indicated that some muscles had elevated deformations while undergoing rear impact scenarios (Figure 4-16, Appendix C). Rectus capitis lateral, omohyoid, sternohyoid, sternocleidomastoid, levator scapula, and scalenus medius experienced the highest fiber-direction strains, exceeding damage thresholds for multiple cases. Considering that the injury threshold is lower for activated muscles, the models using muscle contraction had significantly more muscles with strains entering the damage region. For all groups, the models with a 60.5° head rotation had the highest fiber-direction strains and, consequently, the highest risk of muscle damage.

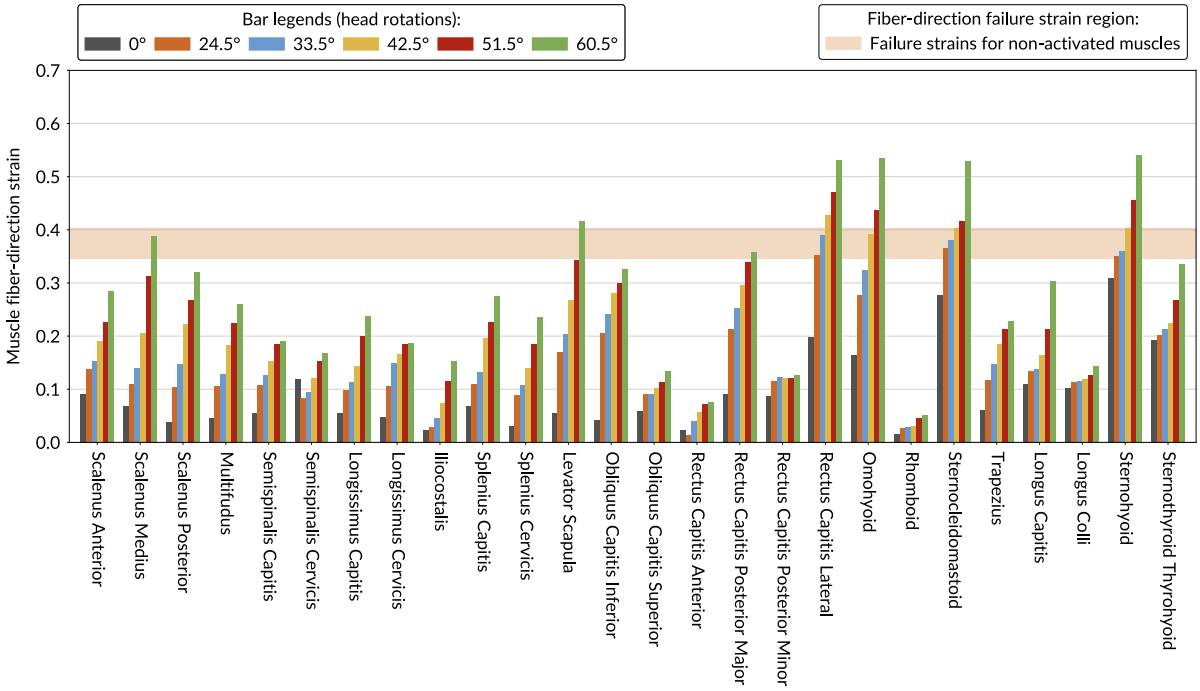


Figure 4-16: 95th percentile muscle fiber-direction strains during a 7g rear impact scenario without muscle activation compared with the failure region for non-activated muscles (Best et al., 1995; Morrow et al., 2010).

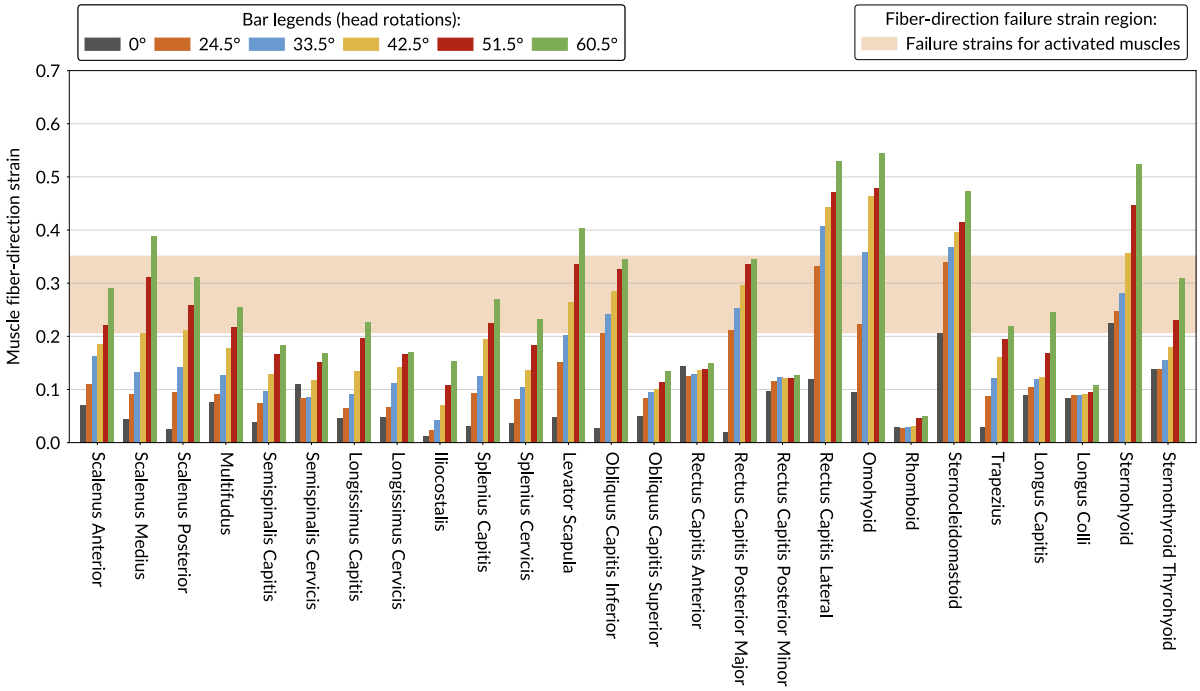


Figure 4-17: 95th percentile muscle fiber-direction strains during a 7g rear impact scenario with muscle activation compared with the failure region for activated muscles (Hasselman et al., 1995).

As they were crucial to the head rotation movement, the muscles had their fiber-direction strains highly affected by head position. Higher fiber-direction strains were experienced with increasing head rotations, reaching a maximum for 60.5° axial head rotation. The neutral position cases had the lowest muscle fiber-direction strains, which mostly did not reach the damage region. In contrast, the model with a head rotation of 60.5° had at least seven muscles that exceeded the failure strain threshold for all impact severities and muscle activation schemes. The number of affected muscles increased to seventeen when considering muscle activation, due to the decrease in the damage threshold. The head rotations between 0° and 60.5° showed intermediate behaviors to those two cases. However, even for low head rotations, the model predicted high strains that could potentially damage the muscles.

The addition of muscle activation to the models had different effects on each muscle, depending on the head position. For elevated head rotations, the activation scheme had a low effect on the muscle outcomes and did not affect the injury evaluation. Conversely, the models with low head rotations experienced strain reductions for most muscles when contracted. The exceptions were the rectus capitis anterior and omohyoid, having a considerable strain increase for all head rotations. Regarding the

change in impact conditions, the cases with higher head rotation also had slight differences for increasing severities. The impact severity had more visible effects for lower head rotations, with higher fiber-direction strains being experienced for increasing impact conditions.

4.2.4 Nerve Root Compression Evaluation

The reduction of the IVF heights (Figure 4-18, Appendix D) and widths (Figure 4-19, Appendix D) was small for all head rotations, impact severities, and activation schemes. The IVF height reduction was generally below 2 mm for C2-C3 and below 1 mm for all lower levels. While the upper levels had higher height reductions, they also had increased threshold values and low risks of nerve root impingement. The IVF widths had even smaller reductions, with maximum values of 0.8 mm and higher variations for lower intervertebral levels. Multiple cases did not experience any width reduction, and the changes in this IVF dimension also showed low risks of impingement.

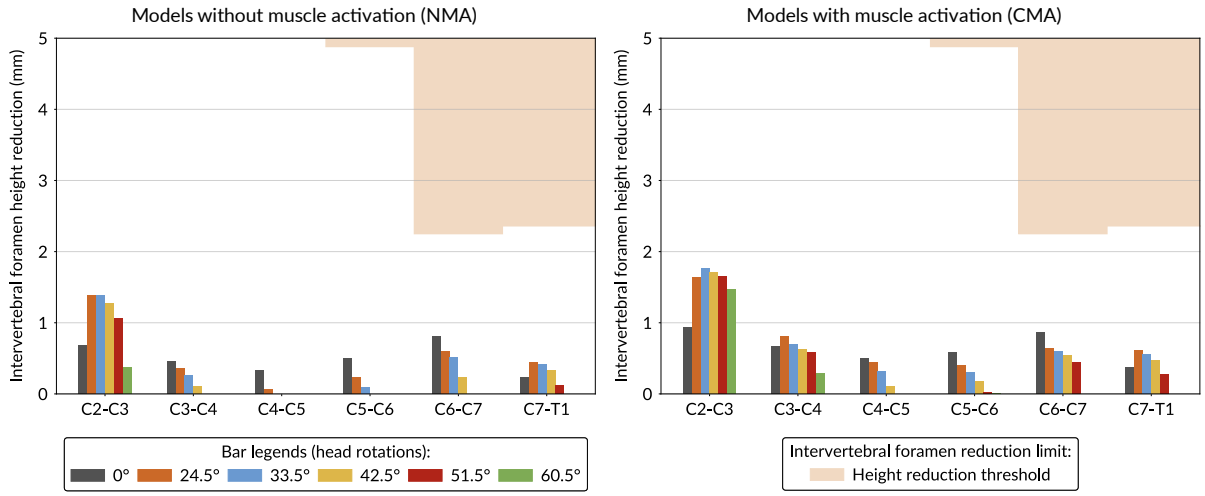


Figure 4-18: Maximum intervertebral foramen height reductions during a 7g rear impact scenario without and with muscle activation compared with the threshold values.

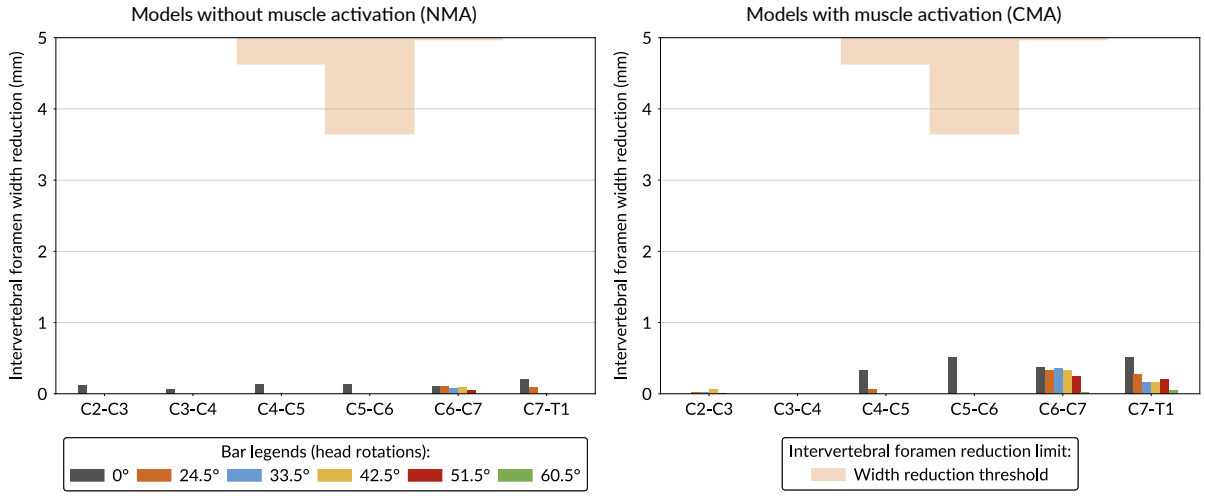


Figure 4-19: Maximum intervertebral foramen width reductions during a 7g rear impact scenario without and with muscle activation compared with the threshold values.

Comparing the IVF height variations for different head rotations, two opposite trends could be verified depending on the intervertebral level. Lower cervical levels experienced decreases in height reduction for higher head rotations, while C2-C3 and C3-C4 mostly had the highest reductions for intermediate rotations. While few changes in the IVF widths were noticed, their reductions were generally lower with increasing head rotations. The impact severity also seemed to have a low effect on the width variation, with small increases in C6-C7 and C7-T1 levels. The IVF height reduction also had minor increases with increasing impact severity. Muscle activation further reduced the IVF space and slightly increased the chance of nerve root impingement.

4.2.5 Annulus Fibrosus Strain Evaluation

The evaluation of the quadrant fiber-direction strain of the AF showed differences depending on the intervertebral level (Figure 4-20, Appendix E). C5-C6 was the region that generally showed the highest strains, entering the damage region for some 7g and 10g rear impact cases. The spinal levels above C5-C6 experienced intermediate strains in most cases. The exceptions were some models undergoing the 10g rear impact using muscle activation with quadrant strains reaching the reported failure strain. The levels below C5-C6 showed low strain values during the impact, mostly below 20%, and did not enter the damage region for the AF.

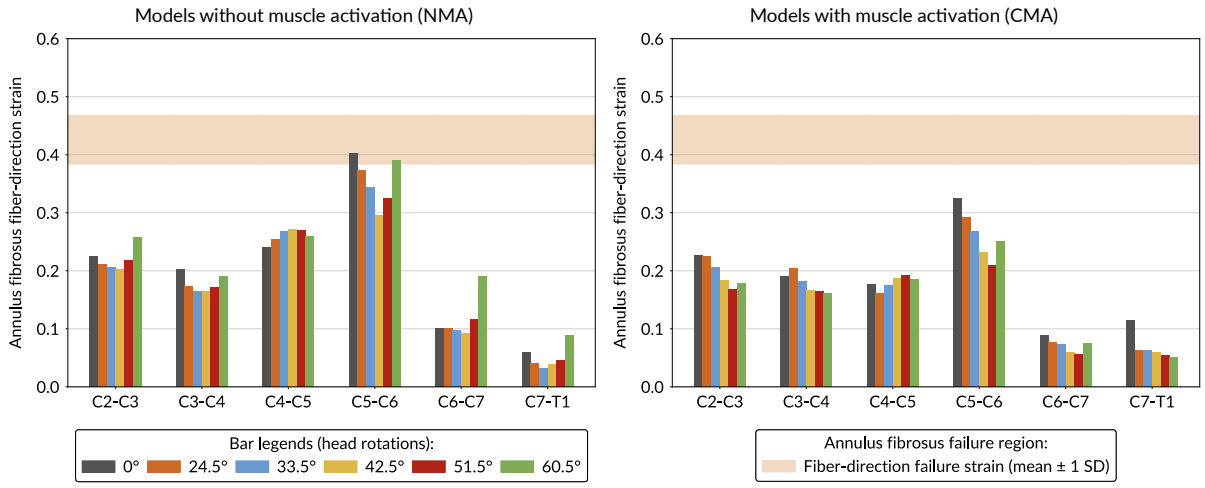


Figure 4-20: Maximum quadrant fiber-direction strain of annulus fibrosus during a 7g rear impact scenario without and with muscle activation compared with the failure corridor (Iatridis et al., 2005) for each intervertebral level.

The effect of head rotation in the fiber-direction strain of the AF was also mixed with different trends for each region and group. For models without muscle activation, the lowest strains generally happened with intermediate head rotations, meaning that peak strains occurred for head rotations of 0° and 60.5°. The opposite trend was observed for the C4-C5 level as the peak strains were identified for head rotations between 33.5° and 51.5°. These responses caused some intermediate cases, such as a head rotation of 42.5°, to not experience injurious strains for any impact severity or muscle activation scheme. Alternatively, the limit cases (0° and 60.5° head rotation) had at least one level experiencing strains that could damage the fibers when the model underwent impact severities of 7g and 10g. The AF quadrants with the highest displacements were generally the same for different head positions, and the peak C5-C6 strains were concentrated in the right portion of the disk. Some spinal levels, such as C2-C3 and C7-T1, had a transition of the critical regions from the longitudinal to the lateral sections.

In general, muscle activation helped to reduce the maximum strains and the risk of tissue damage in the AFs. These reductions also made the models behave more similarly for different head rotations. In contrast, models with low head rotation experienced substantial increases in strain for C2-C3 and C3-C4 when using the CMA scheme, which made those regions have a strain reduction for increasing head rotation. Lastly, increasing the impact severity gradually increased the AF outcomes, and the maximum fiber-direction strain values were achieved for the 10g rear impact scenarios.

Chapter 5
Discussion

5.1 Head Equilibrium and Intervertebral Kinematics in Reference Geometry-Based Head Repositioning

5.1.1 Development of a Novel Repositioning Method

The main goal of the study was to simulate non-neutral position rear impact scenarios and calculate the injury risk in different neck soft tissues. To achieve a biofidelic representation of such impacts, the head repositioning needed to realistically mimic the in vivo neck movements and interactions. Previous numerical studies have been limited in achieving a stable head and neck non-neutral position with biofidelic intervertebral movements for a detailed FE human model. A novel repositioning method using stress initialization was proposed to pre-stretch neck soft tissues and rotate the head to a desired non-neutral position. The method was divided into an initial model to obtain the new stress-free positions of the soft tissues (Stage 1) and a final model to reposition the model to a desired orientation with the stress initialization of these soft tissues (Stage 2).

The reference geometry-based repositioning method was iterative, so several simulations needed to be tested before achieving the desired rotations. After obtaining the results of the initial repositioning models, a logarithmic fit was used to estimate the head rotations required in Stage 1 to obtain the target rotations in Stage 2 (Figure 4-1). This correlation verified that the models needed to use soft tissue reference geometries from head rotations that were considerably higher than the target positions. Using the logarithmic fit, the five axial head rotations of 24.5°, 33.5°, 42.5°, 51.5°, and 60.5° were achieved within the 5% predefined tolerance. To achieve these head rotations, the repositioning method used rotations of up to 146.1° to obtain the soft tissue nodal positions in Stage 1. This rotation was close to the maximum axial head rotation that the GHBMC M50-O neck model supported, so a head rotation of 60.5° represented the upper limit of the method.

The head and neck stabilization was verified during repositioning by tracking the variation of head-T1 axial rotation, lateral bending and flexion/extension. For all five target rotations, the models reached equilibrium after a simulation time of 150 ms. The neck model comprises multiple non-linear elastic structures, which were susceptible to high oscillations after stress initialization. The additional boundary conditions, including axial skull rotation and damping, were fundamental to reducing the

oscillations and, consequently, the time for equilibrium. During the repositioning, the head-T1 axial rotation movement was coupled with lateral bending and flexion. An in vivo experiment investigated the intervertebral motion during axial head rotation, verifying that lateral bending occurred in the same direction as axial rotation for all intervertebral levels (Ishii et al., 2004). Extension was reported for the spinal levels between C2-C3 and C4-C5, while flexion occurred for the spinal levels between C5-C6 and C7-T1 in slightly lower angles. Another similar study confirmed coupled flexion-extension angles with intervertebral axial rotations and verified that upper cervical levels experienced lateral bending in the opposite direction of the axial rotation (Salem et al., 2013). The current models experienced head-T1 lateral bending angles of up to 21.8° and flexion angles of up to 14.1°, indicating an agreement for lateral bending and some differences for flexion when compared to in vivo motion. The lower cervical spine of the model contributed the most to the right lateral bending and flexion, while the upper cervical spine had lower coupled rotations.

5.1.2 Validation against Experimental Intervertebral Motion

To evaluate the biofidelity of the reference geometry-based repositioning method, the intervertebral kinematics of the model with an axial head rotation of 51.5° was compared with the values from a cadaveric experiment in ligamentous cervical spine models (Ivancic, 2013). In this assessment, most intervertebral levels showed axial rotations close to the experimental values. The level that contributed the most to the head axial movement, C1-C2, had approximately the same rotation as the experimental average. This trend is also consistent with in vivo studies, which have identified this spinal level as the main contributor to axial head rotation (Guo et al., 2021; Salem et al., 2013). Given that the primary function of the atlanto-axial joint is to facilitate axial rotation, the C1-C2 motion served as a crucial validation of the head-rotated model. In contrast, C7-T1 axial rotation, 8.5°, was considerably above the measured value, 3.3°. This intervertebral rotation was particularly high compared to the other lower cervical levels, which may be explained by the T1 constraints during the simulations. As this vertebra was restricted from rotating axially, the relative difference between the C7 and T1 axial rotations was increased. Consequently, the evaluation of ligaments, nerve roots, and AFs at this spinal level may have been affected by the additional deformations added prior to the impact condition. The other two levels outside the measured ranges of motion, C0-C1 and C2-C3, had smaller differences than C7-T1. Their axial rotations were less than 1° below the lower measured boundaries, showing acceptable differences when accounting for experimental variability. Therefore, the reference geometry-based repositioning method demonstrated a biofidelic axial head rotation by accurately representing intervertebral motion.

5.2 Head Motion Analysis in Neutral and Non-Neutral Position Rear Impact Scenarios

The comparison of head-T1 rotations provided an initial evaluation of the models with different head positions undergoing rear impacts. The differences during the hyperextension phase were particularly relevant to understanding the variations in injury risk in these scenarios. For all impact severities and muscle activation schemes, the peak extension value during hyperextension reduced with increasing axial head rotations (Figure 5-1). This trend was in accordance with previous studies that reported that axial head rotations decrease the physiological range of extension (Macnab, 1971). The initial deformations generated by axial head rotation increased the overall stiffness of the neck, reducing the extension range for the same impact load. In addition, the initial flexion generated by the head repositioning creates additional resistance to the hyperextension of models with higher head rotations. Models with head rotations up to 33.5° had decreased peak extensions with the addition of muscle activation during the impact conditions. These reductions happened due to the increased muscle stiffness generated during contraction. In contrast, models with head rotations from 42.5° experienced higher peak head-T1 extensions with muscle activation, reducing the differences to the neutral position values in all three impact severities. While the muscles had increased stiffness, the lateral bending of these repositioned models was considerably reduced, contributing to a decrease in global neck stiffness.

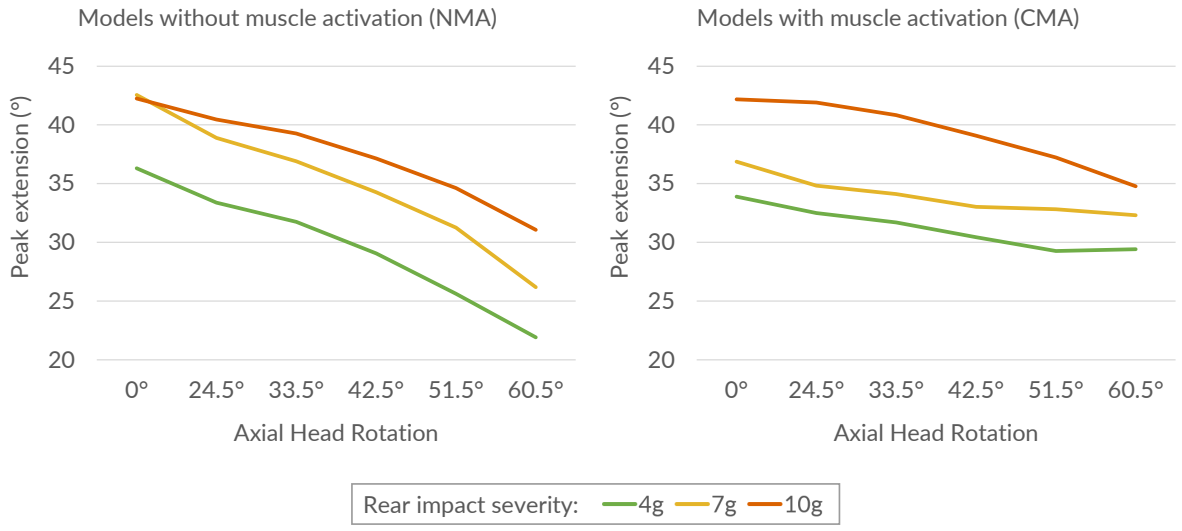


Figure 5-1: Peak head-T1 extension for the three impact severities, without and with muscle activation.

Due to the greater accelerations acting on the head and neck, increasing impact severities were expected to increase peak head extension and reduce the time to reach this peak. In general, the peak extension of the model increased with impacting severity, and the models had the highest angles for the 10g rear impact scenario (Figure 5-1). The maximum extension was limited to approximately 42°, meaning that the increased neck stiffness restricted further movement beyond this point. As a result, no further increase in peak extension was observed in the neutral position model between 7g and 10g rear impacts, as the maximum value had already been reached at 7g. Regarding the time for peak extension, the results varied depending on the impact conditions. Among the three scenarios, the models undergoing an impact of 10g experienced the soonest hyperextension phase, happening at simulation times of 133 to 143 ms. These values were considerably lower than the peak times for 7g (203 to 208 ms), which agrees with the initial expectations. In contrast, the hyperextension peak happened at similar times for the 4g (195 to 200 ms) and 7g (203 to 208 ms) rear impacts. A possible explanation for this behavior may be the experiments used to obtain T1 boundary conditions, as the 4g and 7g inputs used data from different subjects (Deng, 1999; Ono et al., 1997; Sato et al., 2014). The volunteer and cadaveric subjects may have responded differently to the sled impacts due to their distinct biomechanical properties.

The head-T1 lateral bending was significantly affected by the initial head rotation since higher axial rotations induced higher lateral bending during repositioning. The general trend for the repositioned models was reducing the lateral bending during the hyperextension phase of whiplash. Models with higher axial head rotations had higher reductions due to their initial level of lateral bending (Figure 5-2). The variations in the lateral bending were even higher with the use of muscle activation during the impacts. The CMA scheme was designed for neutral position impacts and, therefore, caused the neck muscles to contract and further rotate the head back to the sagittal plane in non-neutral position impacts. The impact severity had minimal effect on the maximum variation in the head lateral bending.

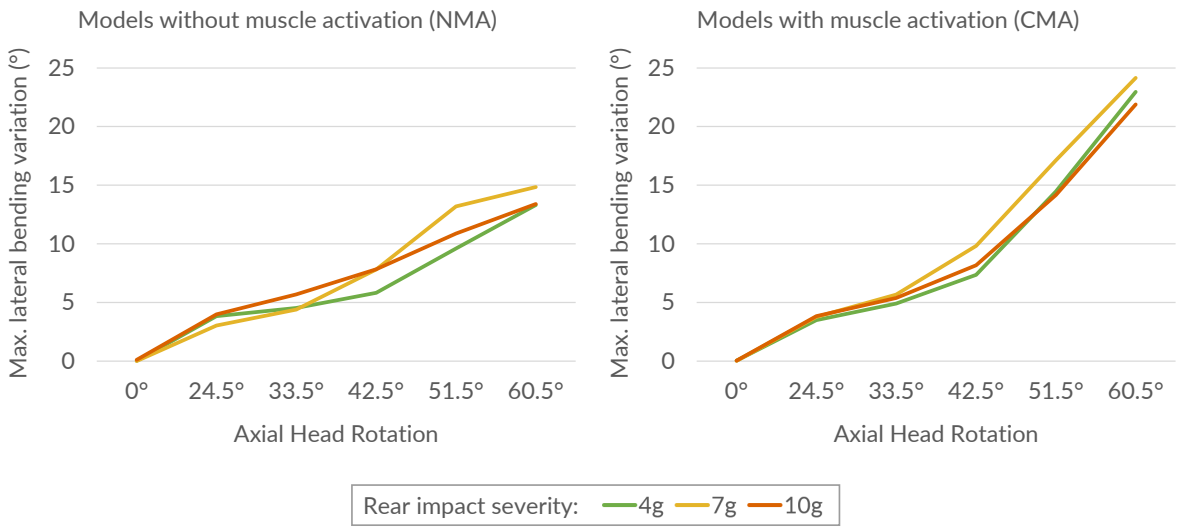


Figure 5-2: Maximum variation in head-T1 lateral bending for the three impact severities, without and with muscle activation.

The head-T1 axial rotations, which were the target positions at the beginning of the sled pulses, did not vary significantly throughout the impact scenarios. While the axial rotation profiles also showed decreases during the hyperextension phase, the variations were limited when compared to the initial axial head rotation. Similar to lateral bending, the variations in the axial rotation angles were higher with muscle activation (Figure 5-3). The CMA scheme contributed to rotating the head back to the sagittal plane and reducing the level of axial rotation, but the effect was again reduced when compared to the initial axial head rotation. The impact severity increased the variation of axial rotation when muscle activation was considered.

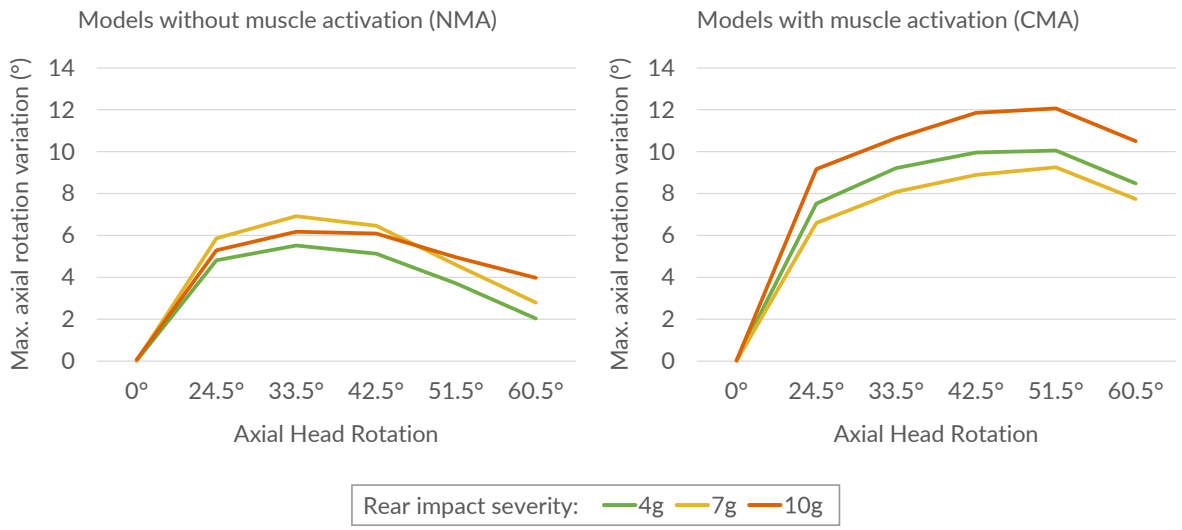


Figure 5-3: Maximum variation in head-T1 axial rotation for the three impact severities, without and with muscle activation.

5.3 Tissue-Level Response in Neutral and Non-Neutral Position Rear Impact Scenarios

Thirty-six rear impact simulations were performed to verify the effect of the initial head position, muscle activation, and impact severity on the tissue-level neck responses. Four soft tissues frequently associated with pain occurrence during whiplash were investigated. The injury assessments were performed by directly calculating deformation components or indirectly estimating changes in the tissue dimensions. The ligament displacements were calculated and compared with their measured response regions to obtain the potentials for pain and failure. Similarly, the muscles and AFs had their strains calculated in the fiber direction and assessed with reported failure strains. In contrast, nerve root compressions were estimated by evaluating the dimension reductions of the IVF spaces and comparing them with narrowing thresholds calculated from experimental dimensions of the nerve roots.

5.3.1 Influence of Initial Head Position on Soft Tissue Responses

Among the injury mechanisms investigated during rear impacts, ligament distractions and muscle strains were affected the most by the initial head position. Regarding the cervical ligaments, the study demonstrated that higher CL displacements were experienced with increasing axial head rotation. This trend agreed with in-vitro tests in cervical spine motion segments that observed significant increases in the facet capsule strains for non-neutral posture rear impacts (Siegmund et al., 2008). The intervertebral

levels and facet joint regions with elevated displacements also corresponded well with experimental data. For a similar rear impact severity of 8g, Panjabi et al. (2006) verified a significant increase in three-plane injury potentials for the lower cervical spine levels (below C3) when the head was rotated. The CL responses confirmed this behavior by showing that these same regions had the highest sensitivity to head rotation. Regarding the critical location of the facet joint, Siegmund et al. (2008) found that turning the head during rear impact increased the capsular ligament strains further on the side toward the cervical rotation. For the right axial head rotation, the model successfully predicted increased ligament distractions in the right portion of the facet joints.

The ISL, ALL, AA-AM, and alar ligaments also showed consistent increases in displacement with increasing axial head rotation. Among them, the C1-C2 ISL had the most substantial growths, varying from the beginning of the toe region (neutral position) to the linear limit (60.5° head rotation). This trend can be explained by the elevated axial rotation experienced in the atlanto-axial joint, which induced shearing effects in the ISL. Regarding the alar ligament, the displacement increases agreed with previous MRI studies that verified more severe injuries in the alar and TL ligaments for head-rotated whiplash patients (Kaale et al., 2005a). This trend was not verified in the TL, which experienced minimal displacements for all cases. The PLL, LF, and the other upper cervical spine ligaments had the lowest differences in distraction for different head rotations. These ligaments are positioned closer to the axial rotation axis of the vertebrae, which minimizes the movement of their attachments and consequently reduces their displacements.

Higher axial head rotations significantly increased strains in the neck muscles along the fiber directions. The head repositioning pre-stretched the neck muscles to desired orientations, which increased their baseline strains before the impact phase. Consequently, these baseline strains underwent further deformations during whiplash, increasing the peak strains experienced. Therefore, the strain increases during the rear impacts were particularly expected in muscles with the highest contributions to the axial head rotation, which was verified for the sternocleidomastoid, levator scapula, and scalenus medius. These muscles had some of the highest increases, varying from low to medium strains in neutral position models to injurious values in the models with a 60.5° head rotation.

The head position had a limited effect on the two other injury mechanisms, nerve root compression and AF strain. The IVF height reduction slightly decreased with increasing head rotations, indicating a higher potential for nerve root compression for the neutral position. The exceptions were some upper

cervical spine levels that showed the highest reductions for intermediate rotations. In contrast, the IVF width reduction was minimal and did not experience considerable changes with the initial head position. These findings differ from previous experiments with whole cervical spine models that reported significant IVF height and width reductions for 5 g and 8 g accelerations when the head was rotated, respectively (Tominaga et al., 2006). The lack of musculature and other soft tissues may have decreased the neck stiffness in the experimental model, inducing greater intervertebral motion and higher IVF narrowing. The AF strains also did not show a consistent trend regarding the axial head rotation. For the models without muscle activation, the maximum AF strains usually occurred for head rotations of 0° and 60.5°. Considering muscle activation, the models experienced reduced strains for higher head rotation, indicating that non-neutral positions could mitigate injury at some spinal levels.

5.3.2 Influence of Muscle Activation on Soft Tissue Responses

The addition of muscle contraction during the rear impact simulations had different effects for each injury mechanism. In general, the cervical ligament displacements and muscle strains decreased when the muscle activation scheme was changed from NMA to CMA. The contraction stress from the 1D Hill-type elements increased the stiffness of the whole muscle and, consequently, the neck. The increased stiffness assisted in neck stabilization and reduced head extension, which also decreased ligament and muscle deformations. The anterior cervical ligaments, including the ALL, AA-AM, apical, and alar (occipital portion), had the highest reductions as their primary function is to control neck extension. The influence of muscle activation was more significant for models with lower head rotations, so the neutral position cases generally had the highest reductions in ligament displacements and muscle strains. The muscle activation stresses generated from 1D Hill-type elements were highly dependent on the stretches experienced by the muscle elements (Equation 2-2, Figure 2-38a). Therefore, models with high head rotations already experienced elevated muscle deformations prior to the impact phase, which scaled down the muscle active stress (Figure 5-4).

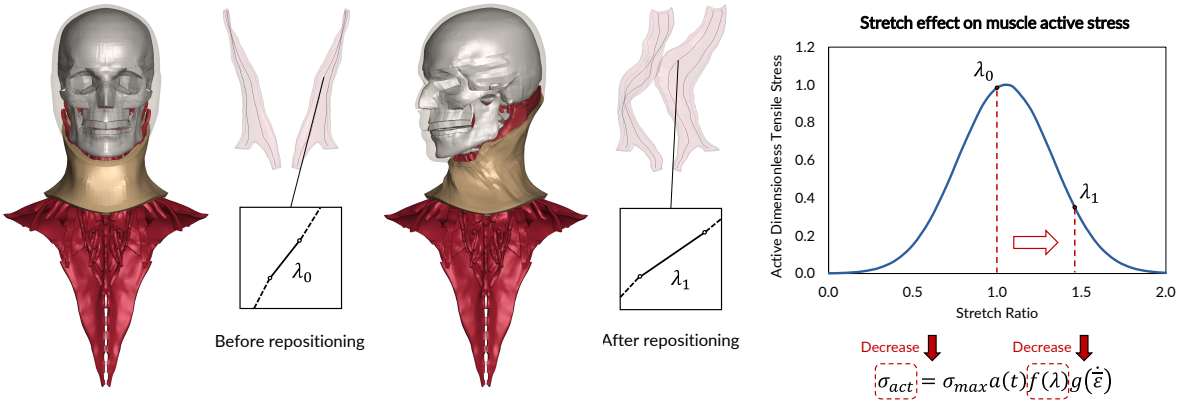


Figure 5-4: Stretching of Hill-type muscle elements reducing the effect of muscle activation on models with high head rotation.

The AF strains mainly followed the same trend from the ligaments and muscles, with decreasing values for the CMA schemes. The main differences happened in the C2-C3 and C3-C4 levels during a 10g rear impact condition, where muscle activation increased the AF strains for low head rotations. The additional stiffness in the neck increased the local flexion peak during the rebound phase for models with axial head rotations up to 24.5°. This alteration modified the loading mechanism in the AF, so the portion responsible for limiting the flexion was more affected and had increasing strains. The IVF space had the opposite trend from the other soft tissues, with increasing risks of injury when using muscle contraction. The IVF heights had the highest increases in narrowing, particularly in the C2-C3 and C3-C4 levels. The previous three injury mechanisms are triggered when the soft tissue is stretched beyond a specific tensile strain. In contrast, nerve root injury occurs due to excessive compression, estimated by the reduction in the IVF space. As a result, muscle contraction brings neck structures closer together, further narrowing the foraminal space and increasing the risk of nerve root impingement.

5.3.3 Influence of Impact Severity on Soft Tissue Responses

As a general trend, increasing the severity of the rear impact generated higher deformations in the studied soft tissues. Higher impact accelerations increased the head peak extension during whiplash, which amplified soft tissue strains and raised injury risks. The ligament displacements and muscle strains generally increased with impact severity, achieving peak values for the 10g rear impact condition. Most ligaments had progressive displacement variations with similar increases between 4g and 7g and between 7g and 10g. The exceptions were the PLL, alar, apical, and TM ligaments, which

had considerably higher increases from a 7g to 10g rear impact. The main reason for these differences was the inclusion of the rebound phase in the T1 boundary conditions for the 10g rear impact scenario. Therefore, ligaments more affected by flexion, such as the PLL, had increasing strains during this phase. These increases in cervical ligament displacements agreed with in vitro whiplash simulations that verified higher CL, ALL, TL, alar, and apical ligament strains for increasing rear impact accelerations (Ivancic et al., 2004; Maak et al., 2006; Panjabi et al., 1998; Pearson et al., 2004). The muscles also exhibited a progressive increase in strain with higher rear impact severities, having a more significant effect in models with lower head rotations. The strain contribution during the repositioning phase was higher than the one added during the impact for some muscles in models with higher head rotations, reducing the strain growth with the impact severity.

The AF showed consistent strain increases with impact severities for all head positions. For the neutral position case, the trend was in accordance with rear impact tests performed in osseoligamentous cervical spine models that verified increases in peak AF strains for increasing impact accelerations between 3.5 g and 8g (Panjabi, Ito, et al., 2004). While most cases showed progressive increases in strain, some spinal levels had particularly high increases between 7g and 10g impact severities when muscle activation was used. Finally, the IVF height and width reductions were the least affected by the variation of impact severity among the injury mechanisms studied. Cadaveric experiments with cervical spine models also did not verify relevant changes in IVF narrowing with increasing rear impact severities between 2g and 8g (Panjabi, Maak, et al., 2006; Tominaga et al., 2006).

5.3.4 Evaluation of Soft Tissue Injury Risks

The ligaments, muscles, and AFs were the soft tissues with the highest potential for injury during rear impact scenarios (Table 5-1). Following the trends from the previous analyses, the model with a head rotation of 60.5° undergoing a 10g rear impact had the highest risks. While none of the cases had ligaments entering the post-traumatic region, several models had CLs, ISLs, and ALLs with displacements reaching the end of the linear region. Experimental studies in the facet capsules verified that the activation of nociceptors can occur before the sub-catastrophic failure, leading to the initiation of the pain process (Lu et al., 2005a, 2005b). Therefore, ligaments close to their linear limit had a high chance of experiencing pain. In the current study, the CLs (at C3-C4 and C5-C6) and the ALLs (at C4-C5 and C5-C6) had displacements close to their linear limit for axial head rotations starting from 51.5° and rear impact severities from 7g. The C1-C2 ISLs for a head rotation of 60.5° under all impact

severities had the closest displacements to the linear limit and the highest risks of pain among the cervical ligaments. Previous in vitro studies verified that CLs exceeded physiological strains starting at 2.5 g rear impacts, particularly in the lower cervical spine (Panjabi et al., 1998; Pearson et al., 2004). The current evaluation complemented this experiment by indicating that the risk of pain response started to be relevant at an impact severity of 7g. Another cadaveric study verified that the alar, TL, and apical ligaments did not experience injuries for any impact condition up to 8 g (Maak et al., 2006). This behavior was verified in the present analysis, and all ligaments from the occipital-atlanto-axial joints had low risks of injuries for impact severities up to 10g. Therefore, these results showed that a 4g rear impact severity was sufficient to generate injurious ligament displacements when the occupant experienced an elevated head rotation.

Table 5-1: Summary of neck injury evaluation.

Mechanism	Injury assessment	Locations with higher risks
Ligament distraction	High risk of injury	CL (C3-C4 and C5-C6) and ALL (C4-C5 and C5-C6) for high head rotations at 7g and 10g impact ISL (C1-C2) for high head rotations
Muscle strain	High risk of injury	Rectus capitis lateral, omohyoid, sternohyoid, sternocleidomastoid, levator scapula, and scalenus medius for high head rotations at all impacts Rectus capitis lateral, sternohyoid, and sternocleidomastoid for non-neutral positions at 7g and 10g impacts
Nerve root compression	Low risk of injury	No location with significant risk
AF strain	High risk of injury	C5-C6 at 7g and 10g impacts C2-C3 and C3-C4 at 10g impact

The 95th percentile fiber-direction strain of the muscle indicated that up to seven muscles exceeded the failure strain during non-neutral position rear impacts. The failure strain threshold was reduced when muscle activation was considered, which increased the number of muscles that entered the damage

region up to seventeen. The models with head rotations higher than 33.5° experienced injurious strains for at least two muscles during all impact conditions. In contrast, a head rotation of 24.5° just induced injurious strains for impact severities starting at 7g. Considering the selection of the 95th percentile values, the results showed multiple muscles with approximately 5% of their volume experiencing strains higher than the damage threshold. These findings indicated an elevated potential for injury in the neck muscles. Regarding the injury locations, the muscles that collaborated with the axial head rotation had some of the highest strains and, consequently, elevated risk of damage. However, the muscle with the highest strains was the rectus capitis lateral. This muscle collaborates mainly with the lateral bending of the head, and its excessive strain values were associated with its size. The rectus capitis lateral is the smallest neck muscle with a volume fifty times lower than the average neck muscle volume. Therefore, the 95th percentile strain of this muscle represents a strain experienced by a reduced number of elements, which increased the strain value compared to other muscles. In contrast, the sternocleidomastoid and levator scapula are large muscles with volumes higher than the average muscle volume for the neck. This indicates that these muscles had a considerably higher number of elements experiencing injurious strains when compared to small muscles.

The current model lacked an explicit implementation of nerve roots, so it could not identify the mechanical changes in the spinal canal. Therefore, the evaluation of nerve root injury was limited to the compression mechanism, estimated by tracking the variation in IVF heights and widths. The IVF space narrowing was reduced and considerably lower than the dimension reduction thresholds for all spinal levels and models, representing a low risk of injury. These results contradict previous tests with whole cervical spines that verified a high potential for nerve root compression between C3-C4 and C6-C7 in head-forward and head-rotated rear impacts (Panjabi, Maak, et al., 2006; Tominaga et al., 2006). A possible explanation for this difference is that the osseoligamentous cervical spine models in the experiment may not have captured the effect of musculature and other neck soft tissues, which decreased the neck stiffness and contributed to higher dimension reductions. In addition, these studies used literature values for the IVF dimensions to estimate the narrowing threshold, while the current assessments used the same model to obtain the IVF dimensions and estimate its reductions.

Lastly, the AF had the maximum fiber-direction strains concentrated in the C5-C6 spinal level. This region had strains exceeding the experimental failure threshold for models with axial head rotations of 0° and 60.5° starting at an impact severity of 7g. The models had AF strains at C5-C6 reaching the damage region for all head rotations during 10g rear impacts, indicating a high potential for injury at

this intervertebral level. The models with low head rotations also showed AF strains exceeding the failure threshold for C2-C3 and C3-C4 during the 10g impact severity when muscle activation was considered. Neutral position rear impact tests with cervical spine models showed that AF strains started to exceed physiologic limits for accelerations of 3.5 g and had their highest values located at C5-C6 (Panjabi, Ito, et al., 2004). The present findings agreed with this experimental study, verifying that the AF with the highest strains is C5-C6, and accelerations of 7g start to generate annular fiber failure.

5.4 Study Limitations

While most intervertebral levels rotated according to the expected range of motion after repositioning, the model overpredicted C7-T1 kinematics. This may have affected the deformations of soft tissues located in this spinal region during the impact. Despite raising concerns about influencing the injury evaluation, the models did not predict high potentials for soft tissue injuries in the C7-T1 region. Another limitation was that the detailed FE model was validated against cadaveric osseoligamentous spine specimens (Ivancic, 2013). The validation case was one of the most complete experiments available that measured intervertebral motion between C0 and T1, showing similar trends to in vivo studies (Guo et al., 2021; Salem et al., 2013). However, the differences between cadaveric and in vivo tissue properties, combined with the absence of neck musculature, may have contributed to variations in the overall response dynamics of the experimental models during axial rotation.

The proposed repositioning method was appropriate to simulate the hyperextension phase of non-neutral position rear impacts but was limited to modelling the rebound phase. The soft tissue deformation leading to the axial reposition of the head was maintained throughout the simulation, so the head could not return to the neutral position after the impact. Some specific cervical ligaments, such as the PLLs and TMs, showed to have considerably higher increases in displacements with the addition of the rebound phase from 7g to 10g rear impact conditions. These findings highlighted the importance of improving the representation of all phases of whiplash since each can uniquely affect different parts of the cervical spine and result in distinct potentials of injury.

Another aspect for improvement was the T1 boundary conditions and constraints during the non-neutral position rear impacts. The simulation of the impact scenarios used T1 kinematics from volunteer and cadaveric specimens subjected to head-forward rear impacts (Deng, 1999; Ono et al., 1997; Sato et al., 2014). As discussed in the current study, the initial head position considerably affects the motion of the cervical vertebrae during whiplash. While the same sled acceleration could generate distinct T1 motion

profiles during head-forward and head-rotated impacts, the current simulations only considered inputs from neutral position experiments. In addition, the T1 movement was constrained around the sagittal plane, which was a reasonable assumption for approximately symmetric load cases such as the head-forward rear impacts. However, for the increasing asymmetry around the sagittal plane added by the head-rotated cases, the T1 motion can be more complex and involve other anatomical planes. A similar adaptation was performed to implement muscle activation in the non-neutral position models. The current activation strategies for the GHBMC models were developed and tested for neutral position frontal and rear impacts (Correia et al., 2020). The CMA scheme used in the current simulations was based on the division of muscles into extensors and flexors, showing an appropriate correlation with real-life scenarios. This activation scheme was not validated in head-rotated impacts and, therefore, used as an approximation for all the head positions. For higher asymmetry added by the initial position, the muscles in the same group tend to activate differently when reacting to whiplash.

For the head rotation of 60.5°, some muscles also experienced injurious strains before the impact phase, meaning that the head repositioning would be able to cause injury. An axial rotation of 60.5° is inside the head-T1 range of motion for humans (Ferrario et al., 2002) and should not initiate injury in the neck muscles. These results indicated a potential disagreement between the calculation of the muscle fiber-direction strains and the reported failure values from the literature. The muscle lengths from the neutral position model were assumed to be the neutral muscle lengths to calculate the stretches in the model. However, the neck muscles can already be elongated or slightly contracted during the neutral position, which can lead to the overestimation of strains during head repositioning. In addition, the repositioning method may have been limited to simulating some muscle movements for the highest target rotation due to the unphysical position used to obtain the reference nodes.

Chapter 6
Conclusions

A novel repositioning method was proposed to pre-stretch the neck soft tissues of a detailed FE head and neck model, achieving equilibrium in a non-neutral head position. The method was able to axially rotate and maintain the head in five target positions, defined from in-car studies to represent deviations from the neutral driving position. The models reached equilibrium in their target positions, within the prescribed tolerance, at a simulation time of 150 ms. The model with a 51.5° axial head rotation was used to validate the repositioning against an in vitro experiment, demonstrating a general agreement in intervertebral motion. Therefore, the reference geometry-based repositioning resulted in realistic head rotation movements and, consequently, biofidelic simulations of head-rotated rear impacts.

Thirty-six rear impact simulations were conducted to evaluate the influence of initial head position, impact severity, and muscle activation on head motion and tissue-level responses. Increasing axial head rotations reduced the peak extension during the hyperextension phase of whiplash, while higher impact severities showed the opposite effect. Muscle activation had mixed effects on peak extension: decreased for low head rotations and increased for high head rotations. The head-T1 lateral bending was significantly influenced by axial head rotation, with higher lateral bending angles induced by the repositioning having higher variations during the impact. The assessment of head kinematics revealed that higher axial head rotations increased the combined three-plane rotation during rear impacts.

Head position significantly affected ligament distractions and muscle strains during rear impacts, with increased axial head rotation leading to higher deformations. The IVF heights slightly decreased with head rotations, while the IVF widths showed minimal variations. The trends for AF strains were also mixed: peak strains were observed at 0° and 60.5° for models without muscle activation and only at 0° for models with muscle activation. Muscle activation generally decreased ligament distractions and muscle strains, especially in locations most affected by head extension and in models with lower head rotations. The AF strains followed the same trend, except for C2-C3 and C3-C4 during the 10g rear impact condition. In contrast, the IVF space experienced increasing narrowing with muscle activation, slightly raising the risk of nerve root impingement. Impact severity also affected the soft tissue deformations, with higher impact accelerations causing increased risks of injury for the ligaments, muscles, and AFs. Some specific ligaments, including the PLLs, TM, alar, and apical, demonstrated a particular increase with the addition of the rebound phase between 7g and 10g rear impact conditions.

The IVF dimensions showed minimal sensitivity to impact severity, consistent with findings from cadaveric studies with cervical spine models.

The ligaments, muscles, and AFs had the highest potentials for injury during rear impacts, especially at high head rotations and impact severities. The ISL at C1-C2 had displacements close to the linear limit for a head rotation of 60.5°, indicating an increased risk of pain for all impact severities. The CLs at C3-C4 and C5-C6 and the ALLs at C4-C5 and C5-C6 had high risks of pain for axial head rotations starting from 51.5° and impact accelerations from 7g. The potential for muscle injury was elevated for head rotations higher than 33.5° during all impact severities and for a rotation of 24.5° during severities of 7g and higher. The model with a 60.5° head rotation experienced the highest strains, with at least seven muscles exceeding the failure threshold. The AF exhibited the highest risk of injury at C5-C6 for all head positions, reaching failure strains for impact severities starting at 7g. Models with low head rotations had AF strains entering the failure regions at C2-C3 and C3-C4 during 10g rear impacts when muscle activation was considered. Lastly, the risk of nerve root impingement was low as the narrowing of the IVF dimensions was significantly below the compression threshold across all spinal levels.

The rear impact results highlight the complex interactions of initial head position, muscle activation, and impact severity on head kinematics and tissue-level responses. Increasing impact severity leads to increased deformations of neck soft tissues, often exceeding injury thresholds. Muscle contraction can reduce tissue deformations, mitigating the injury risks. Head rotation introduces initial deformations in the soft tissues that lead to even greater deformations during impact. The impact response is not a pure superposition of the effect of these three factors, but increased head rotations generally lead to increased tissue deformation and a higher risk of injury, as reported in epidemiology.

Chapter 7
Recommendations

Based on the repositioning and rear impact results, several recommendations can be proposed to improve the biofidelity of the repositioning models, extend the soft tissue injury analysis, and test safety measures. Future work should conduct in vivo tests with volunteer subjects undergoing the targeted axial rotations to obtain the intervertebral motion between C0-C1 and C7-T1 and compare it with the repositioned models. The experiment should also monitor the flexion/extension and lateral bending to verify if the coupled movements are being captured in the model. This step will enhance the validation of the head-rotated model and increase the biofidelity of the subsequent impact analysis. Another source of improvement is the muscle activation scheme, which can be changed from an open-loop to a closed-loop approach. The muscle contraction levels should vary with the initial head position, so using pre-determined activation profiles for the head-rotated cases may reduce their effectiveness during impact conditions. A closed-loop scheme can improve the muscle activation representation by continuously adjusting muscle contraction levels based on the model responses. For the tissue-level evaluation, the nerve roots and vertebral arteries should be implemented in the model to investigate additional sources of whiplash injuries. While nerve root compression could be estimated by tracking the variation of IVF dimensions, adding this soft tissue to the model can help investigate other types of injuries in the nervous system, such as pressure changes. Additionally, the vertebral artery models can be used to calculate their elongations and evaluate the risk of injury, which was reported to increase during non-neutral position rear impact experiments.

With improved muscle activation strategies and soft tissue representations, the head repositioning and rear impact simulations can be extended to include age- and gender-specific FE human models. These additional HBMs can be used to better understand the variability in whiplash injury risks across different populations during non-neutral position impacts. Aged subjects, for example, may raise a particular concern due to their altered tissue properties and reduced ranges of motion. Finally, future studies should test mechanisms to mitigate injury in rear impacts, including adding head restraints and improving the seat design. These mechanisms should be optimized to reduce the potential for soft tissue damage in both neutral position and non-neutral position impacts.

Letters of Copyright Permission

Outlook

Re: Copyright Inquiry

From Kathy Cookman <[redacted]>
Date Tue 11/26/24 4:14 PM
To Matheus Seif Reis <[redacted]>

That is correct, you do not need a letter of copyright permission if you cite it accordingly. You can also consider this email, my approval of the use as you described.

On Tue, Nov 26, 2024 at 3:56 PM Matheus Seif Reis <[redacted]> wrote:

> Hi Kathy,
>
> Thank you very much for your help. I am only reusing the table to illustrate how AAAM assesses the severity of whiplash injuries in the cervical spine (AIS Codes and Injury Examples). After the table, I do not use its content for any of the purposes mentioned.
>
> Below the table, I am writing a note mentioning that it was reproduced from the Association of the Advancement of Automotive Medicine, The Abbreviated Injury Scale 2005 Update 2008, AAAM, Des Plaines Illinois, 2008.
>
> Just to confirm, there is no need for a letter of copyright permission in this case, correct?
>
> Thanks,
> Matheus

From: Kathy Cookman <[redacted]>
Sent: November 26, 2024 3:43 PM
To: AAAM Info <[redacted]>
Cc: Matheus Seif Reis <[redacted]>; [redacted] <[redacted]>
Subject: Re: Copyright Inquiry

Greetings Matheus Sief Reis,
The following attachment shows how you can reference the use of the AIS code within your thesis.
Utilizing the code for purposes of developing a database, shared materials for data collection, etc. requires the purchase of a license to use the code. However, from your email, it sounds as though that is not the case and you are just citing the code in your work.

Best regards!

On Wed, Nov 20, 2024 at 5:23 PM AAAM Info <[redacted]> wrote:

> Dear Matheus,
>
> Thank you for your inquiry.
>
> This email is to confirm receipt of your request. Your request is being forwarded to our Technical Specialist for assistance. Please allow 3 – 5 business days to receive a response.
>
> You may also email her directly at [redacted]
>
> ***Please note: The response may be delayed when the expert who replies to these requests is instructing a course. Thanks in advance for your patience.***

Sincerely,

The Association for the Advancement of Automotive Medicine

From: Matheus Seif Reis <[redacted]>
Sent: Tuesday, November 19, 2024 9:52 AM
To: [redacted] ; [redacted]
Subject: Inquiry about Copyright Permission for Academic Purposes

Hi, my name is Matheus Seif Reis, and I am a Master's student at the University of Waterloo. I am contacting you because I would like to obtain a letter of copyright permission for the following reference:

- AAAM. (2008). Abbreviated Injury Scale 2005 Update 2008. Barrington, Illinois: Association for the Advancement of Automotive Medicine.

I want to reuse the table that shows the Abbreviated Injury Scale (AIS) grades and some examples of cervical spine injuries. This will be used in the Background section of my thesis.

Thank you for your assistance.

Warm regards,

Matheus Seif Reis

--
Respectfully,

Kathy J. Cookman, BS, CSTR, CAISS, EMT-P, FMNP
AIS Business Director/International Technical Coordinator
Association for the Advancement of Automotive Medicine (AAAM)
[redacted]
www.aaam.org
C [redacted] **(Eastern Time Zone)**
Email: [redacted]

--
Respectfully,

Kathy J. Cookman, BS, CSTR, CAISS, EMT-P, FMNP
AIS Business Director/International Technical Coordinator
Association for the Advancement of Automotive Medicine (AAAM)
[redacted]
www.aaam.org
C [redacted] **(Eastern Time Zone)**
Email: [redacted]

WOLTERS KLUWER HEALTH, INC. LICENSE TERMS AND CONDITIONS

Nov 15, 2024

This Agreement between Matheus Seif Reis ("You") and Wolters Kluwer Health, Inc. ("Wolters Kluwer Health, Inc.") consists of your license details and the terms and conditions provided by Wolters Kluwer Health, Inc. and Copyright Clearance Center.

License Number	5902670532726
License date	Nov 05, 2024
Licensed Content Publisher	Wolters Kluwer Health, Inc.
Licensed Content Publication	Spine
Licensed Content Title	Section 3. Consensus Findings
Licensed Content Date	Apr 15, 1995
Licensed Content Volume	20
Licensed Content Issue	8
Type of Use	Dissertation/Thesis
Requestor type	University/College
Sponsorship	No Sponsorship
Format	Electronic
Will this be posted online?	Yes, on a secure website
Portion	Figures/tables/illustrations
Number of figures/tables/ illustrations	1
Author of this Wolters Kluwer article	No
Will you be translating?	No
Intend to modify/change the content	No
Title of new work	Neck Injury Risk in Non-Neutral Position Rear Impact Scenarios Using a Reference Geometry-Based Repositioning
Institution name	University of Waterloo
Expected presentation date	Dec 2024
Portions	Table 7
The Requesting Person / Organization to Appear on the License	Matheus Seif Reis
Requestor Location	Matheus Seif Reis [redacted]
Publisher Tax ID	895524239 RT0001
Billing Type	Invoice

Billing Address	Matheus Seif Reis [redacted] [redacted] [redacted]
Total	**0.00 CAD**

Terms and Conditions

Wolters Kluwer Health Inc. Terms and Conditions

1. **Duration of License:** Permission is granted for a one time use only. Rights herein do not apply to future reproductions, editions, revisions, or other derivative works. This permission shall be effective as of the date of execution by the parties for the maximum period of 12 months and should be renewed after the term expires.
    i. When content is to be republished in a book or journal the validity of this agreement should be the life of the book edition or journal issue.
    ii. When content is licensed for use on a website, internet, intranet, or any publicly accessible site (not including a journal or book), you agree to remove the material from such site after 12 months, or request to renew your permission license
2. **Credit Line:** A credit line must be prominently placed and include: For book content: the author(s), title of book, edition, copyright holder, year of publication; For journal content: the author(s), titles of article, title of journal, volume number, issue number, inclusive pages and website URL to the journal page; If a journal is published by a learned society the credit line must include the details of that society.
3. **Warranties:** The requestor warrants that the material shall not be used in any manner which may be considered derogatory to the title, content, authors of the material, or to Wolters Kluwer Health, Inc.
4. **Indemnity:** You hereby indemnify and hold harmless Wolters Kluwer Health, Inc. and its respective officers, directors, employees and agents, from and against any and all claims, costs, proceeding or demands arising out of your unauthorized use of the Licensed Material
5. **Geographical Scope:** Permission granted is non-exclusive and is valid throughout the world in the English language and the languages specified in the license.
6. **Copy of Content:** Wolters Kluwer Health, Inc. cannot supply the requestor with the original artwork, high-resolution images, electronic files or a clean copy of content.
7. **Validity:** Permission is valid if the borrowed material is original to a Wolters Kluwer Health, Inc. imprint (J.B Lippincott, Lippincott-Raven Publishers, Williams & Wilkins, Lea & Febiger, Harwal, Rapid Science, Little Brown & Company, Harper & Row Medical, American Journal of Nursing Co, and Urban & Schwarzenberg - English Language, Raven Press, Paul Hoeber, Springhouse, Ovid), and the Anatomical Chart Company
8. **Third Party Material:** This permission does not apply to content that is credited to publications other than Wolters Kluwer Health, Inc. or its Societies. For images credited to non-Wolters Kluwer Health, Inc. books or journals, you must obtain permission from the source referenced in the figure or table legend or credit line before making any use of the image(s), table(s) or other content.
9. **Adaptations:** Adaptations are protected by copyright. For images that have been adapted, permission must be sought from the rightsholder of the original material and the rightsholder of the adapted material.
10. **Modifications:** Wolters Kluwer Health, Inc. material is not permitted to be modified or adapted without written approval from Wolters Kluwer Health, Inc. with the exception of text size or color. The adaptation should be credited as follows: Adapted with permission from Wolters Kluwer Health, Inc.: [the author(s), title of book, edition, copyright holder, year of publication] or [the author(s), titles of article, title of journal, volume number, issue number, inclusive pages and website URL to the journal page].
11. **Full Text Articles:** Republication of full articles in English is prohibited.
12. **Branding and Marketing:** No drug name, trade name, drug logo, or trade logo can be included on the same page as material borrowed from *Diseases of the Colon & Rectum, Plastic Reconstructive Surgery, Obstetrics & Gynecology (The Green Journal), Critical Care Medicine, Pediatric Critical Care Medicine, the American Heart Association publications and the American Academy of Neurology publications.*
13. **Open Access:** Unless you are publishing content under the same Creative Commons license, the following statement must be added when reprinting material in Open Access journals: "The Creative Commons license does not apply to this content. Use of the material in any format is prohibited without written permission from the publisher, Wolters Kluwer Health, Inc. Please contact permissions@lww.com for further information."
14. **Translations:** The following disclaimer must appear on all translated copies: Wolters Kluwer Health, Inc. and its Societies take no responsibility for the accuracy of the translation from the published English original and are not liable for any errors which may occur.
15. **Published Ahead of Print (PAP):** Articles in the PAP stage of publication can be cited using the online publication date

and the unique DOI number.

i. Disclaimer: Articles appearing in the PAP section have been peer-reviewed and accepted for publication in the relevant journal and posted online before print publication. Articles appearing as PAP may contain statements, opinions, and information that have errors in facts, figures, or interpretation. Any final changes in manuscripts will be made at the time of print publication and will be reflected in the final electronic version of the issue. Accordingly, Wolters Kluwer Health, Inc., the editors, authors and their respective employees are not responsible or liable for the use of any such inaccurate or misleading data, opinion or information contained in the articles in this section.

16. **Termination of Contract:** Wolters Kluwer Health, Inc. must be notified within 90 days of the original license date if you opt not to use the requested material.
17. **Waived Permission Fee:** Permission fees that have been waived are not subject to future waivers, including similar requests or renewing a license.
18. **Contingent on payment:** You may exercise these rights licensed immediately upon issuance of the license, however until full payment is received either by the publisher or our authorized vendor, this license is not valid. If full payment is not received on a timely basis, then any license preliminarily granted shall be deemed automatically revoked and shall be void as if never granted. Further, in the event that you breach any of these terms and conditions or any of Wolters Kluwer Health, Inc.'s other billing and payment terms and conditions, the license is automatically revoked and shall be void as if never granted. Use of materials as described in a revoked license, as well as any use of the materials beyond the scope of an unrevoked license, may constitute copyright infringement and publisher reserves the right to take any and all action to protect its copyright in the materials.
19. **STM Signatories Only:** Any permission granted for a particular edition will apply to subsequent editions and for editions in other languages, provided such editions are for the work as a whole in situ and do not involve the separate exploitation of the permitted illustrations or excerpts. Please view: STM Permissions Guidelines
20. **Warranties and Obligations:** LICENSOR further represents and warrants that, to the best of its knowledge and belief, LICENSEE's contemplated use of the Content as represented to LICENSOR does not infringe any valid rights to any third party.
21. **Breach:** If LICENSEE fails to comply with any provisions of this agreement, LICENSOR may serve written notice of breach of LICENSEE and, unless such breach is fully cured within fifteen (15) days from the receipt of notice by LICENSEE, LICENSOR may thereupon, at its option, serve notice of cancellation on LICENSEE, whereupon this Agreement shall immediately terminate.
22. **Assignment:** License conveyed hereunder by the LICENSOR shall not be assigned or granted in any manner conveyed to any third party by the LICENSEE without the consent in writing to the LICENSOR.
23. **Governing Law:** The laws of The State of New York shall govern interpretation of this Agreement and all rights and liabilities arising hereunder.
24. **Unlawful:** If any provision of this Agreement shall be found unlawful or otherwise legally unenforceable, all other conditions and provisions of this Agreement shall remain in full force and effect.

For Copyright Clearance Center / RightsLink Only:

1. **Service Description for Content Services:** Subject to these terms of use, any terms set forth on the particular order, and payment of the applicable fee, you may make the following uses of the ordered materials:
   i. **Content Rental:** You may access and view a single electronic copy of the materials ordered for the time period designated at the time the order is placed. Access to the materials will be provided through a dedicated content viewer or other portal, and access will be discontinued upon expiration of the designated time period. An order for Content Rental does not include any rights to print, download, save, create additional copies, to distribute or to reuse in any way the full text or parts of the materials.
   ii. **Content Purchase:** You may access and download a single electronic copy of the materials ordered. Copies will be provided by email or by such other means as publisher may make available from time to time. An order for Content Purchase does not include any rights to create additional copies or to distribute copies of the materials

Other Terms and Conditions:
v1.18

Questions? E-mail us at customercare@copyright.com.

RightsLink

MS

Taylor & Francis
Taylor & Francis Group
Traffic Injury Prevention

Influence of Crash Pulse Characteristics on Whiplash Associated Disorders in Rear Impacts--Crash Recording in Real Life Crashes

Author: Anders Ydenius, Maria Krafft, Claes Tingvall, et al
Publication: Traffic Injury Prevention
Publisher: Taylor & Francis
Date: Sep 15, 2010

Rights managed by Taylor & Francis

Thesis/Dissertation Reuse Request

Taylor & Francis is pleased to offer reuses of its content for a thesis or dissertation free of charge contingent on resubmission of permission request if work is published.

BACK CLOSE

© 2024 Copyright - All Rights Reserved | Copyright Clearance Center, Inc. | Privacy statement | Data Security and Privacy | For California Residents | Terms and ConditionsComments? We would like to hear from you. E-mail us at customercare@copyright.com

Outlook

RE: Request for Copyright Permission

From Duane Cronin <[redacted]>
Date Thu 12/12/24 10:26 PM
To Matheus Seif Reis <[redacted]>

Hi Matheus, yes, of course you are welcome to use this figure.
Thanks,
Duane

From: Matheus Seif Reis <[redacted]>
Sent: December 11, 2024 10:39 AM
To: Duane Cronin <[redacted]>
Subject: Request for Copyright Permission

Hi Duane,

I am writing to request copyright permission to recreate and use one of your figures in my thesis. Figure 2-26 (attached) was recreated from Figure 1 (attached) from the following conference proceeding: *Cronin, D. S. (2011). Explicit finite element method applied to impact biomechanics problems. 2011 IRCOBI Conference Proceedings - International Research Council on the Biomechanics of Injury.*

Let me know if you approve the adapted figure and if I can use it in my thesis.

Thanks,
Matheus

References

Aldman, B. (1986). An analytical approach to the impact biomechanics of head and neck injury. *Proceedings of the 39th American Association for Automotive Medicine Conference*.

Alizadeh, M., Aurand, A., Knapik, G. G., Dufour, J. S., Mendel, E., Bourekas, E., & Marras, W. S. (2020). An electromyography-assisted biomechanical cervical spine model: Model development and validation. *Clinical Biomechanics*, *80*. https://doi.org/10.1016/j.clinbiomech.2020.105169

Alizadeh, M., Knapik, G. G., Mageswaran, P., Mendel, E., Bourekas, E., & Marras, W. S. (2020). Biomechanical musculoskeletal models of the cervical spine: A systematic literature review. In *Clinical Biomechanics* (Vol. 71). https://doi.org/10.1016/j.clinbiomech.2019.10.027

Alleyne, C. H., Cawley, C. M., Barrow, D. L., & Bonner, G. D. (1998). Microsurgical anatomy of the dorsal cervical nerve roots and the cervical dorsal root ganglion/ventral root complexes. *Surgical Neurology*, *50*(3), 213–218. https://doi.org/10.1016/S0090-3019(97)00315-7

Aprill, C., & Bogduk, N. (1992). The prevalence of cervical zygapophyseal joint pain-a first approximation. *Spine*, *17*(7). https://doi.org/10.1097/00007632-199207000-00003

Association for the Advancement of Automotive Medicine. (2008). The Abbreviated Injury Scale 2005 Update 2008. *AAAM, Des Plaines, Illinois*.

Baker, S. P., O'Neill, B., Haddon, W., & Long, W. B. (1974). The injury severity score: a method for describing patients with multiple injuries and evaluating emergency care. *Journal of Trauma*, *14*(3). https://doi.org/10.1097/00005373-197403000-00001

Barker, J. B., & Cronin, D. S. (2021). Multilevel Validation of a Male Neck Finite Element Model with Active Musculature. *Journal of Biomechanical Engineering*, *143*(1). https://doi.org/10.1115/1.4047866

Barker, J. B., & Cronin, D. S. (2022). Muscle Activation Affects Kinematic Response and Injury Risk in Non-Traditional Oblique Impact Scenarios Assessed with a Head and Neck Finite Element Model. *SAE International Journal of Transportation Safety*, *10*(2), 135–162. https://doi.org/10.4271/09-10-02-0008

Barker, J. B., Cronin, D. S., & Nightingale, R. W. (2017). Lower cervical spine motion segment computational model validation: Kinematic and kinetic response for quasistatic and dynamic

loading. *Journal of Biomechanical Engineering*, *139*(6), 1–11. https://doi.org/10.1115/1.4036464

Barnsley, L., Lord, S., & Bogduk, N. (1994). Whiplash injury. *Pain*, *58*(3), 283–307. https://doi.org/10.1016/0304-3959(94)90123-6

Barnsley, L., Lord, S. M., Wallis, B. J., & Bogduk, N. (1995). The prevalence of chronic cervical zygapophysial joint pain after whiplash. *Spine*, *20*(1). https://doi.org/10.1097/00007632-199501000-00004

Barrett, J. M., McKinnon, C., & Callaghan, J. P. (2020). Cervical spine joint loading with neck flexion. *Ergonomics*, *63*(1), 101–108. https://doi.org/10.1080/00140139.2019.1677944

Barton, J. W., & Margolis, M. T. (1975). Rotational obstruction of the vertebral artery at the atlantoaxial joint. *Neuroradiology*, *9*(3). https://doi.org/10.1007/BF00332957

Berglund, A., Alfredsson, L., Jensen, I., Bodin, L., & Nygren, Å. (2003). Occupant- and crash-related factors associated with the risk of whiplash injury. *Annals of Epidemiology*, *13*(1). https://doi.org/10.1016/S1047-2797(02)00252-1

Best, T. M., McElhaney, J. H., Garrett, W. E., & Myers, B. S. (1995). Axial strain measurements in skeletal muscle at various strain rates. *Journal of Biomechanical Engineering*, *117*(3), 262–265. https://doi.org/10.1115/1.2794179

Binder, A. (2007). The diagnosis and treatment of nonspecific neck pain and whiplash. In *Europa Medicophysica* (Vol. 43, Issue 1).

Boakye-Yiadom, S., & Cronin, D. S. (2018). On the importance of retaining stresses and strains in repositioning computational biomechanical models of the cervical spine. *International Journal for Numerical Methods in Biomedical Engineering*, *34*(1). https://doi.org/10.1002/cnm.2905

Bogduk, N. (2003). The anatomy and pathophysiology of neck pain. In *Physical Medicine and Rehabilitation Clinics of North America* (Vol. 14, Issue 3). https://doi.org/10.1016/S1047-9651(03)00041-X

Bogduk, N. (2006). Chapter 53 Whiplash injury. *Handbook of Clinical Neurology*, *81*. https://doi.org/10.1016/S0072-9752(06)80057-6

Bogduk, N., & Mercer, S. (2000). Biomechanics of the cervical spine. I: Normal kinematics. *Clinical Biomechanics*, *15*(9), 633–648. https://doi.org/10.1016/S0268-0033(00)00034-6

Borst, J., Forbes, P. A., Happee, R., & Veeger, D. (H. E. J. . (2011). Muscle parameters for musculoskeletal modelling of the human neck. *Clinical Biomechanics*, *26*(4), 343–351. https://doi.org/10.1016/j.clinbiomech.2010.11.019

Brault, J. R., Siegmund, G. P., & Wheeler, J. B. (2000). Cervical muscle response during whiplash: Evidence of a lengthening muscle contraction. *Clinical Biomechanics*, *15*(6), 426–435. https://doi.org/10.1016/S0268-0033(99)00097-2

Carlson, E. J., Tominaga, Y., Ivancic, P. C., & Panjabi, M. M. (2007). Dynamic vertebral artery elongation during frontal and side impacts. In *Spine Journal* (Vol. 7, Issue 2). https://doi.org/10.1016/j.spinee.2006.07.003

Carroll, L. J., Hogg-Johnson, S., Van Der Velde, G., Haldeman, S., Holm, L. W., Carragee, E. J., Hurwitz, E. L., Côté, P., Nordin, M., Peloso, P. M., Guzman, J., & Cassidy, J. D. (2008). Course and prognostic factors for neck pain in the general population: Results of the Bone and Joint Decade 2000-2010 Task Force on Neck Pain and Its Associated Disorders. *Spine*, *33*(4 SUPPL.). https://doi.org/10.1097/BRS.0b013e31816445be

Carter, J. W., Mirza, S. K., Tencer, A. F., & Ching, R. P. (2000). Canal geometry changes associated with axial compressive cervical spine fracture. *Spine*, *25*(1). https://doi.org/10.1097/00007632-200001010-00010

Cassidy, J. D., Carroll, L. J., Côté, P., Lemstra, M., Berglund, A., & Nygren, Å. (2000). Effect of Eliminating Compensation for Pain and Suffering on the Outcome of Insurance Claims for Whiplash Injury. *New England Journal of Medicine*, *342*(16). https://doi.org/10.1056/nejm200004203421606

Cassidy, J. J., Hiltner, A., & Baer, E. (1989). Hierarchical structure of the intervertebral disc. *Connective Tissue Research*, *23*(1). https://doi.org/10.3109/03008208909103905

Cavanaugh, J. M. (2000). Neurophysiology and Neuroanatomy of Neck Pain. In N. Yoganandan & F. A. Pintar (Eds.), *Frontiers in whiplash trauma: clinical and biomechanical* (Vol. 38, pp. 79–95). IOS Press.

Cazzola, D., Holsgrove, T. P., Preatoni, E., Gill, H. S., & Trewartha, G. (2017). Cervical spine injuries: A whole-body musculoskeletal model for the analysis of spinal loading. *PLoS ONE*, *12*(1). https://doi.org/10.1371/journal.pone.0169329

Chung, Y. S., & Han, D. H. (2002). Vertebrobasilar dissection: A possible role of whiplash injury in its pathogenesis. *Neurological Research*, *24*(2). https://doi.org/10.1179/016164102101199666

Combest, J. J. (2018). Current Status and Future Plans of the GHBMC (Global Human Body Models Consortium). *7th International Symposium: Human Modeling and Simulation in Automotive Engineering*.

Comley, K., & Fleck, N. (2012). The compressive response of porcine adipose tissue from low to high strain rate. *International Journal of Impact Engineering*, *46*. https://doi.org/10.1016/j.ijimpeng.2011.12.009

Committee on Medical Aspects of Automotive Safety. (1971). Rating the Severity of Tissue Damage: I. The Abbreviated Scale. *JAMA: The Journal of the American Medical Association*, *215*(2). https://doi.org/10.1001/jama.1971.03180150059012

Correia, M. A., McLachlin, S. D., & Cronin, D. S. (2020). Optimization of muscle activation schemes in a finite element neck model simulating volunteer frontal impact scenarios. *Journal of Biomechanics*, *104*. https://doi.org/10.1016/j.jbiomech.2020.109754

Correia, M. A., McLachlin, S. D., & Cronin, D. S. (2021). Vestibulocollic and Cervicocollic Muscle Reflexes in a Finite Element Neck Model During Multidirectional Impacts. *Annals of Biomedical Engineering*, *49*(7). https://doi.org/10.1007/s10439-021-02783-2

Cronin, D. S. (2011). Explicit finite element method applied to impact biomechanics problems. *2011 IRCOBI Conference Proceedings - International Research Council on the Biomechanics of Injury*.

Crowe, H. (1928). *Injuries to the cervical spine*. Presentation to the annual meeting of the Western Orthopaedic Association, San Francisco.

Crowe, H. (1964). A New Diagnostic Sign in Neck Injuries. *California Medicine*, *100*.

Cusick, J. F., Pintar, F. A., & Yoganandan, N. (2001). Whiplash syndrome: Kinematic factors influencing pain patterns. *Spine*, *26*(11). https://doi.org/10.1097/00007632-200106010-00015

Davidsson, J., Deutscher, C., Hell, W., Lövsund, P., & Svensson, M. Y. (2001). Human Volunteer Kinematics in Rear-End Sled Collisions. *Journal of Crash Prevention and Injury Control*, *2*(4). https://doi.org/10.1080/10286580008902576

Davis, A. G. (1945). Injuries of the Cervical Spine. *Journal of the American Medical Association*, *127*(3), 149. https://doi.org/10.1001/jama.1945.02860030021006

Davis, J., Kaufman, K. R., & Lieber, R. L. (2003). Correlation between active and passive isometric force and intramuscular pressure in the isolated rabbit tibialis anterior muscle. *Journal of Biomechanics*, *36*(4), 505–512. https://doi.org/10.1016/S0021-9290(02)00430-X

Deng, B. (1999). *Kinematics of Human Cadaver Cervical Spine during Low Speed Rear End Impacts* [Wayne State University, Detroit, MI]. https://digitalcommons.wayne.edu/oa_dissertations/3152/

DeWit, J. A., & Cronin, D. S. (2012). Cervical spine segment finite element model for traumatic injury prediction. *Journal of the Mechanical Behavior of Biomedical Materials*, *10*. https://doi.org/10.1016/j.jmbbm.2012.02.015

Dobrin, P. B. (1978). Mechanical properties of arteries. *Physiological Reviews*, *58*(2). https://doi.org/10.1152/physrev.1978.58.2.397

Drottning, M., Staff, P. H., & Sjaastad, O. (2002). Cervicogenic headache (CEH) after whiplash injury. *Cephalalgia*, *22*(3). https://doi.org/10.1046/j.1468-2982.2002.00315.x

Ebara, S., Iatridis, J. C., Setton, L. A., Foster, R. J., Van Mow, C., & Weidenbaum, M. (1996). Tensile properties of nondegenerate human lumbar anulus fibrosus. *Spine*, *21*(4). https://doi.org/10.1097/00007632-199602150-00009

Eichberger, A., Darok, M., Steffan, H., Leinzinger, P. E., Boström, O., & Svensson, M. Y. (2000). Pressure measurements in the spinal canal of post-mortem human subjects during rear-end impact and correlation of results to the neck injury criterion. *Accident Analysis and Prevention*, *32*(2). https://doi.org/10.1016/S0001-4575(99)00097-4

Evans, R. W. (1992). Some observations on whiplash injuries. In *Neurologic Clinics* (Vol. 10, Issue 4). https://doi.org/10.1016/s0733-8619(18)30191-9

Faber, H., Van Soest, A. J., & Kistemaker, D. A. (2018). Inverse dynamics of mechanical multibody systems: An improved algorithm that ensures consistency between kinematics and external forces. *PLoS ONE*, *13*(9). https://doi.org/10.1371/journal.pone.0204575

Ferrario, V. F., Sforza, C., Serrao, G., Grassi, G., & Mossi, E. (2002). *Active range of motion of the head and cervical spine : a three-dimensional investigation in healthy young adults*. *20*, 122–129.

https://doi.org/10.1016/S0736-0266(01)00079-1

Fice, J. B., Blouin, J. S., & Siegmund, G. P. (2018). Head postures during naturalistic driving. *Traffic Injury Prevention*, *19*(6), 637–643. https://doi.org/10.1080/15389588.2018.1493582

Fice, J. B., Cronin, D. S., & Panzer, M. B. (2011). Cervical spine model to predict capsular ligament response in rear impact. *Annals of Biomedical Engineering*, *39*(8), 2152–2162. https://doi.org/10.1007/s10439-011-0315-4

Franz, U., Schuster, P., & Stahlschmidt, S. (2004). Influence of Pre-Stressed Parts in Dummy Modeling: Simple Considerations. *8th International LS-DYNA Users Conference*.

Freeman, M. D. (1998). *A study of chronic neck pain following whiplash injury*. Oregon State University.

Fujita, Y., Duncan, N. A., & Lotz, J. C. (1997). Radial tensile properties of the lumbar annulus fibrosus are site and degeneration dependent. *Journal of Orthopaedic Research*, *15*(6). https://doi.org/10.1002/jor.1100150605

Galasko, C. S. B., Mussay, P., & Stephenson, W. (2002). Incidence of Whiplash-Associated Disorder. *BC Medical Journal*, *44*(5).

Gargan, M. F., & Bannister, G. C. (1994). The rate of recovery following whiplash injury. *European Spine Journal*, *3*(3). https://doi.org/10.1007/BF02190579

Gash, M. C., Kandle, P. F., Murray, I. V., & Varacallo, M. (2018). Physiology, Muscle Contraction. In *StatPearls*. Treasure Island (FL): StatPearls Publishing. https://www.ncbi.nlm.nih.gov/books/NBK537140/

Gayzik, F. S., Moreno, D. P., Vavalle, N. A., Rhyne, A. C., & Stitzel, J. D. (2011). Development of the Global Human Body Models Consortium mid-sized male full body model. *Injury Biomechanics Research, Proceedings of the Thirty-Ninth International Workshop*, 39–12.

Gierczycka, D., Rycman, A., & Cronin, D. (2021). Importance of passive muscle, skin, and adipose tissue mechanical properties on head and neck response in rear impacts assessed with a finite element model. *Traffic Injury Prevention*, *22*(5), 407–412. https://doi.org/10.1080/15389588.2021.1918685

Giles, L. G. F., & Harvey, A. R. (1987). Immunohistochemical demonstration of nociceptors in the

capsule and synovial folds of human zygapophyseal joints. *Rheumatology*, *26*(5). https://doi.org/10.1093/rheumatology/26.5.362

Giroux, M. (1991). Les blessures a la colonne cervicale: importance du probléme. *Le Médecin Du Québec*.

Greening, J., Dilley, A., & Lynn, B. (2005). In vivo study of nerve movement and mechanosensitivity of the median nerve in whiplash and non-specific arm pain patients. *Pain*, *115*(3). https://doi.org/10.1016/j.pain.2005.02.023

Guo, R., Zhou, C., Wang, C., Tsai, T. Y., Yu, Y., Wang, W., Li, G., & Cha, T. (2021). In vivo primary and coupled segmental motions of the healthy female head-neck complex during dynamic head axial rotation. *Journal of Biomechanics*, *123*. https://doi.org/10.1016/j.jbiomech.2021.110513

Hadagali, P. (2024). *Assessing the Tissue-Level Response and the Risk of Neck Pain in Rotary-Wing Aircrew using a Finite Element Model of the Neck*. University of Waterloo.

Hadagali, P., & Cronin, D. S. (2023). Enhancing the Biofidelity of an Upper Cervical Spine Finite Element Model Within the Physiologic Range of Motion and Its Effect on the Full Ligamentous Neck Model Response. *Journal of Biomechanical Engineering*, *145*(1), 1–11. https://doi.org/10.1115/1.4055037

Happee, R. (1994). Inverse dynamic optimization including muscular dynamics, a new simulation method applied to goal directed movements. *Journal of Biomechanics*, *27*(7). https://doi.org/10.1016/0021-9290(94)90267-4

Happee, R., Hoofman, M., Van Den Kroonenberg, A. J., Morsink, P., & Wismans, J. (1998). A mathematical human body model for frontal and rearward seated automotive impact loading. *SAE Technical Papers*. https://doi.org/10.4271/983150

Hasselman, C. T., Best, T. M., Seaber, A. V., & Garrett, W. E. (1995). A Threshold and Continuum of Injury During Active Stretch of Rabbit Skeletal Muscle. *The American Journal of Sports Medicine*, *23*(1), 65–73. https://doi.org/10.1177/036354659502300111

Hill, R. (1979). Aspects of Invariance in Solid Mechanics. *Advances in Applied Mechanics*, *18*(C). https://doi.org/10.1016/S0065-2156(08)70264-3

Holm, L. W., Carroll, L. J., Cassidy, J. D., Hogg-Johnson, S., Côté, P., Guzman, J., Peloso, P., Nordin,

M., Hurwitz, E., van der Velde, G., Carragee, E., & Haldeman, S. (2009). The Burden and Determinants of Neck Pain in Whiplash-Associated Disorders After Traffic Collisions. Results of the Bone and Joint Decade 2000-2010 Task Force on Neck Pain and Its Associated Disorders. *Journal of Manipulative and Physiological Therapeutics*, *32*(2 SUPPL.). https://doi.org/10.1016/j.jmpt.2008.11.011

Holzapfel, G., Feigl, G. G., & Regitnig, P. (2005). *Single LamellarMechanics of the Human Lumbar Anulus Fibrosus Single lamellar mechanics of the human lumbar anulus fibrosus*. *1*(March). https://doi.org/10.1007/s10237-004-0053-8

Huang, Y., King, A. I., & Cavanaugh, J. M. (1994). Finite element modeling of gross motion of human cadavers in side impact. *Stapp Car Crash Conference Proceedings*, *P-279*.

Hubbard, R. D., Chen, Z., & Winkelstein, B. A. (2008). Transient cervical nerve root compression modulates pain: Load thresholds for allodynia and sustained changes in spinal neuropeptide expression. *Journal of Biomechanics*, *41*(3). https://doi.org/10.1016/j.jbiomech.2007.09.026

Hubbard, R. D., & Winkelstein, B. A. (2005). Transient cervical nerve root compression in the rat induces bilateral forepaw allodynia and spinal glial activation: Mechanical factors in painful neck injuries. *Spine*, *30*(17). https://doi.org/10.1097/01.brs.0000176239.72928.00

Iatridis, J. C., MacLean, J. J., & Ryan, D. A. (2005). Mechanical damage to the intervertebral disc annulus fibrosus subjected to tensile loading. *Journal of Biomechanics*, *38*(3), 557–565. https://doi.org/10.1016/j.jbiomech.2004.03.038

Iatridis, J. C., Setton, L. A., Foster, R. J., Rawlins, B. A., Weidenbaum, M., & Mow, V. C. (1998). Degeneration affects the anisotropic and nonlinear behaviors of human anulus fibrosus in compression. *Journal of Biomechanics*, *31*(6). https://doi.org/10.1016/S0021-9290(98)00046-3

Inami, S., Shiga, T., Tsujino, A., Yabuki, T., Okado, N., & Ochiai, N. (2001). Immunohistochemical demonstration of nerve fibres in the synovial fold of the human cervical facet joint. *Journal of Orthopaedic Research*, *19*(4). https://doi.org/10.1016/S0736-0266(00)00048-6

Ishii, T., Mukai, Y., Hosono, N., Sakaura, H., Nakajima, Y., Sato, Y., Sugamoto, K., & Yoshikawa, H. (2004). Kinematics of the upper cervical spine in rotation: in vivo three-dimensional analysis. *Spine*, *29*(7), 2826–2831.

Ito, S., Ivancic, P. C., Panjabi, M. M., & Cunningham, B. W. (2004). Soft Tissue Injury Threshold

during Simulated Whiplash: A Biomechanical Investigation. *Spine*, *29*(9). https://doi.org/10.1097/00007632-200405010-00006

Ito, S., Ivancic, P. C., Pearson, A. M., Tominaga, Y., Gimenez, S. E., Rubin, W., & Panjabi, M. M. (2005). Cervical intervertebral disc injury during simulated frontal impact. *European Spine Journal*, *14*(4). https://doi.org/10.1007/s00586-004-0783-4

Ivancic, P. C. (2013). Effects of orthoses on three-dimensional load-displacement properties of the cervical spine. *European Spine Journal*, *22*(1), 169–177. https://doi.org/10.1007/s00586-012-2552-0

Ivancic, P. C., Ito, S., Tominaga, Y., Carlson, E. J., Rubin, W., & Panjabi, M. M. (2006). Effect of rotated head posture on dynamic vertebral artery elongation during simulated rear impact. *Clinical Biomechanics*, *21*(3), 213–220. https://doi.org/10.1016/j.clinbiomech.2005.10.011

Ivancic, P. C., Panjabi, M. M., Ito, S., Cripton, P. A., & Wang, J. L. (2005). Biofidelic whole cervical spine model with muscle force replication for whiplash simulation. *European Spine Journal*, *14*(4), 346–355. https://doi.org/10.1007/s00586-004-0758-5

Ivancic, P. C., Pearson, A. M., Panjabi, M. M., & Ito, S. (2004). Injury of the anterior longitudinal ligament during whiplash simulation. *European Spine Journal*, *13*(1). https://doi.org/10.1007/s00586-003-0590-3

Iwamoto, M., Nakahira, Y., & Kimpara, H. (2015). Development and Validation of the Total HUman Model for Safety (THUMS) Toward Further Understanding of Occupant Injury Mechanisms in Precrash and During Crash. *Traffic Injury Prevention*, *16*. https://doi.org/10.1080/15389588.2015.1015000

Jakobsson, L. (2004). Field analysis of AIS1 neck injuries in rear-end car impacts - Injury reducing effect of the WHIPS seat. *Journal of Whiplash and Related Disorders*, *3*(2), 37–53. https://doi.org/10.1300/J180v03n02_04

John, J., Klug, C., Kranjec, M., Svenning, E., & Iraeus, J. (2022). Hello, world! VIVA+: A human body model lineup to evaluate sex-differences in crash protection. *Frontiers in Bioengineering and Biotechnology*, *10*. https://doi.org/10.3389/fbioe.2022.918904

Jónsson, H., Bring, G., Rauschning, W., & Sahlstedt, B. (1991). Hidden cervical spine injuries in traffic accident victims with skull fractures. *Journal of Spinal Disorders*, *4*(3).

https://doi.org/10.1097/00002517-199109000-00001

Jonsson, H., Cesarini, K., Sahlstedt, B., & Rauschning, W. (1994). Findings and outcome in whiplash-type neck distortions. *Spine*, *19*(24). https://doi.org/10.1097/00007632-199412150-00001

Kaale, B. R., Krakenes, J., Albrektsen, G., & Wester, K. (2005a). Head position and impact direction in whiplash injuries: Associations with MRI-verified lesions of ligaments and membranes in the upper cervical spine. *Journal of Neurotrauma*, *22*(11). https://doi.org/10.1089/neu.2005.22.1294

Kaale, B. R., Krakenes, J., Albrektsen, G., & Wester, K. (2005b). Whiplash-associated disorders impairment rating: Neck disability index score according to severity of MRI findings of ligaments and membranes in the upper cervical spine. *Journal of Neurotrauma*, *22*(4). https://doi.org/10.1089/neu.2005.22.466

Kallakuri, S., Singh, A., Chen, C., & Cavanaugh, J. M. (2004). Demonstration of substance P, calcitonin gene-related peptide, and protein gene product 9.5 containing nerve fibers in human cervical facet joint capsules. *Spine*, *29*(11). https://doi.org/10.1097/00007632-200406010-00005

Kamper, S. J., Rebbeck, T. J., Maher, C. G., McAuley, J. H., & Sterling, M. (2008). Course and prognostic factors of whiplash: A systematic review and meta-analysis. *Pain*, *138*(3). https://doi.org/10.1016/j.pain.2008.02.019

Kaneoka, K., Ono, K., Inami, S., & Hayashi, K. (1999). Motion analysis of cervical vertebrae during whiplash loading. *Spine*, *24*(8). https://doi.org/10.1097/00007632-199904150-00006

Kasra, M., Parnianpour, M., Shirazi-Adl, A., Wang, J. L., & Grynpas, M. D. (2004). Effect of strain rate on tensile properties of sheep disc anulus fibrosus. *Technology and Health Care*, *12*(4). https://doi.org/10.3233/thc-2004-12405

Kato, D., Nakahira, Y., Atsumi, N., & Iwamoto, M. (2018). Development of human-body model THUMS version 6 containing muscle controllers and application to injury analysis in frontal collision after brake deceleration. *Conference Proceedings International Research Council on the Biomechanics of Injury, IRCOBI*, *2018-September*.

Keaveny, T. M., Morgan, E. F., Niebur, G. L., & Yeh, O. C. (2001). Biomechanics of trabecular bone. In *Annual Review of Biomedical Engineering* (Vol. 3). https://doi.org/10.1146/annurev.bioeng.3.1.307

Kito, T., Haraguchi, M., Funatsu, T., Sato, M., & Kondo, M. (1989). Measurements of gaze movements while driving. *Perceptual and Motor Skills*, *68*(1). https://doi.org/10.2466/pms.1989.68.1.19

Koelbaek Johansen, M., Graven-Nielsen, T., Schou Olesen, A., & Arendt-Nielsen, L. (1999). Generalised muscular hyperalgesia in chronic whiplash syndrome. *Pain*, *83*(2). https://doi.org/10.1016/S0304-3959(99)00106-2

Kojima, Y., Maeda, T., Arai, R., & Shichikawa, K. (1990). Nerve supply to the posterior longitudinal ligament and the intervertebral disc of the rat vertebral column as studied by acetylcholinesterase histochemistry. I. Distribution in the lumbar region. *Journal of Anatomy*, *169*.

Krafft, M., Kullgren, A., Sigrun, M., & Ydenius, A. (2005). Influence of Crash Severity on Various Whiplash Injury Symptoms: A Study based on Real-Life Rear-End Crashes with Recorded Crash Pulses. *The 19th International Technical Conference on the Enhanced Safety of Vehicle (ESV), Washington D.C. (USA)*, *Paper No. 05-0363*.

Krafft, M., Kullgren, A., Ydenius, A., & Tingvall, C. (2002). Influence of crash pulse characteristics on whiplash associated disorders in rear impacts-crash recording in real life crashes. *Traffic Injury Prevention*, *3*(2). https://doi.org/10.1080/15389580212001

Krakenes, J., & Kaale, B. R. (2006). Magnetic resonance imaging assessment of craniovertebral ligaments and membranes after whiplash trauma. In *Spine* (Vol. 31, Issue 24). https://doi.org/10.1097/01.brs.0000245871.15696.1f

Kullgren, A., Stigson, H., & Krafft, M. (2013). Development of whiplash associated disorders for male and female car occupants in cars launched since the 80s in different impact directions. *2013 IRCOBI Conference Proceedings - International Research Council on the Biomechanics of Injury*.

Lasswell, T. L., Cronin, D. S., Medley, J. B., & Rasoulinejad, P. (2017). Incorporating ligament laxity in a finite element model for the upper cervical spine. *Spine Journal*, *17*(11). https://doi.org/10.1016/j.spinee.2017.06.040

Lee, K. E., Thinnes, J. H., Gokhin, D. S., & Winkelstein, B. A. (2004). A novel rodent neck pain model of facet-mediated behavioral hypersensitivity: Implications for persistent pain and whiplash injury. *Journal of Neuroscience Methods*, *137*(2). https://doi.org/10.1016/j.jneumeth.2004.02.021

Lim, J., Hong, J., Chen, W. W., & Weerasooriya, T. (2011). Mechanical response of pig skin under

dynamic tensile loading. *International Journal of Impact Engineering*, *38*(2–3). https://doi.org/10.1016/j.ijimpeng.2010.09.003

Lindahl, O. (1976). Mechanical properties of dried defatted spongy bone. *Acta Orthopaedica*, *47*(1). https://doi.org/10.3109/17453677608998966

Livermore Software Technology Corporation. (2016). *LS-DYNA R9.0 Keyword's User Manual Volume I*. www.lstc.com

Lord, S. M., Barnsley, L., Wallis, B. J., & Bogduk, N. (1996). Chronic cervical zygapophysial joint pain after whiplash: A placebo- controlled prevalence study. *Spine*, *21*(15). https://doi.org/10.1097/00007632-199608010-00005

Lu, Y., Chen, C., Kallakuri, S., Patwardhan, A., & Cavanaugh, J. M. (2005a). Neural Response of Cervical Facet Joint Capsule to Stretch: A Study of Whiplash Pain Mechanism. *SAE Technical Papers*, *2005-November*(November). https://doi.org/10.4271/2005-22-0003

Lu, Y., Chen, C., Kallakuri, S., Patwardhan, A., & Cavanaugh, J. M. (2005b). Neurophysiological and biomechanical characterization of goat cervical facet joint capsules. *Journal of Orthopaedic Research*, *23*(4), 779–787. https://doi.org/10.1016/j.orthres.2005.01.002

Lutz, T. J., Starr, H., Smith, C. A., Stewart, A. M., Monroe, M. J., Joines, S. M. B., & Mirka, G. A. (2001). Technical note: the use of mirrors during an assembly task: A study of ergonomics and productivity. *Ergonomics*, *44*(2). https://doi.org/10.1080/00140130120518

Maak, T. G., Tominaga, Y., Panjabi, M. M., & Ivancic, P. C. (2006). Alar, transverse, and apical ligament strain due to head-turned rear impact. *Spine*, *31*(6). https://doi.org/10.1097/01.brs.0000202739.05878.d3

Macnab, I. (1971). The "Whiplash Syndrome." *Orthopedic Clinics of North America*, 389–403. https://doi.org/10.1016/S0030-5898(20)31114-7

Martin, J. L., Pérez, K., Marí-Dell'Olmo, M., & Chiron, M. (2008). Whiplash risk estimation based on linked hospital-police road crash data from France and Spain. *Injury Prevention*, *14*(3). https://doi.org/10.1136/ip.2007.016600

Mattucci, S. F. E., Moulton, J. A., Chandrashekar, N., & Cronin, D. S. (2012). Strain rate dependent properties of younger human cervical spine ligaments. *Journal of the Mechanical Behavior of*

Biomedical Materials, *10*, 216–226. https://doi.org/10.1016/j.jmbbm.2012.02.004

Mattucci, S. F. E., Moulton, J. A., Chandrashekar, N., & Cronin, D. S. (2013). Strain rate dependent properties of human craniovertebral ligaments. *Journal of the Mechanical Behavior of Biomedical Materials*, *23*, 71–79. https://doi.org/10.1016/j.jmbbm.2013.04.005

Mertz, H. J. (1993). Anthropomorphic Test Devices. In A. M. Nahum & J. W. Melvin (Eds.), *Accidental Injury: Biomechanics and Prevention* (1st ed., pp. 66–84). Springer Science+Business Media, LLC.

Morgan, E. F., Unnikrisnan, G. U., & Hussein, A. I. (2018). Bone Mechanical Properties in Healthy and Diseased States. In *Annual Review of Biomedical Engineering* (Vol. 20). https://doi.org/10.1146/annurev-bioeng-062117-121139

Morrow, D. A., Haut Donahue, T. L., Odegard, G. M., & Kaufman, K. R. (2010). Transversely isotropic tensile material properties of skeletal muscle tissue. *Journal of the Mechanical Behavior of Biomedical Materials*, *3*(1), 124–129. https://doi.org/10.1016/j.jmbbm.2009.03.004

Mortensen, J. D., Vasavada, A. N., & Merryweather, A. S. (2018). The inclusion of hyoid muscles improve moment generating capacity and dynamic simulations in musculoskeletal models of the head and neck. *PLoS ONE*, *13*(6). https://doi.org/10.1371/journal.pone.0199912

Myers, B. S., Woolley, C. T., Slotter, T. L., Garrett, W. E., & Best, T. M. (1998). The influence of strain rate on the passive and stimulated engineering stress-large strain behavior of the rabbit tibialis anterior muscle. *Journal of Biomechanical Engineering*, *120*(1), 126–132. https://doi.org/10.1115/1.2834292

Niv, D., & Devor, M. (2007). Position paper of the European Federation of IASP Chapters (EFIC) on the subject of pain management. *European Journal of Pain*, *11*(5). https://doi.org/10.1016/j.ejpain.2007.03.005

Norris, S. H., & Watt, I. (1983). The prognosis of neck injuries resulting from rear-end vehicle collisions. *Journal of Bone and Joint Surgery - Series B*, *65*(5). https://doi.org/10.1302/0301-620x.65b5.6643566

Nowitzke, A., Westaway, M., & Bogduk, N. (1994). Cervical zygapophyseal joints: geometrical parameters and relationship to cervical kinematics. *Clinical Biomechanics*, *9*(6), 342–348. https://doi.org/10.1016/0268-0033(94)90063-9

Ono, K., Ejima, S., Suzuki, Y., Kaneoka, K., Fukushima, M., & Ujihashi, S. (2006). Prediction of neck injury risk based on the analysis of localized cervical vertebral motion of human volunteers during low-speed rear impacts. *International Research Council on the Biomechanics of Impact - 2006 International IRCOBI Conference on the Biomechanics of Impact, Proceedings*, *September*, 103–113.

Ono, K., Kaneoka, K., Wittek, A., & Kajzer, J. (1997). Cervical injury mechanism based on the analysis of human cervical vertebral motion and head-neck-torso kinematics during low speed rear impacts. *Stapp Car Crash Conference Proceedings*, *P-315*.

Östh, J., Mendoza-Vazquez, M., Linder, A., Svensson, M. Y., & Brolin, K. (2017). The VIVA OpenHBM finite element 50th percentile female occupant model: Whole body model development and kinematic validation. *Conference Proceedings International Research Council on the Biomechanics of Injury, IRCOBI*, *2017-September*.

Östh, J., Mendoza-Vazquez, M., Svensson, M. Y., Linder, A., & Brolin, K. (2016). Development of a 50th percentile female human body model. *2016 IRCOBI Conference Proceedings - International Research Council on the Biomechanics of Injury*.

Palepu, V. (2013). *Biomechanical effects of initial occupant seated posture during rear end impact injury*. http://utdr.utoledo.edu/theses-dissertations/167

Panjabi, M. M., Cholewicki, J., Nibu, K., Grauer, J., & Vahldiek, M. (1998). Capsular ligament stretches during in vitro whiplash simulations. *Journal of Spinal Disorders*, *11*(3). https://doi.org/10.1097/00002517-199806000-00009

Panjabi, M. M., Ito, S., Pearson, A. M., & Ivancic, P. C. (2004). Injury mechanisms of the cervical intervertebral disc during simulated whiplash. *Spine*, *29*(11). https://doi.org/10.1097/00007632-200406010-00011

Panjabi, M. M., Ivancic, P. C., Tominaga, Y., & Malcolmson, G. F. (2006). Predicting multiplanar cervical spine injury due to head-turned rear impacts using IV-NIC. *Traffic Injury Prevention*, *7*(3), 264–275. https://doi.org/10.1080/15389580500488499

Panjabi, M. M., Maak, T. G., Ivancic, P. C., & Ito, S. (2006). Dynamic intervertebral foramen narrowing during simulated rear impact. *Spine*, *31*(5), 128–134. https://doi.org/10.1097/01.brs.0000201243.81745.ba

Panjabi, M. M., Oxland, T., Takata, K., Goel, V., Duranceau, J., & Krag, M. (1993). Articular facets of the human spine:Quantitative three-dimensional anatomy. *Spine*, *18*(10), 1298–1310. https://doi.org/10.1097/00007632-199308000-00009

Panjabi, M. M., Pearson, A. M., Ito, S., Ivancic, P. C., Gimenez, S. E., & Tominaga, Y. (2004). Cervical spine ligament injury during simulated frontal impact. *Spine*, *29*(21). https://doi.org/10.1097/01.brs.0000143173.92241.ab

Panzer, M. B. (2006). Numerical Modelling of the Human Cervical Spine in Frontal Impact. In *UWSpace*. University of Waterloo.

Panzer, M. B., Fice, J. B., & Cronin, D. S. (2011). Cervical spine response in frontal crash. *Medical Engineering and Physics*, *33*(9), 1147–1159. https://doi.org/10.1016/j.medengphy.2011.05.004

Pearson, A. M., Ivancic, P. C., Ito, S., & Panjabi, M. M. (2004). Facet Joint Kinematics and Injury Mechanisms during Simulated Whiplash. *Spine*, *29*(4), 390–397. https://doi.org/10.1097/01.BRS.0000090836.50508.F7

Pettersson, K., Hildingsson, C., Toolanen, G., Fagerlund, M., & Björnebrink, J. (1997). Disc pathology after whiplash injury: A prospective magnetic resonance imaging and clinical investigation. *Spine*, *22*(3). https://doi.org/10.1097/00007632-199702010-00010

Plank, G. R., & Eppinger, R. H. (1989). Computed dynamic response of the human thorax from a finite element model. *12th International Technical Conference of Experimental Safety Vehicle*.

Quinn, K. P., Lee, K. E., Ahaghotu, C. C., & Winkelstein, B. A. (2007). Structural changes in the cervical facet capsular ligament: potential contributions to pain following subfailure loading. *Stapp Car Crash Journal*, *51*.

Reed, M. P., Ebert, S. M., Jones, M. L. H., & Hallman, J. J. (2020). Prevalence of non-nominal seat positions and postures among front-seat passengers. *Traffic Injury Prevention*, 1–6. https://doi.org/10.1080/15389588.2020.1793971

Reilly, D. T., Burstein, A. H., & Frankel, V. H. (1974). The elastic modulus for bone. *Journal of Biomechanics*, *7*(3). https://doi.org/10.1016/0021-9290(74)90018-9

Richter, M., Otte, D., Pohlemann, T., Krettek, C., & Blauth, M. (2000). Whiplash-type neck distortion in restrained car drivers: Frequency, causes and long-term results. *European Spine Journal*, *9*(2).

https://doi.org/10.1007/s005860050220

Rothman, S. M., Kreider, R. A., & Winkelstein, B. A. (2005). Spinal neuropeptide responses in persistent and transient pain following cervical nerve root injury. *Spine*, *30*(22). https://doi.org/10.1097/01.brs.0000186316.38111.4b

Saldinger, P., Dvorak, J., Rahn, B. A., & Perren, S. M. (1990). Histology of the alar and transverse ligaments. *Spine*, *15*(4). https://doi.org/10.1097/00007632-199004000-00001

Salem, W., Lenders, C., Mathieu, J., Hermanus, N., & Klein, P. (2013). Invivo three-dimensional kinematics of the cervical spine during maximal axial rotation. *Manual Therapy*, *18*(4). https://doi.org/10.1016/j.math.2012.12.002

Sarichter, S., Koller, A., Hold, C., Wicke, K., Judmaier, W., Werner, P., & Raas, E. (1995). Light concentric exercise and heavy eccentric muscle loading: Effects on CK, MRI and markers of inflammation. *International Journal of Sports Medicine*, *16*(5). https://doi.org/10.1055/s-2007-973007

Sato, F., Nakajima, T., Ono, K., Svensson, M., Brolin, K., & Kaneoka, K. (2014). Dynamic cervical vertebral motion of female and male volunteers and analysis of its interaction with head/neck/torso behavior during low-speed rear impact. *2014 IRCOBI Conference Proceedings - International Research Council on the Biomechanics of Injury*.

Schwartz, D., Guleyupoglu, B., Koya, B., Stitzel, J. D., & Gayzik, F. S. (2015). Development of a Computationally Efficient Full Human Body Finite Element Model. *Traffic Injury Prevention*, *16*. https://doi.org/10.1080/15389588.2015.1021418

Scott, D., Jull, G., & Sterling, M. (2005). Widespread sensory hypersensitivity is a feature of chronic whiplash-associated disorder but not chronic idiopathic neck pain. *Clinical Journal of Pain*, *21*(2). https://doi.org/10.1097/00002508-200503000-00009

Scott, S., & Sanderson, P. (2002). Whiplash: A biochemical study of muscle injury. *European Spine Journal*, *11*(4). https://doi.org/10.1007/s00586-002-0410-1

Shateri, H. (2012). *Neck Response in Out of Position Rear Impact Scenarios*. University of Waterloo.

Shateri, H., & Cronin, D. S. (2015). Out-of-Position Rear Impact Tissue-Level Investigation Using Detailed Finite Element Neck Model. *Traffic Injury Prevention*, *16*(7), 698–708.

https://doi.org/10.1080/15389588.2014.1003551

Shen, D., & Cronin, D. S. (2017). Effect of Active Musculature Parameters on Neck Response and Potential for Injury. *IRCOBI Conference 2017*.

Shergold, O. A., Fleck, N. A., & Radford, D. (2006). The uniaxial stress versus strain response of pig skin and silicone rubber at low and high strain rates. *International Journal of Impact Engineering*, *32*(9). https://doi.org/10.1016/j.ijimpeng.2004.11.010

Shugg, J. A. J., Jackson, C. D., & Dickey, J. P. (2011). Cervical spine rotation and range of motion: Pilot measurements during driving. *Traffic Injury Prevention*, *12*(1), 82–87. https://doi.org/10.1080/15389588.2010.529973

Siegmund, G. P., Davis, M. B., Quinn, K. P., Hines, E., Myers, B. S., Ejima, S., Ono, K., Kamiji, K., Yasuki, T., & Winkelstein, B. A. (2008). Head-turned postures increase the risk of cervical facet capsule injury during whiplash. *Spine*, *33*(15), 1643–1649. https://doi.org/10.1097/BRS.0b013e31817b5bcf

Siegmund, G. P., Myers, B. S., Davis, M. B., Bohnet, H. F., & Winkelstein, B. A. (2001). Mechanical Evidence of Cervical Facet Capsule Injury During Whiplash. *Spine*, *26*(19). https://doi.org/10.1097/00007632-200110010-00010

Siegmund, G. P., Sanderson, D. J., Myers, B. S., & Inglis, J. T. (2003). Rapid neck muscle adaptation alters the head kinematics of aware and unaware subjects undergoing multiple whiplash-like perturbations. *Journal of Biomechanics*, *36*(4), 473–482. https://doi.org/10.1016/S0021-9290(02)00458-X

Siegmund, G. P., Winkelstein, B. A., Ivancic, P. C., Svensson, M. Y., & Vasavada, A. (2009). The Anatomy and Biomechanics of Acute and Chronic Whiplash Injury. *Traffic Injury Prevention*, *10*(2). https://doi.org/10.1080/15389580802593269

Skaggs, D. L., Weidenbaum, M., Latridis, J. C., Ratcliffe, A., & Mow, V. C. (1994). Regional variation in tensile properties and biochemical composition of the human lumbar anulus fibrosus. *Spine*, *19*(12). https://doi.org/10.1097/00007632-199406000-00002

Spitzer, W. O., Skovron, M. L., Salmi, L. R., Cassidy, J. D., Duranceau, J., Suissa, S., Zeiss, E., Weinstein, J. N., & Nogbuk, N. (1995). Scientific monograph of the Quebec Task Force on whiplash-associated disorders: Redefining “Whiplash” and its management. *Spine*, *20*(8).

Standring, S. (2016). *Gray's Anatomy: The Anatomical Basis of Clinical Practice* (41st ed.). Elsevier: Amsterdam.

Storvik, S. G., & Stemper, B. D. (2011). Axial head rotation increases facet joint capsular ligament strains in automotive rear impact. *Medical and Biological Engineering and Computing*, *49*(2), 153–161. https://doi.org/10.1007/s11517-010-0682-2

Straker, L., Skoss, R., Burnett, A., & Burgess-Limerick, R. (2009). Effect of visual display height on modelled upper and lower cervical gravitational moment, muscle capacity and relative strain. *Ergonomics*, *52*(2). https://doi.org/10.1080/00140130802331609

Sturzenegger, M., DiStefano, G., Radanov, B. P., & Schnidrig, A. (1994). Presenting symptoms and signs after whiplash injury: The influence of accident mechanisms. *Neurology*, *44*(4). https://doi.org/10.1212/wnl.44.4.688

Sturzenegger, M., Radanov, B. P., & Di Stefano, G. (1995). The effect of accident mechanisms and initial findings on the long-term course of whiplash injury. *Journal of Neurology*, *242*(7). https://doi.org/10.1007/BF00873547

Svensson, M. Y., Boström, O., Davidsson, J., Hansson, H. A., Håland, Y., Lövsund, P., Suneson, A., & Säljö, A. (2000). Neck injuries in car collisions - A review covering a possible injury mechanism and the development of a new rear-impact dummy. In *Accident Analysis and Prevention* (Vol. 32, Issue 2). https://doi.org/10.1016/S0001-4575(99)00080-9

Szabo, T. J., & Welcher, J. B. (1996). Human subject kinematics and electromyographic activity during low speed rear impacts. *Stapp Car Crash Conference Proceedings*, *P-305*.

Taylor, J. R., & Twomey, L. T. (1993). Acute injuries to cervical joints: An autopsy study of neck sprain. *Spine*, *18*(9). https://doi.org/10.1097/00007632-199307000-00001

Tominaga, Y., Maak, T. G., Ivancic, P. C., Panjabi, M. M., & Cunningham, B. W. (2006). Head-turned rear impact causing dynamic cervical intervertebral foramen narrowing: Implications for ganglion and nerve root injury. *Journal of Neurosurgery: Spine*, *4*(5). https://doi.org/10.3171/spi.2006.4.5.380

Van Ee, C. A., & Nightingale, R. W. (2000). Tensile Properties of the Human Muscular and Ligamentous Cervical Spine. *SAE Technical Papers*, *2000-November*(November). https://doi.org/10.4271/2000-01-SC07

Van Sligtenhorst, C., Cronin, D. S., & Wayne Brodland, G. (2006). High strain rate compressive properties of bovine muscle tissue determined using a split Hopkinson bar apparatus. *Journal of Biomechanics*, *39*(10), 1852–1858. https://doi.org/10.1016/j.jbiomech.2005.05.015

Vasavada, A. N., Brault, J. R., & Siegmund, G. P. (2007). Musculotendon and fascicle strains in anterior and posterior neck muscles during whiplash injury. *Spine*, *32*(7). https://doi.org/10.1097/01.brs.0000259058.00460.69

Wagner, D. R., & Lotz, J. C. (2004). Theoretical model and experimental results for the nonlinear elastic behavior of human annulus fibrosus. *Journal of Orthopaedic Research*, *22*(4). https://doi.org/10.1016/j.orthres.2003.12.012

Winkelstein, B. A., Nightingale, R. W., Richardson, W. J., & Myers, B. S. (2000). The cervical facet capsule and its role in whiplash injury: A biomechanical investigation. *Spine*, *25*(10). https://doi.org/10.1097/00007632-200005150-00007

Winters, J. M., & Stark, L. (1988). Estimated mechanical properties of synergistic muscles involved in movements of a variety of human joints. *Journal of Biomechanics*, *21*(12). https://doi.org/10.1016/0021-9290(88)90249-7

Winters, J. M., & Woo, S. L.-Y. (1990). Multiple Muscle Systems. In *Multiple Muscle Systems*. Springer New York. https://doi.org/10.1007/978-1-4613-9030-5

Yang, J., Liu, K., Li, X., & Liu, Z. (2020). Stress initialization methods for dynamic numerical simulation of rock mass with high in-situ stress. *Journal of Central South University*, *27*(10). https://doi.org/10.1007/s11771-020-4535-3

Yang, K. H. (2018). Basic finite element method as applied to injury biomechanics. In *Basic Finite Element Method as Applied to Injury Biomechanics*. https://doi.org/10.1016/c2015-0-06702-8

Yang, K. H., Begeman, P. C., Muser, M., Niederer, P., & Walz, F. (1997). On the role of cervical facet joints in rear end impact neck injury mechanisms. *SAE Technical Papers*. https://doi.org/10.4271/970497

Yang, K. H., & King, A. I. (2003). Neck kinematics in rear-end impacts. *Pain Research and Management*, *8*(2). https://doi.org/10.1155/2003/839740

Yang, K. H., & Kish, V. L. (1988). Compressibility Measurement of Human Intervertebral Nucleus

Pulposus. *Journal of Biomechanics*, *21*(10), 865.

Yoganandan, N., Kumaresan, S., & Pintar, F. A. (2001). Biomechanics of the cervical spine. Part 2. Cervical spine soft tissue responses and biomechanical modeling. In *Clinical Biomechanics* (Vol. 16, Issue 1). https://doi.org/10.1016/S0268-0033(00)00074-7

Yoo, J. U., Zou, D., Edwards, W. T., Bayley, J., & Yuan, H. A. (1992). Effect of cervical spine motion on the neuroforaminal dimensions of human cervical spine. *Spine*, *17*(10). https://doi.org/10.1097/00007632-199210000-00001

Appendix A

Rear Impact Kinematics

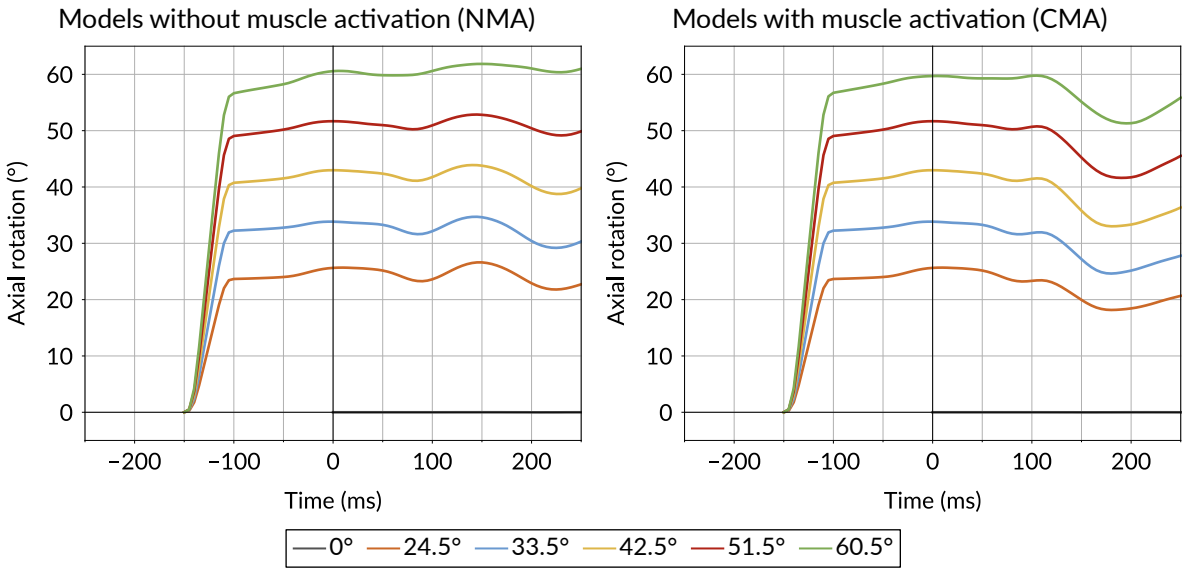


Figure A-1: Head-T1 axial rotation under a 4g rear impact condition without and with muscle activation for each head position.

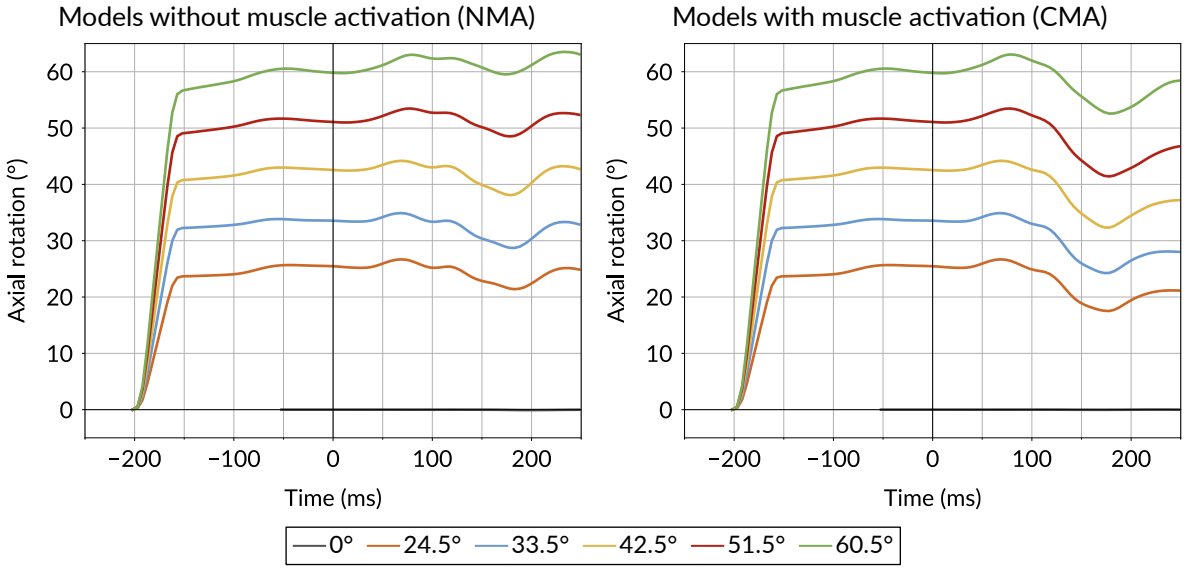


Figure A-2: Head-T1 axial rotation under a 10g rear impact condition without and with muscle activation for each head position.

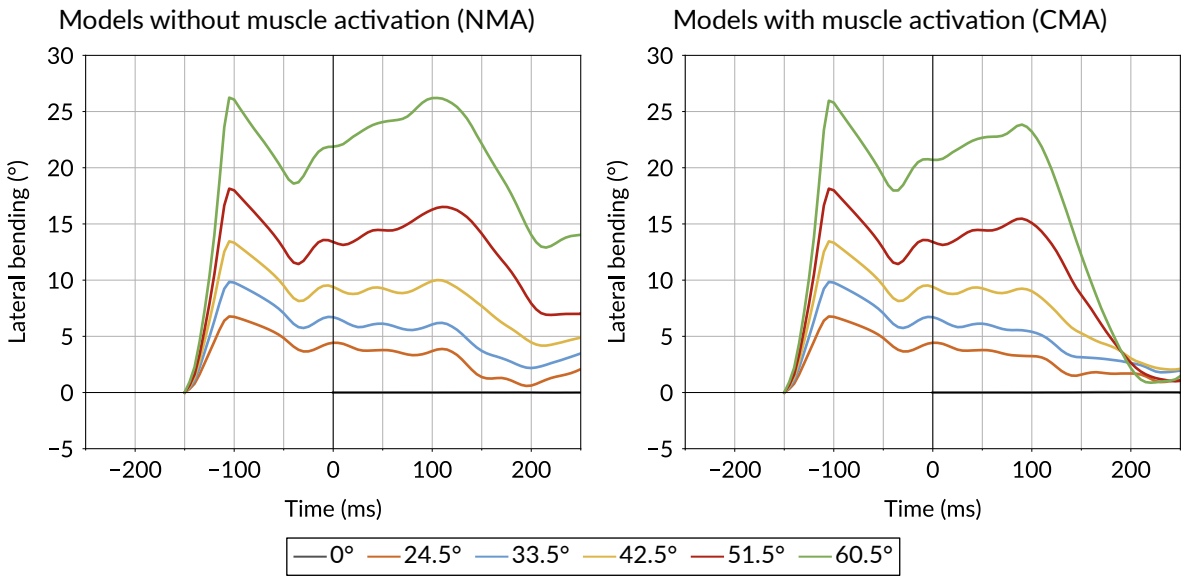


Figure A-3: Head-T1 lateral bending under a 4g rear impact condition without and with muscle activation for each head position.

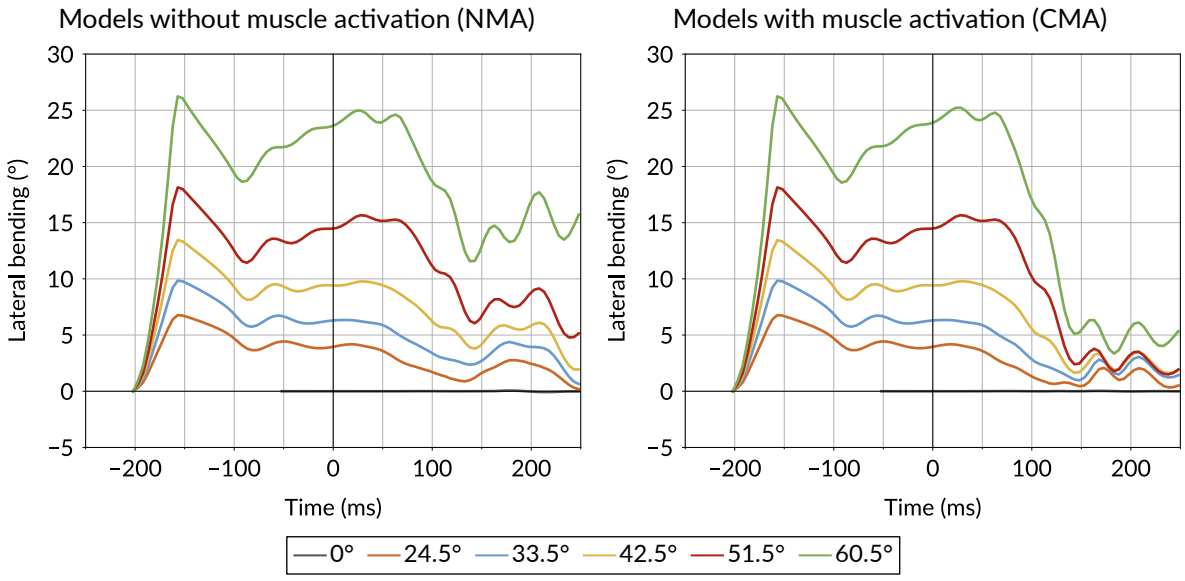


Figure A-4: Head-T1 lateral bending under a 10g rear impact condition without and with muscle activation for each head position.

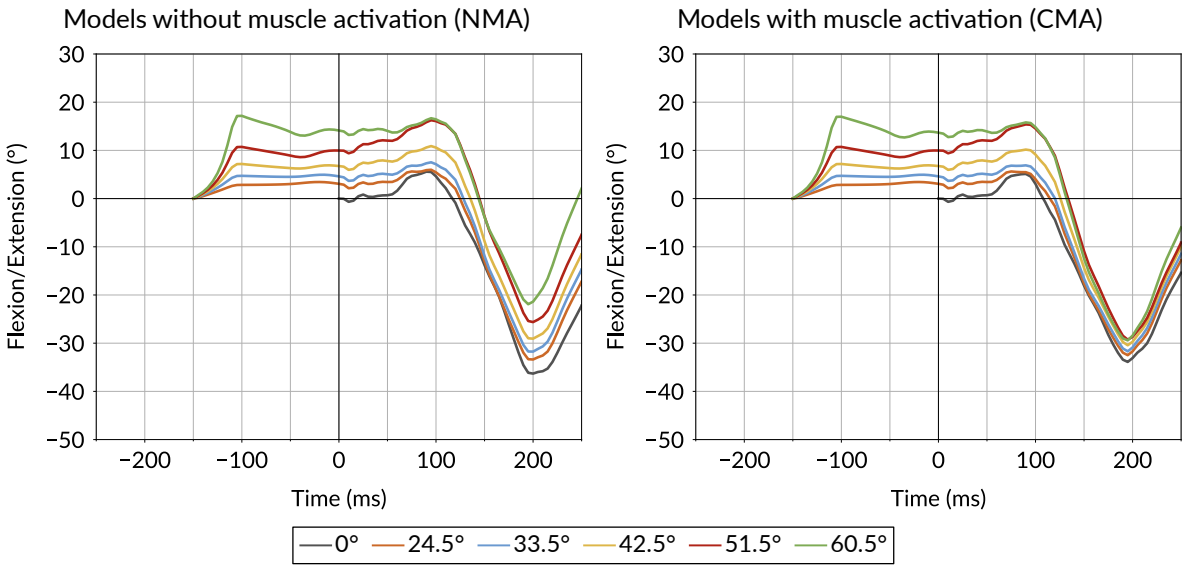


Figure A-5: Head-T1 flexion/extension under a 4g rear impact condition without and with muscle activation for each head position.

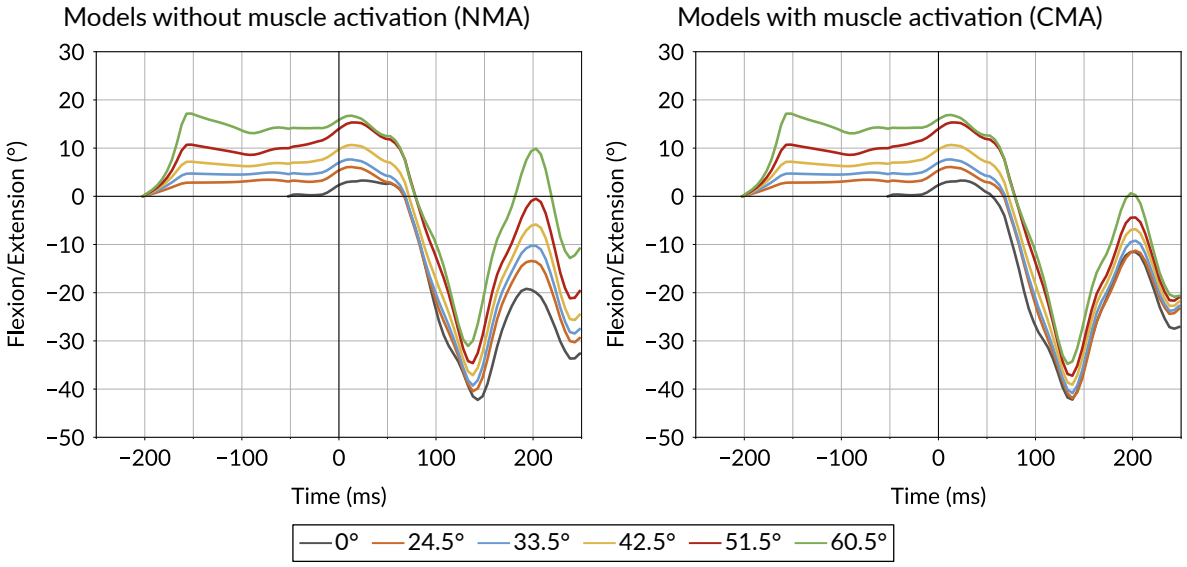


Figure A-6: Head-T1 flexion/extension under a 10g rear impact condition without and with muscle activation for each head position.

Appendix B

Ligament Distraction Results

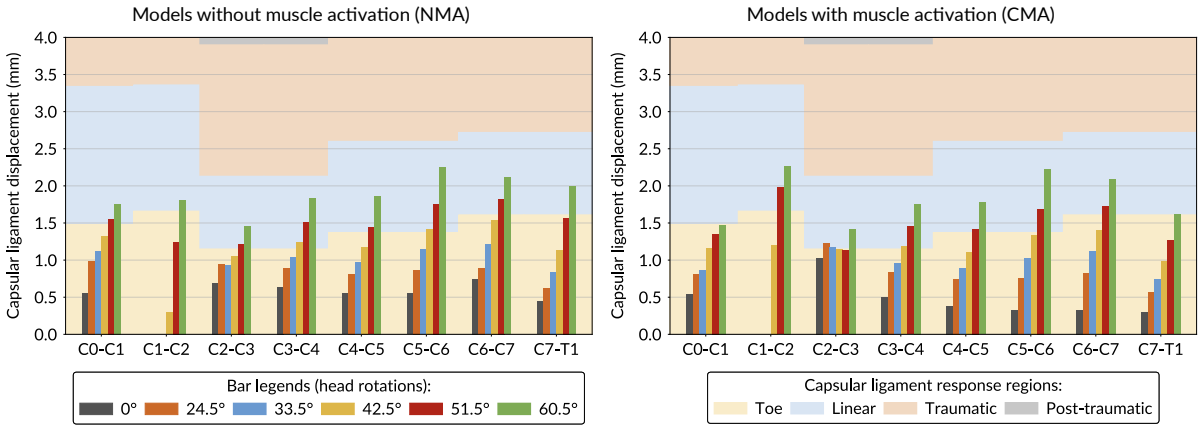


Figure B-1: Maximum quadrant displacement of capsular ligaments during a 4g rear impact scenario without and with muscle activation compared with the response regions (Mattucci et al., 2012, 2013) for each intervertebral level.

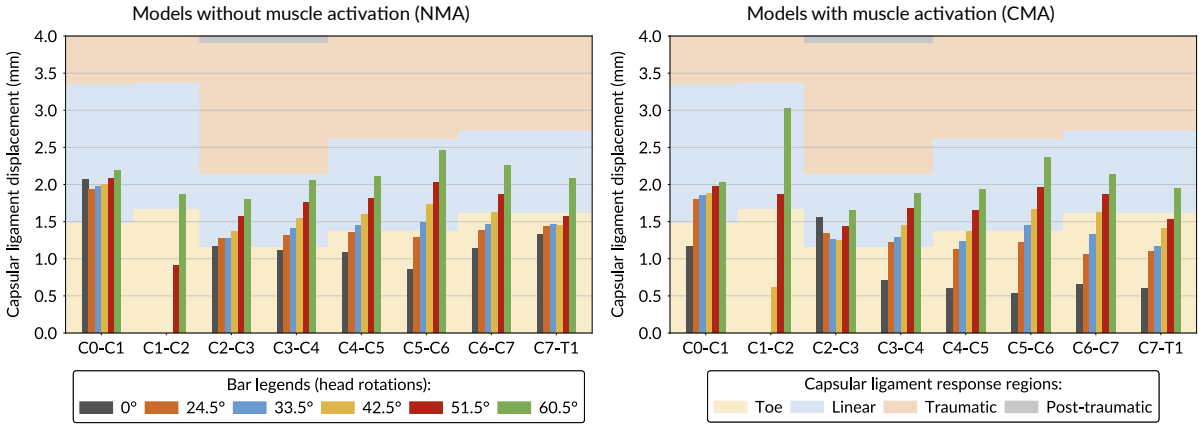


Figure B-2: Maximum quadrant displacement of capsular ligaments during a 10g rear impact scenario without and with muscle activation compared with the response regions (Mattucci et al., 2012, 2013) for each intervertebral level.

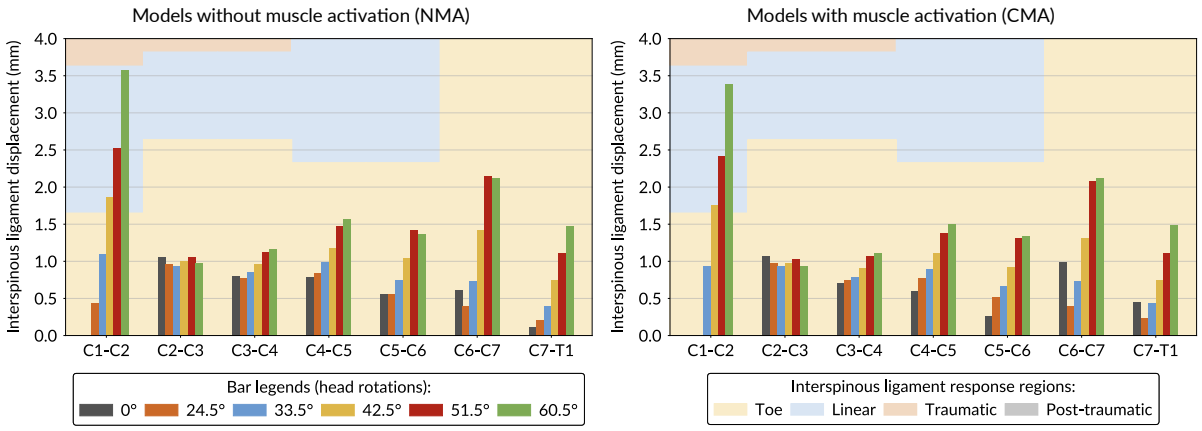


Figure B-3: Average displacement of interspinous ligaments during a 4g rear impact scenario without and with muscle activation compared with the response regions (Mattucci et al., 2012) for each intervertebral level.

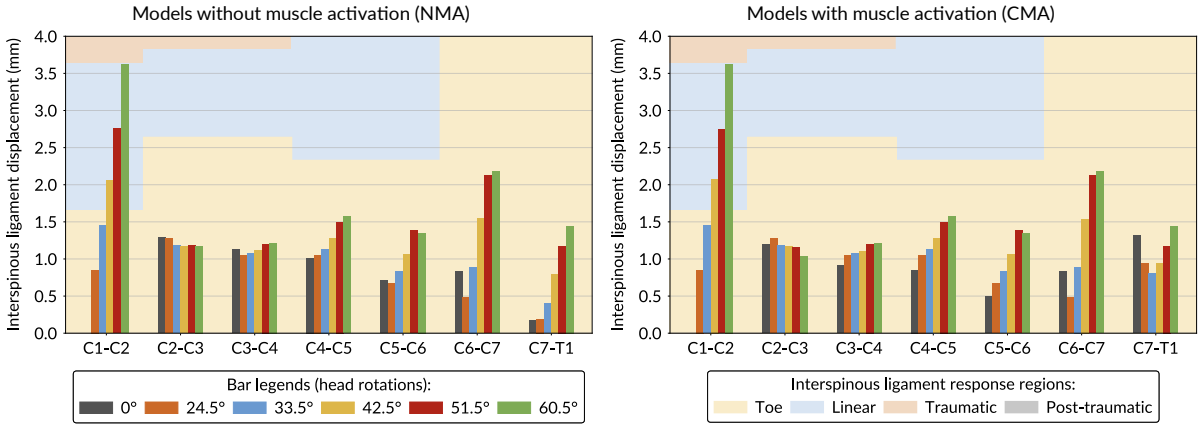


Figure B-4: Average displacement of interspinous ligaments during a 10g rear impact scenario without and with muscle activation compared with the response regions (Mattucci et al., 2012) for each intervertebral level.

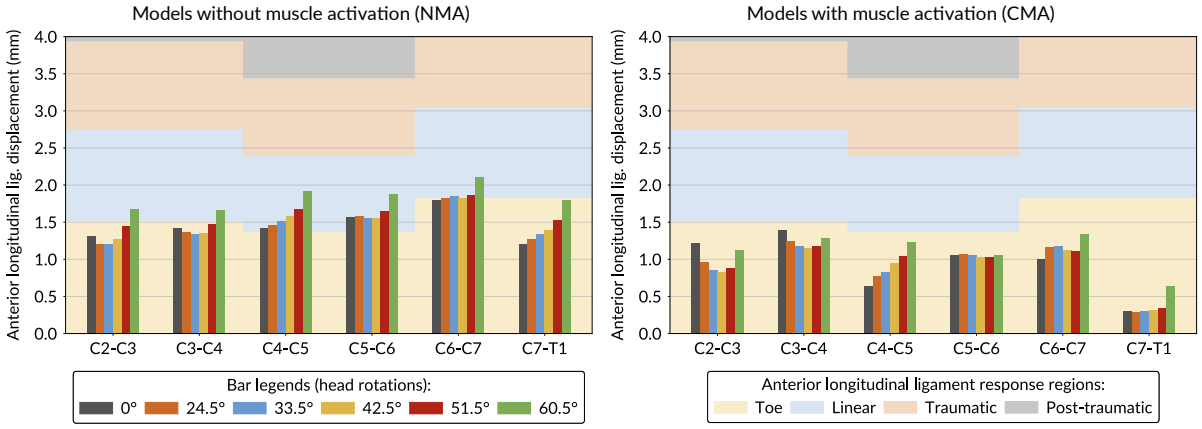


Figure B-5: Average displacement of anterior longitudinal ligaments during a 4g rear impact scenario without and with muscle activation compared with the response regions (Mattucci et al., 2012) for each intervertebral level.

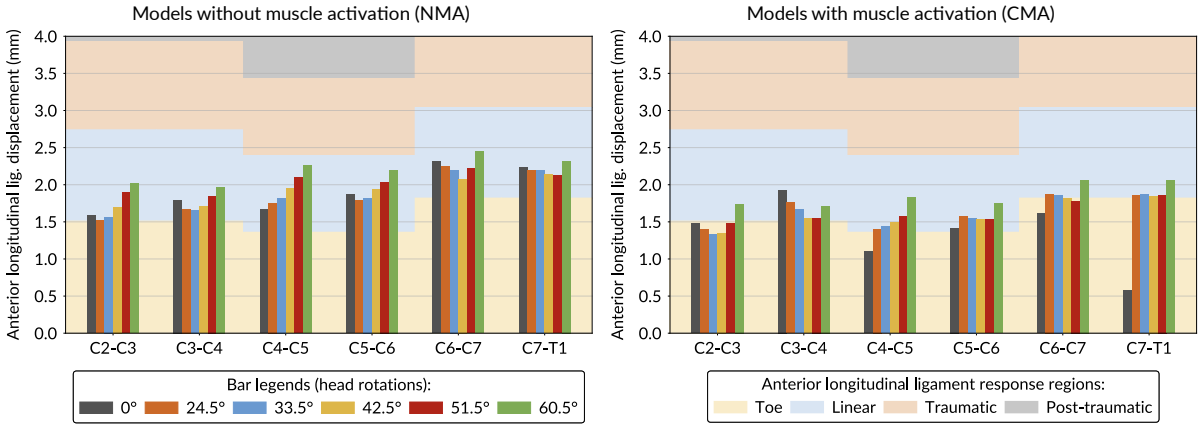


Figure B-6: Average displacement of anterior longitudinal ligaments during a 10g rear impact scenario without and with muscle activation compared with the response regions (Mattucci et al., 2012) for each intervertebral level.

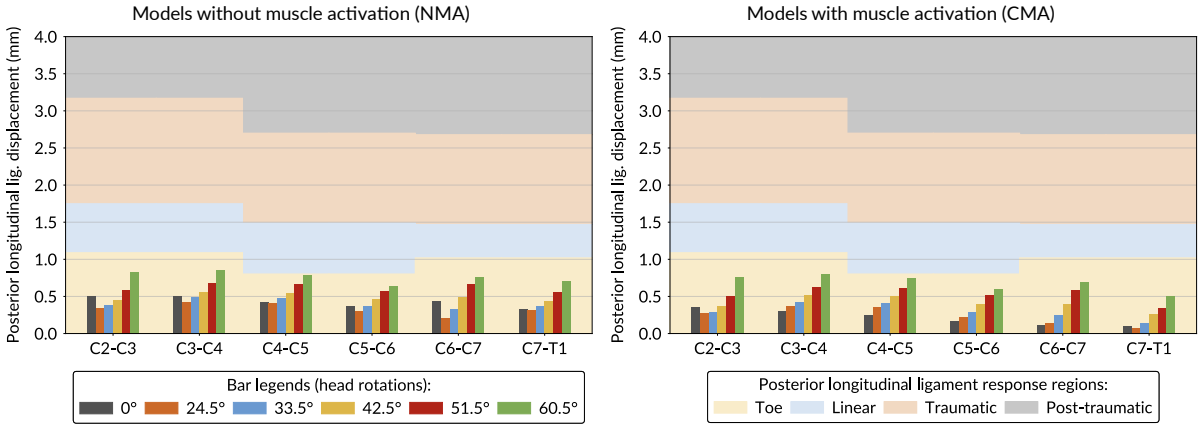


Figure B-7: Average displacement of posterior longitudinal ligaments during a 4g rear impact scenario without and with muscle activation compared with the response regions (Mattucci et al., 2012) for each intervertebral level.

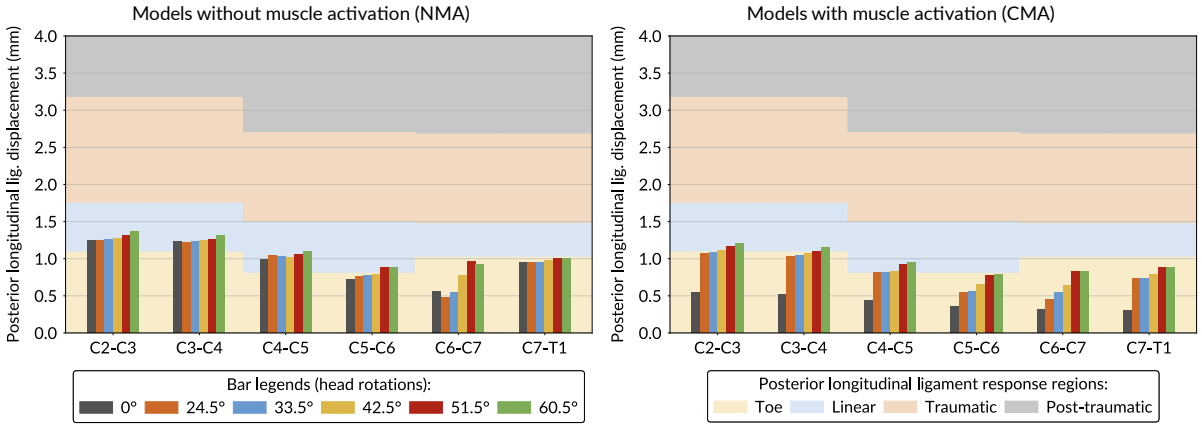


Figure B-8: Average displacement of posterior longitudinal ligaments during a 10g rear impact scenario without and with muscle activation compared with the response regions (Mattucci et al., 2012) for each intervertebral level.

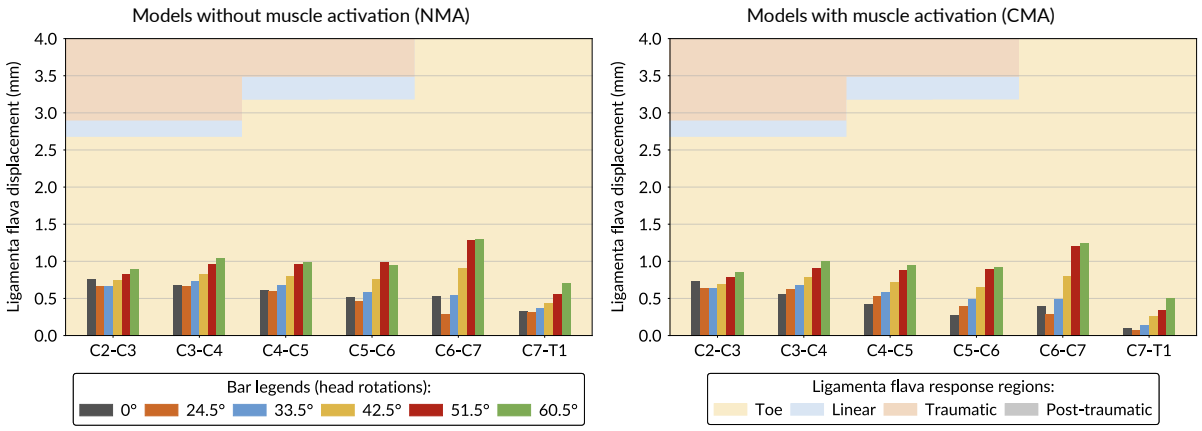


Figure B-9: Average displacement of ligamenta flava during a 4g rear impact scenario without and with muscle activation compared with the response regions (Mattucci et al., 2012) for each intervertebral level.

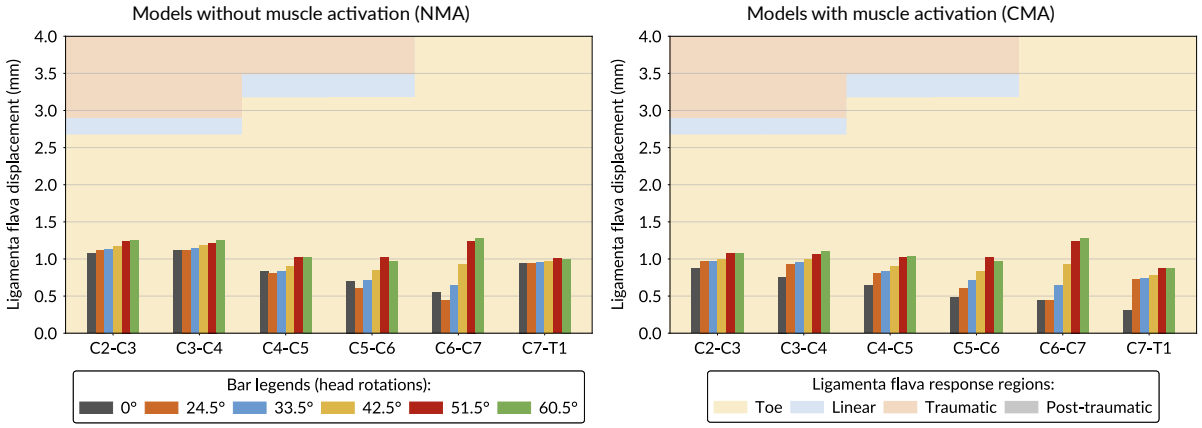


Figure B-10: Average displacement of ligamenta flava during a 10g rear impact scenario without and with muscle activation compared with the response regions (Mattucci et al., 2012) for each intervertebral level.

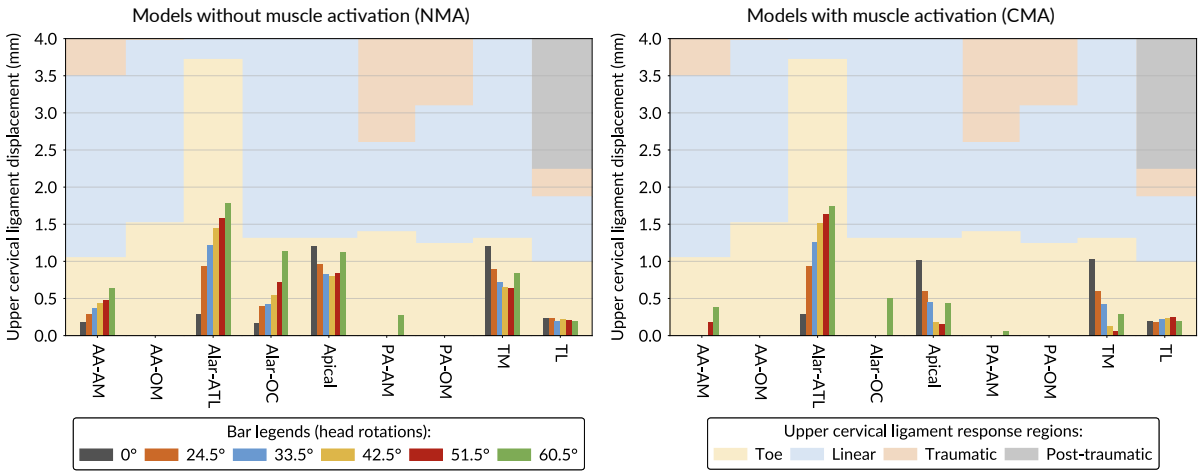


Figure B-11: Average displacement of upper cervical spine ligaments during a 4g rear impact scenario without and with muscle activation compared with the response regions (Mattucci et al., 2013) for each ligament.

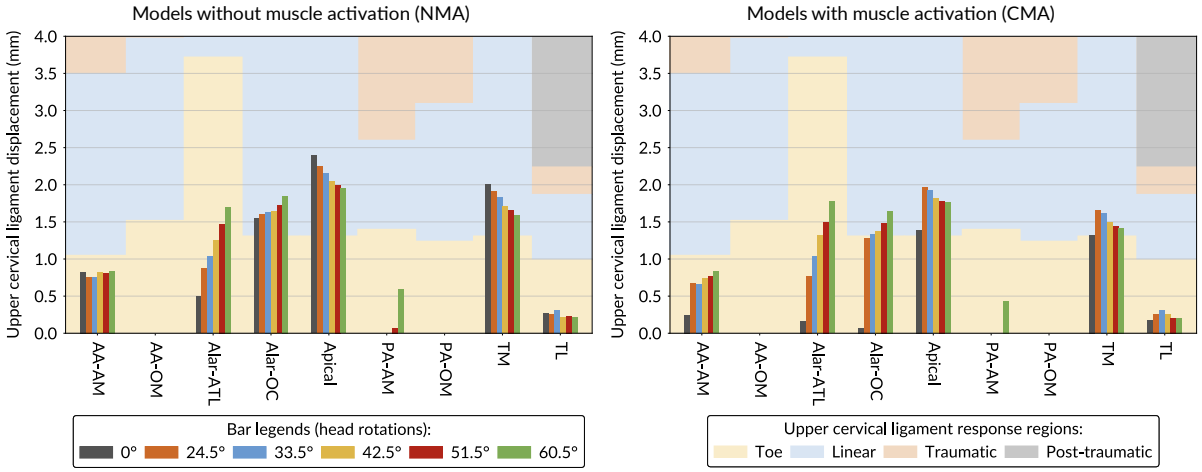


Figure B-12: Average displacement of upper cervical spine ligaments during a 10g rear impact scenario without and with muscle activation compared with the response regions (Mattucci et al., 2013) for each ligament.

Appendix C

Muscle Strain Results

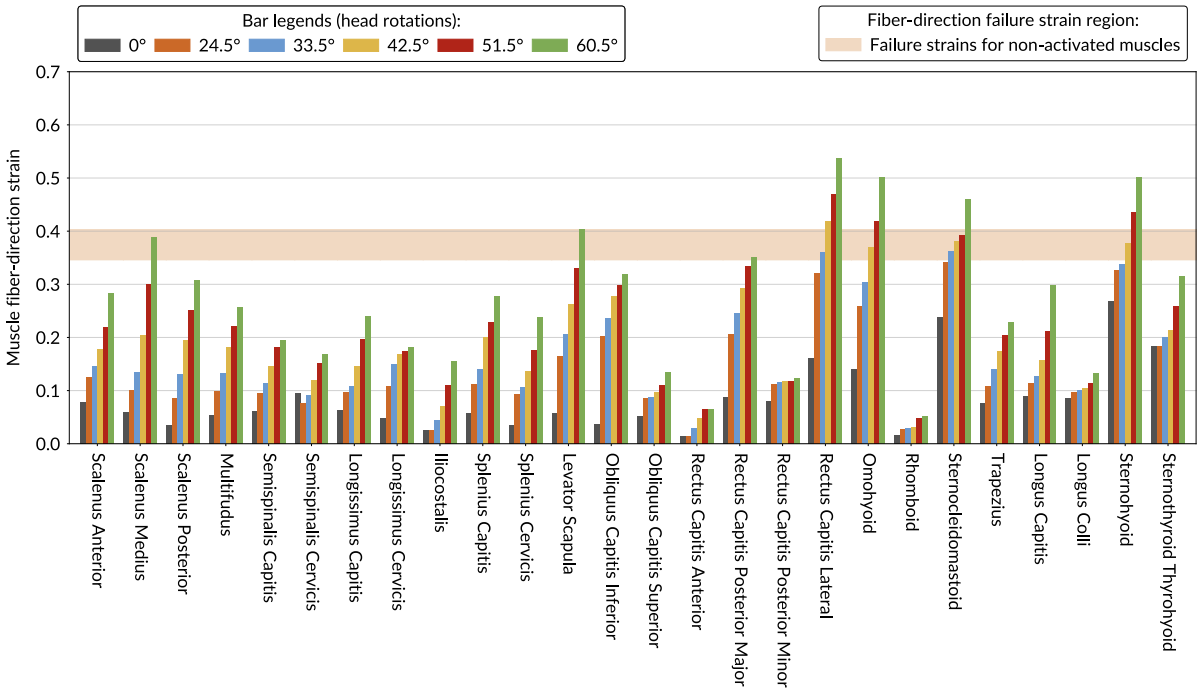


Figure C-1: 95th percentile muscle fiber-direction strains during a 4g rear impact scenario without muscle activation compared with the failure region for non-activated muscles (Best et al., 1995; Morrow et al., 2010).

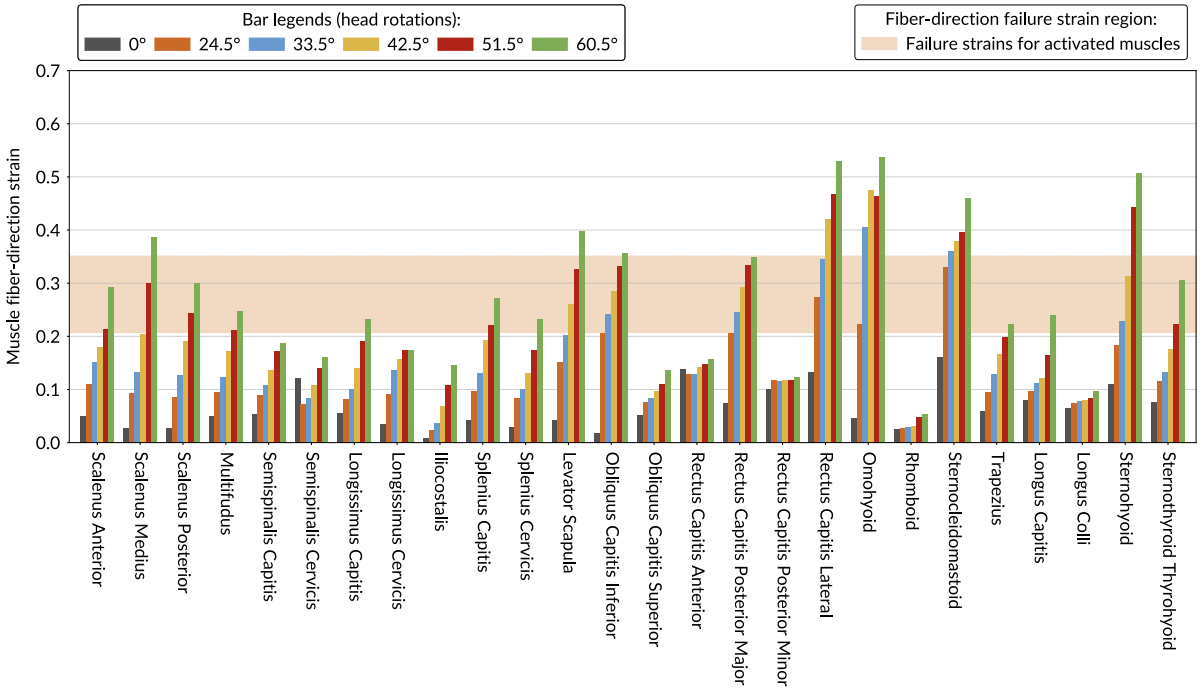


Figure C-2: 95th percentile muscle fiber-direction strains during a 4g rear impact scenario with muscle activation compared with the failure region for activated muscles (Hasselman et al., 1995).

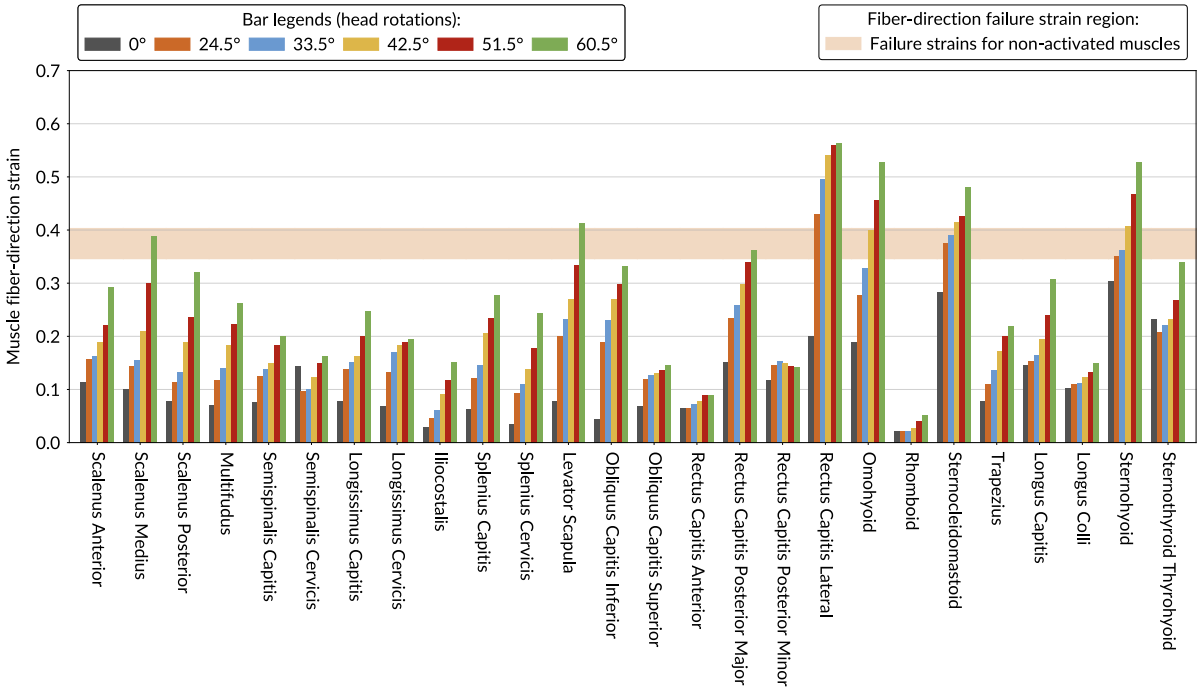


Figure C-3: 95th percentile muscle fiber-direction strains during a 10g rear impact scenario without muscle activation compared with the failure region for non-activated muscles (Best et al., 1995; Morrow et al., 2010).

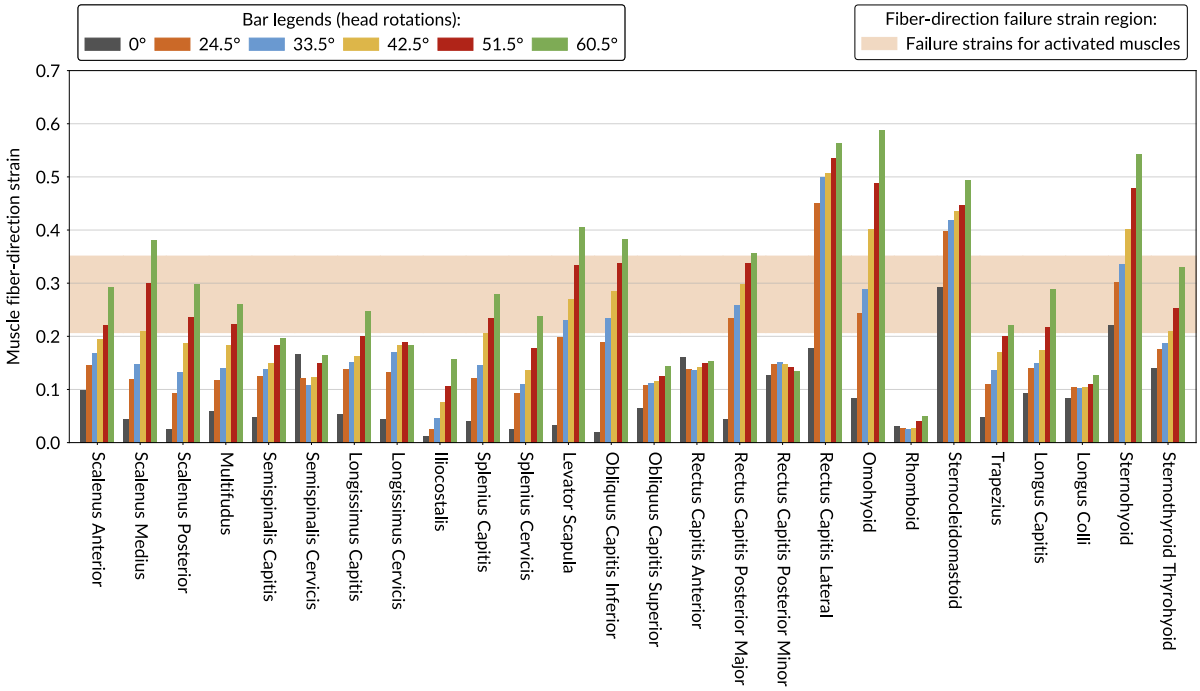


Figure C-4: 95th percentile muscle fiber-direction strains during a 10g rear impact scenario with muscle activation compared with the failure region for activated muscles (Hasselman et al., 1995).

Appendix D

Intervertebral Foramen Height and Width Reduction Results

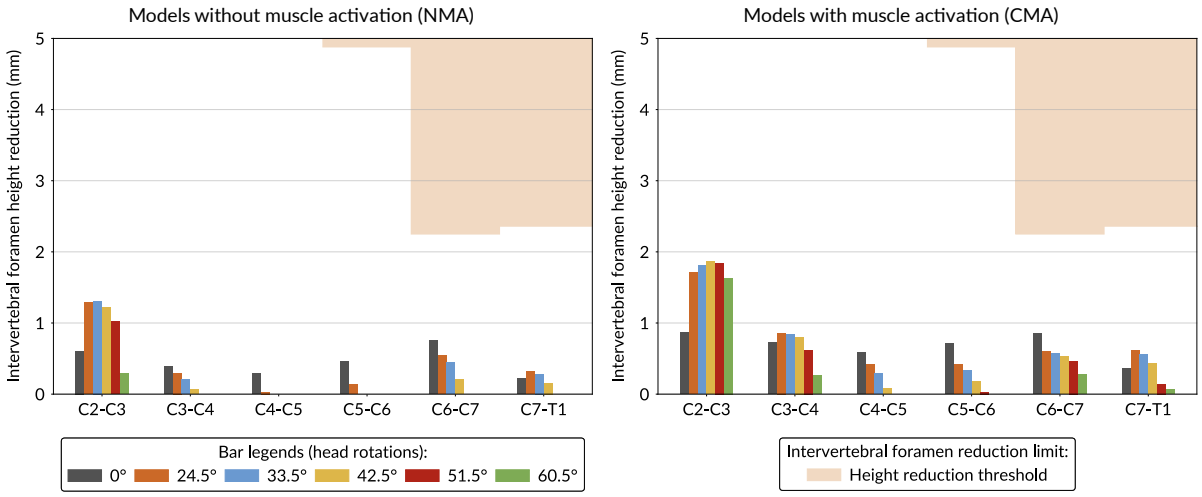


Figure D-1: Maximum intervertebral foramen height reductions during a 4g rear impact scenario without and with muscle activation compared with the threshold values.

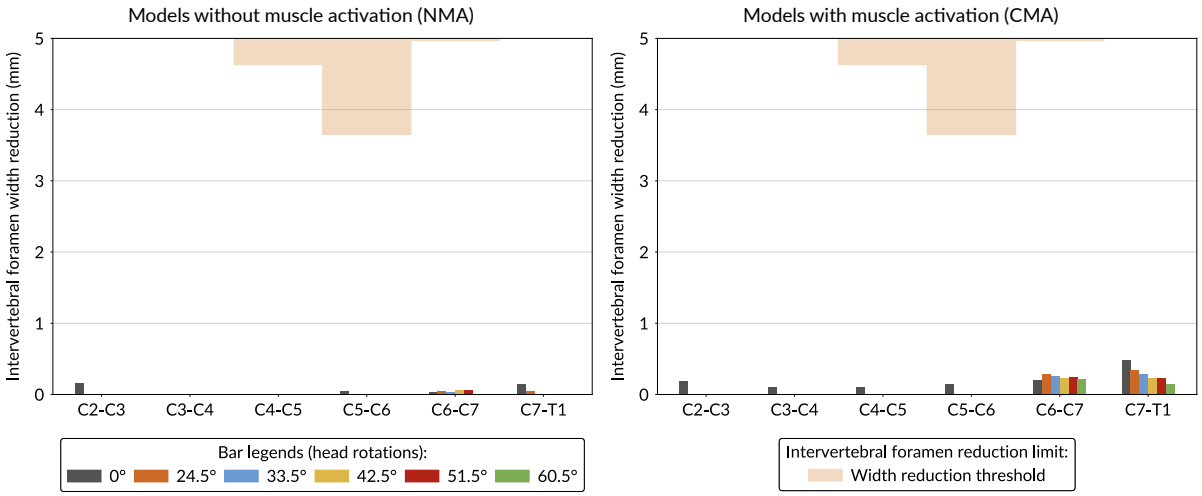


Figure D-2: Maximum intervertebral foramen width reductions during a 4g rear impact scenario without and with muscle activation compared with the threshold values.

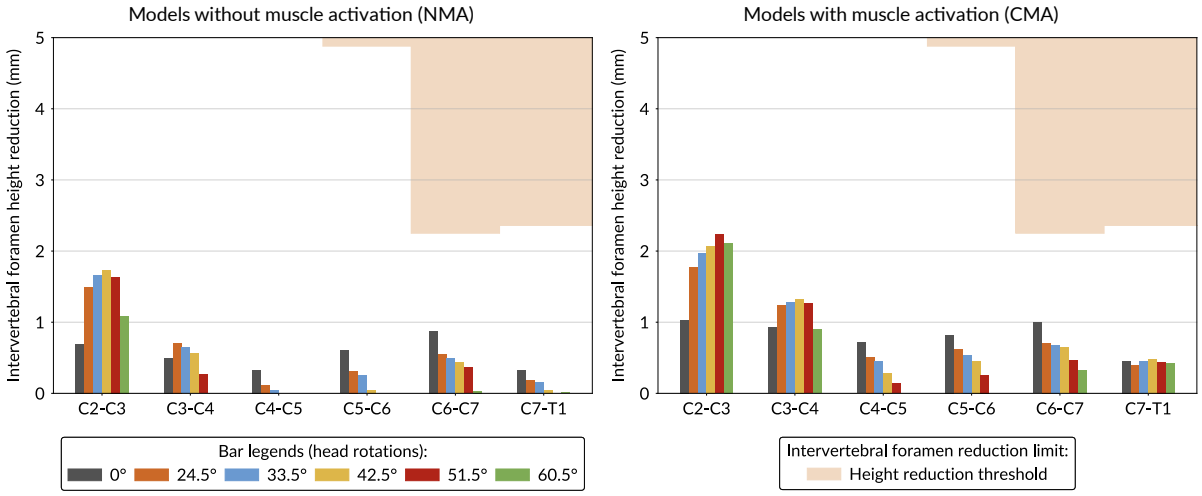


Figure D-3: Maximum intervertebral foramen height reductions during a 10g rear impact scenario without and with muscle activation compared with the threshold values.

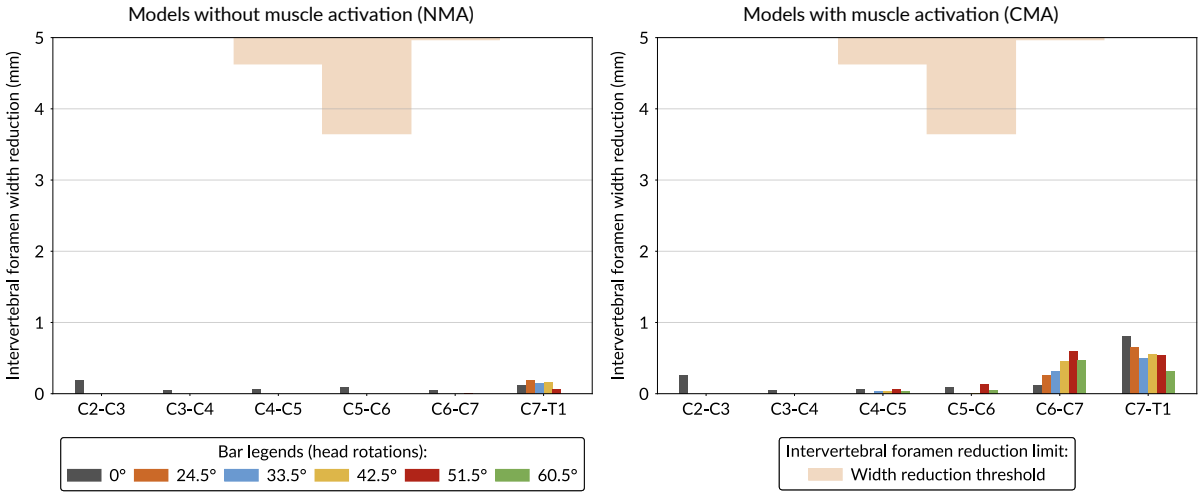


Figure D-4: Maximum intervertebral foramen width reductions during a 10g rear impact scenario without and with muscle activation compared with the threshold values.

Appendix E

Annulus Fibrosus Strain Results

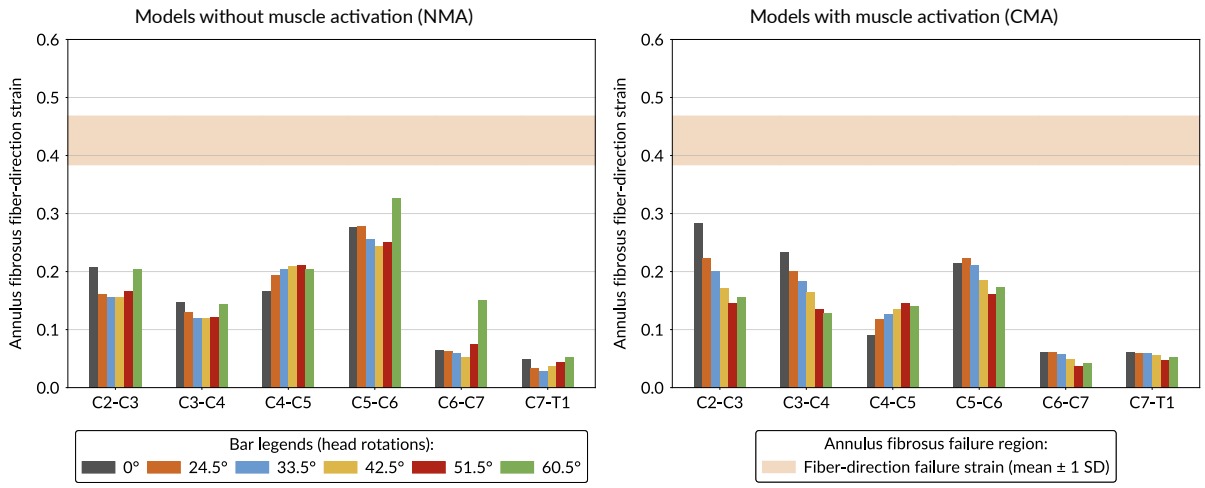


Figure E-1: Maximum quadrant fiber-direction strain of annulus fibrosus during a 4g rear impact scenario without and with muscle activation compared with the failure corridor (Iatridis et al., 2005) for each intervertebral level.

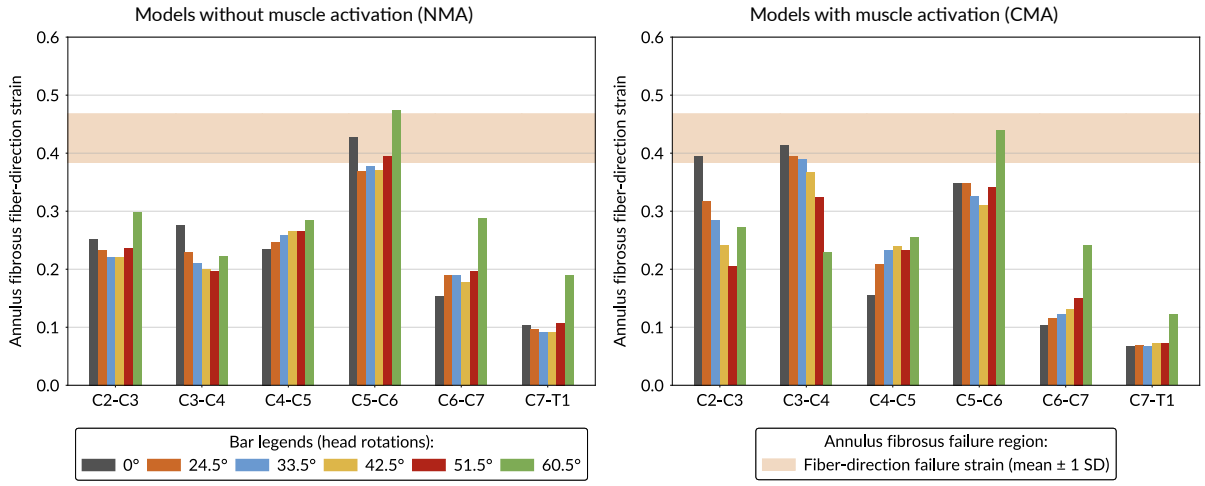


Figure E-2: Maximum quadrant fiber-direction strain of annulus fibrosus during a 10g rear impact scenario without and with muscle activation compared with the failure corridor (Iatridis et al., 2005) for each intervertebral level.